

Studies of Spin Relaxation and Recombination at the HERMES Hydrogen/Deuterium Gas Target

Dissertation der Fakultät für Physik
der
Ludwig-Maximilians Universität München

vorgelegt von Christian Baumgarten
aus Hannover

München, den 31. Mai 2000

*The universe may
Be as great as they say,
But it wouldn't be missed
If it didn't exist.*

Piet Hein

1. Gutachter: Prof. Dr. Gerhard Graw
2. Gutachter: Prof. Dr. Erhard Steffens

Tag der mündlichen Prüfung: 26. Juli 2000

Zusammenfassung

Das HERMES Experiment untersucht die Spinstruktur der Nukleonen mit Hilfe tiefinelastischer Streuung spin-polarisierter Elektronen bzw. Positronen des HERA-Strahls an den polarisierten Wasserstoff- bzw. Deuteriumkernen eines internen Speicherzellen-Gastargets. Das Targetgas wird mittels einer Stern-Gerlach Atomstrahlquelle (ABS) in eine mit Drifilm beschichtete Speicherzelle injiziert, die Teil des Elektronenstrahlrohrs des Speicherrings HERA am DESY ist.

Während ihres Aufenthalts in der Speicherzelle kollidieren die Atome miteinander und mit den Wänden der Speicherzelle, wodurch die Polarisierung des Targetgases reduziert werden kann. Die Polarisierung der Atome in einem Probenstrahl aus der Speicherzelle wird mithilfe eines Breit-Rabi Polarimeters (BRP) bestimmt. Da die Polarisierung der Moleküle mit den bei HERMES verfügbaren Mitteln nicht gemessen werden kann und auch nicht theoretisch herleitbar ist, tragen Moleküle, die durch Rekombination entstehen, wesentlich zur Unsicherheit in der Kenntnis der Targetpolarisation bei. Der relative Anteil der Atome in dem Probestrahl aus dem Targetgas - der sogenannte Dissoziationsgrad - wird mit dem Target Gas Analysator (TGA) gemessen.

Für die Bestimmung der Targetpolarisation aus den am Probestrahl bestimmten Werten der Polarisierung und des atomaren Anteils werden sogenannte *Sampling*-Korrekturen benötigt. Für eine als homogen angenommene Zelloberfläche sind dies eindeutige Relationen, die z.B. mithilfe einer Molekularstromrechnung ermittelbar sind. Die Analyse der Daten zeigt jedoch, daß die Zelloberfläche durch den Einfluß des Elektronenstrahls verändert wird, wodurch die Annahme einer homogenen Zelloberfläche nicht aufrechterhalten werden kann. Es werden Modelle entwickelt, die es erlauben, den Bereich möglicher *Sampling*-Korrekturen mithilfe der am Probestrahl gemessenen Werte einzugrenzen. Es zeigt sich, daß die systematische Unsicherheit der Targetpolarisation etwa proportional zur Stärke von Rekombination und Wandstoßrelaxation ist. Eine präzise Unterscheidung des molekularen Anteils, der durch Rekombination verursacht wird, und anderen molekularen Anteilen wie z.B. dem Restgasdruck sowie der einzelnen Faktoren, die die atomare Polarisierung reduzieren, ist daher für eine genaue Bestimmung der Targetpolarisation unerlässlich.

Erster Teil: Mess- und Analysesystem. Es wird eine systematische Untersuchungen einzelner Komponenten des Targets, insbesondere des BRPs, vorgenommen. Die Effizienzen der Hochfrequenzübergänge des BRP werden für den Betrieb mit Wasserstoff als auch für Deuterium mit einer typischen Genauigkeit von 1 – 2 % bestimmt. Auch das Verhältnis der Transmissionen für die Hyperfeinstrukturzustände $|1\rangle$ und $|2\rangle$ des Wasserstoffs wird in Abhängigkeit von der Speicherzellentemperatur experimentell bestimmt.

Mithilfe der neu entwickelten Methode der Verwendung pulsmodulierter Hochfrequenzübergänge konnte die geschwindigkeitsabhängige Transmission der Atome im BRP Sechspolssystem gemessen und die Abhängigkeit der Zählraten im BRP von der Speicherzellentemperatur bestimmt werden. Der Vergleich der atomaren Strahlintensitäten zwischen BRP und TGA ermöglicht Aussagen über die Oberflächeneigenschaften des Probenstrahlrohres. Mithilfe der Technik modulierter Hochfrequenzübergänge wird eine experimentelle Überprüfung der Vorhersagen der Molekularstrom-Simulation zum Teilchentransport durch die Speicherzelle durchgeführt. Für die konventionelle Speicherzellen-Geometrie konnte die mittlere gesamte Trajektorienlänge von Atomen, die in den Probestrahl des BRP gelangen, zwischen Eintritt und Austritt aus der Speicherzelle in Übereinstimmung mit der Simulation zu 417 cm bestimmt werden.

Zweiter Teil: Physik der Rekombination und Spinrelaxation. Es wird die Physik der Rekombination und Spinrelaxation der Wasserstoff- und Deuteriumatome in Abhängigkeit von Speicherzellentemperatur und magnetischem Haltefeld anhand der Daten, die am HERMES Target gemessen wurden, analysiert.

Anhand der Temperatur- und Dichteabhängigkeit der Rekombination konnten drei Reaktionsmechanismen unterschieden werden: Der erste Mechanismus, der bei Temperaturen ober-

halb 120 K dominiert, konnte als aktivierter Eley-Rideal Prozess mit Aktivierungsenergien von 31.6 meV für Wasserstoff bzw. 68 meV für Deuterium interpretiert werden. Für die Rekombination bei tieferen Temperaturen wurden zwei unterschiedliche Mechanismen gefunden, ein dichteabhängiger Prozess, der als chemische Reaktion zwischen physisorbierten Atomen interpretiert werden kann und ein dichteunabhängiger Prozess, der vermutlich auf die Reaktion der physisorbierten Atome mit den Wasserstoffatomen der Methylgruppen der Beschichtung zurückzuführen ist. Es wird gezeigt, daß diese Prozesse sich auch in ihrer Temperaturabhängigkeit unterscheiden. Beide Prozesse sind zur Aufenthaltsdauer auf der Oberfläche, der dichteabhängige jedoch zusätzlich zur Anzahl der besuchten Oberflächenplätze proportional. Die Bindungsenergie E_b konnte mithilfe dieser Annahmen für beide Isotope zu etwa 23 meV und die Aktivierungsenergie E_j für Oberflächendiffusion zu etwa 8 meV bestimmt werden. Des Weiteren konnte gezeigt werden, wie der laufende Betrieb des Targets im HERA-Strahl die Oberflächenstruktur der Speicherzellenbeschichtung derart beeinflußt, daß bei einer neuen Speicherzelle der dichteunabhängige und bei einer alten der dichteabhängige Prozeß das Rekombinationsverhalten dominiert.

Die Analyse der Spinrelaxationsmessungen ergab neben der Bestimmung der Relaxationsparameter auch den Wert der injizierten Polarisation und somit Abschätzungen der Effizienzen der Hochfrequenzübergänge der ABS. Bei Wasserstoff konnte die injizierte Polarisation am Arbeitspunkt zu $\pm 97.3\%$, der mittlere Verlust an Kernpolarisation durch Spinaustauschstöße zu etwa 3.3% und der durch Wandstoßdepolarisation zu 2% ermittelt werden. Die Relaxationsmessungen ergaben für das Wasserstofftarget eine typische Targetflächendichte von $7.4 \cdot 10^{13} \text{ nucl cm}^{-2}$, woraus sich ein atomarer Fluß der ABS von etwa $6.4 \cdot 10^{16} \text{ s}^{-1}$ errechnet. Aus den Messungen mit Deuterium ergab sich eine typische Targetflächendichte von $1.05 \cdot 10^{14} \text{ nucl/cm}^2$ und somit ein atomarer Fluß der ABS bei drei injizierten Hyperfeinstrukturzuständen von etwa $4.5 \cdot 10^{16} \text{ s}^{-1}$. Dieser Fluß ist etwa 30% geringer als für Wasserstoff. Die Targetpolarisation wurde für das Jahr 1997 zu ± 0.852 mit einem syst. Fehler von ± 0.03 bestimmt. Die vorläufigen Ergebnisse ergeben eine Targetpolarisation von ± 0.82 und einen syst. Fehler von etwa ± 0.02 für die Datennahme 1999 mit Deuterium.

Die Messungen zur Wandstoßdepolarisation ergaben eine im erreichbaren Frequenzbereich konstante spektrale Dichte, woraus sich ein Hochtemperaturlimit τ_c^0 der Korrelationszeit von weniger als $2.3 \cdot 10^{-12} \text{ s}$ ergibt. Es zeigte sich ein Sättigungsverhalten der Wandstoßdepolarisation weit unterhalb einer Spinflipwahrscheinlichkeit von $\frac{1}{2}$, das so noch nicht beobachtet oder beschrieben wurde, jedoch theoretisch verstanden werden kann. Insbesondere zeigten die Messungen mit Wasserstoff bei tiefen Temperaturen eine Zunahme der Elektronenpolarisation, die nur durch Austauschwechselwirkung mit einer statisch magnetisierten Speicherzellenoberfläche erklärbar scheint.

Die Messungen zur Wandstoßrelaxation von Deuterium zeigen bei schwachem Haltefeld eine Zunahme der Relaxation, die z.T. durch die Multipletstruktur und z.T. durch einen Mechanismus erklärt werden kann, der üblicherweise *cross-relaxation* genannt wird. Andere Unterschiede in der Spin-Relaxation der beiden Isotope konnten auf Unterschiede in der Beschichtung der Speicherzellen zurückgeführt werden.

Die Bündelung des HERA-Elektronenstrahls in *bunchen* erzeugt ein elektromagnetisches Hochfrequenzfeld, das im Resonanzfall die Polarisation des Targetgases stark reduzieren kann. Die Messung am Deuteriumtarget zeigt schon bei relativ geringen Strahlströmen ein Sättigungsverhalten, das qualitativ gut verstanden ist. Die Haltefelder, bei denen die Resonanzen auftreten, sind in Übereinstimmung mit den Berechnungen und die Resonanzen konnten den einzelnen Hyperfeinstrukturübergängen zugeordnet werden.

Acknowledgements

Mein besonderer Dank gilt Herrn Prof. Dr. G. Graw für die Ermöglichung und Betreuung dieser Arbeit, sowie Herrn Prof. Dr. E. Steffens für seine Unterstützung und Betreuung sowohl meiner Diplomarbeit am HERMES Target als auch bei der Durchführung der vorliegenden Arbeit. Bei Dr. B. Braun, Dr. H. Kolster, Dr. R. Hertenberger, Dr. J. Stewart und T. Wise bedanke ich mich für die hervorragende Zusammenarbeit und Unterstützung bei der Erstellung dieser Arbeit, ebenso bei Dr. G. Court, Dr. U. Stoesslein und M. Heno für die vielen Anregungen und Diskussionen. Bei den Mitarbeitern und dem Direktorium des DESY bedanke ich mich für die Möglichkeit, diese Arbeit durchführen zu können.

Allen Mitgliedern des HERMES Experiments danke ich für die freundliche Aufnahme in der HERMES Kollaboration und die herzliche und produktive Zusammenarbeit. Allen am Targetaufbau und Betrieb beteiligten Personen, insbesondere auch in den am Target beteiligten Instituten und ihren Werkstätten, die ich hier weder vollständig aufzählen noch angemessen würdigen kann, spreche ich meinen herzlichen Dank für ihre Beiträge aus. Besonders genannt seien Dr. J. Stenger und Dr. C. Grosshauser für ihren Beitrag am Aufbau des Target Gas Analyzers, B. Braun, H. Kolster, M. Heno, C. Simani und für die gute Zusammenarbeit am Target Polarimeter, Dr. R. Hertenberger und Dr. P. Schiemenz für die Unterstützung bei der Vorbereitung des Deuterium Targets, A. Golendoukhin, Dr. N. Koch und A. Nass für ihre Arbeit an der Atomstrahlquelle, Dr. G. Court, Dr. J. Stewart, J. Morton, D. Muskett, für ihre Arbeit am Targetmagneten und der Kryotechnik, T. Wise und Dr. P. Lenisa für ihre Arbeit an der Targetzelle, Prof. Dr. R. Milner, M. Sutter, J. Martin und T. Shin für ihre Arbeit am unpolarisierten Gaseinlaßsystem, Dr. M. Kirsch, Dr. W. Brückner und V. Shutov für ihre Beiträge am Aufbau und Pflege der Datennahme, sowie J. Plett, V. Prahl und K. Hakelberg und M. Krüger für ihre technische Unterstützung. Mein Dank für die hervorragende Teamarbeit und das gute Arbeitsklima gilt neben den schon genannten I. Brunn, Prof. Dr. P. Dalpiaz, S. Frabetti, E. Garutti, R. Mussa, D. Reggiani und S. Tessarin, sowie allen Mitgliedern der Targetgruppe.

B. Braun und H. Kolster bin ich für ihre hervorragende Arbeit am Target Polarimeter, der Betriebs- und Datenaufbereitungs-Software sowie für unzählige Diskussionen und Anregungen, ohne die diese Arbeit so nicht zustande gekommen wäre, zu besonderem Dank verpflichtet.

Den Mitgliedern der HERMES Polarimeter Gruppe meinen herzlichen Dank für ihr Interesse, ihre Geduld und ihr Engagement im Rahmen des gemeinsamen Schichtbetriebs. Viele der in dieser Arbeit vorgestellten Messungen sind durch ihre stete Bereitschaft zur Mitarbeit zustande gekommen.

Des weiteren danke ich Prof. Dr. D. Fick und Dr. H. J. Jänsch für wertvolle Diskussionen und Anregungen.

Bei der HERMES Software Gruppe, insbesondere Dr. K. Ackerstaff, Dr. M. A. Funk und Dr. W. Wander bedanke ich mich für ihre Arbeit an den Softwarepaketen PinK und DAD sowie für die Geduld, mit der sie meine Fragen beantwortet haben.

Den Linux-Entwicklern, dem GNU-Projekt sowie der CERN Softwaregruppe danke ich für die Verfügbarmachung des hervorragenden Betriebssystems Linux sowie der unzähligen Programme, die bei der Durchführung dieser Arbeit benutzt wurden. Besonders erwähnt seien PAW, ADAMO sowie die Libraries vom CERN, \LaTeX , XEmacs und der C-Compiler von GNU.

Meiner Familie und insbesondere meinen Eltern danke ich für die Möglichkeit des Physik Studiums.

Und vor allem danke ich Britta für ihre Geduld und ihr Vertrauen.

Contents

1	Introduction	1
1.1	The Polarized Internal Hydrogen/Deuterium Target	2
1.2	The Target Polarization	3
1.3	Motivation	4
2	Extended Introduction	5
2.1	The Hyperfine Structure of Hydrogen and Deuterium	5
2.2	Hyperfine Transitions	8
2.3	Spin Separation in Sextupole Magnets	10
2.4	Diffusive Molecular Flow in Long Tubes	11
2.5	Recombination and the Atomic Fraction α	14
2.6	The Concept of Collision Ages	16
3	The Experimental Setup	17
3.1	The Target Chamber and the Superconducting Magnet	17
3.2	The Storage Cell	18
3.3	The Unpolarized Gas Feed System (UGFS)	20
3.4	The Atomic Beam Source (ABS)	20
3.5	The Target Gas Analyzer (TGA)	24
3.5.1	Interpretation of the TGA Beam Rates	25
3.5.2	Calibration of the TGA	27
3.5.3	Calibration of the TGA with a HERA Beam Loss	28
3.5.4	The Separation of Initial Atomic Fraction (α_0^{TGA}) and the Fraction of Atoms Surviving Recombination (α_r^{TGA})	29
3.5.5	Interpretation of the Atomic Fraction α_r^{TGA}	31
3.6	The Breit Rabi Polarimeter (BRP)	33
3.6.1	Theory of Polarization Measurement	35
3.6.2	Calibration of the BRP	37
3.6.3	Systematic Uncertainty of the Polarization Measurement	38
3.6.4	Sextupole Transmissions of the BRP	39
3.6.5	Total Intensity I_{tot} of the BRP	41
3.6.6	Time of Flight Measurements with the BRP	42
3.7	The Luminosity Monitor	45
3.8	Summary	47
4	Sampling of BRP and TGA	48
4.1	Measurement of the Diffusion Time Distributions	50
4.2	Influence of Recombination on the Diffusion Time	52
5	Analysis of the Measurements of Recombination	54
5.1	Introduction	54
5.2	Physisorption and Surface Diffusion	55
5.2.1	Surface Coverage and Diffusion of Physisorbed Atoms	56
5.2.2	Sticking Time in Case of Low Binding Energy	58
5.3	The Temperature Dependence of Recombination	58
5.3.1	High Temperature Behavior of Recombination	59
5.4	Low Temperature Behavior of Recombination	60

5.4.1	The Density Dependent Contribution to Recombination	62
5.4.2	The Density Independent Contribution of Recombination	64
5.5	The Effect of the HERA Beam and of Water on Recombination	65
5.6	Summary	68
6	Analysis of Spin Relaxation Measurements	69
6.1	Introduction	69
6.2	The Master Equation	71
6.2.1	The Depolarization Probabilities	73
6.3	The Dependence of Spin Exchange Relaxation on Density	73
6.4	The Effect of Recombination on Spin Relaxation	74
6.5	Direct Determination of the Injected Polarization for Hydrogen	76
6.6	Theory of Wall Depolarization	78
6.7	The Temperature Dependence of Hydrogen Spin Relaxation	81
6.7.1	Interpretation of the Measurements by Exchange Interaction	84
6.7.2	Collection of Hydrogen Temperature Dependence Measurements	88
6.8	The Magnetic Field Dependence of Hydrogen Spin Relaxation	88
6.8.1	ABS Efficiencies and Injected Polarization for Hydrogen	92
6.8.2	Determination of the Hydrogen Density from the Spin Exchange Effect	92
6.9	Measurement and Analysis of the Transition Spectra	95
6.9.1	The Spectrum of Hydrogen Spin Relaxation	96
6.10	Measurements of Deuterium Spin Relaxation	98
6.10.1	The Temperature Dependence of Deuterium Relaxation Measurements	98
6.10.2	The Injected Polarization in Deuterium Running	100
6.10.3	The Spectrum of Deuterium Spin Relaxation	102
6.10.4	The Magnetic Field Dependence of Deuterium Spin Relaxation	106
6.10.5	Relaxation of $\langle \vec{I}\vec{S} \rangle$, Spin-Exchange and Target Density	107
6.11	Bunch Field Induced Resonant Depolarization	109
6.12	Summary	112
7	Target Polarization and Sampling Corrections	113
7.1	The Sampling Corrections c_α and c_P	114
7.2	The Atomic Polarization P_a	117
7.3	The Reduction of the Target Polarization by Recombination	118
7.4	Summary	120
8	Discussion and Outlook	121
	Appendix	123
A	Results of Deuterium Spin Relaxation	123
B	The Hyperfine Structure of Hydrogen and Deuterium	128
B.1	The Diagonalization of the Static Hamiltonian	128
B.2	Hyperfine Transitions	130
B.2.1	σ -Transitions	130
B.2.2	π -Transitions	131
B.2.3	Adiabatic High Frequency Transitions	132

B.2.4	Strong Field Transitions	134
B.2.5	Weak/Medium Field Transitions	135
B.3	The Stern-Gerlach-Force of Sextupole Magnets	138
C	Diffusion by Molecular Flow	140
C.1	Wall Collisions	140
C.2	Calculation of the Diffusion Constant for Long Tubes	142
C.3	Diffusion and Wall Collision Ages	143
C.3.1	Moments of Collision Age Distributions (CAD)	145
C.4	Diffusion and Recombination	146
C.4.1	Moments of the CAD by Laplace Transformation	148
C.4.2	First Order Approximation of Collision Age Distributions	149
C.4.3	Expected Effect of the Density Dependence of Recombination	151
C.5	Differential Collision Ages	152
C.6	Diffusion and Spin Relaxation - the Rate Equation	153
C.6.1	The Master Equation	154
C.6.2	Spin Exchange Collisions and The Correlation Factor	155
C.7	The Model of Distributed Sources	156
C.8	The Model of Localized Sources	158
D	Spin Relaxation	164
D.1	Theory of Spin Relaxation by a Fluctuating Field	164
D.2	Theory of Resonant Relaxation	165
D.2.1	The Transition Probabilities	167
D.2.2	The Saturation Factor	168
D.2.3	The Spectrum of a Transition	169
D.3	The Matrix Elements of Wall Depolarization	170
D.4	Spin Exchange Collisions	171
D.5	The Transformed Master Equation for Hydrogen	175
D.5.1	Hydrogen Spin Exchange Relaxation	176
D.5.2	Approximate Solution of the Master Equation for Hydrogen	177
D.5.3	Exact Solution of the Master Equation for Hydrogen	178
D.6	Deuterium Spin Exchange Collisions	180
D.6.1	The High Field Limit of Deuterium Spin Relaxation	181
E	Target Setup For Deuterium Running	182
F	Geometry of Target Hardware	185
G	Slow Control, Data Aquisition and Online Monitoring	187
H	Data Analysis	190
I	Physical Constants	192
	List of Figures	193
	List of Tables	195
	References	196

1 Introduction

The HERMES (HERA measurement of spin) experiment is located in the eastern straight section of the HERA storage ring at DESY in Hamburg. It is designed to study the spin structure of the nucleons by deep inelastic scattering of polarized positrons resp. electrons provided by the HERA storage ring at 27.5 GeV impinging on the nucleons of internal polarized gas targets [Mil 97, HER 90, HER 93]. The setup of the HERMES experiment is shown in fig. 1.1.

First results are the measurement of the spin structure functions g_1^n with the polarized ^3He target (1995) and of g_1^p with the polarized atomic hydrogen target, which was operated in 1996 and 1997 [She 98, HER 97, HER 98a]. Beneath the *inclusive* physics, the possibility to detect and identify hadronic scattering products allows the measurement of *semi-inclusive* processes with the HERMES spectrometer [HER 98c] using polarized and unpolarized targets, which is the central item of the HERMES physics program. First results are published [HER 98e, HER 98d, HER 99b, HER 99a].

HERMES extends the results of previous high energy spin experiments with polarized solid state targets, as they have been performed by the SMC-Collaboration at CERN [Ade 93, Ada 94, Ada 97a, Ada 97b] and the SLAC-experiments E142 [Ant 93], E143 [Abe 95], E154 [Abe 97] and E155 [Bor 98].

The positrons of the HERA ring are transversally polarized by the Solokov-Ternov effect [Sol 64]. Spin rotators, located up and downstream of the HERMES experiment, are used to provide longitudinal polarization at the HERMES target. A transversal polarimeter (TPOL) - located in the west section of HERA - and a longitudinal polarimeter (LPOL) near the HERMES experiment are used to measure the polarization of the positron beam [Bar 93, Bar 94, Loz 97].

Internal polarized gas targets in storage rings have also been used by other recent experiments at IUCF [Rat 98, Prz 98, Mey 98] and at COSY [Alb 97].

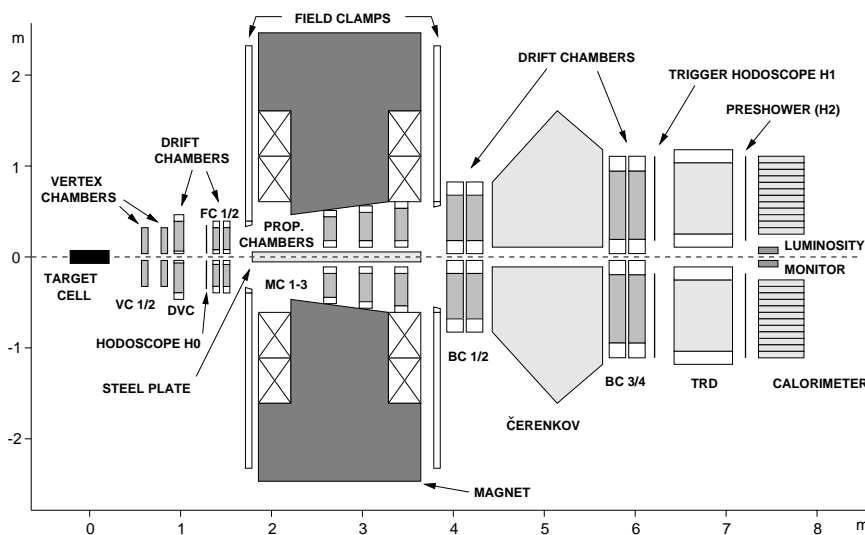


Fig. 1.1: Schematic side view of the HERMES experiment. The target section is on the left. The HERA beam passes target and spectrometer from the left to the right.

1.1 The Polarized Internal Hydrogen/Deuterium Target

Fig. 1.2 shows the components of the polarized hydrogen/deuterium target. It consists of an atomic beam source (ABS), which injects a spin polarized beam of hydrogen or deuterium atoms into a thin walled storage cell, a Breit-Rabi-type polarimeter (BRP) and a target gas analyzer (TGA). The storage cell increases the target nucleon density by about two orders of magnitude compared to a free jet target. A superconducting magnet around the storage cell provides a longitudinal magnetic holding field of up to 350 mT, which defines the quantization axis for the spins and reduces relaxation processes of the nuclear spins such as wall depolarization and spin exchange collisions because of the field dependent decoupling of the nuclear from the electron spin. The strong holding field is also required to achieve high polarization of the mixed hyperfine states.

The target storage cell, which is part of the HERA beam tube, is made out of 70 μm thin aluminum foil and is coated with Drifilm [Swe 88, Tho 87]. It has an elliptical shape of $29.8 \times 9.8 \text{ mm}$ and is 400 mm long. The cell is mounted on aluminum rails, which are cooled by gaseous helium. Two side tubes are connected to the storage cell at the center, one for the injection of the atomic beam and the other one to enable a sample of atoms to enter the BRP and the TGA.

The atomic beam source (ABS) is composed of a radio frequency dissociator¹, in which the H_2 respectively D_2 molecules are dissociated, a sextupole system to select the atoms in the electron spin state $m_S = +\frac{1}{2}$ and reject atoms with $m_S = -\frac{1}{2}$ by means of Stern Gerlach separation, and adiabatic high frequency transition (HFT) units, which are used to transfer the polarization of the electron spin to the nuclear spin. The polarized atomic beam is *ballistically* injected via the injection tube into the target storage cell, where the

¹Since beginning 2000, the rf-dissociator is replaced by the recently developed microwave dissociator [Koc 99].

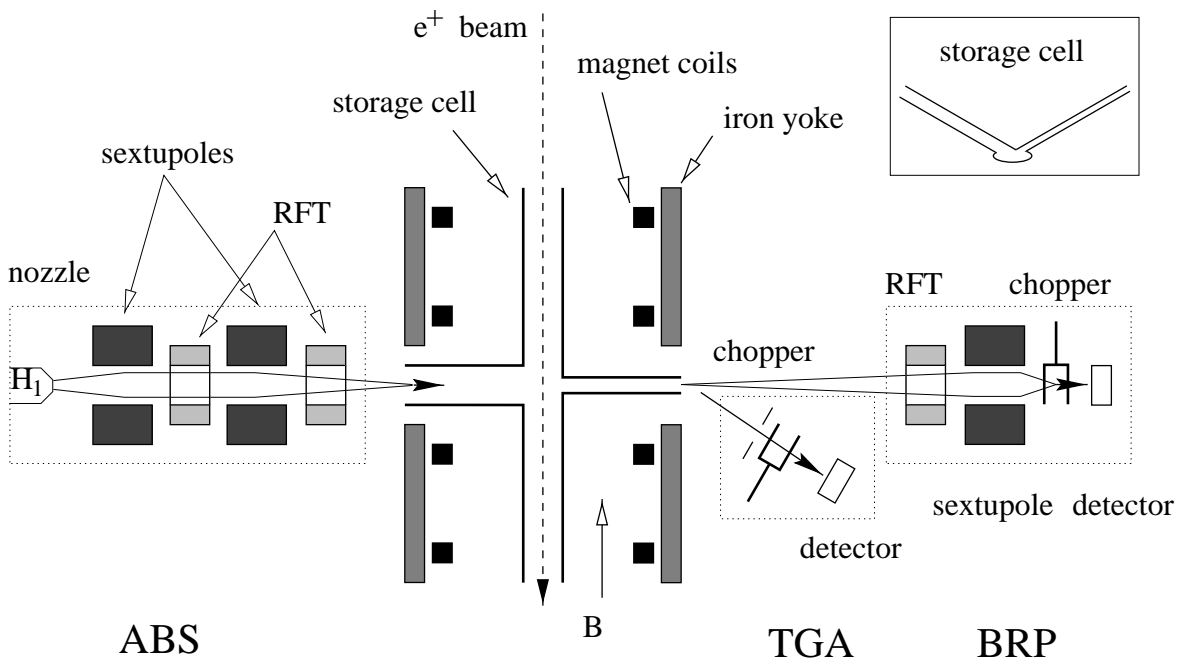


Fig. 1.2: Schematic top view of the HERMES polarized hydrogen/deuterium target assembly.

atoms start to diffuse towards the openings. During the diffusion process, the atoms are subject of processes like spin relaxation and recombination.

The target gas analyzer (TGA) consists of a chopper, a cross beam ionizer and a quadrupole mass spectrometer (QMS) in combination with a channeltron for single ion detection. It is used to measure the relative amount of atoms and molecules in the sample beam. This measurement is used to determine the atomic fraction inside the storage cell, which enters the calculation of the target polarization.

The Breit-Rabi polarimeter (BRP) consists of two adiabatic high frequency transition units (HFTs), a sextupole system, a chopper and a QMS. Switching the HFT units allows to select atoms in different combinations of hyperfine states, which have to pass the sextupole spin separator. The transmitted atomic beam is detected as described for the TGA. A set of at least 4 (6) measurements with different setups of the HFTs is required to determine the hyperfine population of the sampled hydrogen (deuterium) beam. These informations are used to calculate the polarization of the atomic sample.

1.2 The Target Polarization

The average polarization P^T of nucleons in the target is described by the following equation:

$$P^T = \alpha_0 \cdot (\alpha_r + (1 - \alpha_r) \cdot \beta) \cdot P_a, \quad (1.1)$$

where α_0 represents the initial fraction of nucleons in the atomic state, α_r the fraction of nucleons in atoms surviving recombination², P_a the polarization of the atoms in the target and βP_a the polarization of the molecules produced by recombination. The factor β , which describes the ratio of the polarization of the molecules produced by recombination relative to the polarization of the atoms, is not precisely known. A detailed analysis of HERMES measurements limits its possible range for hydrogen to $0.2 \leq \beta \leq 1$ [Ko 98].

The quantities α_0 , α_r and P_a are calculated using the measurements of TGA and BRP³. Both devices measure the properties of a sample of the target gas, which enters the BRP/TGA through the sample tube by means of diffusive molecular flow. The fraction of atoms surviving recombination, measured with the TGA, is α_r^{TGA} . The polarization of the gas sample analyzed by the BRP, is called P^{BRP} . The properties of the sampled gas and the properties of the gas inside the storage cell are related by the *sampling corrections* c_α

$$\alpha_r = c_\alpha \cdot \alpha_r^{TGA}, \quad (1.2)$$

and c_P

$$P_a = c_P \cdot P^{BRP}. \quad (1.3)$$

Both sampling corrections and their systematic uncertainties depend on the measured values of α_r^{TGA} and P^{BRP} respectively, on the geometry of the storage cell and its surface properties.

²If $n_{a,m}$ are the number of atoms - respectively molecules - inside the storage cell, the fraction of nucleons in atoms α is defined by $\alpha = \frac{n_a}{n_a + 2n_m}$.

³Information of several other devices like pressure gauges, temperature sensors or the HERMES luminosity monitor is used for corrections, cross checks and for the determination of the target holding field.

1.3 Motivation

The determination of the sampling corrections and their systematic uncertainties requires first of all an investigation of the diffusion process of atoms resp. molecules by molecular flow. B. Braun developed a molecular flow Monte Carlo simulation (MC) and presented first predictions of a sampling correction for storage cells with geometry similar to the one used in the HERMES target [Br 91]. Further investigations, that used the final HERMES geometry, followed and included an analytical model of the diffusion process, which was able to reproduce the results of the simulation [Bau 96]. But the predictions were still limited to a homogeneous scenario, assuming a uniform storage cell surface.

First measurements of the target density and the electron polarization of the target by the measurement of bhabha asymmetry with the HERMES luminosity monitor showed a significant deviation from the predicted behavior, indicating a non-uniform surface and a change of the surface properties by the influence of the HERA beam [Ko 98, Wei 98]. Refined studies with the MC simulation allowed investigations of the influence of non-uniformities of the storage cell surface on the sampling corrections and it was found, that the measured values of α_r^{TGA} and P^{BRP} can in general only deliver limits for the average values of α_r and P_a of the target [Hen 98]. In case of strong recombination or spin relaxation these limits are fairly wide and an acceptable uncertainty in the determination of the target polarization can only be achieved, if these processes are weak.

The requirement is to have a target with close to optimal performance and a careful analysis of all contributions that are leading to a reduction of α_r^{TGA} and P^{BRP} . The investigation and modeling of the processes and conditions leading to recombination and spin relaxation is therefore crucial for the determination and systematic uncertainty of the knowledge of the target polarization. H. Kolster presented a detailed analysis of the contributions entering the measured atomic fraction for hydrogen [Ko 98]. The sampling correction of the polarization requires a precise model of the spin relaxation processes and the determination of the polarization of the injected atomic beam P^{inj} . First studies of hydrogen and deuterium spin relaxation in storage cells with the BRP have been performed by B. Braun in preparation of the HERMES experiment [Br 95].

The starting point of this work has been the analysis of measurements of recombination and spin relaxation with hydrogen in 1997. During the winter shutdown of HERA, modifications of soft- and hardware have been done to allow the operation of the target with deuterium. The aim of the analysis is a common and consistent description of the processes of recombination and spin relaxation for both - hydrogen and deuterium. In order to obtain insight in the relevant physical processes, measurements at conditions far off the target working point are essential.

2 Extended Introduction

2.1 The Hyperfine Structure of Hydrogen and Deuterium

The hyperfine structure of atomic hydrogen and deuterium can be derived from a Hamilton operator, which describes the interaction of the magnetic moments with an external field \vec{B} and the coupling of the spin \vec{S} of the electron with the spin \vec{I} of the nucleus:

$$\mathcal{H} = \mathcal{A}_{H,D} \vec{I} \vec{S} + \frac{g_S \mu_B}{\hbar} \vec{S} \vec{B} - \frac{g_I \mu_N}{\hbar} \vec{I} \vec{B}. \quad (2.1)$$

The constant $\mathcal{A}_{H,D}$ is a measure of the coupling strength between \vec{S} and \vec{I} for hydrogen and deuterium respectively, g_S and g_I are the gyromagnetic factors of electron and nucleus. $\mathcal{A}_{H,D}$ can approximately be calculated using the following formula⁴:

$$\mathcal{A}_{H,D} = \frac{2}{3} g_s g_{p,d} \frac{m_e}{m_p} m_e c^2 \alpha^4 \left(1 + \frac{m_e}{m_p}\right)^{-3} \frac{1}{\hbar^2}, \quad (2.2)$$

with the fine structure constant α , the mass of electron m_e and proton m_p respectively, the gyromagnetic factor of the proton g_p and deuteron g_d and the speed of light c . A basis for the Hamilton operator is given by the product wave functions - $|\uparrow + \rangle$, $|\uparrow - \rangle$, $|\downarrow - \rangle$ and $|\downarrow + \rangle$ in case of hydrogen and $|\uparrow 1 \rangle$, $|\uparrow 0 \rangle$, $|\uparrow -1 \rangle$, $|\downarrow -1 \rangle$, $|\downarrow 0 \rangle$ and $|\downarrow 1 \rangle$ in case of deuterium⁵. Using this basis, one can find the eigenvectors and eigenenergies of \mathcal{H} by an orthogonal transformation⁶, represented by a matrix U_0 . The expectation values of spin operators like I_z and S_z , which are known for the product wave functions, are then given by $U_0^T I_z U_0$ and $U_0^T S_z U_0$ in the new basis.

Fig. 2.1 shows the energy levels of hydrogen and deuterium as a function of the magnetic holding field. The energy and field values are scaled with the corresponding values of E_{HFS} and B_C respectively, which are defined by⁷:

$$\begin{aligned} E_{HFS}^H &= \mathcal{A}_H \hbar^2 \simeq 2\pi\hbar 1.42 \text{ GHz} & E_{HFS}^D &= \frac{3}{2} \mathcal{A}_D \hbar^2 \simeq 2\pi\hbar 327 \text{ MHz} \\ B_C^H &= E_{HFS}^H / g_S \mu_B \simeq 50.7 \text{ mT} & B_C^D &= E_{HFS}^D / g_S \mu_B \simeq 11.7 \text{ mT}. \end{aligned} \quad (2.3)$$

The new basis, which is called *Breit-Rabi-Basis*, consists of eigenvectors of \mathcal{H} , usually denoted as $|1 \rangle \dots |4 \rangle$ (resp. $|1 \rangle \dots |6 \rangle$ for \vec{D}), which are given by:

Hydrogen	Deuterium
	$ 1 \rangle = \uparrow +1 \rangle$
$ 1 \rangle = \uparrow + \rangle$	$ 2 \rangle = \cos \theta_+ \uparrow 0 \rangle + \sin \theta_+ \downarrow +1 \rangle$
$ 2 \rangle = \cos \theta \uparrow - \rangle + \sin \theta \downarrow + \rangle$	$ 3 \rangle = \cos \theta_- \uparrow -1 \rangle + \sin \theta_- \downarrow 0 \rangle$
$ 3 \rangle = \downarrow - \rangle$	$ 4 \rangle = \downarrow -1 \rangle$
$ 4 \rangle = -\sin \theta \uparrow - \rangle + \cos \theta \downarrow + \rangle$	$ 5 \rangle = -\sin \theta_- \uparrow -1 \rangle + \cos \theta_- \downarrow 0 \rangle$
	$ 6 \rangle = -\sin \theta_+ \uparrow 0 \rangle + \cos \theta_+ \downarrow +1 \rangle$

⁴Experimental results of much higher accuracy are available [Coh 77].

⁵The arrows refer to the electron spin.

⁶Details of this transformation as well as a list of the eigenenergies are given in app. B.

⁷Precise values are listed in tab. I.2.

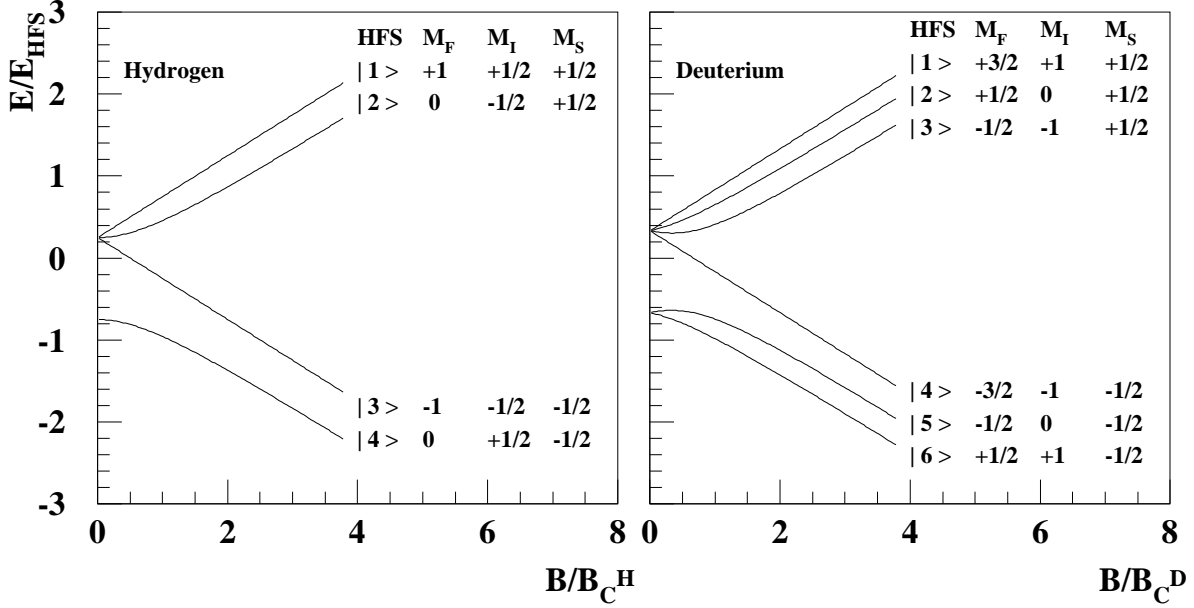


Fig. 2.1: The hyperfine energy levels of hydrogen (left) and deuterium (right) atoms as a function of the magnetic holding field (Breit-Rabi diagram). The field values are scaled with the corresponding critical field and the energy values with the corresponding hyperfine energy.

The *mixing angles* θ , θ_+ and θ_- , which appear in the coefficients, are functions of the magnetic holding field $B = B_z$, as listed in tab. B.1. They vanish in the high field limit $B_z \rightarrow \infty$ and the Breit-Rabi basis converges towards the uncoupled product states. The holding field is typically expressed by the dimensionless *Breit-Rabi* variable x , which is defined by

$$x = \frac{B_z}{B_C}. \quad (2.4)$$

The polarization of the electrons P_e and nucleons P_z of the state $|i\rangle$ are given by the normalized expectation values of the operators S_z and I_z respectively.

Using the hyperfine population numbers N_a , which represents the probability of an atom to be found in state $|a\rangle$, the polarization values are - in case of hydrogen - given by:

$$\begin{aligned} P_e &= N_1 - N_3 + (N_2 - N_4) \cos 2\theta \\ P_z &= N_1 - N_3 - (N_2 - N_4) \cos 2\theta. \end{aligned} \quad (2.5)$$

For deuterium the calculation yields:

$$\begin{aligned} P_e &= N_1 - N_4 + (N_2 - N_6) \cos 2\theta_+ + (N_3 - N_5) \cos 2\theta_- \\ P_z &= N_1 + N_6 - N_3 - N_4 + (N_2 - N_6) \sin^2 \theta_+ + (N_3 - N_5) \sin^2 \theta_-. \end{aligned} \quad (2.6)$$

The *mixed* states of hydrogen, $|2\rangle$ and $|4\rangle$ are unpolarized in the limiting case $B_z \rightarrow 0$, while they are close to 100% polarized in case of a strong holding field $B_z \gg B_C^H$. The polarization of the *pure* states - $|1\rangle$ and $|3\rangle$ for hydrogen and $|1\rangle$ and $|4\rangle$ in case of deuterium - is independent of the holding field as shown in fig. 2.2.

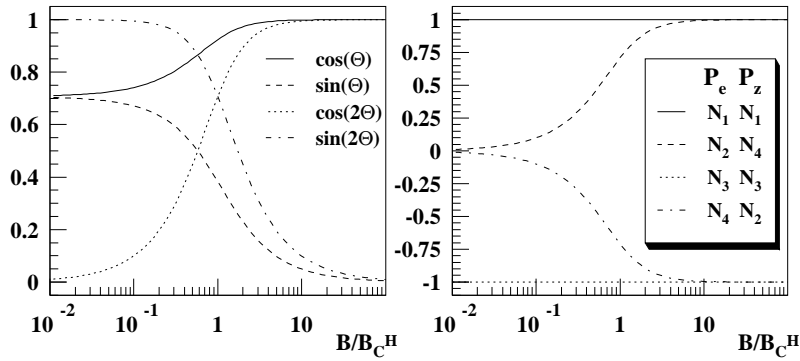


Fig. 2.2: Hydrogen mixing coefficients (left) and expectation values for the polarization of the hyperfine states (right), plotted vs. the magnetic holding field in units of the critical field $B_{C^H}^H$.

As the deuteron has 3 states $m_I = 1, 0, -1$, its spin state is not completely characterized by the value of the *vector polarization* P_z . In addition to P_z one often uses the *tensor polarization* P_{zz} , which is defined as the $z - z$ component of the tensor operator $I_{ij} = \frac{3}{2}(I_i I_j + I_j I_i) - 2\delta_{ij}$ [Fic 71]. The tensor polarization of the deuteron is given by

$$P_{zz} = \langle I_{zz} \rangle = \langle 3I_z^2 - 2 \rangle. \quad (2.7)$$

and hence:

$$\begin{aligned} P_{zz} = & N_1 + N_4 - N_2 \frac{1}{2}(3 \cos 2\theta_+ + 1) + N_3 \frac{1}{2}(3 \cos 2\theta_- - 1) \\ & - N_5 \frac{1}{2}(3 \cos 2\theta_- + 1) + N_6 \frac{1}{2}(3 \cos 2\theta_+ - 1) \end{aligned} \quad (2.8)$$

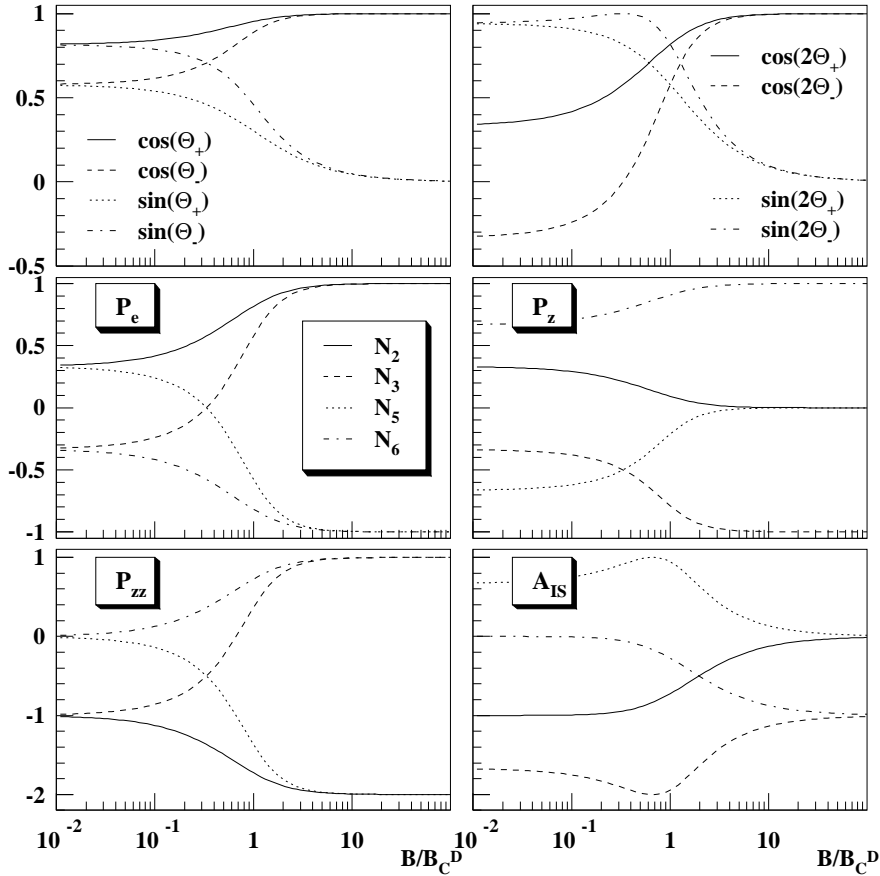


Fig. 2.3: Deuterium mixing coefficients (up) and expectation values for the polarization of the mixed hyperfine states, plotted vs. the magnetic holding field in units of the critical field $B_{C^D}^D$. The polarization of the pure states $|1\rangle$ and $|4\rangle$ is field independent.

Another operator of interest is $\vec{I}\vec{S}$, which quantifies the relative orientation of the spins of the electron and nucleon and one may define the asymmetry A_{IS} in case of hydrogen by

$$A_{IS} = \frac{4}{\hbar^2} \langle \vec{I}\vec{S} \rangle = N_1 + N_3 - N_2 - N_4 + (N_2 - N_4) 2 \sin 2\theta, \quad (2.9)$$

and in case of deuterium by

$$A_{IS} = \frac{2}{\hbar^2} \langle \vec{I}\vec{S} \rangle = N_1 + N_4 - N_3 - N_6 - (\sin^2 \theta_+ - \sqrt{2} \sin 2\theta_+) (N_2 - N_6) + (\sin^2 \theta_- + \sqrt{2} \sin 2\theta_-) (N_3 - N_5). \quad (2.10)$$

2.2 Hyperfine Transitions

Hyperfine transitions play a central role in the understanding of the target and its polarization. First, they are used in the high frequency transition (HFT) units as *adiabatic* transitions [Abr 58, Hae 67, Phi 87, Oh 70] in order to exchange the hyperfine population of two hyperfine states in one or several steps. This exchange is for example required to transfer the polarization of the electrons to the nucleons. Second, hyperfine transitions cause depolarization during wall collisions and by resonant depolarization induced by the bunch field of the HERA electron beam.

Usually one distinguishes hyperfine transitions with $\Delta m_F = 0$ from those with $\Delta m_F = 1$ and those with $\Delta F = 1$ from those with $\Delta F = 0$. Tab. 2.1 summarizes the different transition types. A hyperfine transition has a defined frequency ν_{ab} , related to the energy difference $E_a - E_b$ of the transition $a \leftrightarrow b$:

$$\nu_{ab} = \frac{|E_a - E_b|}{2\pi\hbar}. \quad (2.11)$$

As the energy levels of the hyperfine states depend on the magnetic holding field, this is also true for the frequencies of the hyperfine transitions. The operation of an adiabatic high frequency transition (HFT) requires a careful tuning of either the frequency and/or of the magnetic field setting, in order to obtain an optimal transition efficiency.

Strong field transitions (SFT) are characterized by $\Delta F = 1$, **weak-** and **medium field transitions** [Hlm 71, Oh 70, Dre 83, Ro 92] (WFT/MFT) by $\Delta F = 0$. Typically, SFTs run with a frequency higher than $\nu_{HFS} = E_{HFS}/h$ ⁸, while the transition frequency of a WFT/MFT transition⁹ is - in the limiting case of $B_z \rightarrow 0$ - proportional to the field. SFTs are therefore realized by resonator cavities and WFTs/MFTs by high frequency coils. The cavities are kept in resonance with the help of feedback loops, while the impedance matching of the coils is realized by Collins filters [Br 95]. Since the cavities are tuned to

⁸The exceptions are the SFT*-transitions (see tab. 2.1), whose transition frequency decreases with the magnetic field. This transition type is not used, as single transitions with $\Delta m_S = 0$ are of no practical use in combination with sextupole systems. Another exception is the SFT 3 \leftrightarrow 5 of deuterium; its transition frequency is slightly below ν_{HFS} between 0 and 8 mT.

⁹Some authors have chosen a different notation for the transition types. Philpott for example named transitions with $\Delta F = 1$ MFT and those with $\Delta F = 0$ WFT [Phi 87]. Other authors distinguish between a WFT and a MFT in a technical sense - they refer to different ways to run *adiabatic* high frequency transitions [Br 95, St 95a]. In the present work the meaning of MFT has to be taken from the context. In the physical context a MFT is a transition with $\Delta F = 0$, in a technical context, it is any combination of one or several subsequent physical MFTs, operated as single-photon transitions. A WFT is then a special way to run a cascade of MFTs in a multi-photon mode.

a fixed frequency, they have to be replaced for a change of the target gas from hydrogen to deuterium or vice versa.

A high frequency field parallel to the static field can be used to induce transitions with $\Delta m_F = 0$ between the mixed states, a high frequency field perpendicular to the static field can induce transitions with $\Delta m_F = 1$. A detailed description of the differences of these transitions is given in app. B.2.

If an atom stays in resonance with a magnetic high frequency field, the spin starts to oscillate between the two eigen states $|a\rangle$ and $|b\rangle$ (see app. D.2). An efficient exchange of two hyperfine states is possible only, if the time, that the atoms stays within the high frequency field, is well defined - a condition, which is not fulfilled for an atomic beam with a thermal velocity distribution. A reliable and efficient exchange of two hyperfine states can be realized with a so-called *adiabatic transition*. A field gradient along the axis of the atomic beam guarantees, that the atoms passes the resonance condition exactly once. A detailed calculation, which can be found in app. B.2, shows that the hyperfine states of the atoms can in the presence of the high frequency field - in a rotating frame - be described by a mixture of the original eigenstates. This so-called *adiabatic eigenstates* do not overlap. If an atom, that moves along the gradient field from either low to high field values (or vice versa), stays in its adiabatic eigenstate, the transition efficiency is 100%. Fig. 2.4 illustrates the adiabatic passage. This ideal situation can only be reached in a slow (adiabatic) passage through the resonance. Practically, efficiencies of more than 98% can be reached with resonant regions of a few *cm* length for atoms of thermal velocity.

If one uses the vector of hyperfine population numbers $N_a = (N_1, N_2, \dots)^T$ for the description of an atomic sample, the effect of a HFT on the hyperfine population can be described by a matrix T_{ab} :

$$N_a \rightarrow \sum_b T_{ab} N_b. \quad (2.12)$$

Orientation	σ/π	Type	Δm_F	ΔF	Δm_I	Δm_S	Hydrogen	Deuterium
$B_{hf} \parallel B_z$	σ	SFT	0	1	1	1	2 ↔ 4	2 ↔ 6
$B_{hf} \parallel B_z$	σ	SFT	0	1	1	1		3 ↔ 5
$B_{hf} \perp B_z$	π	SFT	1	1	0	1	1 ↔ 4	1 ↔ 6
$B_{hf} \perp B_z$	π	SFT	1	1	0/2	1		2 ↔ 5, 3 ↔ 6
$B_{hf} \perp B_z$	π	SFT*	1	1	1	0	3 ↔ 4	4 ↔ 5
$B_{hf} \perp B_z$	π	MFT	1	0	1	0	1 ↔ 2	1 ↔ 2
$B_{hf} \perp B_z$	π	MFT	1	0	1	0		2 ↔ 3, 5 ↔ 6
$B_{hf} \perp B_z$	π	MFT	1	0	0	1	2 ↔ 3	3 ↔ 4

Tab. 2.1: Hyperfine transitions of hydrogen and deuterium. Transitions with $\Delta F = 1$ are called *strong field transitions*, transitions with $\Delta m_F = 0$ are called *medium field transitions*. Transitions with $\Delta m_F = 0$ are called σ -transitions, those with $\Delta m_F = 1$ are called π -transitions - in contrast to the conventions in optical spectroscopy. The transitions with $\Delta m_I \neq 0$ are proton/deuteron transitions, with $\Delta m_S \neq 0$ are electron transitions. The σ transitions are both - electron and proton respectively deuteron transitions. In case of deuterium, there are transitions, which have the same transition frequency.

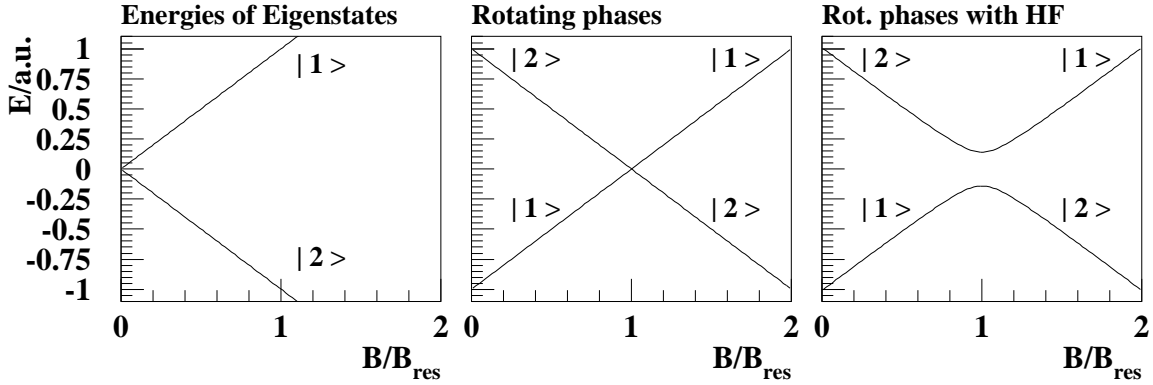


Fig. 2.4: Schematic diagram of the adiabatic passage through a resonance. Left: Eigenenergies of two hyperfine states in linear approximation versus the holding field (relative to the field value of the resonance B_{res}). As the atom is passing a gradient field, its position is proportional to the field value, so that the horizontal axis represents also position and time. Center: The high frequency terms within the Hamilton operator are equivalent to a phase rotation of both states in combination with a shift of the eigen energies. Right: The strength of the high frequency field causes a separation of the eigenenergies at the cross point. Atoms in state $|1\rangle$ entering the resonant region ($B/B_{res} \simeq 1$) from low static field values, pass once through the resonance and leave the system in state $|2\rangle$ on the other side and vice versa.

This matrix can - in case of a SFT 1-4 transition of hydrogen for example - be written as:

$$T_{14} = \begin{pmatrix} 1 - \varepsilon_{41} & 0 & 0 & \varepsilon_{41} \\ 0 & 1 & 0 & 0 \\ 0 & 0 & 1 & 0 \\ \varepsilon_{14} & 0 & 0 & 1 - \varepsilon_{14} \end{pmatrix}, \quad (2.13)$$

where ε_{14} is the efficiency of the transition. Medium and weak field transitions have to be modeled by subsequent separate transitions, each with an individual transition efficiency. The order of the matrix multiplications depends on the sign of the gradient field. A deuterium weak field transition with negative gradient can - as explained in app. B.2.5 - approximately be described by 7 separate transitions¹⁰:

$$T^{wft} = T_{56} T_{34} T_{24} T_{14} T_{23} T_{13} T_{12}. \quad (2.14)$$

As shown in app. B.2.5, there are good reasons to assume for a WFT, that the efficiencies of single-photon transitions ε_{12} , ε_{23} , ε_{34} and ε_{56} are higher than the efficiencies of transitions that require multiple photon interactions as ε_{13} , ε_{24} and ε_{14} .

2.3 Spin Separation in Sextupole Magnets

In a magnetic gradient field, the Stern-Gerlach force acts on atoms with a magnetic dipole moment [Stn 21]. In case of atoms with hyperfine structure the magnetic moments of the single hyperfine states are proportional to the change of the eigenenergies with the external

¹⁰The exchange between state 5 and 6 in case of a deuterium WFT/MFT transition is not really intended and can not be avoided, as the transition frequency of the 5-6 transition is identical with the 2-3 transition.

field. The eigenenergies are given by the relations in tab. B.1. The Lagrange function \mathcal{L} for an atom in hyperfine state $|a\rangle$ is given by:

$$\mathcal{L} = \frac{m}{2}(\dot{x}^2 + \dot{y}^2 + \dot{z}^2) - E_{|a\rangle}(|\vec{B}|). \quad (2.15)$$

The absolute value of the magnetic field inside a sextupole magnet depends quadratically on the distance to the sextupole axis forming so an harmonic potential, if the magnetic moment is field independent, which is the case for the pure states and in the high field limit of the mixed states. The direction of the axial force on the atoms depends on the sign of the magnetic moment and therefore on the value of $\langle m_s \rangle$. The axial distance of atoms with a negative value of $\langle m_s \rangle$ increases within the sextupole - they are defocused. Atoms with a positive value of $\langle m_s \rangle$ start to oscillate within the attractive harmonic potential. The defocused atoms hit either the inner walls of the sextupoles or the vacuum chambers and are pumped away. Only atoms with $m_s = +\frac{1}{2}$ of a matching velocity v_z are able to transmit the system. The atomic beam, which leaves the sextupole system, is - in high holding field - nearly 100% electron polarized. More details are given in sec. B.3. Fig. 2.5 shows the result of a trajectory calculation using a tracking program [Br 95] for the HERMES atomic beam source.

2.4 Diffusive Molecular Flow in Long Tubes

In this subchapter the basic equations will be introduced, that are used to describe the behavior of atoms and molecules in thin gases, diffusing in long thin tubes like the HERMES storage cell by means of molecular flow. A *thin* gas in this context refers to gas in a pressure regime, where the mean free pathlength is large compared to the typical distances inside the tube, so that particle-particle collisions in the gas phase are negligible in this context of flow. An atom, that hits the wall of the storage cell, is physisorbed with a certain probability c called the *condensation coefficient*. Measurements of c have been

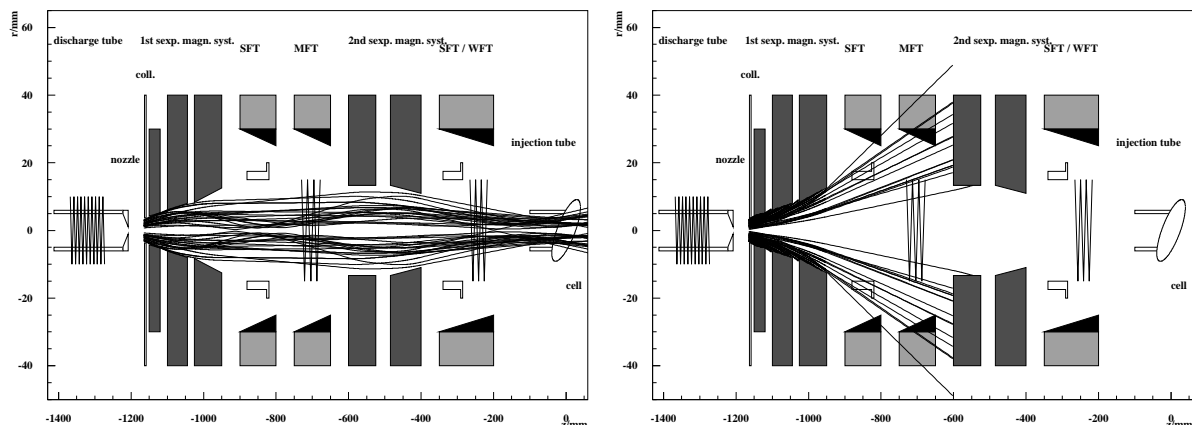


Fig. 2.5: Some trajectories of hydrogen/deuterium atoms within in the sextupole system of the HERMES ABS, calculated in a Monte Carlo simulation. Left: Focused pure hyperfine state $|1\rangle$. Right: Defocused pure hyperfine states (state $|3\rangle$ of hydrogen, state $|4\rangle$ of deuterium respectively.).

performed in a variety of experiments and for several gases, surfaces and conditions¹¹. While an atom is adsorbed, it may either stay at a certain surface site or diffuse from site to site by means of surface jump diffusion until it acquires sufficient thermal energy to desorb back into the gas phase. During this process, the information of the kinetic parameters of the adsorption gets lost and the desorption process is isotropic, which is described by a $\cos \theta$ -distribution of the desorption angle θ relative to the surface normal. Molecular beam scattering experiments showed, that the assumption of isotropic desorption is reasonable, if the impinging molecules are adsorbed on the surface. Nevertheless, in special cases also nearly specular reflection was found in some experiments¹². For the situation under study, a condensation coefficient near unity and isotropic desorption are assumed.

Particle flow fulfills the continuity equation

$$\dot{n} + \vec{\nabla} \vec{j} = q, \quad (2.16)$$

where the n is the particle density, \vec{j} represents the particle flux density and q is the particle source density, which is typically zero. The source density can be used to describe the (non-diffusive) appearance of atoms, which are injected *ballistically* by the ABS into the cell center, or their disappearance by chemical reactions like recombination ($H_1 + H_1 \rightarrow H_2$). The second equation, which is commonly used to describe the diffusion in thin gases, is [Bec 85]:

$$\vec{j} = -D \vec{\nabla} n, \quad (2.17)$$

with the *diffusion constant* D in [$m^2 s^{-1}$]. Both equations can be combined and one obtains

$$\dot{n} - (\vec{\nabla} D) (\vec{\nabla} n) - D \vec{\nabla}^2 n = q. \quad (2.18)$$

If the gradient of the diffusion constant D vanishes - as it is the case for tubes with constant cross section and temperature - one finds the *diffusion equation*¹³:

$$\dot{n} - D \vec{\nabla}^2 n = q. \quad (2.19)$$

In a one dimensional system like a long tube of small diameter along the z -axis, eq. 2.19 can be simplified to

$$\dot{n} = D \frac{\partial^2 n}{\partial z^2} + q. \quad (2.20)$$

In case of a steady flow ($\dot{n} = 0$) and in absence of sources $q = 0$, one obtains:

$$D \frac{\partial^2 n}{\partial z^2} = 0. \quad (2.21)$$

The solution of this equation for a tube of length L , which fulfills the boundary conditions $n(0) = n_0$ and $n(L) = 0$, is¹⁴:

$$n(z) = n_0 \left(1 - \frac{|z|}{L}\right). \quad (2.22)$$

This solution is valid (positive) for $|z| < L$ and implies a source in form of a Dirac- δ -function at $z = 0$, that represents the injection by the ABS. In vacuum technology, one

¹¹See for examples the references in the article of J.P. Hobson in [Flo 67]. Typically, the value of c was found to be in the order of unity - especially for low pressures and temperatures.

¹²See [Sti 67] and references in the article of J.P. Hobson in [Flo 67].

¹³It is for example also used to describe thermal transport.

¹⁴The condition $n(L) = 0$ is an approximation for long tubes and negligible background pressures. Fig. 2.6 shows a more realistic density profile.

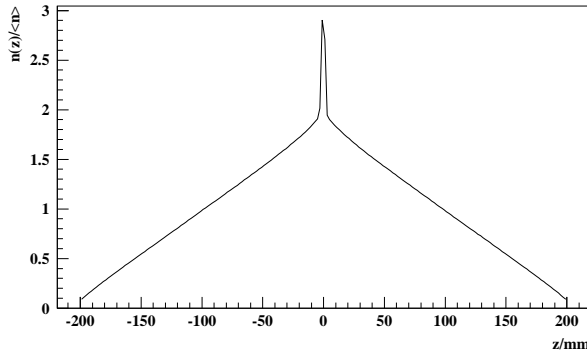


Fig. 2.6: Density profile of atoms in the HERMES storage cell. The peak above the triangular density distribution corresponds to the injected atomic jet. In contrast to the approximation of eq. 2.22, the density is only close to zero at the storage cell ends. The distribution was produced by a molecular flow Monte Carlo simulation [Bau 96].

usually uses the flow Φ in [$mbar\ l\ s^{-1}$] through a given surface and the pressure p in [$mbar$] defined by

$$\begin{aligned} p &= n kT \\ \Phi &= \dot{N} kT, \end{aligned} \quad (2.23)$$

instead of \vec{j} and n^{15} , where \dot{N} is the net number of particles passing the position z along the z -axis per unit time:

$$\dot{N} = \int \vec{j} d\vec{S}, \quad (2.24)$$

where S is the cross section of the tube. Eq. 2.17 can then be rewritten for the one-dimensional case:

$$\Phi = -D S \frac{\partial p}{\partial z}, \quad (2.25)$$

and for eq. 2.20 one obtains:

$$\dot{p} = D \frac{\partial^2 p}{\partial z^2} + Q, \quad (2.26)$$

with $Q = kT q$. Corresponding to eq. 2.22, one obtains for the pressure:

$$p(z) = p(0) \left(1 - \frac{|z|}{L}\right). \quad (2.27)$$

while eq. 2.25 predicts a constant flux:

$$\Phi = D S \frac{p(0) - p(L)}{L}, \quad (2.28)$$

which is usually written as

$$\Phi = C \Delta p. \quad (2.29)$$

C is called the *conductance* of the tube and is related to the diffusion constant D by:

$$C = D \frac{S}{L} \quad (2.30)$$

¹⁵ T is the absolute Temperature and k Boltzmann's constant.

2.5 Recombination and the Atomic Fraction α

One goal of the investigation of particle transport is the calculation of the atomic fraction inside the HERMES target cell and its relation to the atomic fraction in the sample beam. In the following we consider only molecules, which have their origin in the recombination of atoms. In the molecular flow regime, volume recombination can be neglected, recombination appears on the surface of the storage cell only. Atomic quantities are subscribed with an 'a', molecular quantities with an 'm', whenever it is necessary. The continuity equation 2.16 has in the presence of recombination to be modified in the following way:

$$\dot{n}_a + \vec{\nabla} \vec{j}_a + 2(\dot{n}_m + \vec{\nabla} \vec{j}_m) = 0. \quad (2.31)$$

This equation leads - in case of steady flow ($\dot{n}_a = \dot{n}_m = 0$) - to:

$$\frac{d}{dz}(\Phi_a + 2\Phi_m) = 0, \quad (2.32)$$

so that

$$\Phi_a + 2\Phi_m = -C_a L \frac{dp_a}{dz} - 2C_m L \frac{dp_m}{dz} = \Phi_{tot} = const. \quad (2.33)$$

If one can assume, that the hot molecules, as they are produced by the recombination process, cool down to storage cell temperature within a few wall collisions, then atoms and molecules have about the same temperature. Since the molecules have twice the corresponding atomic mass, the conductance for molecules C_m is (see eq. C.15):

$$C_m = \frac{1}{\sqrt{2}} C_a, \quad (2.34)$$

so that:

$$\frac{dp_a}{dz} + \sqrt{2} \frac{dp_m}{dz} = const, \quad (2.35)$$

and by integration with the common requirement of vanishing pressures at the end of the tube, where z equals L :

$$p_a + \sqrt{2} p_m = p_0 \frac{L - |z|}{L}. \quad (2.36)$$

This means, that the sum $p_a + \sqrt{2} p_m$ depends on the z -position only and the intensity of the ABS - represented by p_0 - and is independent on recombination. It is therefore useful to define the normalized atomic and molecular densities ρ_a and ρ_m by

$$\begin{aligned} \rho_a(z) &= \frac{p_a}{p_a + \sqrt{2} p_m} \\ \rho_m(z) &= \frac{\sqrt{2} p_m}{p_a + \sqrt{2} p_m}, \end{aligned} \quad (2.37)$$

which are connected by the relation

$$\rho_a + \rho_m = 1. \quad (2.38)$$

The total density ρ_t is given by

$$\rho_t = \rho_a + \sqrt{2} \rho_m = \sqrt{2} - (\sqrt{2} - 1) \rho_a, \quad (2.39)$$

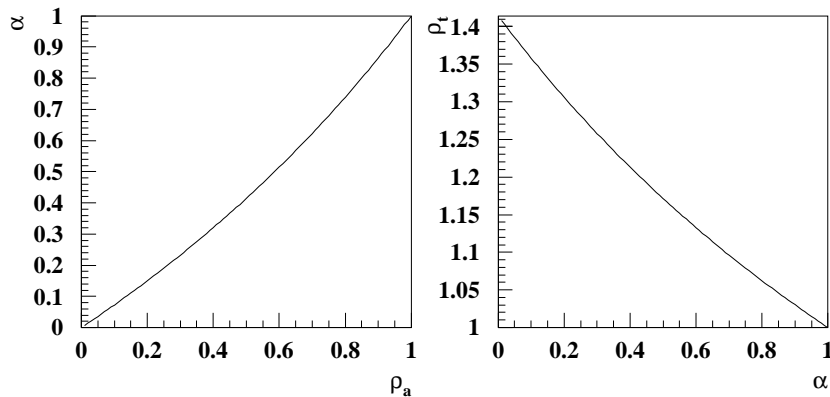


Fig. 2.7: Left: The atomic fraction α in a storage cell is plotted vs. the normalized atomic density ρ_a . Right: Normalized total density plotted vs. the atomic fraction α .

and depends on the strength of the recombination process. It is convenient to define the atomic fraction α as a relative quantity, which describes the fraction of nucleons in atoms n_a to the total number of nucleons $n_t = n_a + 2n_m$:

$$\alpha = \frac{n_a}{n_a + 2n_m} = \frac{\rho_a}{\rho_a + \sqrt{2}\rho_m} = \frac{\rho_a}{\rho_t}, \quad (2.40)$$

and the molecular fraction $\mu = 1 - \alpha$ correspondingly by:

$$\mu = \frac{2n_m}{n_a + 2n_m} = \sqrt{2} \frac{\rho_m}{\rho_t}, \quad (2.41)$$

Using these equations, one can derive the relations of tab. 2.2. The left part of fig. 2.7 shows α plotted versus the normalized atomic density ρ_a . The graph on the right side represents the total density ρ_t as a function of the atomic fraction α .

As the HERMES luminosity monitor measures the absolute target density ρ_t , it can in principle be used to measure α , given, that the normalization constant for ρ_t is known [Ko 98]. Nevertheless - this method has its systematical problems and will not be discussed in the present work.

	α	μ	ρ_a	ρ_m	ρ_t	range
$\alpha =$		$1 - \mu$	$\frac{\rho_a}{\sqrt{2} - (\sqrt{2} - 1)\rho_a}$	$\frac{1 - \rho_m}{1 + (\sqrt{2} - 1)\rho_m}$	$\frac{\sqrt{2} - \rho_t}{(\sqrt{2} - 1)\rho_t}$	$0 \dots 1$
$\mu =$	$1 - \alpha$		$\frac{\sqrt{2}(1 - \rho_a)}{\sqrt{2} - (\sqrt{2} - 1)\rho_a}$	$\frac{\sqrt{2}\rho_m}{1 + (\sqrt{2} - 1)\rho_m}$	$\frac{\sqrt{2}(\rho_t - 1)}{(\sqrt{2} - 1)\rho_t}$	$0 \dots 1$
$\rho_a =$	$\frac{\sqrt{2}\alpha}{1 + (\sqrt{2} - 1)\alpha}$	$\frac{\sqrt{2}(1 - \mu)}{\sqrt{2} - (\sqrt{2} - 1)\mu}$		$1 - \rho_m$	$\frac{\sqrt{2} - \rho_t}{\sqrt{2} - 1}$	$0 \dots 1$
$\rho_m =$	$\frac{1 - \alpha}{1 + (\sqrt{2} - 1)\alpha}$	$\frac{\mu}{\sqrt{2} - (\sqrt{2} - 1)\mu}$	$1 - \rho_a$		$\frac{\rho_t - 1}{\sqrt{2} - 1}$	$0 \dots 1$
$\rho_t =$	$\frac{\sqrt{2}}{1 + (\sqrt{2} - 1)\alpha}$	$\frac{\sqrt{2}}{\sqrt{2} + (\sqrt{2} - 1)\mu}$	$\sqrt{2} - (\sqrt{2} - 1)\rho_a$	$1 + (\sqrt{2} - 1)\rho_m$		$1 \dots \sqrt{2}$

Tab. 2.2: Relations between atomic and molecular fraction - α and μ - and the normalized densities ρ_a , ρ_m and ρ_t .

2.6 The Concept of Collision Ages

If the probability for an atom to recombine with another atom during a wall collision is γ_r , then the probability ρ_a , that the atom has not recombined after b wall collisions, is given by

$$\rho_a = (1 - \gamma_r)^b = e^{b \ln(1 - \gamma_r)} \simeq e^{-\gamma_r b}, \quad (2.42)$$

where it was assumed, that $\gamma_r \ll 1$. The *collision age distribution* (CAD) $N_{CAD}(b)$ is defined by the probability to find an atom within a sample, that experienced b wall collisions. The average normalized atomic density ρ_a then is

$$\rho_a = \sum_{b=0}^{\infty} N_{CAD}(b) e^{-\gamma_r b} \simeq \int_0^{\infty} db N_{CAD}(b) e^{-\gamma_r b}, \quad (2.43)$$

where it is assumed, that the average collision age $\langle b \rangle$ of the sample is high. In case of a storage cell of a geometrical trivial form like a sphere, where the atoms are injected ballistically through a hole in the wall and the sample is formed by atoms exiting through another hole, it is by the same arguments as above evident, that the CAD $\tilde{N}_{CAD}(b)$ is given by the (normalized) exponential decay

$$\tilde{N}_{CAD}(b) = \frac{1}{\langle b \rangle} \exp\left(-\frac{b}{\langle b \rangle}\right), \quad (2.44)$$

and hence

$$\rho_a = \frac{1}{1 + \langle b \rangle \gamma_r}. \quad (2.45)$$

In case of the HERMES storage cell, the geometry is more complex and one has a variety of different CADs with different average collision ages $\langle b \rangle$ for different atomic samples - atoms inside the beam tube (at a certain position z along the axis or in average), atoms entering the acceptance of the BRP or TGA etcpp. In app. C, a mathematical formalism on the basis of the diffusion equation is developed, that allows to calculate density profiles, CADs and average collision ages for tubes and storage cells with and without recombination. Parts of the calculations are compared to results of molecular flow simulations, that have been developed for the description of the HERMES target [Br 91, Bau 96, Hen 98].

It is shown in sec. C.4.2, that eq. 2.45 delivers a good approximation of eq. 2.43 for the measurements of TGA and BRP for sufficiently small values of γ_r . For higher values, the agreement is less good, but still sufficient for the purpose of studying the temperature and magnetic field dependence of the processes of recombination and spin relaxation. The reason is, that the injected atoms are - after a certain number of wall collisions - distributed all over the storage cell, independent on the details of the geometry, so that *any* CAD decreases exponentially for $b \rightarrow \infty$. The calculation of the target polarization (see sec. 7) however requires more precise calculations, which are described in app. C.7 and app. C.8.

3 The Experimental Setup

3.1 The Target Chamber and the Superconducting Magnet

Fig. 3.1 shows a schematic of the target vacuum chamber, which is surrounded by the coils and the iron yoke of the superconducting magnet (SCM). The chamber is evacuated by two molecular turbo pumps with a total pumping speed of 4400 l s^{-1} as shown in the right part of fig. 3.1. A thin walled exit window downstream of the target chamber allows the scattered electrons and hadronic recoil products to leave the target region and to be detected in the HERMES spectrometer. A dewar below the target platform provides gaseous helium, which circulates through the superconducting magnet and a controllable electric heater, before it flows through the aluminum rails, on which the storage cell is mounted.

The superconducting magnets consist of 4 coils around the target chamber as indicated by the black squares in the right part of the figure. It provides a highly homogeneous longitudinal holding field over the storage cell of up to 350 mT . The holding field provides the quantization axis for the spins of the polarized atoms in the storage cell and decouples the spins of nucleons and electrons. It has to be of high homogeneity to avoid bunch field induced nuclear depolarizing resonances¹⁶. H. Kolster showed for hydrogen, that nuclear resonances within the storage cell can indeed be avoided by a proper setting of the holding field value [Ko 98]. This item was found to be less critical for deuterium (see sec. 6.11). Fig. 3.2 shows the longitudinal component of the SCM-field vs. the z -axis at four different distances to the axis.

¹⁶The calculation of the bunch field depolarization delivered the design criteria for the homogeneity of the magnetic field.

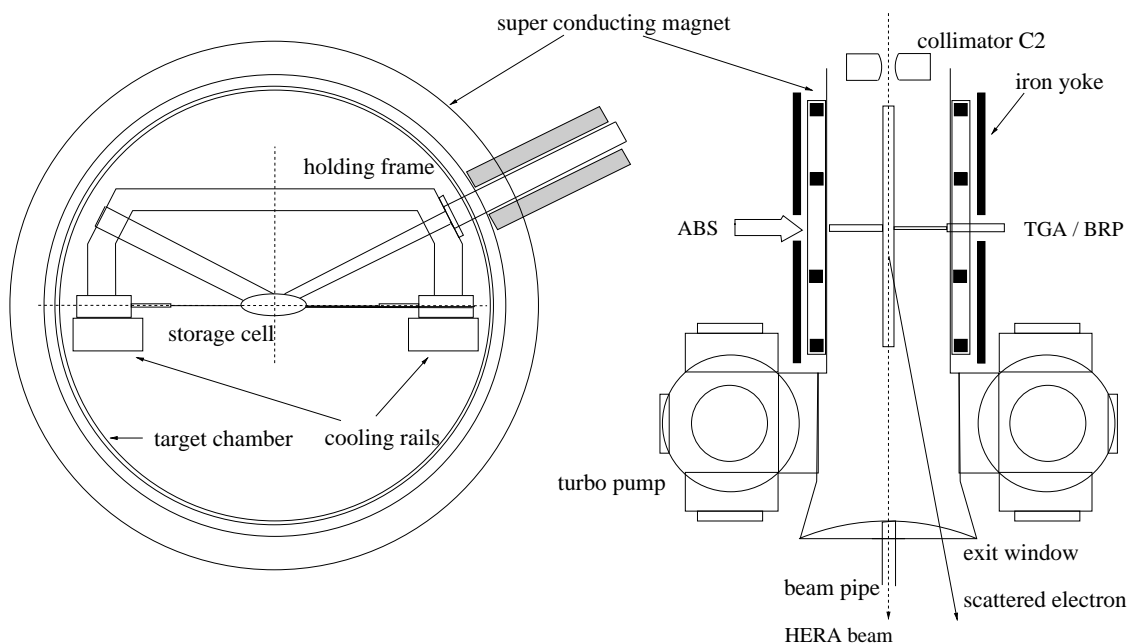


Fig. 3.1: Left: The target chamber with the storage cell viewed along the HERA beam direction. Right: The target chamber from the top.

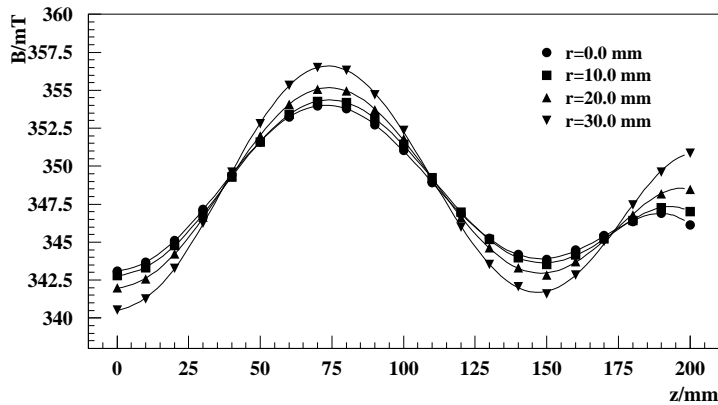


Fig. 3.2: Longitudinal component of the magnetic field of the target magnet, measured at four different distances r to the axis, plotted vs. the distance z from the center.

A fixed collimator C2 protects the storage cell from direct synchrotron light of the HERA electron beam and from electrons hitting the cell wall. Upstream of C2, an adjustable collimator C1 is located, which is operated with a narrower opening and widened during electron injection into the HERA storage ring.

3.2 The Storage Cell

The HERMES target storage cell [Stw 95] is made from $75 \mu\text{m}$ thin pure aluminum sheets and coated with Drifilm [Wit 56, Tho 87, Ca 87a, Ca 87b, Ste 94, St 95a, Br 95, Fed 97]. The coating helps to minimize depolarization and recombination caused by wall collisions¹⁷ [Swe 88, Ca 87a, Lev 88]. The cell has an elliptical shape of $9.8 \times 29 \text{ mm}$ cross section and is 400 mm long.

The storage cell is electrically connected on to the HERA electron beam pipe by wake field suppressors, which are made of copper and designed to guide the electromagnetic high frequency field of the bunched HERA electron beam. The storage cell is mounted on cooling rails, which are temperature regulated with the help of gaseous Helium. The optimal operating temperature for hydrogen was found to be about 100 K , where recombination is minimal and wall depolarization sufficiently low. The lower conductance at this temperature increases the target thickness by a factor of $\sqrt{3}$ compared to room temperature.

¹⁷Teflon as a potentially equivalent or even better coating material is less radiation hard and may not be used within the HERA environment.

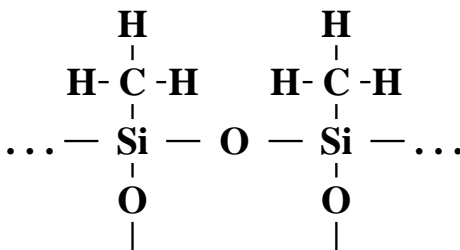


Fig. 3.3: Schematic diagram of a proper Drifilm coating [Ca 87a, Ste 94, St 95a]. Possible chemical structures of misformed coatings are discussed in the same references. Proper Drifilm coatings are hydrophobic, so that the simplest proof of the quality of a coating is done by testing the adhesion of water drops.

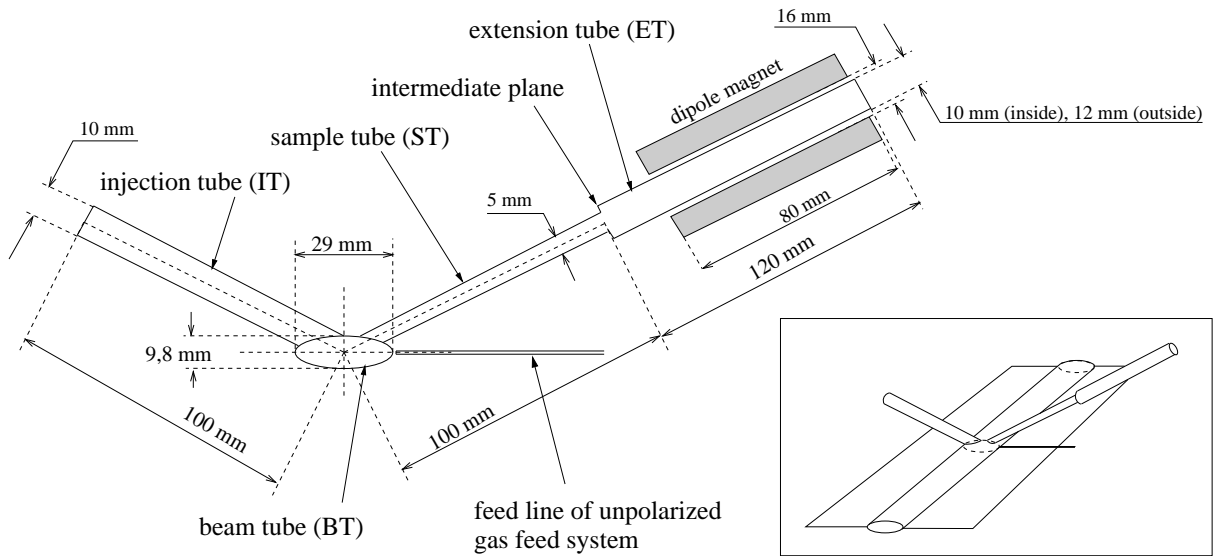


Fig. 3.4: Onscale schematic of the large storage cell. The inlay on the right side gives a 3-dimensional display of the storage cell. The main figure shows the details of the elliptical cross section and the side tubes with their dimensions.

In order to monitor the temperature 3 platinum resistors are mounted at different positions of the cell holding rails. In addition, since 1999 a thermo couple wire is attached to the aluminum foil close to the cell ellipse to monitor the cell temperature during the injection of the HERA beam. Fig. 3.4 shows the storage cell in upstream beam direction and 3-dimensional. The dipole magnet around the extension tube (ET) extends the magnetic holding field of the superconducting magnet (SCM) to prevent depolarization inside the ET. The injection line of the unpolarized gas feed system (UGFS) is connected to the cell center below the sample tube.

The cooling rails of the storage cell are connected to the target chamber in upstream direction. Due to the thermal contraction of the cell, the position of the cell center relative to target chamber, ABS and BRP changes with the storage cell temperature. Fig. 3.5 shows the expected relative alignment position of the storage cell center in z-direction as a function of the cooling rail temperature¹⁸. The effect was taken into account by an offset

¹⁸Calculated with the thermal contraction coefficients of pure aluminum [Ard 73] for a 200 mm long piece of aluminum.

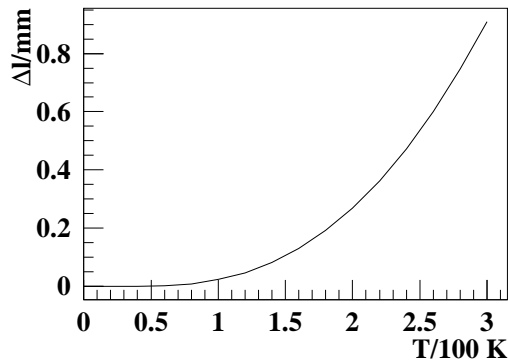


Fig. 3.5: Expected change in the z-position of the cell center caused by thermal expansion of the aluminum rails of the storage cell versus temperature. The alignment of ABS and BRP relative to the storage cell includes an offset which compensates the effect at the target working point of 100 K.

of about 0.9 mm in the relative alignment of ABS and BRP at 300 K in order to obtain the optimal relative position at the target working point of about 100 K or below.

In January 1999 a smaller storage cell was installed and tested. A smaller storage cell provides a higher target thickness due to the reduced conductance. Details of the geometry of the large and (new) small cell are listed in app. F.

3.3 The Unpolarized Gas Feed System (UGFS)

The unpolarized gas feed system is required for the unpolarized physics program of the HERMES experiment and can be used to inject gas into the storage cell or the target chamber directly. The density of the unpolarized gas in the storage cell or the target chamber can be controlled with the gas flow rate of the UGFS, which is adjusted by a thermo valve. A differential baratron is used to measure the pressure drop caused by the flow resistance of a small capillary, which is about proportional to the flow through the capillary.

The UGFS is also used to determine the molecular flow rate into the TGA, caused by the residual gas pressure in the target chamber as described in sec. 3.5.

3.4 The Atomic Beam Source (ABS)

The Atomic Beam Source (ABS) consists of a dissociator, a skimmer and a collimator for the formation of the atomic beam, a sextupole system to focus atoms with $m_S = +\frac{1}{2}$ into the storage cell (see fig. 2.5) by means of Stern-Gerlach separation and several adiabatic high frequency units to transfer the polarization of the electrons to the nucleons [Sto 94a, Sto 94c, Sch 91, Fun 95]. Fig. 3.6 shows a simplified scheme of the ABS setup. The molecular hydrogen/deuterium enters from the left. The molecules are dissociated by a radio frequency discharge in a glass tube of the dissociator¹⁹ with a degree of dissociation of about 80% [Koc 99]. For the normal operation of the hydrogen target, only

¹⁹In the end of 1999, the radio frequency dissociator has been replaced by a microwave discharge [Koc 99].

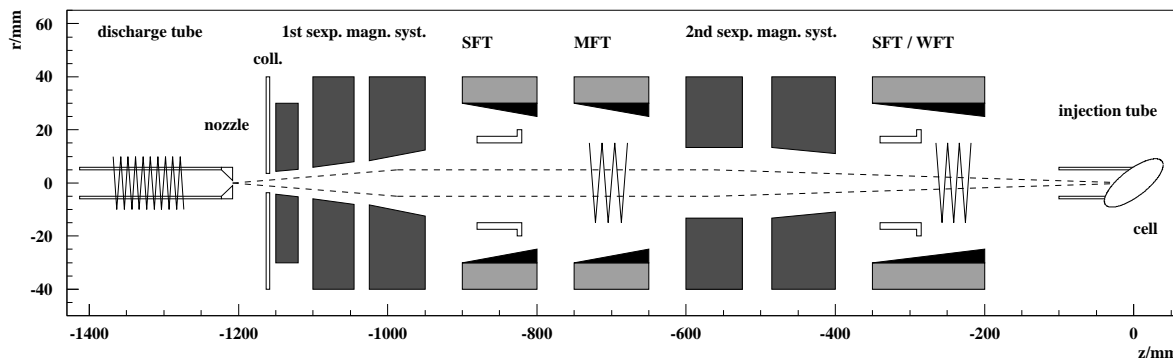


Fig. 3.6: Schematic of the ABS setup. H_2 - or D_2 molecules are dissociated in the discharge tube of the radio frequency dissociator. Adiabatic gas expansion after the nozzle creates a peaked atomic beam. Skimmer and collimator are limiting its spread to the acceptance of the entrance of the first sextupole magnet. Between the two parts of the sextupole system HFTs can optionally be used to manipulate the hyperfine population of the atomic beam. A transition unit in the ABS appendix, which can either be run as a SFT or WFT transition, is used to transfer the polarization of the electrons to the nucleons.

the transition units in the appendix are used. In case of deuterium, the transition units between the two sextupole subsystems are relevant also during normal operation.

A general description of the transmission probabilities of atoms in the hyperfine state $|a\rangle$ through the ABS requires - if the transitions between the sextupole subsystems are used - matrices instead of vectors, as the trajectories depend on the individual history of the atom. σ_{ab} is the transmission probability of an atom, which enters the first sextupole subsystem in state $|a\rangle$ and the second in state $|b\rangle$. The effect of an adiabatic hyperfine transition i on the hyperfine population can be represented by a matrix $T^{(i)}$ as described in sec. 2.2. If all transitions *between* the sextupole subsystems are represented by the matrix $B = \prod_i T^{(i)}$ and all transitions in the appendix by $A = \prod_j T^{(j)}$, then the number of atoms injected into the storage cell per unit time (beam intensity) I_a in HFS $|a\rangle$ is given by

$$I_a = \sum_c A_{ac} \sum_b \sigma_{bc} B_{bc}. \quad (3.1)$$

If there are no transitions operating between the sextupole subsystem, the equation simplifies significantly:

$$I_a = \sum_b A_{ab} \sigma_{bb}, \quad (3.2)$$

If there are no transitions in the appendix $A_{ab} = \delta_{ab}$, one has:

$$I_a = \sigma_{aa}, \quad (3.3)$$

which describes the injection mode P_e .

If for example a hydrogen MFT 2-3 transition is operated between the two sextupole subsystems, the transmission can be described in the following way:

$$\begin{pmatrix} 1 \\ 1 \\ 1 \\ 1 \end{pmatrix} \xrightarrow{1. \text{ sexp.}} \begin{pmatrix} \sigma_{11} \\ \sigma_{2x} \\ \sigma_{3x} \\ \sigma_{44} \end{pmatrix} \xrightarrow{\text{MFT 2-3}} \begin{pmatrix} \sigma_{11} \\ \sigma_{2x}(1 - \varepsilon_{23}) + \sigma_{3x}\varepsilon_{23} \\ \sigma_{3x}(1 - \varepsilon_{23}) + \sigma_{2x}\varepsilon_{23} \\ \sigma_{44} \end{pmatrix} \xrightarrow{2. \text{ sexp.}} \begin{pmatrix} \sigma_{11} \\ \sigma_{22}(1 - \varepsilon_{23}) + \sigma_{32}\varepsilon_{23} \\ \sigma_{33}(1 - \varepsilon_{23}) + \sigma_{23}\varepsilon_{23} \\ \sigma_{44} \end{pmatrix}. \quad (3.4)$$

The sextupole system of the ABS is optimized for highest initial polarization and intensity in case of hydrogen running, where the use of the transition units between the sextupole subsystems is not required and the initial polarization depends dominantly on the efficiencies of the transition units in the ABS appendix and the target holding field. As the transmission probabilities of the HERMES ABS are nearly ideal in this case ($\sigma_{11} \simeq \sigma_{22} \simeq 0.45$ and $\sigma_{33} \simeq \sigma_{44} \simeq 0$) [Br 95], the initial hyperfine population (or normalized intensity) is given by²⁰:

$$P_{z+} : \frac{1}{2} \begin{pmatrix} 1 \\ 1 - \varepsilon_{24} \\ 0 \\ \varepsilon_{24} \end{pmatrix} \quad P_{z-} : \frac{1}{2} \begin{pmatrix} 1 - \varepsilon_{13} \\ 1 \\ \varepsilon_{13} \\ 0 \end{pmatrix}. \quad (3.5)$$

If the ABS is supposed to inject a single hyperfine state as described for example by eq. 3.4, the transmission probabilities σ_{23} and σ_{32} are not negligible and lead to a reduced

²⁰In case of hydrogen, it was found, that the effect of the WFT can be described reasonably well by a direct exchange between state $|1\rangle$ and $|3\rangle$ with one efficiency only.

Pol.	Inj. HFS	high frequency transitions	
		appendix	betw. sext.
P_e	$ 1\rangle, 2\rangle$	OFF	OFF
P_{z+}	$ 1\rangle, 4\rangle$	SFT 2-4	OFF
P_{z-}	$ 2\rangle, 3\rangle$	WFT 1-3	OFF
P_{e+}, P_{z-}	$ 2\rangle$	OFF	WFT 1-3 / MFT 1-3
P_{e-}, P_{z+}	$ 4\rangle$	SFT 2-4	WFT 1-3 / MFT 1-3
P_{e+}, P_{z+}	$ 1\rangle$	OFF	MFT 2-3
P_{e-}, P_{z-}	$ 3\rangle$	WFT 1-3	MFT 2-3

Tab. 3.1: Injection modes of the ABS for polarized hydrogen running. During HERMES data taking, the injection mode is randomly switched between P_{z+} and P_{z-} . Spin relaxation measurements were performed between HERA positron fills and were almost always done with the modes P_e , P_{z+} and P_{z-} . The single state injection modes have been used for bhabha-measurements with the luminosity monitor [Wei 98] and for the BRP calibration (see sec. 3.6).

injected polarization. This is also the case for the nuclear polarization modes of \vec{D} as listed in tab. 3.2 and for the injection modes for a single hyperfine state of hydrogen in tab. 3.1.

The default injection modes of the ABS for hydrogen running are listed in tab. 3.1, the deuterium modes are given by tab. 3.2.

The transmission probability matrix can be estimated²¹ by a computer simulation [Br 95]. In case of deuterium, the results of this calculation predicts no significant influence of m_I on the transmission. The reason is, that the critical field of deuterium is much smaller than of hydrogen, so that the difference between hyperfine states with the same m_s , which scales with $x = B/B_C$, is less pronounced. It is therefore sufficient to describe the ABS

²¹As the precise circumstances of the beam formation at the ABS nozzle and therefore the starting conditions are not known, the simulation can only deliver an *estimation* of the transmissions. Braun used a so-called *molecularity parameter* μ to describe the laminarity of the formed atomic beam, which had to be maximal to be in agreement with his measurements [Br 95]. The same assumption is used in the present work to obtain a first estimate of the transmissions.

Pol.	Inj. HFS	high frequency transitions	
		appendix	between sextupole subsystems
P_e	$ 1\rangle, 2\rangle, 3\rangle$	OFF	OFF
P_{z+}	$ 1\rangle, 6\rangle$	SFT 2-6 (s26)	SFT 3-5 (t35)
P_{z-}	$ 3\rangle, 4\rangle$	WFT 1-4/2-3 (w14)	SFT 3-5 (t35)
P_{zz+}	$ 3\rangle, 6\rangle$	SFT 2-6 (s26)	MFT 1-4 (m14)
P_{zz-}	$ 2\rangle, 5\rangle$	SFT 3-5 (s35)	MFT 1-4 (m14)
P_{e+}, P_{z+}	$ 1\rangle$	OFF	MFT 3-4 (m34), SFT 2-6 (t26)
P_{e+}, P_{zz-}	$ 2\rangle$	OFF	WFT 1-4/2-3 (v14), SFT 2-6 (t26)
P_{e+}, P_{z-}	$ 3\rangle$	OFF	WFT 1-4/2-3 (v14), SFT 3-5 (t35)
P_{e-}, P_{z-}	$ 4\rangle$	WFT 1-4/2-3 (w14)	MFT 3-4 (m34), SFT 2-6 (t26)
P_{e-}, P_{zz-}	$ 5\rangle$	SFT 3-5 (s35)	WFT 1-4/2-3 (v14), SFT 3-5 (t35)
P_{e-}, P_{z+}	$ 6\rangle$	SFT 2-6 (s26)	WFT 1-4/2-3 (v14), SFT 2-6 (t26)

Tab. 3.2: Injection modes of the ABS for deuterium running. The bold printed shortcuts were introduced to distinguish the transitions in the appendix (s26,s35,w14) from the transitions between the sextupoles (t26,t35,v14). More injection modes are possible, but were not used by default.

State	$ 1\rangle$	$ 2\rangle$	$ 3\rangle$	$ 4\rangle$
$ 1\rangle$	0.45	0.45	0.033	0.047
$ 2\rangle$	0.45	0.45	0.03	0.043
$ 3\rangle$	0.009	0.0085	0	0
$ 4\rangle$	0.013	0.013	0	0

State	\uparrow	\downarrow
\uparrow	0.45	0.035
\downarrow	0.009	0.0

Tab. 3.3: Absolute transmission probabilities σ_{ab} of the ABS sextupole system calculated by a tracking program for hydrogen (left table) and deuterium (right table) at the working point of the ABS. The number of the row refers to the hyperfine state in the first subsystem and the number of the column to the state in the second subsystem. The relative transmitted intensity of the rejected state of the nuclear polarized states of deuterium is $0.035/0.45 \simeq 7.8\%$. For the discussion of the injected polarization, one can use the relative transmissions, which are defined by $\sigma_{ab} = \sigma_{ab}^{abs}/\sigma_{11}$. Due to the low critical field $B_C^D = 11.68 \text{ mT}$ of Deuterium, the transmissions probabilities depend only on the value of m_S . $\sigma_{\uparrow\downarrow}$ is the transmission probability for an atom, which is in state $m_S = \frac{1}{2}$ in the first sextupole subsystem and in state $m_S = -\frac{1}{2}$ in the second.

transmissions for \vec{D} by $\sigma_{\uparrow\uparrow}$, $\sigma_{\downarrow\downarrow}$, $\sigma_{\uparrow\downarrow}$ and $\sigma_{\downarrow\uparrow}$, where the arrows refer to the electron spin of the atom. Tab. 3.3 lists the results of the simulation program for hydrogen and deuterium.

The deuterium setup of the ABS is significantly more complex than the hydrogen setup:

- The MFT 1-4 between the sextupole systems can remove state $|1\rangle$ from the atomic beam only, if the MFT is operated with a positive gradient.
- The SFT unit between the sextupole subsystems allows σ -transitions only and thus can not be used as a SFT 1-6 transition. Due to the ordering of the transitions units between the sextupoles (e.g. the SFT is first along the beam axis), the MFT can not be used together with the SFT to obtain a single state injection mode with state $|3\rangle$ only. The reason is, that an effective exchange 1-4 by the subsequent transitions 3-4, 2-3 and 1-2 with a MFT requires, that all upper hyperfine states are equally populated, which is not the case, if the SFT unit depopulates state $|2\rangle$ or state $|3\rangle$. The operation of the WFT/MFT unit requires therefore a setup as WFT (**v14** in tab. 3.2, with negative gradient) to realize this injection mode.
- The originally planned deuterium setup used a MFT 3-4 transition between the sextupole subsystems for the vector polarized modes $P_{z\pm}$. Due to the relatively high value of the *leakage* $\sigma_{\uparrow\downarrow}$, it was found that the use of the SFT 3-5 (**t35**) instead of the MFT 3-4 has the advantage, that the *leaking* hyperfine state ($|5\rangle$ instead of $|4\rangle$) is unpolarized in the high field limit ($P_z \rightarrow 0$).

Generally, it was found, that the setup of the individual transitions is less robust in case of deuterium, which is for example related to the required low field values for the MFT/WFT transitions, which are more sensitive to surrounding fringe fields and other distortions. An additional problem is the location of the transitions units within the ABS. The small distance of the SFT unit to the first sextupole subsystem leads to an influence of the fringe fields of the sextupole magnets on the transition setup and (presumably) performance.

3.5 The Target Gas Analyzer (TGA)

The Target Gas Analyzer (TGA) shares the vacuum system with the Breit-Rabi Polarimeter [Bau 96, Ko 98]. It consists of a chopper, two baffles and a quadrupole mass spectrometer (QMS) with a cross beam ionizer. A channeltron is used for the detection of the ionized atoms and molecules. One baffle is mounted in short distance to the extension tube (ET), another one directly in front of the ionizer volume. The baffles ensure, that atoms entering the ionizer volume can not hit the inner ionizer walls and recombine, which could cause a virtual molecular beam signal. Fig. 3.7 shows a schematic of the setup of the TGA. The ions are detected by a channeltron behind the mass spectrometer. The channeltron pulses are counted and stored with a multichannel time resolving counter on a **digital signal processor** (DSP) board. Fig. 3.8 shows a typical time spectrum of the TGA countrates taken with hydrogen. A trigger signal produced by the chopper is used for the synchronization of bin numbers and chopper status. Frequency drifts of the chopper motor are compensated by an adjustment of the binlength by the DSP software. The *beam* rates are calculated by the difference of the counts per time in the periods of open and closed chopper. The statistical error of the beam rates is estimated by the analysis of the time spectrum [Bau 96].

The beam rates have to be corrected, if

- the absolute count rates are high ($\geq 1\text{ MHz}$). In this case a dead time correction has to be applied. The emission current of the TGA cross beam ionizer has to be reduced, when the background rates exceed about 1 MHz , in order to keep this correction small.
- a measurable water beam is present. The water causes a virtual atomic hydrogen or deuterium beam signal by means of dissociative ionization. At the target working point of a storage cell temperature of 100 K or below, the water beam rate can be neglected due to the low water vapour pressure.

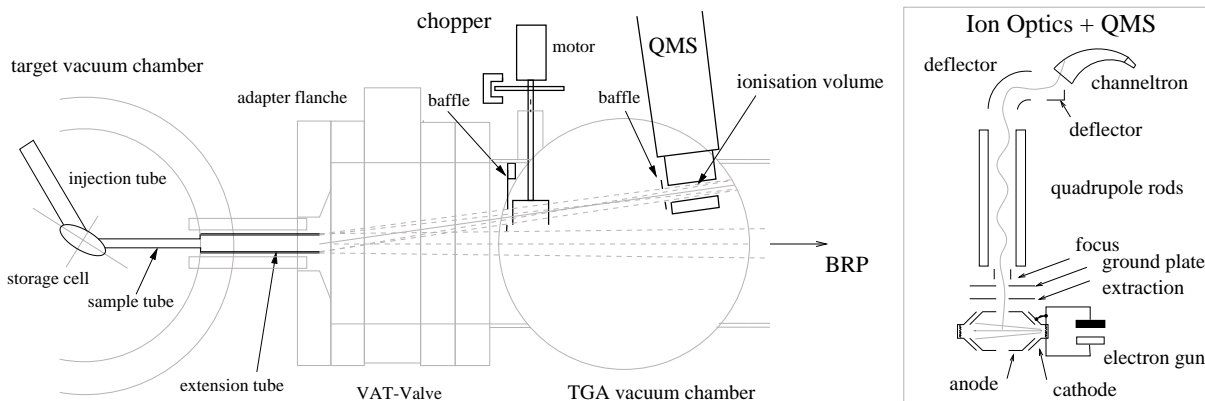


Fig. 3.7: The setup of the Target Gas Analyzer (TGA). Atoms and molecules diffuse towards the end of the extension tube (ET) and enter the TGA. A chopper is used to subtract the background rate of the residual gas in the TGA vacuum chamber. The baffles prevent atoms from hitting the inner walls of the cross beam ionizer. The axis of the ET is tilted by 30° relative to the horizontal plane.

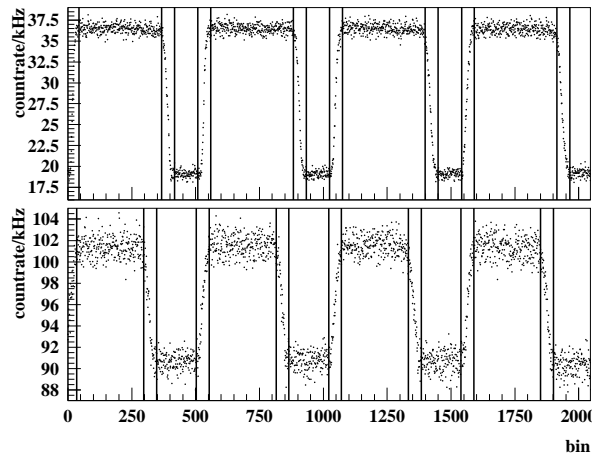


Fig. 3.8: Time spectrum of atomic count rates of the BRP (upper figure) and TGA (lower figure). The vertical lines indicate the bin numbers corresponding to the limits between the chopper positions *open*, *undefined* and *closed*. The bin length is adjustable and typically set to $175 \mu s$, so that with a chopper frequency of about $5.5 Hz$ two chopper turns are collected within the 2048 bins. This is the minimal time period for the beam intensity measurement and is called a *single cycle*. Typically 8 to 16 single cycles are collected for a beam intensity measurement.

3.5.1 Interpretation of the TGA Beam Rates

The measured atomic S_a and molecular S_m beam rates of the TGA are proportional to the corresponding fluxes Φ_a and Φ_m into the TGA times the ionization cross section $\sigma_{a,m}^{ion}$ and the detection probability $\varepsilon_{a,m}$ ²². In addition, the signals are proportional to the particles mean inverse velocity $\left\langle \frac{1}{v_{a,m}} \right\rangle$ ²³ and depend on the emission current I_{emis} of the electron gun of the cross beam ionizer²⁴ and the magnetic fringe fields of the target and spectrometer magnet²⁵:

$$S_{a,m} \propto \Phi_{a,m} \cdot \sigma_{a,m}^{ion} \cdot \varepsilon_{a,m} \cdot \left\langle \frac{1}{v_{a,m}} \right\rangle \cdot f(B, I_{emis}). \quad (3.6)$$

The total flux Φ^{TGA} into the TGA is given by the sum of the atomic and molecular flux (see eq. 2.33) and is proportional to the injected flux of the atomic beam source:

$$\Phi^{TGA} = \Phi_a^{TGA} + 2 \Phi_m^{TGA} \propto \Phi^{ABS}, \quad (3.7)$$

The partial beam rates S_a and S_m can therefore be interpreted as parts of a total rate²⁶

$$S_{tot} = S_a + \sqrt{2} \kappa S_m, \quad (3.8)$$

²²The *detection probabilities* $\varepsilon_{a,m}$ include the transmission probabilities of the ions through the quadrupole mass spectrometer (QMS). Magnetic fringe fields in the target region, caused by the HERMES spectrometer magnet and the target magnet have an influence on the trajectories of the ions inside the cross beam ionizer and the mass spectrometer, so that the detection probability and the absolute count rates of the TGA depend on the magnetic fields. During calibration measurements and HERMES data taking periods, the magnetic field values of this magnets were kept constant. The BRP QMS is - due to the higher distance - not sensitive to the target magnet.

²³The probability for ionization in the cross beam ionizer is proportional to the time τ , that the atoms or molecules need to pass by the ionization volume: $S_{a,m} \propto \langle \tau_{a,m} \rangle \propto \left\langle \frac{1}{v_{a,m}} \right\rangle$.

²⁴The dependence on I_{emis} is not necessarily linear, as space charge effects in the electron gun can lead to a change in the trajectories of the ionizing electrons and to a change in the ionizing efficiency. A measurement of the TGA count rate as a function of the emission current shows, that the signals are only proportional to the emission current in case of the low values $I_{emis} < 100 \mu A$ (see fig. 3.9).

²⁵This dependencies - caused by the change of the trajectories of the electrons in the cross beam ionizer and the ions within the QMS - can usually be ignored, as both magnets are kept on constant field values during data taking and all relevant TGA calibration measurements.

²⁶The factor of $\sqrt{2}$ instead of 2 is related to the different average velocities of atoms and molecules.

if one defines the relative sensitivity of the TGA for the atomic and molecular beam by the constant κ ²⁷:

$$\kappa = \frac{\sigma_a^{ion} \cdot \varepsilon_a}{\sigma_m^{ion} \cdot \varepsilon_m}. \quad (3.9)$$

It follows from eq. 2.33, that the total flux into the TGA is directly proportional to the injected flux, independent on the strength of recombination, if all parts of the storage cell are on the same temperature. However, the measurements show, that the extension tube, which is only connected by a thread to the storage cell frame, has typically a higher temperature T_{ET} . If one assumes, that all parts except the extension tube are on the same temperature ($T_{BT} = T_{IT} = T_{ST} = T$), one obtains²⁸:

$$\Phi^{TGA} \propto \Phi^{ABS} \frac{C^{TGA}}{2C^{BT} + C^{IT} + C^{TGA}}, \quad (3.10)$$

where

$$C^{TGA} = \frac{C^{ST} C^{ET}}{C^{ST} + C^{ET}} = \frac{C^{ST}}{1 + \frac{C^{ST}}{C^{ET}}}. \quad (3.11)$$

If the conductance C^{xx} is expressed by $C^{xx} = \tilde{C}^{xx} \sqrt{\frac{T_{xx}}{M}}$, one finds with $2C^{BT} + C^{IT} \gg C^{TGA}$:

$$\Phi^{TGA} \propto \Phi^{ABS} \frac{1}{1 + \frac{\tilde{C}^{ST}}{C^{ET}} \sqrt{\frac{T}{T_{ET}}}}. \quad (3.12)$$

The temperature of the extension tube T^{ET} can be approximated by [Ko 98]:

$$T^{ET}(T) = T_0 + \frac{300 K - T_0}{300 K} T, \quad (3.13)$$

²⁷If one assumes, that the ratio of the detection probabilities is close to one $\varepsilon_a \simeq \varepsilon_m$, then κ is approximately given by $\kappa \simeq \frac{\sigma_a^{ion}}{\sigma_m^{ion}} = 0.626$ for 70 eV ionization energy of the electron gun. The cross sections have been measured by [Sha 87, Rap 65]. This method can of course only deliver an the order of magnitude of κ .

²⁸The indices *BT*, *IT*, *ST* and *ET* stand for **beam tube**, **injection tube**, **sample tube** and **extension tube** respectively (see fig. 3.4).

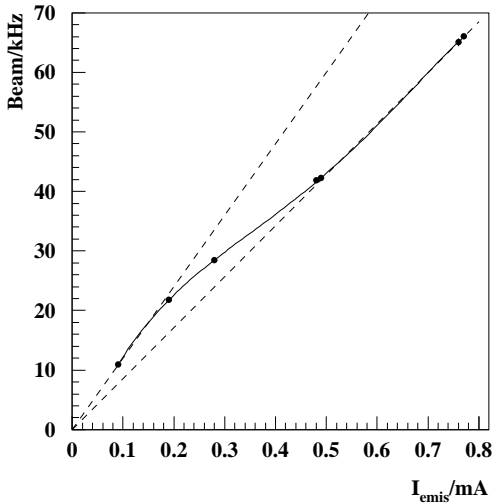


Fig. 3.9: Beam signal of the TGA as function of emission current $f(B, I_{emis})$. The plot contains a fit to the measured data with a polynomial of 4th degree and two lines, which indicate the transition between two regions of proportionality. The measurement was performed using a constant gas flow of the unpolarized gas feed system (UGFS) into the cell center. The storage cell temperature was constant within 1 K during the measurement.

where T is the storage cell temperature and T_0 is a constant. The temperature dependence of the countrates resp. the flux can then be expressed by a function $g(T)$:

$$g(T) = \frac{1}{g(T_{norm})} \frac{1}{\sqrt{T_{ET}}} \frac{1}{1 + \frac{\tilde{C}^{ST}}{\tilde{C}^{ET}} \sqrt{\frac{T}{T_{ET}}}}. \quad (3.14)$$

If one defines the normalized flowrates $\phi_{a,m}$ into the TGA by:

$$\phi_a = \frac{S_a}{g(T)f(B, I_{emis})} \quad (3.15)$$

$$\phi_m = \frac{\sqrt{2}\kappa S_m}{g(T)f(B, I_{emis})}, \quad (3.16)$$

then the sum of these flowrates is directly proportional the injected intensity²⁹:

$$\phi_a + \phi_m = \frac{S_a + \sqrt{2}\kappa S_m}{g(T)f(B, I_{emis})} = c_{TGA} \Phi^{ABS}, \quad (3.17)$$

so that the TGA is a direct monitor of the ABS intensity. The constant c_{TGA} can for instance be obtained by a comparison of ϕ_{tot} with the rates of the luminosity monitor. It is convenient to define the measured degree of dissociation α^{TGA} by

$$\alpha^{TGA} = \frac{\phi_a}{\phi_a + \phi_m} = \frac{S_a}{S_a + \sqrt{2}\kappa S_m}, \quad (3.18)$$

which is independent of temperature and emission current I_{emis} .

3.5.2 Calibration of the TGA

The calibration of the TGA requires first of all the determination of the relative sensitivity κ in order to make use of eq. 3.18. As the ABS intensity (right side of eq. 3.17) is constant during normal operation, any variation of α^{TGA} can be used to determine κ by a linear fit of ϕ_m versus ϕ_a or vice versa, if the temperatures and the emission current are kept constant or the functions $f(B, I_{emis})$ and $g(T)$ are known. During data taking, strong variations in α^{TGA} have been observed after accidental losses of the HERA electron respectively positron beam near the HERMES target region³⁰. Besides these unintended events, calibrations have been performed by so-called *temperature scans*, as α^{TGA} depends on the cell temperature.

The knowledge of the parameter T_0 in eq. 3.13 is crucial for the interpretation of the data. Unfortunately, a temperature sensor on the extension tube was not installed before 1999, so that T_0 has to be obtained from the temperature data as well. This causes some

²⁹The difference in the velocities of atoms and molecules results a factor of $\sqrt{2}$ in the relative weight between S_a and S_m and a common factor $\frac{1}{\sqrt{T_{ET}}}$.

$$\left\langle \frac{1}{v_m} \right\rangle = \sqrt{2} \left\langle \frac{1}{v_a} \right\rangle \propto \frac{1}{\sqrt{T_{ET}}}.$$

³⁰The HERMES collimator C_2 is the bottleneck of the electron storage ring, which is the most likely cause for events of this kind.

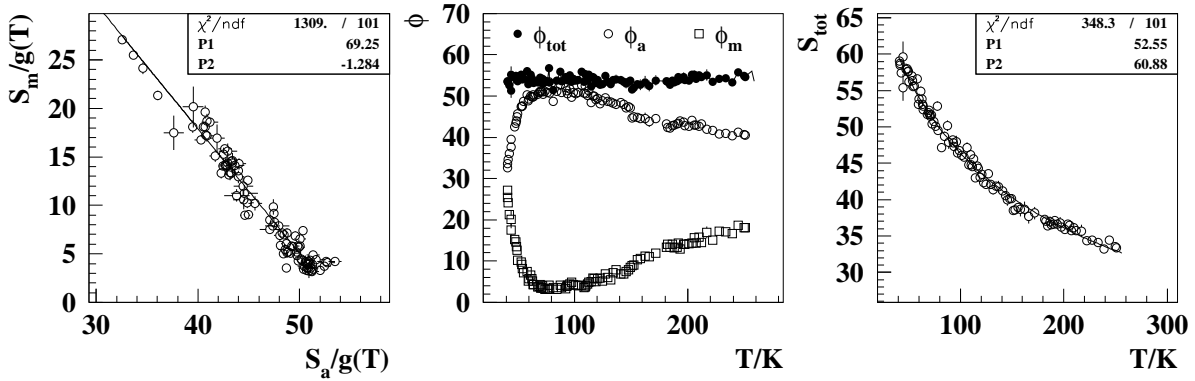


Fig. 3.10: Calibration of the TGA by variation of cell temperature (Aug 16 1997). The left graph shows the linear fit of the temperature corrected molecular beam rate vs. the atomic beam rate. κ can be obtained from the slope. With the fitted value of κ , one obtains the normalized flowrates ϕ_a , ϕ_m and ϕ_{tot} vs. storage cell temperature T as shown in the central graph. The right graph shows the raw beam rates $S_{tot} = S_a + \sqrt{2}\kappa S_m$ vs. T as symbols and the matched temperature dependence as solid line.

additional systematic uncertainty for this calibration method as one typically finds, that the fit results for T_0 and κ are correlated.

Fig. 3.10 shows a calibration of the TGA by a variation of the cell temperature. The fitted values are:

$$\kappa = 0.5507 \pm 0.00226(\text{stat}) \quad T_0 = 52.5 \pm 0.59 K. \quad (3.19)$$

The value of κ obtained by this method differs from the value obtained by a fit to the beam loss data (see next section) by about 4%. This is a measure of the systematic uncertainty of this method³¹. A thin wire temperature sensor was mounted to the extension tube at the beginning of 1998, so that the temperature model could be replaced by a direct measurement. A calibration measurement of 27th Aug. 1998 delivered the following calibration constant:

$$\kappa = 0.861 \pm 0.015.$$

The difference in κ between 1997 and 1998 is related to the change of the target gas from hydrogen to deuterium and the voltages of the TGA ion optics.

3.5.3 Calibration of the TGA with a HERA Beam Loss

Under certain conditions, it was observed, that α^{TGA} is correlated with the HERA beam [Ko 98]. The appearance of a sudden and sharp drop of α^{TGA} in coincidence with an accidental HERA beam loss is one example. Several events of this kind were observed in the data taking periods of the hydrogen/deuterium target. The left side graph of fig. 3.11 shows the atomic signal of the TGA S_a plotted vs. the molecular signal S_m after a beam loss of the HERA beam near the HERMES target section. The negative slope of the fitted line is identical to $\sqrt{2}\kappa$. During this measurement, performed with \vec{H} in Oct. 1997, the cell temperature was constant. The resulting value for κ is:

$$\kappa = 0.572 \pm 0.0026$$

³¹Another calibration measurement (Sep 16) by temperature variation yielded $\kappa = 0.572 \pm 0.0015$, which is in perfect agreement with the beam loss data.

After the beam loss, α^{TGA} increased with the ABS running time due to the recovery of the water layer on the cell surface³² as shown in the right side graph. Due to the uncertainties in the knowledge of T_{ET} , the calibration with the beam loss data can be assumed to be more reliable.

3.5.4 The Separation of Initial Atomic Fraction (α_0^{TGA}) and the Fraction of Atoms Surviving Recombination (α_r^{TGA})

There are additional corrections, which have to be applied in order to separate independently α_0^{TGA} and α_r^{TGA} . The only source of the atomic flux ϕ_a into the TGA is the flux of the ABS, as long as dissociative ionization can be neglected. The molecular flux ϕ_m , however, has several sources:

- Molecules, which are produced by recombination on the cell surface, result the flux ϕ_r . The polarization of the molecules, which are produced by recombination relative to the polarization of the atoms is described by the factor β .
- Molecules, which are ballistically injected by the ABS into the cell: The degree of dissociation of the ABS dissociator is less than 100%. A fraction of the molecules leaving the ABS nozzle enters the storage cell by means of ballistic flow, depending on the peaking of the nozzle, the space angle and the performance of the dissociator. The corresponding molecular flux into the TGA is called ϕ_{ball} . Ballistically injected molecules are unpolarized.
- Molecules of the background (rest) gas of the target chamber. Due to the finite pumping speed of the turbo pumps of the target chamber, a molecular background remains inside the cell and causes a molecular flux ϕ_{rg} into the TGA. Molecules, which are part of the rest gas of the target chamber, are unpolarized, as they have left the holding field of the target magnet and experienced a high number of collisions with the stainless steel walls of the target chamber.

The total molecular flux ϕ_m is the sum of these components:

$$\phi_m = \phi_r + \phi_{ball} + \phi_{rg} \cdot \quad (3.20)$$

³²Even though this is the most likely explanation of the behavior of α^{TGA} , there might be other effects - like for example a cleaning of the cell surface by the atomic hydrogen.

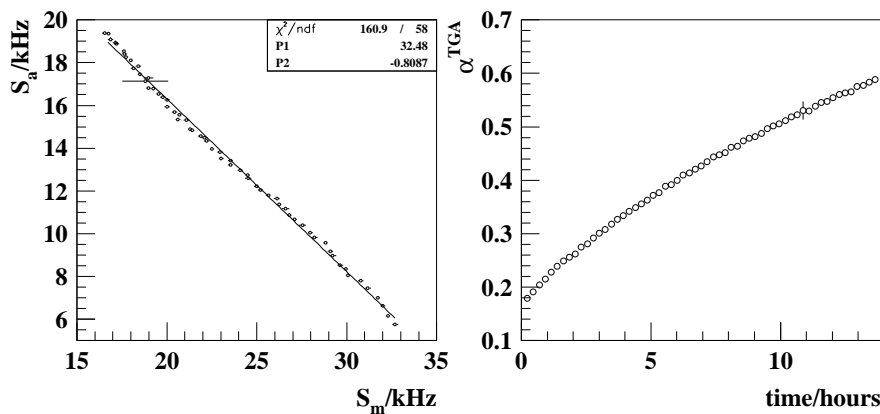


Fig. 3.11: Left: Atomic rate S_a of the TGA vs. molecular rate S_m after a beam loss of the HERA beam. The negative slope of the linear fit is equal to $\sqrt{2}\kappa$. Right: Measured atomic fraction α^{TGA} vs. time for the same period.

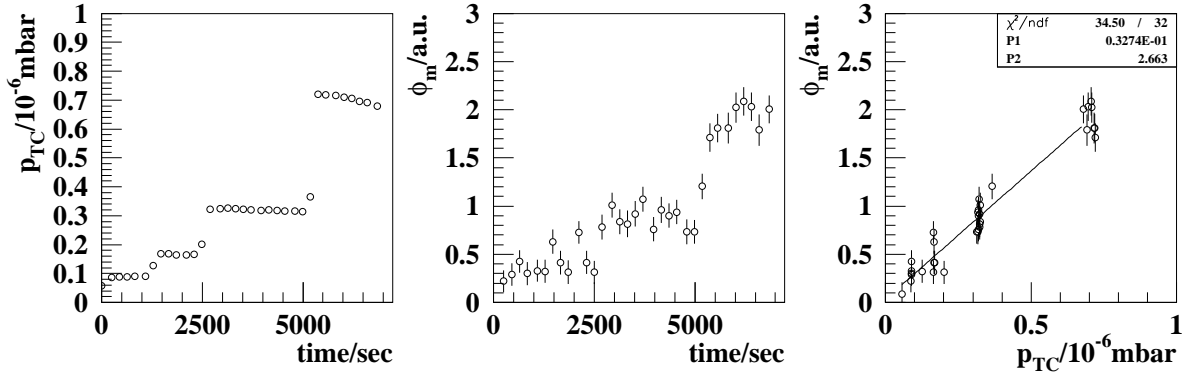


Fig. 3.12: Measurement of rest gas correction. The intensity of a molecular hydrogen beam - injected into the target chamber - is stepwise increased. The molecular flowrate of the TGA increases with the target pressure. The fitted slope of ϕ_m vs. p_{tc} yields the rest gas calibration constant c_{rg} . The measurement was performed in 1997 with hydrogen.

The fraction of atoms surviving recombination α_r^{TGA} as measured by the TGA, is defined by:

$$\alpha_r^{TGA} = \frac{\phi_a}{\phi_a + \phi_r}. \quad (3.21)$$

The initial atomic fraction α_0^{TGA} is defined by:

$$\alpha_0^{TGA} = \frac{\phi_a + \phi_r}{\phi_a + \phi_r + \phi_{ball} + \phi_{rg}}, \quad (3.22)$$

so that $\alpha^{TGA} = \alpha_0^{TGA} \cdot \alpha_r^{TGA}$ holds.

The restgas flow rate can be measured by injecting H_2 respectively D_2 with the unpolarized gas feed system (UGFS) into the target chamber. For this purpose, an additional separate gas feed line is connected to the target chamber, which allows a direct variation of the background pressure with hydrogen and deuterium. The molecular rate measured by the TGA as a function of the target chamber pressure p_{tc} is given by

$$\phi_{rg} = c_{rg} \cdot p_{tc}, \quad (3.23)$$

Fig. 3.12 shows an example for a rest gas calibration measurement. As instabilities of the pressure gauge readings have been observed, this type of calibration has been repeated periodically. The result of the measurement of fig. 3.12 is $c_{rg} = 2.663 \pm 0.107 \cdot 10^{-6}/\text{mbar}$.

If one or both transitions between the two sextupole systems of the ABS are switched on, the atomic flux into the target cell is changed as described in sec. 3.4. As the molecules are not affected by the sextupole system, the *ballistic flux* ϕ_{ball} stays constant. If the fraction of molecules caused by recombination is proportional to the injected atomic flux³³, one obtains the following equations for the molecular flux ϕ_m of the TGA:

$$\phi_m^{(i)} - \phi_{ball} - \phi_{rg}^{(i)} = \left(\frac{1}{\alpha_r^{TGA}} - 1 \right) \phi_a^{(i)}, \quad (3.24)$$

³³If the recombination does not depend on the atomic density inside the storage cell.

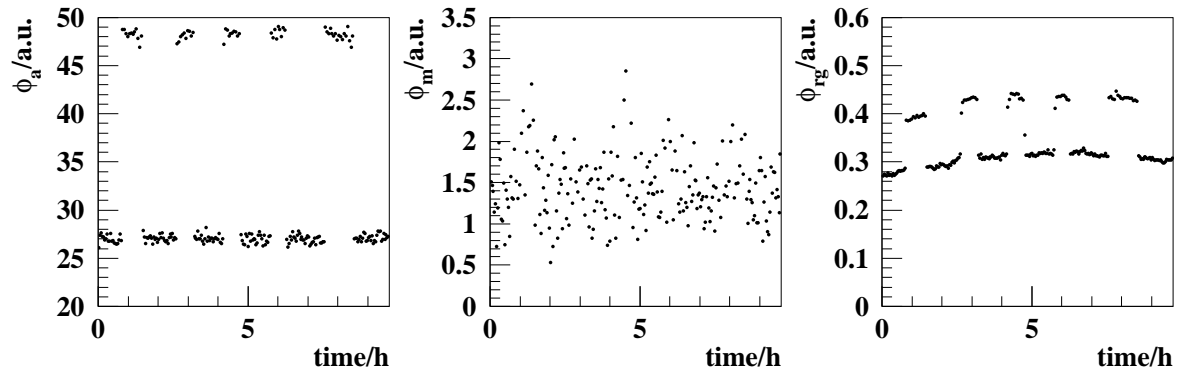


Fig. 3.13: Measurement of the flowrates ϕ_a (left) and ϕ_m (center) in two different injection modes for the determination of the ballistic flowrate ϕ_{ball} , performed in 1997 with hydrogen. The injection mode is switched with the MFT 2-3 transition between the ABS sextupole subsystems. The right figure shows $\phi_{rg} = 2.663 \cdot 10^{-6} p_{tc}/\text{mbar}$ versus time, as calculated from the pressure. The relative change in the target chamber pressure (right) is smaller than in the atomic flowrate (left). The reason for this behavior is, that atoms in state $|2\rangle$, which are focussed by the first sextupole subsystem of the ABS, are flipped to state $|3\rangle$ and then defocussed by the second subsystem. A fraction of the defocussed atoms ends up in the appendix of the ABS and diffuses into the target chamber. Even though these atoms do not enter the storage cell center ballistically, they contribute to the target chamber pressure.

By the division of the equations for two different injection modes, one obtains:

$$\phi_{ball} = \frac{(\phi_m^{(2)} - \phi_{rg}^{(2)})\phi_a^{(1)} - (\phi_m^{(1)} - \phi_{rg}^{(1)})\phi_a^{(2)}}{\phi_a^{(1)} - \phi_a^{(2)}}. \quad (3.25)$$

Fig. 3.13 shows an example of the described technique to measure the ballistic flow ϕ_{ball} , that resulted a value $\phi_{ball} = 0.74 \pm 0.112$ in the (arbitrary) units³⁴ of fig. 3.13.

3.5.5 Interpretation of the Atomic Fraction α_r^{TGA}

If there is no recombination inside the sample and extension tube, the flowrates ϕ_a and ϕ_r are directly proportional to the corresponding atomic and molecular partial pressures³⁵ in the storage cell center³⁶:

$$\begin{aligned} \phi_a &\propto p_a(0) C_a \\ \phi_r &\propto 2 p_r(0) C_m, \end{aligned} \quad (3.26)$$

³⁴Actually the unit is KHz/mA , but is arbitrary insofar, as it depends on the design of the ionizer, the setup of the ion optics etc.

³⁵This refers only to the molecules, that are produced by recombination.

³⁶The factor of 2 appears, as the molecular fluxes ϕ_x have been defined in the unit of atoms.

	MFT 1-3 off	MFT 1-3 on
ϕ_a	48.24	27.03
ϕ_m	1.687	1.338
ϕ_{rg}	0.424	0.305
ϕ_{ball}	0.738	
α^{TGA}	0.966	0.953
α_r^{TGA}	0.989	
α_0^{TGA}	0.977	0.963
α_0	0.956	0.935

Tab. 3.4: Example for the analysis of TGA beam rates of the time period from fig. 3.13. The equality of both values of α_r^{TGA} and ϕ_{ball} is the presumption for the calculation of ϕ_{ball} . The values are given in arbitrary units (kHz/mA).

where $C_{a,m}$ are the corresponding atomic and molecular conductances of sample and extension tube. With $C_a = \sqrt{2} C_m$ one finds³⁷:

$$\alpha_r^{TGA} = \frac{\phi_a}{\phi_a + \phi_r} = \frac{p_a(0)}{p_a(0) + \sqrt{2} p_r(0)} = \rho_a(0). \quad (3.28)$$

If recombination inside the sample and extension tube is not negligible, one still has the inequality:

$$\alpha_r^{TGA} \leq \rho_a(0). \quad (3.29)$$

α_r^{TGA} can not exceed the normalized atomic density in the center of the storage cell $\rho_a(0)$ as defined by eq. 2.37.

In correspondence to eq. 3.21 and eq. 3.22 the definitions of α_r and α_0 for the storage cell mean values are:

$$\alpha_r = \frac{N_a}{N_a + 2N_r}. \quad (3.30)$$

The initial atomic fraction α_0 is defined by:

$$\alpha_0 = \frac{N_a + 2N_r}{N_a + 2N_r + 2N_{ball} + 2N_{rg}}. \quad (3.31)$$

with the number of atoms respectively molecules N_x . The normalized total density ρ_t is given by eq. 2.39 as a function of α_r . It follows that:

$$N_a + 2N_r \propto (\phi_a + \phi_r) \cdot \frac{\sqrt{2}}{1 + (\sqrt{2} - 1)\alpha_r}. \quad (3.32)$$

The other molecular fluxes have to be multiplied by a factor of $\sqrt{2}$, if the densities inside the storage cell calculated. Correspondingly N_{ball} is given by:

$$2N_{ball} \propto \sqrt{2} \phi_{ball}. \quad (3.33)$$

³⁷It is worth mentioning, that the definition of α_r^{TGA} using flowrates (instead of densities) implies, that always

$$\alpha_r^{TGA} = \rho_a^{TGA}, \quad (3.27)$$

so that the definition of the *measured atomic fraction* is not consistent with the concept of an atomic fraction as introduced in sec. 2.5, but instead with the normalized atomic density. This has historical reasons.

The density of the rest gas contribution in the storage cell is not of triangular shape, but equally distributed over the storage cell. The number of rest gas molecules N_{rg} must therefore be weighted twice:

$$2N_{rg} \propto 2\sqrt{2}\phi_{rg}. \quad (3.34)$$

Hence α_0 is given by:

$$\alpha_0 = \left(1 + \frac{\phi_{ball} + 2\phi_{rg}}{\phi_a + \phi_r} (1 + (\sqrt{2} - 1)\alpha_r) \right)^{-1}, \quad (3.35)$$

while for the calculation of α_r , the knowledge of the sampling correction c_α is required: $\alpha_r = c_\alpha \alpha_r^{TGA}$. If α_r^{TGA} is close to one, also $\alpha_r \simeq 1$, so that:

$$\alpha_0 \simeq \frac{\phi_a + \phi_r}{\phi_a + \phi_r + \sqrt{2}(\phi_{ball} + 2\phi_{rg})}, \quad (3.36)$$

If one compares α_0 to α_0^{TGA} as given by eq. 3.22, one finds that $\alpha_0 \leq \alpha_0^{TGA}$ holds *always*. There are two reasons: First, the flowrates of ϕ_a and ϕ_m , which are used to define α_0^{TGA} represent the densities in the cell *times* the corresponding conductances C_a and C_m for atoms and molecules respectively, which differ by a factor of $\sqrt{2}$ and second, the rest gas contribution to the target density has not a triangular shape in contrast to the ballistically injected fluxes from the ABS. Using eq. 3.36 one obtains the results given in tab. 3.4 for the period of fig. 3.13. The measurement was performed on 25th of Sep. between two HERA fills and is typical for the high quality periods in 1997.

3.6 The Breit Rabi Polarimeter (BRP)

Two adiabatic high frequency transition (HFT) units, followed by a sextupole system with two magnets and a detector, are the basis of the Breit-Rabi type polarimeter (BRP) [Gau 92, Br 95, Ko 98]. The HFT units and the sextupole system are located in the first vacuum chamber, called *sextupole chamber*, while the *detection chamber* contains the beam chopper and a detector using a cross beam ionizer, a quadrupole mass spectrometer (QMS) and a channeltron for single ion detection. Both chambers form a differential pumping system with typical residual pressures of $2 \cdot 10^{-9}$ mbar in the sextupole chamber, which is pumped by two cryo pumps and $2.5 \cdot 10^{-10}$ mbar in the detection chamber, pumped by a titanium sublimation pump and an ion getter pump. In addition, both chambers can be connected to turbo pumps, which are used to pump the system down and to keep low pressure during the regeneration of the cryo pumps. Both turbo pumps have separate forepump systems. A third forepump/turbo pump system is used for the startup and regeneration of the cryo pumps. If the cryo pumps are connected to the sextupole chamber, they are automatically disconnected from the regeneration system. The detection chamber and the TGA vacuum chamber are baked out with temperatures of up to $220^\circ C$ after startup. The setup of the BRP vacuum system is shown in fig. 3.14.

The first of the HFTs is a SFT unit realized by a resonator cavity with tilted resonators, which can be used for both σ and π transitions, while the second unit is a MFT for π transitions realized by a high frequency coil. An optimization of the impedance matching of the MFT unit is done with an external Collins filter, while the SFT unit is kept in

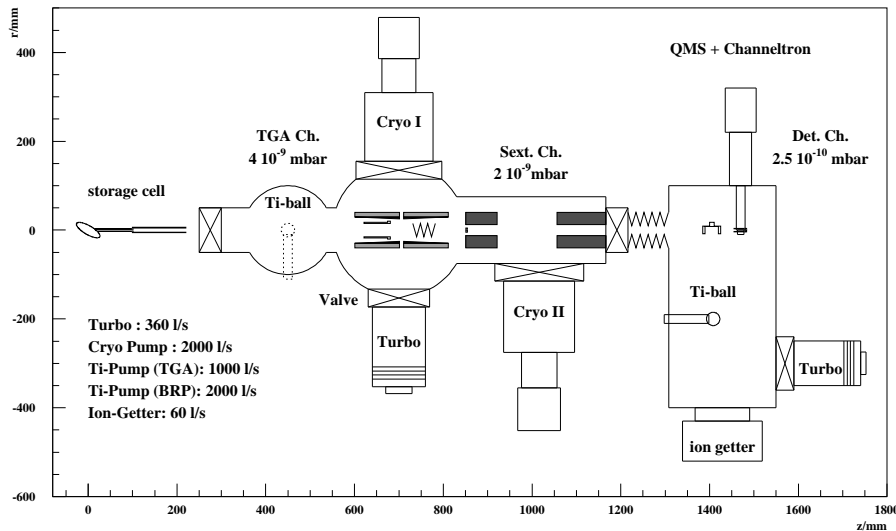


Fig. 3.14: Side view of the vacuum system of BRP and TGA. Details of the TGA are shown in fig. 3.7.

resonance with a feed back loop using a balance mixer [Br 95]. Pickup loops are used to monitor the high frequency amplitude in the transition units³⁸.

A signal proportional to the beam intensity is obtained in the same way as it was already described in context with the TGA by the use of a beam chopper. In fact, both devices, BRP and TGA, are controlled by the same software³⁹ and their countrates are registered and evaluated by the same DSP⁴⁰ module. In contrast to the TGA, the measurement of the BRP detector can be affected by a water beam, which can appear as an artifact of the differential pumping system. The partial pressure of water resp. H_2 in the sextupole system can cause a net water beam resp. H_2 beam into the BRP detector,

³⁸An optical telescope, which can be mounted on the BRP beam axis at the end of the detection chamber, is used to align the BRP optically with respect to the sample tube of the cell and the target chamber respectively. For this procedure the beam blocker, which is located at the entrance of the first sextupole magnet, defines the axis in combination with an alignment cross at the end of the second sextupole.

³⁹A short description is given in app. G.

⁴⁰DSP stands for **D**igital **S**ignal **P**rocessor

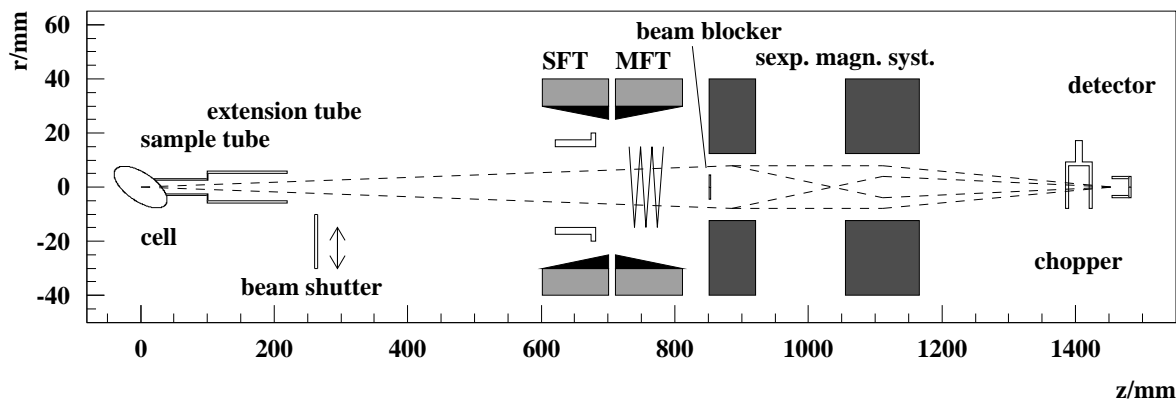


Fig. 3.15: The setup of the Breit-Rabi type polarimeter (BRP). The exact positions of the components are listed in tab. F.3.

which causes a virtual atomic beam rate by means of dissociative ionization. In case of hydrogen, the beam rates of the masses 1, 2 and 18 *amu* have been measured and a net hydrogen beam rate \tilde{S} was calculated by:

$$\tilde{S} = S_1 - k_2 S_2 - k_{18} S_{18}. \quad (3.37)$$

The correction constants k_2 and k_{18} were found by the variation of the partial pressures of water and H_2 during a warmup of the cryogenic pumps in the sextuple chamber with open gate valves. The correction scheme has been tested in regular time intervals by closing the valve between BRP and target chamber. The net atomic beam rate \tilde{S} has to be zero in this case.

For deuterium, there are more reaction channels for dissociative ionization, so that it was decided to install a beam shutter behind the extension tube, which allows to block the atomic beam into the BRP remotely. The beam shutter was designed in such a way, that it can not influence the beam rates of the TGA. A polarization measurement with deuterium includes a measurement of the *background beam* with a closed beam shutter. This *background beam* is subtracted from all other beam results. It was found to be small, so that it could have been neglected most of the time.

The corrected beam signal of the BRP depends on the transition state of both HFTs. A transition is switched on, if the high frequency amplitude is switched on and the currents in the static and gradient field coil are set to the values, which were chosen for this transition. The selection of the transition type (SFT 1-4 or SFT 2-4) of a HFT (BRP SFT in this case) is realized by the setting of the static magnetic field. A change of the operation frequency of a transition unit was only realized in the ABS.

3.6.1 Theory of Polarization Measurement

The sextupole system of the BRP focuses atoms with $m_S = +\frac{1}{2}$ of a certain velocity on the acceptance of the BRP detector. Atoms with $m_S = -\frac{1}{2}$ are defocussed by the sextupole system or deflected by the beam blocker. If σ_a is the probability of atoms in hyperfine state $|a\rangle$ to be transmitted by the sextupole system, the signal in the detector S_{off} ⁴¹ is given by:

$$S_{off} = c_{BRP} \sum_a \sigma_a I_a, \quad (3.38)$$

where I_a is the intensity of atoms in hyperfine state $|a\rangle$ in the sample beam and c_{BRP} a proportionality factor, which describes geometrical acceptance, detection efficiency of the mass spectrometer etc. If a BRP transition i is switched on, which exchanges the population of two or more hyperfine states, the signal S_i is given by:

$$S_i = c_{BRP} \sum_a \left(\sum_b \sigma_b T_{ba}^i \right) I_a, \quad (3.39)$$

where the matrix T_{ba}^i describes the exchange of the hyperfine states with transition i as described in sec. 2.2.

A collection of BRP signals can be described by a set of linear equations as a function of the intensities I_a :

$$S_i = c_{BRP} \sum_a M_{ia} I_a, \quad (3.40)$$

⁴¹The subscription *off* is used to describe the status of the HFT units.

where M_{ia} is the *measurement matrix*. It depends on the transition efficiencies and the transmission probabilities for each hyperfine state. In case of the SFT 1-4 signal, the corresponding equation 3.39 of $\sum_a M_{14,a} I_a$ is given by:

$$S_{SFT1-4} = [\sigma_1(1 - \varepsilon_{14}) + \sigma_4\varepsilon_{14}] I_1 + \sigma_2 I_2 + \sigma_3 I_3 + [\sigma_4(1 - \varepsilon_{14}) + \sigma_1\varepsilon_{14}] I_4. \quad (3.41)$$

If $\sigma_3 = \sigma_4 \simeq 0$ and $\varepsilon_{14} \simeq 1$ holds, eq. 3.41 simplifies to:

$$S_{SFT1-4} \simeq I_2 + I_4. \quad (3.42)$$

The linear equation system 3.39 can be solved, if at least four (six) different beam rates S_i are measured in case of hydrogen (deuterium). The intensities I_a can then be calculated by the inverse matrix $R = M^{-1}$ ⁴²:

$$I_a = c_{BRP}^{-1} \sum_i R_{ai} S_i. \quad (3.43)$$

The total intensity I_{tot} can be calculated by the sum over all hyperfine states

$$I_{tot} = \sum_a I_a, \quad (3.44)$$

and the hyperfine population numbers N_a of the sample beam are obtained by the normalization of the calculated intensities I_a :

$$N_a = \frac{I_a}{I_{tot}}. \quad (3.45)$$

The calculation of the polarization of the atoms requires the knowledge of the target holding field B , as the polarization of the mixed hyperfine states depends on the magnetic field value. With $C_{\pm} = \cos 2\theta_{\pm}$ ⁴³ and the following matrices⁴⁴:

$$\begin{aligned} M_P^H &= \begin{pmatrix} 1 & \cos 2\theta & -1 & -\cos 2\theta \\ 1 & -\cos 2\theta & -1 & \cos 2\theta \end{pmatrix} \\ M_P^D &= \begin{pmatrix} 1 & C_+ & C_- & -1 & -C_- & -C_+ \\ 1 & \sin^2 \theta_+ & -\cos^2 \theta_- & -1 & -\sin^2 \theta_- & \cos^2 \theta_+ \\ 1 & -\frac{1}{2}(3C_+ + 1) & \frac{1}{2}(3C_- - 1) & 1 & -\frac{1}{2}(3C_- + 1) & \frac{1}{2}(3C_+ - 1) \end{pmatrix}, \end{aligned} \quad (3.46)$$

the polarization of the \vec{H} and \vec{D} atoms is given by:

$$\begin{aligned} (P_e, P_z)^T &= M_P^H (N_1, N_2, N_3, N_4)^T \\ (P_e, P_z, P_{zz})^T &= M_P^D (N_1, N_2, N_3, N_4, N_5, N_6)^T. \end{aligned} \quad (3.47)$$

If the statistical error of the BRP beam rates S_i is given by the - diagonal - covariance matrix C_S , then the covariance matrix C_I of the intensities I_a is given by

$$C_I = R C_S R^T = (M^T C_S^{-1} M)^{-1}. \quad (3.48)$$

⁴²If one collects more signals than unknowns, the usage of the *pseudoinverse* matrix $R = (M^T G_S M)^{-1} M^T G_S$ is equivalent to a least square fit of the intensities I_a to the measured signals S_i , where G_S is the inverse covariance matrix of the measured signals [Bra 92].

⁴³The mixing angles are given by the formulas in tab. B.1 as a function of $x = B/B_C^{H,D}$.

⁴⁴The transposed matrix of A is A^T .

The covariance matrix C_N of the hyperfine populations N_a is given by

$$(C_N)_{ab} = \sum_{cd} \left(\frac{\partial N_a}{\partial I_c} \right) (C_I)_{cd} \left(\frac{\partial N_b}{\partial I_d} \right), \quad (3.49)$$

and finally the covariance matrix C_P of the polarization vector:

$$C_P = M_P^{H,D} C_N (M_P^{H,D})^T. \quad (3.50)$$

The statistical error ΔI_{tot} of the total intensity I_{tot} equals the sum over all elements of the covariance matrix C_I :

$$\Delta I_{tot} = \sum_{ab} (C_I)_{ab}. \quad (3.51)$$

3.6.2 Calibration of the BRP

A calibration of the BRP includes the determination of the efficiencies of all used transitions as well as a determination of the transmission probabilities of the sextupole system, as described in sec. 3.6.4. For the SFT unit, two efficiencies are required in case of \vec{H} , namely the ε_{s14} and ε_{s24} and 5 in case of \vec{D} : ε_{s16} , ε_{s26} , ε_{s35} and the two efficiencies of the SFT double transition ε_{s25r25} and ε_{s25r36} . The medium field transitions can be described by several separate transitions, each by its own efficiency [Br 95]. The hydrogen MFT 1-3 is described by the values of ε_{m13r12} and ε_{m13r23} . The same is true for the MFT 2-3, even though the 1-2 transition is not supposed to run in case of this transition.

Due to the limited space, the static field coils of both BRP transitions units are positioned close to each other and can not be controlled independently with the required precision. Namely, the setting of the static field of the SFT unit changes the field of the MFT unit by some percent, so that the setting of the static field of the MFT must be chosen separate for each SFT magnetic field setting. To avoid a third MFT setup, the SFT static and gradient fields are always set to the value of one of the transitions. The SFT is turned off via the high frequency amplitude. In case of hydrogen the MFT unit must be tuned separately for two different SFT field values - the settings of the SFT 1-4 and the SFT 2-4. In case of deuterium four different MFT setups are required. Beneath the setup of the transitions also the number of efficiencies N_{eff} is increased by these factors, so that N_{eff} is 10 in case of hydrogen and 41 in case of deuterium. The number of different signals N_{BRP} , which can be measured with the BRP, is 11 in case of hydrogen and 29 in case of deuterium⁴⁵. Tab. 3.5 gives an overview over the signals of the BRP and their magnetic field settings in case of hydrogen.

B. Braun introduced a calibration method, which makes use of an additional sextupole magnet in front of the transitions units of the BRP, a so-called *calibration magnet*. This magnet rejects the hyperfine states with $m_S = -\frac{1}{2}$ and reduces the number of unknowns for a calibration measurement [Br 95]. Due to several problems with this calibration method, which are described in [Hen 98], an alternative calibration method was developed, which makes use of the possibility to run the ABS in a variety of different injection modes.

⁴⁵If the crosstalk could be avoided, 6 efficiencies would be necessary to describe the hydrogen and 14 for the deuterium setup. The number of possible BRP states (signals) would then be 9 in case of hydrogen and 20 (4 MFT states including *off* times 5 SFT states.) in case of deuterium.

If the ABS can be operated in N_{ABS} different modes, and the BRP beam rates are measured for all possible N_{BRP} HFT states of the BRP, one obtains $N_{BRP} \cdot N_{ABS}$ equations and has to determine $N_{eff} + N_{HFS} \cdot N_{ABS}$ unknowns. If the degree of freedom N_f given by

$$N_f = (N_{BRP} - N_{HFS}) \cdot N_{ABS} - N_{eff} \quad (3.52)$$

can be made positive, the equation system can be solved. In case of hydrogen, 7 ABS modes were typically used for a calibration measurement, which results in $N_f = 39$. In case of deuterium, two calibration modes were prepared, one with 5 ABS injection modes and another one with 6 modes. In the first case, one obtains $N_f = 134$, in the second $N_f = 169$.

In order to evaluate a BRP calibration measurement, one defines the vector \mathbf{x} of parameters by $\mathbf{x} = (\varepsilon, I)^T$ and the vector of the measured values \mathbf{y} by the measured beam signals $\mathbf{y} = (S_a)^T$ and rewrites⁴⁶ eq. 3.40:

$$f_a(\mathbf{x}, \mathbf{y}) = \sum_b M_{ab}(\varepsilon) \cdot I_b - S_a = 0 \quad (3.53)$$

The algorithm, which was used to obtain the fitted efficiencies ε_{xx} and their covariance matrix C_ε , is described in app. H. The covariance matrix C_x , which is obtained by the algorithm, has the following form:

$$C_x = \begin{pmatrix} C_\varepsilon & C_{\varepsilon, I} \\ C_{I, \varepsilon} & C_I \end{pmatrix}. \quad (3.54)$$

Only the covariance matrix C_ε is used for the calculation of the systematic uncertainty of the polarization measurement.

3.6.3 Systematic Uncertainty of the Polarization Measurement

The covariance matrix $C_{I, syst}$ of the systematic uncertainty of the intensities I_a is given by:

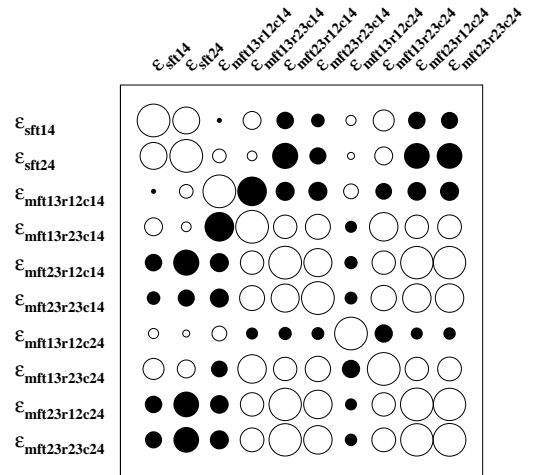
$$C_{I, syst} = T_\varepsilon C_\varepsilon T_\varepsilon^T, \quad (3.55)$$

⁴⁶The proportionality factor can be neglected for this purpose.

BRP-Signal	Name	MFT-RF	MFT-B	SFT-RF	SFT-B
OFF	off	OFF	OFF	OFF	OFF
SFT 1-4	s14	OFF	OFF	ON	1-4
SFT 2-4	s24	OFF	OFF	ON	2-4
MFT 1-3	m13c14	ON	1-3	OFF	1-4
MFT 1-3	m13c24	ON	1-3	OFF	2-4
MFT 2-3	m23c14	ON	2-3	OFF	1-4
MFT 2-3	m23c24	ON	2-3	OFF	2-4
MFT 1-3/SFT 1-4	m13s14	ON	1-3	ON	1-4
MFT 1-3/SFT 2-4	m13s24	ON	1-3	ON	2-4
MFT 2-3/SFT 1-4	m23s14	ON	2-3	ON	1-4
MFT 2-3/SFT 2-4	m23s24	ON	2-3	ON	2-4

Tab. 3.5: Switching modes of the BRP and corresponding signals for hydrogen running.

Efficiency	MFT-B	SFT-B	Value	Error
ε_{s14}	?	1-4	0.993	± 0.0134
ε_{s24}	?	2-4	1.01	± 0.0103
$\varepsilon_{m13r12c14}$	1-3	1-4	1.01	± 0.0106
$\varepsilon_{m13r23c14}$			0.986	± 0.0141
$\varepsilon_{m23r12c14}$	2-3	1-4	-0.00856	± 0.0113
$\varepsilon_{m23r23c14}$			0.949	± 0.0123
$\varepsilon_{m13r12c24}$	1-3	2-4	0.999	± 0.00418
$\varepsilon_{m13r23c24}$			0.903	± 0.00815
$\varepsilon_{m23r12c24}$	2-3	2-4	-0.000247	± 0.011
$\varepsilon_{m23r23c24}$			0.974	± 0.0104



Tab. 3.6: The table lists the transition efficiencies of the BRP for hydrogen running and a transmission ratio $\frac{\sigma_2}{\sigma_1} = 1.0295$. The dependence of the MFT efficiencies on the SFT setting is significant for ε_{m13r23} . The figure visualizes the correlation matrix, which is defined by eq. H.5. The area of the circles is proportional to the absolute value of the correlation; open circles correspond to a positive value, filled circles to a negative value. The circles on the diagonal represent a value of +1, by definition of the correlation matrix. It is obvious, that the correlation between SFT and MFT efficiencies is lower than within the MFT-block and within the SFT-block. For a polarization measurement, where only a subset of BRP states is used, only the upper left 6×6 matrix is required. More detailed results can be found in [Hen 98]. The corresponding results for deuterium are listed in tab. E.2

where the matrix T_ε describes the dependence of the calculated intensities I_k on the efficiencies ε_l :

$$(T_\varepsilon)_{kl} = \left(\frac{\partial I_k}{\partial \varepsilon_l} \right) = \sum_j \left(\frac{\partial I_k}{\partial S_j} \right) \cdot \left(\frac{\partial S_j}{\partial \varepsilon_l} \right). \quad (3.56)$$

The first matrix is identical to \mathbf{R} , the inverse of the measurement matrix \mathbf{M} :

$$R_{kj} = \frac{\partial I_k}{\partial S_j}. \quad (3.57)$$

The second matrix, called A_ε , can be calculated from the measurement matrix \mathbf{M} ⁴⁷:

$$(A_\varepsilon)_{jl} = \frac{\partial S_j}{\partial \varepsilon_l} = \sum_k (M_{jk}(\varepsilon_1, \dots, \varepsilon_l + 1, \dots, \varepsilon_n) - M_{jk}(\varepsilon_1, \dots, \varepsilon_l, \dots, \varepsilon_n)) \cdot I_k. \quad (3.58)$$

The propagation of the systematical error is then treated in the same way as described in sec. 3.6.1 for the statistical covariance matrix C_I .

3.6.4 Sextupole Transmissions of the BRP

The sextupole magnet system of the BRP consists of two cylindrical magnets behind the transition units. A beam blocker at the entrance of the first magnet ensures, that no atoms

⁴⁷ \mathbf{M} is linear in each single efficiency ε_l , even though \mathbf{M} contains products of *different* efficiencies.

in hyperfine states with $m_S = -\frac{1}{2}$ are transmitted on axis⁴⁸. The transmission probability of these states therefore is zero. As there are no transitions between the sextupole magnets, the transmission properties of the sextupole system can be described by the two (three) transmission probabilities σ_1 , σ_2 (and σ_3) in case of hydrogen (deuterium). For the evaluation of the hyperfine population and polarization, the normalization allows to set $\sigma_1 = 1$ and thus to reduce the number of unknowns by one. In this case, only the knowledge of the ratio $r_{21} = \frac{\sigma_2}{\sigma_1}$ (and $r_{31} = \frac{\sigma_3}{\sigma_1}$ for \vec{D}) is required with high precision, as it enters directly into the evaluation of the polarization measurements. The absolute transmission $\sigma_1(T)$ is only required for the correction of I_{tot} ⁴⁹.

Numerical calculations resulted, that the transmission ratios of deuterium r_{21} and r_{31} can assumed to be unity with a maximal uncertainty less than 0.5%. The reason is, that the critical field of deuterium is smaller than for hydrogen. The difference of the Stern Gerlach force for the upper hyperfine states of deuterium vanishes in high field. As the BRP sextupole system is equipped with a beam blocker, which stops atoms with central (low field) trajectories, the transmissions are approximately equal for the deuterium states $|1\rangle$, $|2\rangle$ and $|3\rangle$.

The ratio r_{21} of hydrogen can either be determined by a numerical tracking simulation of the atoms through the BRP sextupole system or it can be fitted to the measured data. The numerical calculations require the precise knowledge of a variety of parameters:

- The geometrical position of all components.
- The detection efficiency of the cross beam ionizer for different trajectories.

⁴⁸The exact geometry of the system is given by tab. F.3.

⁴⁹The absolute value of I_{tot} is of interest, if one wants to compare the atomic beam rates of BRP and TGA. As the population numbers are calculated by beam ratios, the temperature dependence vanishes by the normalization.

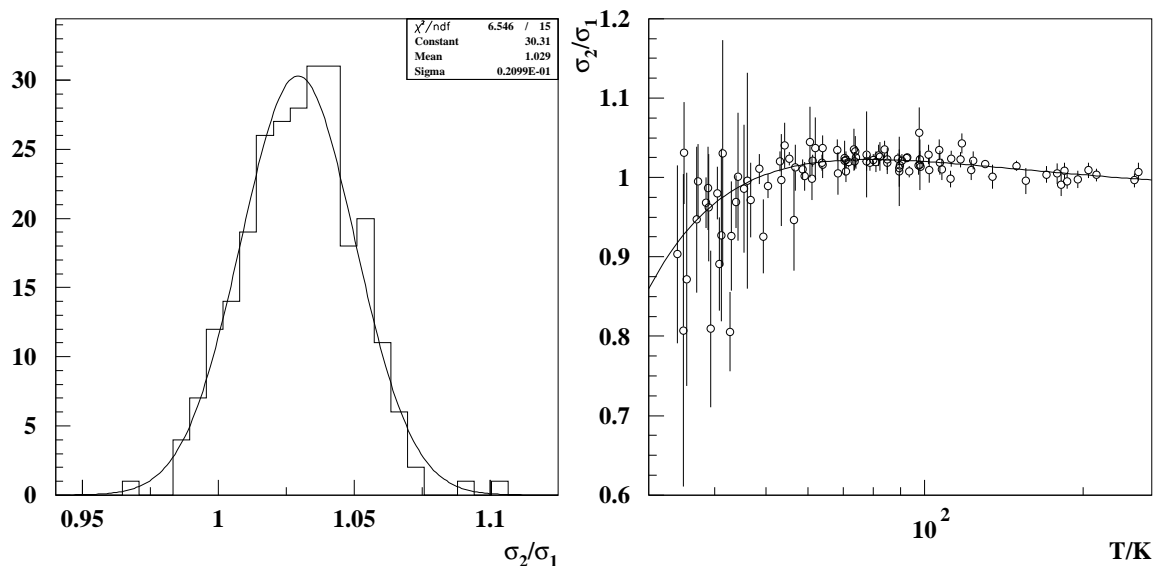


Fig. 3.16: The left graph shows a histogram of the measured ratio r_{21} for hydrogen at 95 K storage cell temperature as determined by an iteration with a calibration measurement. The right graph shows the measured transmission ratio $r_{21} = \frac{\sigma_2}{\sigma_1}$ of the BRP sextupole system for hydrogen atoms versus storage cell temperature (open circles) and a polynomial fit to the data (solid line).

- The exact position of the sample/extension tube in dependence of the storage cell temperature.

Most of these parameters are not known with the required precision. The transmission ratio was therefore extracted from the measured data. The value of r_{21} at a storage cell temperature of 100 K was determined by the χ^2 -minimization of a BRP calibration measurement. With the resulting efficiencies, it is then possible to fit r_{21} to the measured data for all storage cell temperatures in the range of the HERMES target. As the hydrogen polarization measurements were performed with 5 instead of the 4 required BRP signals, the fit of r_{21} to the measured data does not require a special measurement mode as in case of the efficiency calibration⁵⁰. The result is shown in fig. 3.16 and tab. 3.6 respectively⁵¹:

$$r_{21}(95\text{ K}) = \left. \frac{\sigma_2}{\sigma_1} \right|_{95\text{ K}} = 1.029 \pm 0.0015. \quad (3.59)$$

The right graph of fig. 3.16 shows the results for r_{21} vs. the storage cell temperature. If one defines x by $x = \frac{100\text{ K}}{T}$, r_{21} could be fitted with a polynomial in x , which is given by:

$$r_{21}(T) = p_0 + p_1 \cdot x + p_2 \cdot x^2 + p_3 \cdot x^3. \quad (3.60)$$

with

$$\begin{aligned} p_0 &= 0.972 \pm 0.0056, & p_1 &= 0.075 \pm 0.011, \\ p_2 &= -0.025 \pm 0.009, & p_3 &= -0.0022 \pm 0.0027. \end{aligned} \quad (3.61)$$

3.6.5 Total Intensity I_{tot} of the BRP

There are three reasons for an investigation of the total intensity of the BRP and the velocity distribution of the atoms, that are able to pass the sextupole system of the BRP: First, the knowledge of I_{tot} in dependence of the storage cell temperature allows to compare the atomic flux into the BRP with the corresponding flux into the TGA. It will be shown in sec. 4, that this comparison can be used to investigate the recombination probability γ_r of sample and extension tube. This helps to limit the sampling correction c_α . Second, a high value of I_{tot} is required to minimize the statistical uncertainty of the polarization measurement. Third, the knowledge of the velocity distribution of the atoms passing the BRP sextupole system is required for the interpretation of the diffusion time measurements, which will be presented in sec. 4.1.

The number of atoms $N(v, T) dv$ in the target gas of temperature T with absolute velocity between v and $v + dv$ is proportional to Maxwell's velocity distribution $f(v, T)$:

$$N(v, T) dv \propto f(v, T) dv = \left(\frac{m}{k_b T} \right)^{\frac{3}{2}} e^{-\frac{m v^2}{2 k_b T}} v^2 dv. \quad (3.62)$$

The entrance of the first BRP sextupole has a small solid angle $\Delta\Omega$ and the trajectories of the atoms, that are able to enter the BRP, are approximately parallel to the BRP axis.

⁵⁰A (possible) dependence of the transition efficiencies on the temperature can be neglected, as the velocity of the atoms is (more or less) fixed by the transmission windows of the BRP sextupole system. Calibration measurements performed at different temperatures agreed with this assumption. Only the efficiency $\varepsilon_{m13r23c24}$ increases slightly with decreasing temperature; this efficiency does not influence the polarization measurements, as the MFT is operated with the field setting of the SFT 1-4.

⁵¹As the uncertainty of r_{21} is - at the working point - about one order of magnitude below the systematic uncertainty of the transition efficiencies, it is neglected in the error calculation of the polarization.

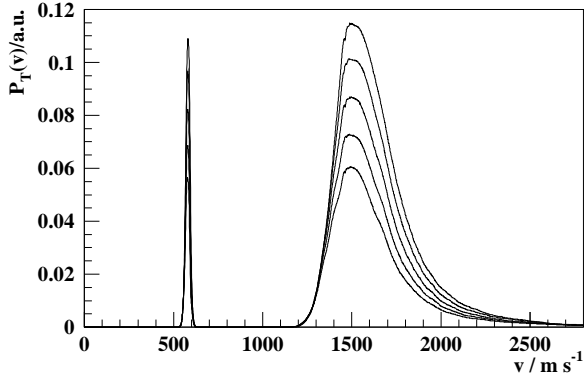


Fig. 3.17: Transmission function $P_T(v)$ of the BRP sextupole system for deuterium atoms in state $|1\rangle$ for a relative misalignment between BRP and storage cell (top to bottom) of 0, 0.25, 0.5, 0.75, 1.0 mm. As the storage cell is moved relative to the BRP by thermal expansion/contraction, a theoretical prediction of $I_{tot}(T)$ is difficult and requires a very precise knowledge of the geometry. Similar strong dependencies were found for several geometrical parameters like for instance the BRP detector acceptance.

The total number of atoms entering the sextupole acceptance of the BRP per unit time \dot{N}_{tot} , depends on the number of atoms injected by the ABS per unit time (\dot{N}_{ABS}) and on the geometry. If recombination is neglected, no temperature dependence of this number is expected. The number of atoms $\dot{N}_v(v, T) dv$ with velocities between v and $v + dv$, that are entering the sextupole entrance per unit time, is then proportional to the *flux*⁵²:

$$\dot{N}_v(v, T) dv = \dot{N}_{tot} \frac{f(v, T) v dv}{\int_0^\infty f(v, T) v dv} = \frac{\dot{N}_{tot}}{\langle v \rangle} f(v, T) v dv, \quad (3.63)$$

where $\dot{N}_{tot} \propto \dot{N}_{ABS} \Delta\Omega$. If $P_T(v)$ is the average probability of an atom in state $|1\rangle$ to be transmitted by the sextupole system, the beam rate I_{tot} in the BRP can be expressed by⁵³:

$$I_{tot} \propto \int_0^\infty P_T(v) \dot{N}_v(v, T) \frac{dv}{v} = \frac{\dot{N}_{tot}}{\langle v \rangle} \int_0^\infty P_T(v) f(v, T) dv. \quad (3.64)$$

The transmission probability $P_T(v)$ was calculated with a sextupole trajectory simulation program. It was found by the simulation, that the exact value of $P_T(v)$ depends on a variety of geometrical parameters, that are not known to the required precision. The influence of the relative misalignment between the sample tube and the BRP is shown in fig. 3.17. As the sample tube is moved relative to the BRP by the thermal contraction of the storage cell (see sec. 3.2), a precise alignment is impossible with the current target setup. The real temperature dependence of the total intensity I_{tot} can therefore not be predicted by the simulation.

3.6.6 Time of Flight Measurements with the BRP

Time of flight (TOF) measurements through the BRP sextupole system have been performed with a modulated beam technique in order to obtain the velocity distribution $P_T(v)$. The beam modulation was realized by switching the high frequency field of the MFT unit of the BRP periodically on and off (pulsed RF). For this purpose, the BRP chopper was stopped in the "open" position and a programmable pulser was connected to the MFT RF generator. The rising edge of the pulser signal was used to trigger the time resolving

⁵²The *flux* density is given by the density of atoms times their velocity v .

⁵³The detection probability of an atom in the cross beam ionizer is proportional to its residence time in the ionization volume, which results a factor $\frac{1}{v}$.

counter. The ABS was operated with deuterium⁵⁴ in injection mode P_{z-} with the BRP transitions SFT 3-5 and MFT 3-4 switched on. If the RF amplitude of the BRP-MFT is off, the signal vanishes (ideal case, no relaxation inside storage cell):

$$\begin{pmatrix} 0 \\ 0 \\ 1 \\ 1 \\ 0 \\ 0 \end{pmatrix} \xrightarrow{\text{BRP SFT 3-5}} \begin{pmatrix} 0 \\ 0 \\ 0 \\ 1 \\ 1 \\ 0 \end{pmatrix} \xrightarrow{\text{BRP sextupoles}} \begin{pmatrix} 0 \\ 0 \\ 0 \\ 0 \\ 0 \\ 0 \end{pmatrix}.$$

If the pulser switches the RF amplitude of the MFT 3-4 on, the signal appears again:

$$\begin{pmatrix} 0 \\ 0 \\ 1 \\ 1 \\ 0 \\ 0 \end{pmatrix} \xrightarrow{\text{BRP SFT 3-5}} \begin{pmatrix} 0 \\ 0 \\ 0 \\ 1 \\ 1 \\ 0 \end{pmatrix} \xrightarrow{\text{BRP MFT 3-4}} \begin{pmatrix} 0 \\ 0 \\ 1 \\ 0 \\ 1 \\ 0 \end{pmatrix} \xrightarrow{\text{BRP sextupoles}} \begin{pmatrix} 0 \\ 0 \\ 1 \\ 0 \\ 0 \\ 0 \end{pmatrix}.$$

The signal in the BRP, measured by the time resolving counter of the DSP board with $5 \mu\text{sec}$ bin length, shows two steps, caused by the two different drift times for the passage of the sextupole system (see fig. 3.18). The integrated distribution of drift times results - besides a constant background - the time distribution of counts in the BRP detector, if the time, the MFT RF amplitude is on, is larger than the maximal drift time of the atoms between MFT unit and BRP detector. The measurement was repeated for 4 different storage cell temperatures and gives the relative weight and the absolute position of both velocity windows. The measured signal $S(\tau, T)$ is given by the following integral:

$$S(\tau, T) = \int_0^\tau \dot{N}(v = \frac{l}{t}, T) \frac{dv}{dt} dt, \quad (3.65)$$

where $l \simeq 700 \text{ mm}$ is the distance between the pulsed MFT and the BRP mass spectrometer. With the assumption, that both velocity windows can be approximated by a Gaussian shaped function $g_i(v)$

$$g_i(v) = \frac{1}{\sqrt{\pi}\sigma_i} e^{-\frac{(v-v_i)^2}{\sigma_i^2}}, \quad (3.66)$$

$P_T(v)$ can be modeled with

$$P_T(v) = (1 - f_1) g_1(v) + f_1 g_2(v). \quad (3.67)$$

The results of fig. 3.18 were obtained with

$$\begin{aligned} v_1 &= 1520 \text{ ms}^{-1} & v_2 &= 570 \text{ ms}^{-1} \\ \sigma_1 &= 173 \text{ ms}^{-1} & \sigma_2 &= 14 \text{ ms}^{-1} \\ f_1 &= 0.935. \end{aligned} \quad (3.68)$$

⁵⁴If the velocity is scaled correspondingly, the results can also be applied to the transmission of state $|1\rangle$ of hydrogen.

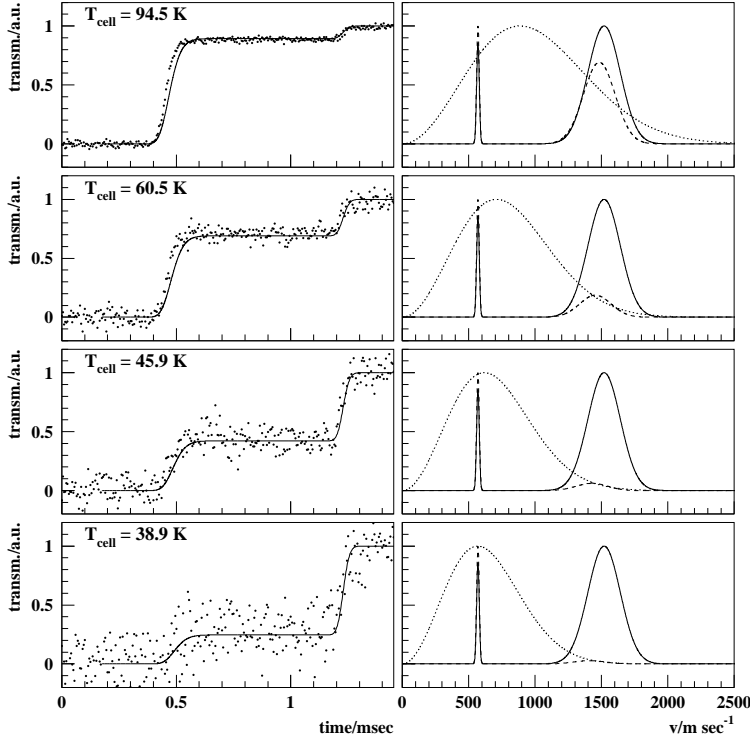


Fig. 3.18: Results of a TOF measurement of deuterium atoms passing the BRP sextupole system for 4 different storage cell temperatures (from upper to lower). Left side: Scaled and normalized measured signal $S(\tau, T)$ as function of τ (dots). Right side: The transmission function $P_T(v)$ of eq. 3.67 (solid line), the Maxwellian velocity distribution $f(v, T)$ (dotted line) and the product of both (dashed line). The graphs are scaled to a maximal value of 1 and the parameters of $P_T(v)$ were fitted to the measured TOF-signals. With eq. 3.67, the parameters of eq. 3.68 and a Maxwellian $f(v, T)$ one obtains a TOF-signal as shown by the solid line in the left side graphs, which matches the measured signals reasonably well.

Center value and width of both velocity windows are in agreement with the results of the simulation shown in fig. 3.17.

The total intensity $I_{tot}(T)$ can - using this model of $P_T(v)$ - be calculated by eq. 3.64. Due to the relative movement between cell and BRP by thermal expansion of the cell (see fig. 3.5) and a high dependence of the BRP acceptance to this position (see fig. 3.17), eq. 3.64 may be used only for temperatures below about 80 K, where the thermal movement of the cell is negligible. Fig. 3.19 shows the result of eq. 3.64, calculated with the parameters of the TOF measurements compared to measured data points. The good agreement at low temperatures is important insofar, as one can use the comparison of the temperature corrected BRP intensity and the atomic flux ϕ_a of the TGA as a cross check on Monte Carlo results and to determine the recombination properties of the sample and extension tube (see sec. 4).

The total intensity is - for storage cell temperatures below 70 K and for the case of no recombination given by:

$$I_{tot}(T) \propto P_1 + P_2 T + P_3 T^2 + P_4 T^3. \quad (3.69)$$

The values of P_i can be taken from the inlet of fig. 3.19. The *absolute* signal value depends beneath the temperature on other parameters as the emission current of the ionizer, the injected atomic flux etc. These parameters have to be kept constant during a measurement of $I_{tot}(T)$. The model of $P_T(v)$ using simple Gaussian velocity windows can not reproduce the measured signal $S(\tau, T)$ with high precision, but it allows to calculate the temperature dependence of $I_{tot}(T)$ reasonably well as shown by fig. 3.19. The misbehavior of $S(\tau, T)$ around $t = 0.5$ ms in fig. 3.18 can be understood by the difference between the exact functional form of $P_T(v)$ and the Gaussian model. Insofar, the agreement is satisfactory.

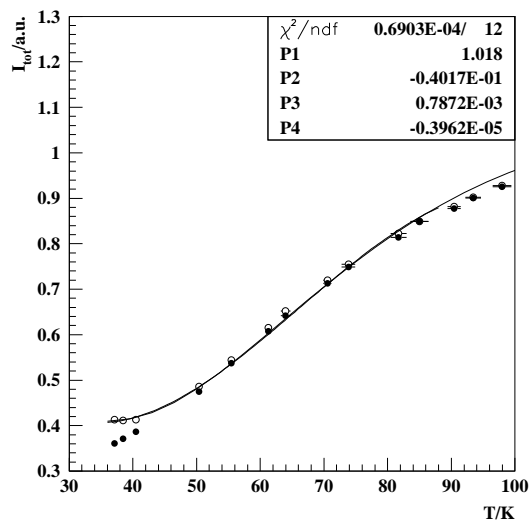


Fig. 3.19: Total intensity of the BRP signal $I_{tot}(T)$ in dependence of the storage cell temperature. The solid line is calculated with the results of the TOF measurement by eq. 3.64. The filled circles represent the measured result, normalized by the total flux ϕ_{tot} of the TGA. The open circles show the same result, divided by α^{TGA} . The values of α^{TGA} were above 0.85 for all temperatures. The inset shows the parameters of a fit to the calculated behavior with a polynomial of third order in T .

Another important result is, that the BRP sextupole system is (for historical reasons) not optimized for the typical target temperature of about 100 K. As shown by the right part of fig. 3.18, the intensity of the BRP signal can - especially for low temperature measurements - be increased by a modification of the sextupole system. Even at the target working point of 100 K, the intensity of the transmitted beam could be increased by nearly 100 %, if weaker or shorter sextupole magnets are used⁵⁵.

3.7 The Luminosity Monitor

The HERMES luminosity monitor (Lumi)[Due 90, Be 94, Be 98, Wei 98] is a part of the HERMES spectrometer and measures the number of e^+e^- (e^-e^-) coincidences caused by Bhabha- (Moeller-) scattering of the HERA positrons (electrons) with the electrons of the target gas under small angles. The number of events is proportional to the electron density inside the storage cell and therefore to the number of nucleons in the target. Besides the density measurement, the luminosity monitor can also be used to determine the polarization of the target electrons by the analysis of the asymmetry for different target injection modes, if the polarization of the HERA beam is known.

The (coincidence-) countrate in the luminosity monitor R_L is given by:

$$R_L = \sigma_T \frac{I_{beam}}{e} D_t, \quad (3.70)$$

where I_{beam} is the HERA beam current, e is the charge of the electron and D_t the integrated target thickness (of electrons). σ_T is the cross section for detectable processes integrated over the detector acceptance and can be obtained by a Monte Carlo simulation. σ_T is $2.22 \pm 0.13 \text{ Hz } \mu\text{barn}^{-1}$ ($3.17 \pm 0.19 \text{ Hz } \mu\text{barn}^{-1}$), if the HERA ring is filled with positrons (electrons) [Ter 99]. The resulting average nucleus⁵⁶ volume density $\langle n \rangle$ then is:

$$\langle n \rangle = \frac{e}{\sigma_T 2L} S_L, \quad (3.71)$$

⁵⁵The significant temperature dependence of the transmission ratio r_{21} below 50 K would also be reduced, as it is caused by the low velocity window, where the atoms pass a radial minimum and the difference in the magnetic moment of the hyperfine states (of hydrogen) is not negligible.

⁵⁶The number of electrons in the target gas is equal to the number of nuclei.

where L is the length of one wing of the storage cell ($L = 20 \text{ cm}$ and $S_L = \frac{R_L}{I_{beam}}$ is the relative Lumi countrate. The calculation yields for positron fills (bhabha scattering):

$$\langle n \rangle_{[10^{12} \text{ cm}^{-3}]} = 1.8 S_{L[Hz/MA]}, \quad (3.72)$$

and for electron fills (Møller scattering):

$$\langle n \rangle_{[10^{12} \text{ cm}^{-3}]} = 1.26 S_{L[Hz/MA]}. \quad (3.73)$$

It is convenient to use a target density $\langle n \rangle$, that is normalized to a certain storage cell temperature - typically 100 K ⁵⁷, as it is a direct measure of the ABS flux:

$$\langle n_{norm} \rangle = \langle n \rangle \sqrt{\frac{T}{100 \text{ K}}}. \quad (3.74)$$

As it is not possible to reconstruct the vertex position and thus to apply a vertex cut on Lumi events, the measured Lumi signal will contain a contribution of events, which are not produced by the target gas, but for instance by gas in the beam pipe between the storage cell and the position of the luminosity detector. Fig.3.20 shows a plot of the target

⁵⁷The target density changes via the storage cell conductance with the temperature.

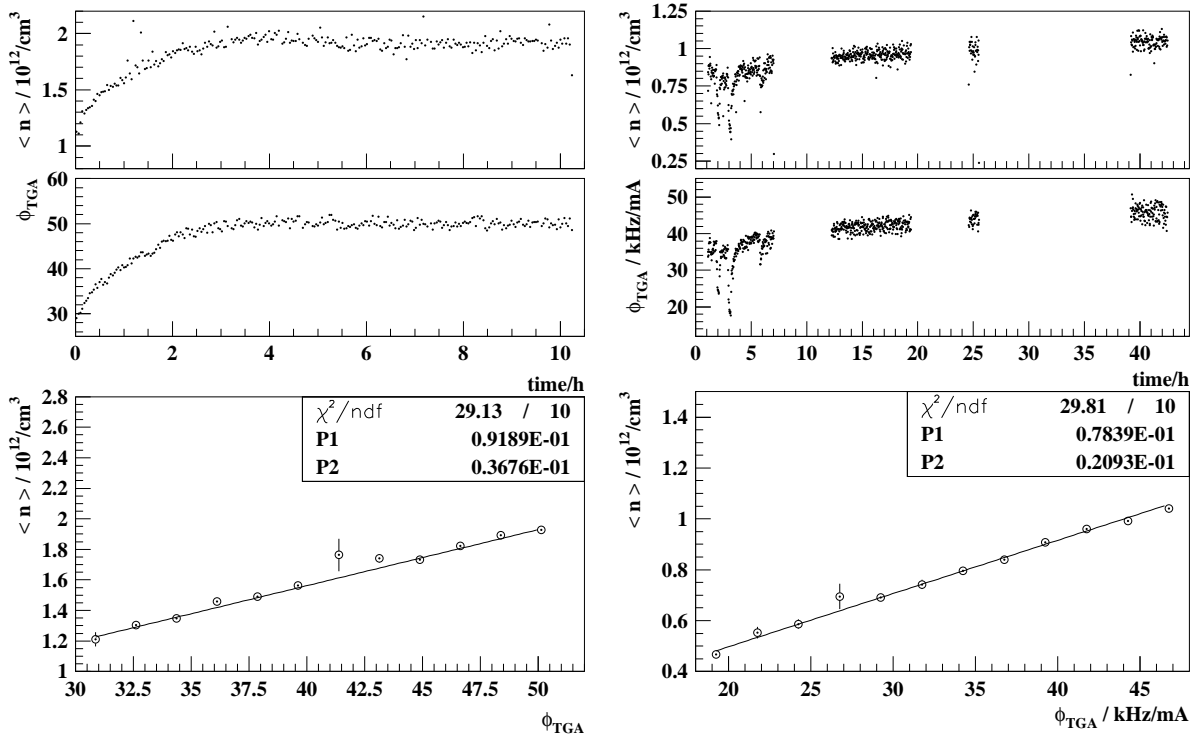


Fig. 3.20: Normalized target density $\langle n \rangle_L$ as measured by the HERMES luminosity monitor (Lumi) vs. measured TGA flux ϕ_{TGA} . The left side graphs show (top to bottom) $\langle n \rangle_L$ vs. time, ϕ_{TGA} vs. time and $\langle n \rangle_L$ vs. ϕ_{TGA} (rebinned) for a period of about 10 h in 1997 (positron fills, hydrogen target). The right side graphs show the same values for a period in 1998 (electron fills, deuterium target, two injected hyperfine states). In both cases one finds a small offset in the count rate, that delivers an estimation of the background rate of the Lumi.

density measured by the Lumi vs. the total flux measured by the TGA ϕ_{TGA} . The flux of the ABS was instable during these time periods. The fitted polynomials of 1st degree indicate a background rate of about 5% in case of hydrogen at $\phi_{TGA} \simeq 50 \text{ kHz/mA}$ and about 7.5% in case of deuterium at $\phi_{TGA} \simeq 44 \text{ kHz/mA}$ ⁵⁸. The measurement delivers the following relations between absolute target density $\langle n \rangle$ in units of $[10^{12} \text{ cm}^{-3}]$ and the TGA flux in units of $[\text{kHz/mA}]$ ⁵⁹:

$$\begin{array}{cc} \text{Hydrogen} & \text{Deuterium} \\ \langle n \rangle = 0.0368 \phi_{TGA} & \langle n \rangle = 0.0209 \phi_{TGA} . \end{array} \quad (3.75)$$

The number of atoms \dot{n}^{ABS} (in units of $[10^{16} \text{ sec}^{-1}]$), that are injected by the ABS per unit time, is given by:

$$\begin{array}{cc} \text{Hydrogen} & \text{Deuterium} \\ \dot{n}^{ABS} = 0.128 \phi_{TGA} & \dot{n}^{ABS} = 0.0514 \phi_{TGA} . \end{array} \quad (3.76)$$

These results for \dot{n}^{ABS} are not corrected for ballistic flow and rest gas, so they might still be about 5% too high. The calibration constants are of course only valid for a period, in which the setup of the TGA is unchanged.

3.8 Summary

An introduction into the components of the HERMES target setup has been presented. It has been explained, how the TGA can be calibrated and how the measured results have to be interpreted and corrected in order to be useful for the calculation of the target polarization.

All important systematic investigations of the BRP have been presented. The efficiencies of the high frequency transitions of the BRP have been determined with a typical precision of 1 – 2% for both, hydrogen and deuterium operation. The transmission ratio between the hyperfine states $|1\rangle$ and $|2\rangle$ of hydrogen has been derived from experimental data in dependence on the storage cell temperature.

The velocity distribution of the atoms passing the BRP sextupole system has been measured with the help of the new developed technique of pulse modulated high frequency transitions at four storage cell temperatures. The results yielded a prediction of the temperature dependence of the BRP signal rate for temperatures below 80 K, which was found to be in good agreement with the measurements.

⁵⁸The actual background rate might be slightly below these values: If the ABS performance is reduced, the injected ballistic flow might be increased. Due to the lower conductance of the storage cell for molecules, the ballistic flow increases the target more than the ϕ_{TGA} indicates.

⁵⁹It will be shown in sec. 6.8.2, that spin relaxation measurements can also be used to determine the (atomic) target density. The results are - within the errors - in agreement.

4 Sampling of BRP and TGA

The properties of the measured samples of BRP and TGA are in general different from each other and from the - density averaged - gas in the beam tube (BT) of the target storage cell. The reason for this difference is the history of wall collisions⁶⁰ of the different gas samples. Several molecular flow Monte Carlo simulations (MC) have been written in order to investigate the relation between the *measured* atomic fraction respectively polarization and the average values in the HERMES storage cell [Br 91, Bau 96, Hen 98]. These averages are - besides the polarization of the HERA beam - important input parameters for the HERMES physics analysis.

It was shown in [Bau 96], that it is possible to model recombination (and spin relaxation) by a rate equation⁶¹, if the *acceptance* of BRP and TGA *and* the recombination/depolarization probabilities γ_r , γ_e and γ_z are known for all surface areas. The acceptance can be obtained from a molecular flow simulation, but a position dependent measurement of γ_r , γ_e and γ_z is - especially inside the beam tube - impossible. The measured values α_r^{TGA} and P^{BRP} can therefore only deliver *boundary conditions*, that can be used to limit the possible range for the corresponding average values α_r and P_a inside the beam tube. This range enters the calculation of the systematic uncertainty of the target polarization. Reasonable assumptions about the properties of the sample and extension tube are still required and can - partially - be verified by measurements.

The simplest assumption is, that all wall collisions are equivalent, no matter where they appeared. This requires a Drifilm coating, that is homogeneous in a macroscopic sense⁶²: The coating inside the beam tube must have the same properties with respect to recombination and spin relaxation as the coating in the sample and extension tube. It will be shown in this section, that this assumption fails to describe the measurements.

Fig. 4.1 shows schematically the geometry, that determines the origin of the measured samples of BRP and TGA respectively. All atoms and molecules entering the TGA, have first to diffuse to the end of the extension tube. The average collision age $\langle b \rangle^{TGA}$ of the TGA sample beam is higher than the one of the BRP sample $\langle b \rangle^{BRP}$. Fig. 4.2 shows the distribution of the location of the last wall collisions for the gas samples of BRP and TGA, obtained by the MC simulation.

⁶⁰Collisions between atoms in the gas phase play only a significant role as spin exchange collisions (refer to sec. 6).

⁶¹The rate equation is a differential equation, which is based on the diffusion equation (see app. C.6).

⁶²Microscopic non-uniformities, e.g. different types of surface sites, are of no interest in this context, as long, as they are uniformly distributed over the surface.

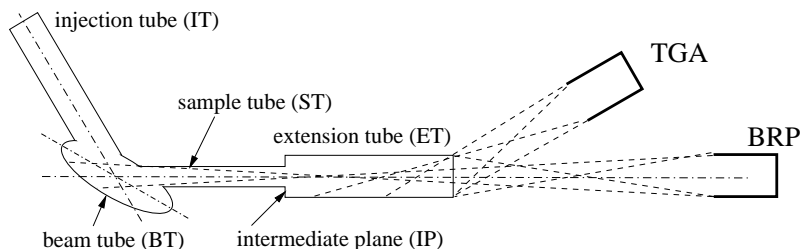


Fig. 4.1: Schematic of the geometrical acceptance of BRP and TGA: Atoms or molecules entering the TGA had their last wall collision in the extension tube, while the acceptance of the BRP contains atoms from any position between the center of the beam tube until the end of the extension tube.

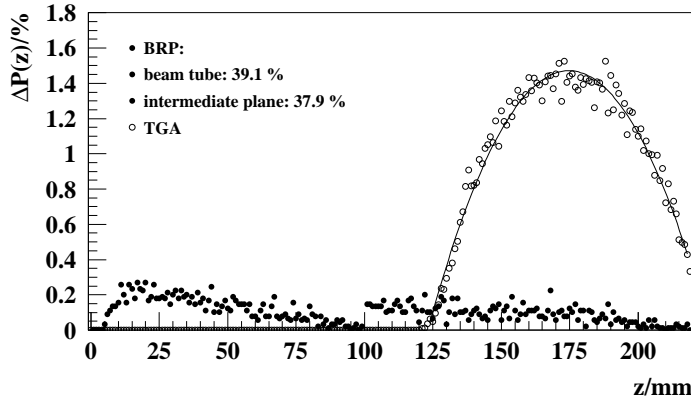


Fig. 4.2: Distribution of the position z along the BRP beam axis of the last wall bounce within sample and extension tube of the gas samples of BRP and TGA as obtained by the MC simulation. Each bin is one mm long. About 38% of the BRP sampled atoms had their last wall bounce in the beam tube of the storage cell and the same amount on the intermediate plane (IP). The solid line shows a fit to the TGA data with a polynomial of 2nd order.

If the recombination probability per wall collision γ_r is sufficiently small inside the sample and extension tube, both samples will have the same atomic fraction - which is the atomic fraction at the storage cell center. The influence of γ_r in the sample and extension tube has on the other hand little influence on the average atomic fraction inside the beam tube. One may also say, that normalized atomic densities ρ_a^{BRP} and ρ_a^{TGA} can approximately be described by a product:

$$\rho_a^{TGA} = \rho_a(0) \frac{1}{1 + \langle b \rangle_{ST}^{TGA} \gamma_r^{ST}} \quad (4.1)$$

$$\rho_a^{BRP} = \rho_a(0) \frac{1}{1 + \langle b \rangle_{ST}^{BRP} \gamma_r^{ST}}, \quad (4.2)$$

where γ_r^{ST} is the average recombination probability for wall bounces in the sample and extension tube, $\rho_a(0)$ is the normalized atomic density in the storage cell center and $\langle b \rangle_{ST}^{XXX}$ are the average number of wall collisions inside sample and extension tube of the sampled gas of BRP and TGA respectively. $\rho_a(0)$ can approximately be described by

$$\rho_a(0) = \frac{1}{1 + \langle b \rangle_{BT} \gamma_r^{BT}}, \quad (4.3)$$

where BT stands for **beam tube** (compare eq. 2.45).

As described in sec. 3.5.3, a HERA beam loss can cause a very sudden reduction of the atomic fraction. α^{TGA} typically recovered slowly within time scales of several ten hours. Fig. 4.3 shows the measured atomic beam intensities of BRP vs. TGA during the recovery period. The proportionality of both signals - corresponding to a constant ratio - indicates, that only $\rho_a(0)$ is changing, while γ_r^{ST} stays constant. The beam loss changes the surface properties of the beam tube only, while the sample and extension tube (and most likely also the injection tube) are not affected. Already this simple measurement shows, that the assumption of surface uniformity fails in the HERA storage ring. Evidently, it is necessary to describe the measurements with (at least) two parameters - γ_r^{BT} and γ_r^{ST} , where one can assume, that typically

$$\gamma_r^{BT} \geq \gamma_r^{ST}. \quad (4.4)$$

The knowledge of the temperature dependence of the beam signals of BRP and TGA provides the condition for a cross check of this claimed behavior. As it will be discussed in

sec. 5, γ_r is temperature dependent. This holds of course for wall collisions inside the beam tube as well as for the sample and extension tube. Fig. 4.4 shows the normalized atomic signal of the BRP - identified with $\rho_a^{BRP} \propto I_{tot}$ - plotted vs. the measured atomic fraction $\alpha_r^{TGA} = \rho_a^{TGA}$ of the TGA for 6 different measurements of the temperature dependence in 1997. The comparison shows, that the beam intensities of BRP and TGA are in general not proportional to each other. The measurements - performed between HERA fills - support the claimed relation 4.4 of γ_r^{ST} and γ_r^{BT} as far as the first storage cell of 1997 is concerned (open symbols). Most data points are close to the diagonal, indicating low values of γ_r^{ST} . Only at very low temperatures, they start to deviate from this behavior.

The situation is different with the second storage cell of 1997, represented by filled symbols. Most of these measurements are close to the dashed line, which is the prediction of the molecular flow simulation for equal recombination probabilities on each surface. This shows, that the surface homogeneity can differ from cell to cell, and the results of the Drifilm coating procedure were - at that time - not reproducible. The results of the spin relaxation measurements, that will be presented in sec. 6.8.2, show the same behavior of the storage cell.

The approximation of eq. 4.2 - plotted as dotted line in fig. 4.4 - delivers a good description of the measured behavior for $\rho_a \geq 0.75$.

4.1 Measurement of the Diffusion Time Distributions

Even though the distribution of collision ages can not be measured directly, a similar distribution was found, that can be compared to measured data - the diffusion time or diffusion length distribution (DTD and DLD respectively). The atoms are diffusing through the target storage cell by means of molecular flow for a certain time τ_d , before it happens to some of them, that they enter the acceptance of BRP or TGA. As it is assumed, that the atoms get physisorbed at every wall collisions, the velocity between two wall bounces is uncorrelated with the velocity between the next two wall bounces, so that the DTD is - besides the scaling factor of the average thermal velocity - identical to the distribution of the integrated trajectory length of the particle's path through the

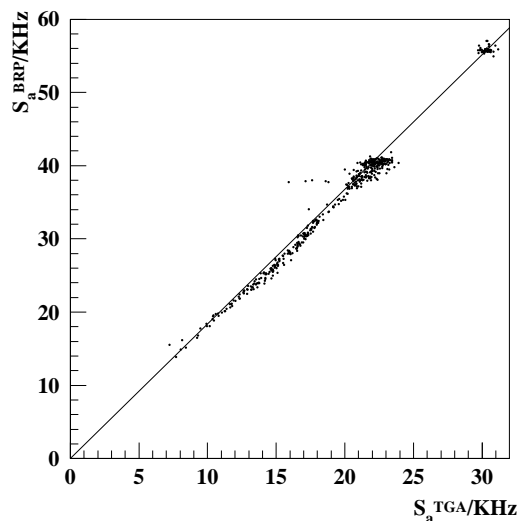


Fig. 4.3: Atomic beam signals of BRP and TGA during the "recovery" period after an accidental HERA beam loss. The proportionality - respectively the constant ratio - of both signals indicates, that the recombination probability γ_r^{ST} for wall collisions inside the sample and extension tube is constant (see text). The intensity of the ABS was unchanged during the measurement and the storage cell temperature was practically constant around 100 K.

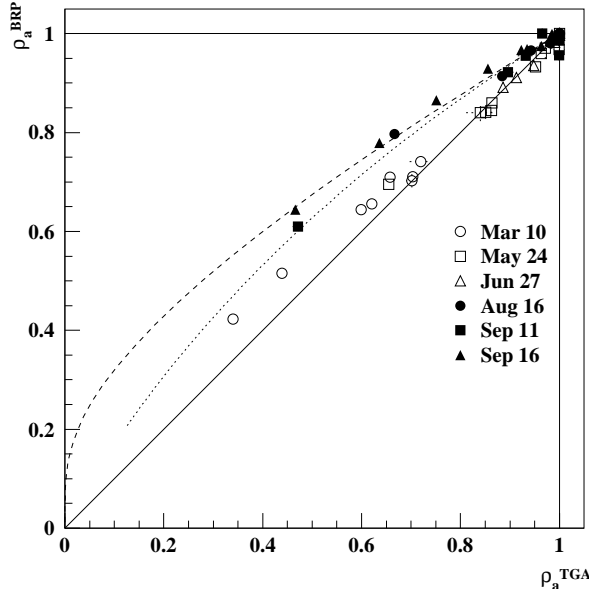


Fig. 4.4: Normalized atomic beam signals of BRP and TGA ρ_a^{BRP} and ρ_a^{TGA} during measurements of the temperature dependence of the recombination process. The solid diagonal line is the claimed physical meaningful limit for $\gamma_r^{ST} \geq 0$. The dashed line is the result of the MC simulation for a homogeneous storage cell ($\gamma_r^{ST} = \gamma_r^{BT}$). For all measurement points between the dashed line and the diagonal, $0 \leq \gamma_r^{ST} \leq \gamma_r^{BT}$ holds. The dotted line shows the prediction of the "first order approximation" of eq. 4.2 for $\gamma_r^{ST} = \gamma_r^{BT}$. Open (filled) symbols represent results obtained with the first (second) target storage cell of 1997.

storage cell, the DLD⁶³. The time t can then be expressed by a (temperature independent) length l with $t = l/\langle v \rangle$ as it was done in fig. 4.5.

The DTD can be measured, if the ABS intensity (or the injected polarization) is modulated much faster than the average diffusion time and if the corresponding intensity change in BRP and TGA can be resolved as a function of time. The measurement technique is analogue to the TOF measurement as described in sec. 3.6.6 and can be called *time of diffusion* (TOD) measurement. The only difference is, that a HFT of the ABS instead of the BRP has to be used for the modulation of the beam intensity or the hyperfine population. Fig. 4.5 shows a comparison between the molecular flow simulation and the measured BRP signal vs. time, performed by the use of a pulsed WFT in the ABS appendix. The measured signal rate is normalized and corrected for background. The TOF

⁶³The sticking time for a wall bounce can assumed to be negligible small and will be discussed later.

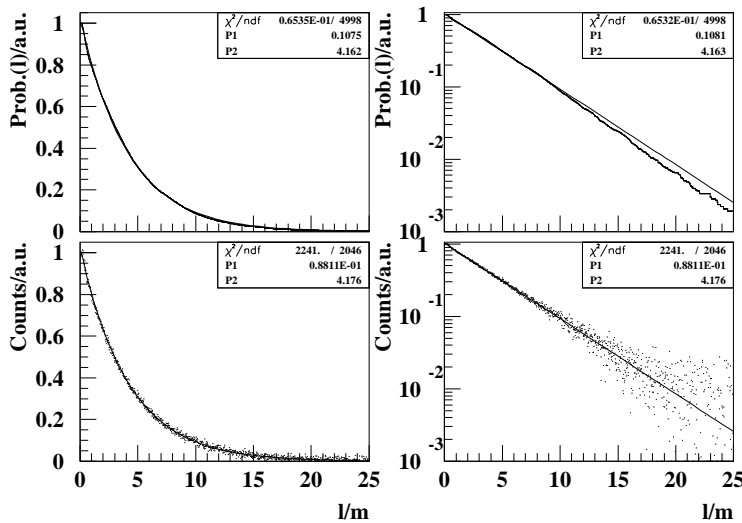


Fig. 4.5: Measurement of diffusion length distribution (DLD) with modulated hyperfine populations realized by a pulsed WFT in the ABS appendix. The upper two plots show the result of the molecular flow simulation, the lower plots the measured signal with linear (left) and semilogarithmic (right) scales. The storage cell was at 94.5 K and the fraction of atoms transmitted by the low velocity window of the BRP sextupole system was neglected for the fit.

between sample tube and BRP detector respectively ABS appendix and storage cell was subtracted. Both - the measured signal and the MC result - were fitted with a function $\eta(l)$ given by:

$$\eta(l) = \begin{cases} 1 & l < l_1 \\ \exp\left(-\frac{l-l_1}{l_2}\right) & l > l_1, \end{cases} \quad (4.5)$$

where $l = t/\langle v \rangle$ is the diffusion length. The results of these fits are:

$$\begin{array}{lll} l_1 = 10.7 \text{ cm} & l_2 = 416.2 \text{ cm} & \text{Monte Carlo Sim.}, \\ l_1 = 8.8 \pm 0.7 \text{ cm} & l_2 = 417.6 \pm 0.9 \text{ cm} & \text{TOD measurement.} \end{array} \quad (4.6)$$

The average diffusion length L_d^0 is the sum of l_1 and l_2 :

$$L_d^0 = l_1 + l_2 \simeq l_2. \quad (4.7)$$

The average diffusion time τ_d^0 depends on the thermal velocity. It is given by

$$\tau_d^0 = \frac{L_d^0}{\langle v \rangle} + \langle b \rangle \tau_s = \langle b \rangle (\tau_f + \tau_s), \quad (4.8)$$

where $\langle b \rangle$ is the average collision age of the gas sample, τ_s the average sticking time on the wall and τ_f the mean time of flight between two wall collisions. As $\tau_s \ll \tau_f$ holds⁶⁴, the second term can be neglected in the temperature range of the HERMES target (33...300 K)⁶⁵ and one may write:

$$\tau_d^0 = \frac{L_d}{\langle v \rangle}. \quad (4.10)$$

4.2 Influence of Recombination on the Diffusion Time

The measurement of fig. 4.5 was performed at a storage cell temperature of 94.5 K and an atomic fraction close to one. In case of stronger recombination, the measured diffusion time is reduced and can therefore be used to determine the atomic fraction α_r^{BRP} of the BRP sample. This will be illustrated with diffusion time measurements at lower storage cell temperatures.

At low temperatures it is no more legitimate to neglect the low velocity window of the transmission in the BRP sextupole system. In addition, the exponent l_2 is reduced by recombination as atoms with a high trajectory length have more wall collisions and are removed from the atomic sample by recombination. This is shown in the measurements

⁶⁴See sec. 5.4.1.

⁶⁵The average differential collision ages, defined as the mean number of wall collisions *on a certain surface*, of the BRP sample are listed in tab. F.5. Atoms of the BRP sample beam had in average 165 wall collisions inside the beam tube, 19 in the injection tube etcpp. The average diffusion length L_d^0 is composed of $\langle b \rangle_j$ wall collisions (and trajectories between wall collisions) of length δl_j in the j-th tube:

$$L_d^0 = \sum_j \langle b \rangle_j \langle \delta l \rangle_j. \quad (4.9)$$

The average trajectory length between two wall collisions $\langle \delta l \rangle$ is listed in tab. F.1. For the BRP sample beam, one obtains $L_d^0 = 406 \text{ cm}$, which is in reasonable agreement with the result of the TOD measurement.

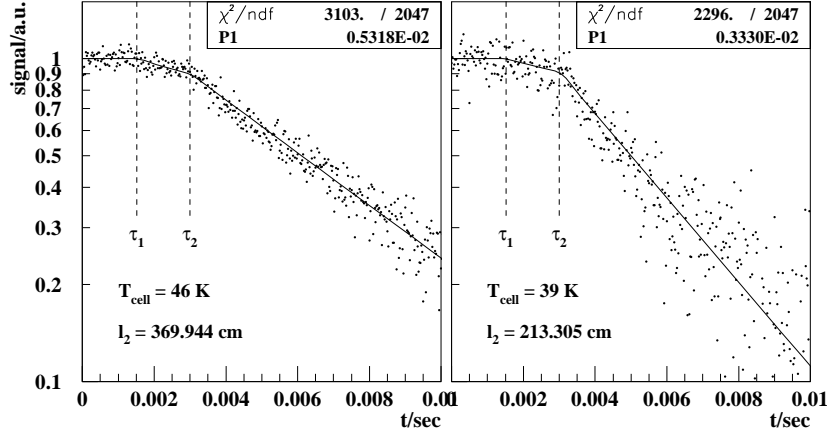


Fig. 4.6: Comparison of two diffusion time distributions at low storage cell temperatures in the presence of recombination. The fraction of atoms passing the low velocity window of the BRP sextupole system causes a change in the slope at $t = \tau_2$. The exponent l_2 describes the diffusion length, reduced by recombination and can be used to determine α_r^{BRP} .

of fig. 4.6, which were performed with a pulsed WFT between the sextupole subsystems of the ABS, so that the injected beam intensity of the ABS is pulsed. The fitting function $\eta(t)$ of this measurements is in contrast to eq. 4.5:

$$\eta(t) = \begin{cases} 1 & t < \tau_1 \\ (1 - f) + f \exp\left(-\frac{t-\tau_1}{\tau_d}\right) & \tau_1 \leq t < \tau_2 \\ (1 - f) \exp\left(-\frac{t-\tau_2}{\tau_d}\right) + f \exp\left(-\frac{t-\tau_1}{\tau_d}\right) & t \geq \tau_2. \end{cases} \quad (4.11)$$

f is the fraction of atoms in the higher velocity window of the BRP sextupole system, which was measured with the TOF measurements in sec. 3.6.6. τ_1 and τ_2 were calculated by the TOF between the ABS WFT and the storage cell ($\tau_{ABS} \simeq 70 \text{ cm}/v_{ABS}$) and the TOF between the storage cell and the BRP detector for both velocity windows of the BRP. The transmission velocity of the ABS sextupole system for deuterium atoms v_{ABS} at a nozzle temperature of 100 K was measured by B. Lorentz and is 1500 m/s [Lor 93]. The number b of wall collisions of an atom in the BRP sample after a diffusion time t is approximately $b = t/\tau_f$. The probability of the atom to survive b wall collisions with a recombination probability γ_r per wall collision is $e^{-b\gamma_r}$. If $w(t) \simeq \frac{1}{\tau_d^0} e^{-t/\tau_d^0}$ is the probability for an atom of the BRP sample beam to have a diffusion time t , then the distribution $w(t, \gamma_r)$ is

$$w(t, \gamma_r) = w(t) e^{-\gamma_r t/\tau_f} = \frac{1}{\tau_d^0} e^{-t/\tau_d}, \quad (4.12)$$

with τ_d given by

$$\tau_d = \frac{\tau_d^0}{1 + \langle b \rangle \gamma_r} = \tau_d^0 \alpha_r^{BRP}, \quad (4.13)$$

where $\langle b \rangle = \tau_d^0/\tau_f$. The value of α_r^{BRP} can then be obtained by

$$\alpha_r^{BRP} = \tau_d/\tau_d^0. \quad (4.14)$$

Equivalent measurements can in principle also be done with the TGA, if the pulsed transition is located between the ABS sextupole subsystems. But the gas flow into the TGA vacuum chamber is high so that the time constant for the signal drop is limited by the pumping speed.

5 Analysis of the Measurements of Recombination

5.1 Introduction

Recombination is a surface catalytic process⁶⁶. Usually one distinguishes between two types of processes of surface catalysis - the Langmuir-Hinshelwood (L-H) process, where two adsorbed atoms or molecules react with each other and the Eley-Rideal (E-R) process, in which an atom or molecule impinging on the surface from the gas phase reacts directly with an adsorbed atom or molecule [Hol 94]. In case of an E-R mechanism, the impinging atoms or molecules do not thermalize with the surface as thermalization is a property of adsorption.

Engel and Ertl (for example) found evidence for catalytic reactions of the L-H type in the reaction $CO + \frac{1}{2}O_2 \rightarrow CO_2$ [Eng 78, Con 78]. For a long time it was unclear, if the proposed E-R mechanism would really exist in nature and strong experimental evidence for an E-R type reaction was first found 1991 by Kuipers *et al* [Kui 91]. More investigations (see for example the work of Rettner [Ret 92, Ret 94]) followed and enhanced the confidence, that E-R reactions take place in a variety of systems and circumstances.

Typically both reaction types were investigated by surface science using chemisorbed atoms or molecules on metal surfaces. The typical binding energy of chemisorption is above 1 eV and chemisorbed atoms can not evaporate at room temperatures. The experimental preparation of surfaces with a certain *coverage* of one or more *monolayers* of chemisorbed atoms is a standard technique in surface science.

Physisorption is caused by the relatively weak Van-der-Waals interaction with typical binding energies between 10 meV and 100 meV. Physisorbed atoms stay - at room temperature - only for short time intervals (less than nanoseconds) on the surface before they evaporate back into the gas phase. Physisorbed atomic or molecular states therefore are difficult to access experimentally.

Harris and Kasemo were the first to find indications for surface catalytic reactions between so-called *precursor* states and chemisorbed atoms [Har 81a, Har 81b]. What they called a precursor state is similar, but not identical to a physisorbed state or to an excited chemisorbed state, as they define a precursor state as being not in thermal equilibrium with the surface (*hot precursor*), while a physisorbed atom is supposed to be equilibrated with the surface. Also Boh and co-workers claimed evidence for *precursor mediated* reactions [Boh 98], where impinging molecules populate a precursor state prior to a chemical reaction with the chemisorbed states.

In terms of surface science, a proper Drifilm coating is a surface without chemisorption sites, as it is chemically saturated and has ideally no "dangling" bonds (unpaired electrons). But one can of course describe the hydrogen atoms of the CH_3 -groups of the Drifilm coating, that are ideally building the surface, in terms of chemisorption. A Drifilm coating can then be understood as a surface with a saturated monolayer of chemisorbed hydrogen.

In the present work, a reaction is said to be of the E-R type, if exactly one of the reactants was not adsorbed (neither physisorbed nor chemisorbed) to the surface prior to

⁶⁶At the low gaseous densities of the HERMES target one can neglect volume recombination.

the reaction, while the other is either physisorbed or chemisorbed. All other reactions are called L-H reactions⁶⁷ [Har 81a, Har 81b].

H. Kolster applied the recombination theory of Gelb and Kim to the recombination data of the HERMES target [Ko 98, Gel 71]. This interpretation is based exclusively on the E-R mechanism, while the L-H mechanism is assumed to be negligible, and distinguishes only between reactions of the impinging atoms from the gas phase with chemisorbed atoms and physisorbed atoms. Due to the different coverage for these two adsorbed "layers", recombination with chemisorbed atoms is dominant at high temperatures (above 120 K), while reactions with the second - physisorbed - layer dominate due to the low activation energy below 80 K.

In the present work, it will be shown, that this interpretation is not sufficient to describe the measurements in at least two aspects: First, it will be shown, that the low temperature behavior of recombination can not be described by a single - density dependent - mechanism. Besides a density dependent process also a density independent process contributes to recombination at low temperatures. And second, it will be argued, that the density dependent process can not - as presumed in the theory of Gelb and Kim - be of the E-R type.

5.2 Physisorption and Surface Diffusion

A comprehensive survey of the knowledge of the physical interaction between gas atoms and solid surfaces is for example given by Hoinkes [Hoi 80]. The physisorption potential consists of two parts. An attractive part is caused by van der Waals interaction and a repulsive part by short-range exchange repulsion due to the Pauli principle. Several mathematical formulas have been used to describe the form of the interaction potential. One of them is the well-known Lennard-Jones potential⁶⁸

$$U = 4 E_m \left\{ \left(\frac{\sigma}{z} \right)^{12} - \left(\frac{\sigma}{z} \right)^6 \right\}, \quad (5.1)$$

which is shown in the left side of fig. 5.1 vs. the distance z to the surface for two different positions on the surface. Along the surface coordinate x , the potential follows the periodic structure of the solid as illustrated by the right graph in fig. 5.1⁶⁹.

Ghio *et al* determined the energy levels of physisorbed hydrogen and deuterium atoms on graphite by the interpretation of atomic beam scattering data. They obtained two energy levels $E_0 = -31.6 \text{ meV}$ and $E_1 = -15.3 \text{ meV}$ for hydrogen and four levels for deuterium with $E_0 = -35.4 \text{ meV}$ up to $E_4 = -5.9 \text{ meV}$ [Ghi 80]. Other measurements with $^1\text{H}_1$ and $^2\text{H}_1$ on LiF and NaF [Fin 75] yielded ground state energies of $-12 \dots 14 \text{ meV}$. Measurements on $\text{K}a\text{Cl}$ were performed on a clean and on a water covered $\text{K}a\text{Cl}$ -surface. The potential depth was found to be unchanged by the water layer. The lowest energy level (binding energy) was about -30 meV for both hydrogen and deuterium [Fra 77].

⁶⁷In the definition of Harris and Kasemo, reactions are of the L-H type only, if both reactants were chemisorbed prior to the reaction. The E-R type is restricted to reactions, where one reactant is chemisorbed and the other is impinging from the gas phase. All other reactions are summarized as *precursor mechanisms*.

⁶⁸See also [Kit 86] or the article of Crowell in [Flo 67].

⁶⁹In case of Drifilm, the structure of $U(x)$ can be less regular but will certainly have maxima and minima and a typical value of E_j .

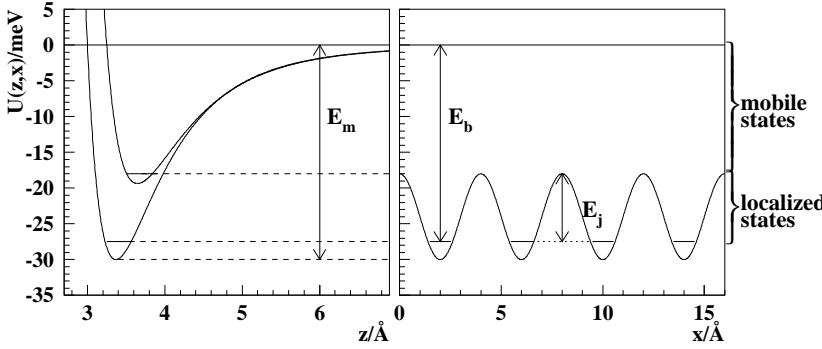


Fig. 5.1: Illustration of the potential energy $U(x, z)$ vs. the distance z to the surface (left) and along the surface (right). The energy difference between the lowest localized state and the unbound state is the binding energy E_b . The activation energy for surface jump diffusion is E_j and E_m is the maximal depth of the potential [Rol 64, Hoi 80].

Measurements on Drifilm are not known, but Hoinkes [Hoi 80] gives a semi-empirical formula for the potential depth E_m using the electronic polarizability α of the adsorbed atom and the optical dielectrical constant ε of the surface material:

$$E_m = K \alpha \frac{\varepsilon - 1}{\varepsilon + 1}. \quad (5.2)$$

where $K \simeq 11.2 \text{ meV}/10^{-25} \text{ cm}^3$ is a constant obtained for hydrogen physisorption. With a polarizability of atomic hydrogen of $\alpha = 6.66793 \cdot 10^{-25} \text{ cm}^3$ [Lid 98] and with ε calculated as the square of the optical index of refraction n , given as $n = 1.4229$ in [Lid 98] for disilane ($C_6H_{18}Si_2$), one obtains $E_m \simeq 25.3 \text{ meV}$ as an estimation of the upper limit for the binding energy of hydrogen on Drifilm. For the ratio E_j/E_b values between 0.3 to 0.8 have been found in physisorption for several adsorbates and adsorbents⁷⁰. It will turn out, that these estimations are close to the results of the measurements at the HERMES target.

5.2.1 Surface Coverage and Diffusion of Physisorbed Atoms

A calculation of the surface coverage Θ for a mobile layer with negligible interactions between the adsorbed atoms by means of statistical thermodynamics can for example be found in [Tom 78]. One obtains in case of low coverages $\Theta \ll 1$ ⁷¹:

$$\Theta = \frac{a h n}{\sqrt{2\pi m k_b T}} q_z(T) \exp\left(\frac{E_b}{k_b T}\right), \quad (5.3)$$

where $q_z(T)$ is the partition function of the adsorbed atom for vibrations normal to the surface, E_b is the binding energy as illustrated by fig. 5.1, n is the gas density and m is the mass of the adsorbed atom. The partition function $q_z(T)$ can be approximated by the partition function of a one-dimensional harmonic oscillator of frequency ν , given by (see for example [Kit 69]):

$$q_z(T) = \sum_n \exp\left(-\frac{E_n}{k_b T}\right). \quad (5.4)$$

⁷⁰See for instance the article of J.P. Hobson and references therein [Flo 67].

⁷¹Respectively negligible interactions among the adsorbed atoms.

where $E_n = n h \nu$ is the eigenenergy of the n -th level. The summation results, cutted at the binding energy⁷² E_b :

$$q_z(T) = \frac{1 - \exp\left(-\frac{E_b}{k_b T}\right)}{1 - \exp\left(-\frac{h\nu}{k_b T}\right)}. \quad (5.5)$$

In case of high binding energies and temperatures ($h\nu \ll k_b T \ll E_b$) one obtains $q_z(T) \simeq \frac{k_b T}{h\nu}$:

$$\Theta = \frac{a n k_b T}{\nu \sqrt{2\pi m k_b T}} \exp\left(\frac{E_b}{k_b T}\right). \quad (5.6)$$

The coverage Θ can also be expressed by

$$\Theta = Z_0 a \tau_s, \quad (5.7)$$

where a is the average area of a surface site, Z_0 is number of indident atoms per area and unit time and τ_s is the average sticking time. With the Hertz-Knudsen equation [Tom 78]

$$Z_0 = \frac{n k_b T}{\sqrt{2\pi m k_b T}} = n \sqrt{\frac{k_b T}{2\pi m}} \quad (5.8)$$

one finds:

$$\Theta = \frac{a Z_0}{\nu} \exp\left(\frac{E_b}{k_b T}\right), \quad (5.9)$$

so that the average sticking time τ_s is given by the Arrhenius law:

$$\tau_s = \frac{1}{\nu} \exp\left(\frac{E_b}{k_b T}\right). \quad (5.10)$$

For a typical energy difference $\Delta E = h \nu$ between two energy levels within $4 \cdots 10 \text{ meV}$ [Fra 77] one expects an oscillator frequency ν of $\nu = \Delta E/h \simeq 10^{12} \text{ s}^{-1}$, which is claimed to be typical by several authors⁷³.

With the estimation⁷⁴ $\nu = 5 \cdot 10^{12} \text{ s}^{-1}$ one obtains for the high temperature limit τ_s^0 a value of $2 \cdot 10^{-13} \text{ s}$. For the lowest achievable storage cell temperature of $T_{min} \simeq 38 \text{ K}$ this results in $\tau_s(38 \text{ K}) \simeq 10^{-10} \text{ s}$, which is much below the mean time of flight between two wall collisions τ_f (in the order of a few μs).

Eq. 5.10 is commonly used and it is typically assumed, that the residence time at one surface site τ_c during the diffusion process can be expressed also by this type of equation [Sth 92, Tom 78, Gom 90, Rie 79, Wea 78, Cam 99, Ehr 94, Ree 80]:

$$\tau_c = \frac{1}{\nu_d} \exp\left(\frac{E_j}{k_b T}\right) = \tau_c^0 \exp\left(\frac{E_j}{k_b T}\right), \quad (5.11)$$

where E_j is the activation energy for surface diffusion with $E_j < E_b$ ⁷⁵.

⁷²The ground state energy $E_m - E_b$ does *not* enter.

⁷³See for example [Tom 78] or the article of J.P. Hobson in [Flo 67]. Swenson and Anderson found the same value, which they obtained by the measurement of the spin relaxation of Na vapor on Drifilm and other surfaces below room temperature [Swe 88].

⁷⁴An estimation can also be obtained by the classical equation $\omega = 2\pi\nu = \sqrt{\frac{k}{m}}$ where $k = \frac{1}{2} \frac{\partial^2 U}{\partial z^2}(z_0)$. With the Lennard-Jones potential 5.1 the value of k one finds $k \simeq 40 E_m/\sigma^2$ and thus $\nu \simeq \frac{1}{\sigma} \sqrt{\frac{E_m}{m}}$. With a value of $E_m = 30 \text{ meV}$ and a binding length $\sigma = 4\text{\AA}$ this yields a frequency of rounded $\nu \simeq 5 \cdot 10^{12} \text{ s}^{-1}$.

⁷⁵Typically one would expect, that both frequencies ν and ν_d are of the same order of magnitude: $\nu \simeq \nu_d$. The jump rate Γ is $\Gamma = \frac{1}{\tau_c}$ and the diffusion constant D of surface diffusion is given by $D = \lambda^2 \Gamma = \lambda^2 \nu_d \exp\left(-\frac{E_j}{k_b T}\right)$, where λ is the average hopping distance [Tom 78].

5.2.2 Sticking Time in Case of Low Binding Energy

In the extreme case of only one bond energy level⁷⁶, the partition function - given by eq. 5.4 - is equal to unity, so that:

$$\tau_s = \frac{h}{k_b T} \exp\left(\frac{E_b}{k_b T}\right), \quad (5.12)$$

In this case there is no high temperature limit and the prefactor yields $\frac{h}{k_b T} = 4.78 \cdot 10^{-13} s$ at 100 K. The difference between eq. 5.10 and eq. 5.12 is - for low temperatures and by the use of an Arrhenius plot with measured data - not very pronounced, if the temperature range is limited⁷⁷. The question, whether eq. 5.10 or eq. 5.12 is a better approximation, can not be decided within the temperature range of the HERMES target.

5.3 The Temperature Dependence of Recombination

As the normalized atomic density ρ_a^{TGA} is identical to the atomic fraction measured by the TGA α_r^{TGA} the recombination probability per wall collision $\langle b \rangle \gamma_r$ can be obtained by eq. 2.45:

$$\langle b \rangle \gamma_r = \frac{1}{\alpha_r^{TGA}} - 1, \quad (5.13)$$

⁷⁶The ground state is then identical to the completely bound state.

⁷⁷In case of the measurement of fig. 5.2 (left graphs), a low temperature behavior of the form of eq. 5.12 fits the data as well. The prefactor is of course different and one obtains for the exponent $223.6 \pm 2.5 K$ instead of $271 \pm 2 K$.

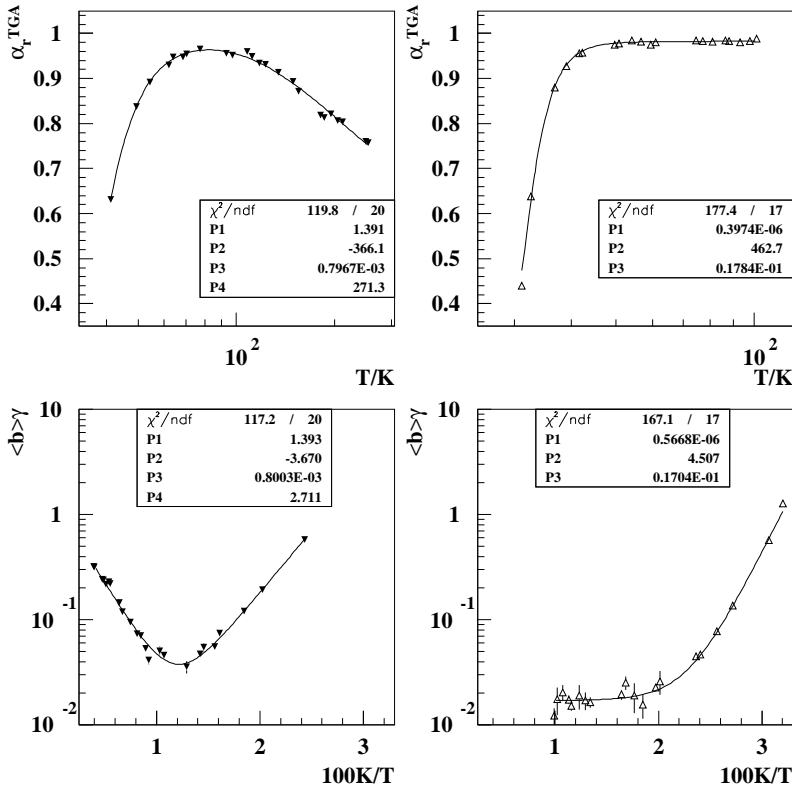


Fig. 5.2: Measured atomic fraction α_r^{TGA} (upper figures) and scaled recombination probability (lower graphs) versus storage cell temperature for a fresh Dri-film coated surface (left figures) and an aged surface (right figures), which was exposed for some weeks to the HERA beam. The measurements were performed with hydrogen. The inlets show the resulting parameters of a fit with eq. 5.14. For the left graph, one has $T_1 = 271.1 K$ and $T_2 = 367 K$, in the right graph one obtains only $T_2 = 450.7 K$.

Fig. 5.2 shows the measured behavior of the atomic fraction α_r^{TGA} as a function of the storage cell temperature (upper graphs) and an Arrhenius plot of the derived value of $\langle b \rangle \gamma_r$ in the lower graphs for a fresh Drifilm coated surface (left plots) and for an aged Drifilm surface after a longer time of operation under HERMES running conditions (right plots). The temperature dependence of the recombination probability $\gamma_r(T)$ was fitted with the following function:

$$\gamma_r(T) = k_1 \exp(T_1/T) + k_2 \exp(-T_2/T) . \quad (5.14)$$

The temperature model matches the data reasonably well. The fact, that γ_r has to be described by a sum of two exponentials indicates, that (at least) two different processes are involved in recombination. The second term on the right side of eq. 5.14 has likely to be interpreted as reactions with chemically bond atoms, as the value of T_2 represents an activation barrier. Only atoms with a thermal energy above $k_b T_2$ are able to react with the surface atoms. The process, which is represented by the first term on the right side of eq. 5.14 can be interpreted by reactions with physisorbed atoms [Ko 98]. The increase of γ_r at low temperatures is then caused by the sticking time of the physisorbed atoms on the surface - following the Arrhenius law $k_1 \exp(T_1/T)$ - while the increase at high temperatures results from an activation barrier for reactions with atoms, which are chemically bound to the surface, resulting in a term $k_2 \exp(-T_2/T)$.

5.3.1 High Temperature Behavior of Recombination

Even though the bond strength of a hydrogen atom with Drifilm ($H - CH_2SiO_3$) is not precisely known, it can assumed to be close to the bond strength of the chemically similar $H - CH_2Si(CH_3)_3$, which is 415.1 kJ/mol [Lid 98]. This is just below the bond strength of a hydrogen molecule $H - H$, which is 435.99 kJ/mol ⁷⁸. Recombination of a hydrogen atom of the gas phase with a hydrogen atom, which is chemically bound to a CH_3 -group of the Drifilm coating, is therefore likely an exothermic process⁷⁹. As shown in fig. 5.2, the recombination probability increases exponentially with the inverse temperature for temperatures above 120 K , indicating a thermally activated reaction⁸⁰.

Koleske and Gates [Kol 94] obtained similar results for the reaction between gaseous atomic hydrogen and deuterium, which was chemisorbed on a single crystal silicon surface and vice versa. Their results showed only little dependence of the reaction rate on the surface temperature. They concluded, that the impinging atoms do not thermalize with the surface in advance to the reaction, which indicates reactions of the E-R type. The reaction rate however had a measurable dependence on the energy of the impinging atoms - indicating an activation energy E_a (as illustrated in fig. 5.3) of about 48 meV for abstraction of chemisorbed hydrogen by deuterium atoms and about 25 meV for chemisorbed deuterium abstracted by gaseous atomic hydrogen. Similar results have - for example - been observed for hydrogen chemisorbed on Ni(110) [Eil 96], on Ni(100) [Kam 95], on Ru(001) [Jac 94] and on Al(100) [Boh 98]. Theoretical calculations of the isotope effect have been performed by Kratzer and Brenig [Kra 96].

⁷⁸ $1 \text{ kJ/mol} = 0.010364 \text{ eV/molecule}$

⁷⁹Of course, one has to take other contributions of the binding into account, as the heat of condensation of the Drifilm coating etc. The total energy balance is not precisely known and likely differs from site to site on the surface.

⁸⁰The missing hydrogen atom in the methyl group can assumed to be replaced soon by an impinging hydrogen atom.

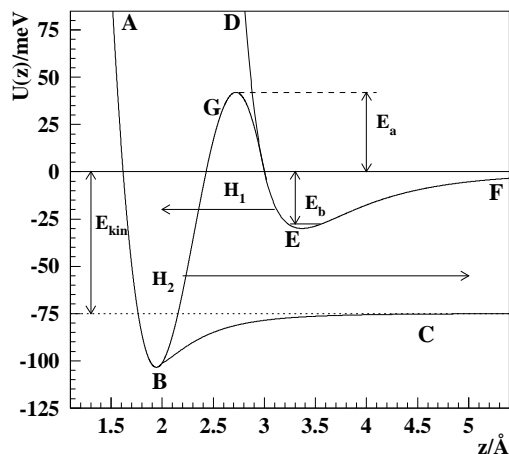


Fig. 5.3: Surface potential scheme for reactions with the surface. The curve DEF represents the physisorption potential for atoms as in fig. 5.1. The curve ABGEF is the potential energy curve, if the possibility of chemical reactions with the H/D atoms of the Methyl groups of Drifilm are taken into account. The curve ABC represents the potential energy for molecules after the reaction. E_a is the activation energy for E-R reactions with atoms impinging from the gas phase of thermal energy $E > E_a$. Physisorbed atoms, that are sticking at position E, may enter the second potential minimum and thus react with the surface by tunneling as indicated by the arrow. The desorbing molecule has an average additional energy E_{kin} by the exothermic reaction, indicated by a lowered energy base line at $-75 meV$.

In case of the HERMES storage cell, the kinetic energy of the impinging atoms is determined by the surface temperature⁸¹. The measurement of fig. 5.2 results an activation energy of $T_2 = E_a/k_b = 367 K$ for hydrogen abstraction on Drifilm by atomic hydrogen, corresponding to $31.6 meV$ and of about $786 K$, corresponding to $68 meV$, for deuterium as shown by fig. 5.4. These values are close to the results of Koleske and Gates, which may be considered as a consequence of the similar covalent binding between hydrogen and silicon in one case and hydrogen with carbon in Drifilm in the other case. If one assumes, that the mechanism is the same, then the activation energies depends on the type (or mass) of the impinging atom and not on the type of the abstracted atom. The fact, that the activation energies are higher in case of a Drifilm coated surface compared to a silicon surface, can be explained by the higher bond strength with the carbon of Drifilm compared to Si. The beam rates of mass 3 (HD) and mass 4 (D_2) shown in fig. 5.5, measured during the first exposure of a new storage cell, are in good agreement with this interpretation.

5.4 Low Temperature Behavior of Recombination

At low temperatures, two kinds of processes have to be considered, which can be distinguished by the density dependence of γ_r :

⁸¹The first few wall collisions, when the atoms have not yet thermalized with the wall, are an exception from this rule.

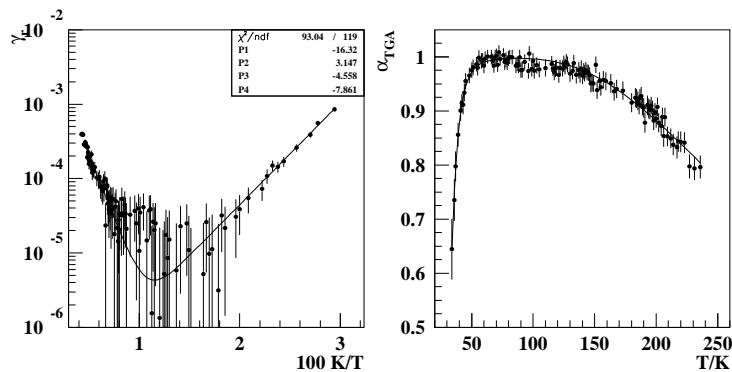


Fig. 5.4: Temperature dependence of recombination measured with deuterium on Drifilm. The left figure shows the extracted value of γ_r vs. the inverse storage cell temperature (circles) and a fit with eq. 5.14 as solid line. The corresponding atomic fraction α_r^{TGA} is shown in the right figure.

- Precursor mediated reactions: Since the chemically bonding sites are almost completely covered, one expects, that γ_r will - for reactions between physisorbed atoms and chemically bond atoms of the coating - not depend on the atomic density of the gas phase⁸². This process can be understood by tunneling (see fig. 5.3).
- Pure precursor mechanism: For reactions *between* physisorbed atoms (L-H type) or direct reactions between impinging atoms and physisorbed atoms (E-R type), the recombination probability γ_r is proportional to the coverage Θ of the physisorption sites, which is for $\Theta \ll 1$ proportional to the gaseous density (see eq. 5.3).

Fig. 5.6 shows a measurement, that verifies the influence of the gas density on the recombination rate. The question remains, if these reactions are of E-R or L-H type. If the reactants are involved in a surface diffusion process, then the L-H mechanism should lead to a significantly higher reaction rate compared to direct reactions between physisorbed atoms and the impinging atoms (E-R reaction). The recombination probability per wall collision γ_r is - for the E-R process - proportional to the probability of an atom to hit a physisorbed atom times the probability of the reaction, described by the reaction cross section σ_r :

$$\gamma_r^{E-R} = \Theta \frac{\sigma_r}{a}, \quad (5.15)$$

⁸²This kind of reaction was for example found by Boh *et al* for adsorption/abstraction of H/D on Al(100)[Boh 98].

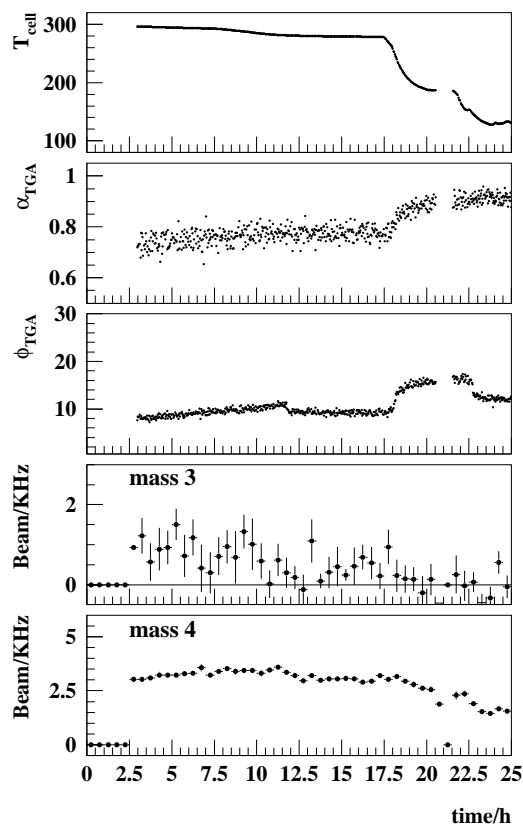


Fig. 5.5: Measured TGA signal rates vs. time during the first exposure of a new storage cell to the atomic deuterium beam of the ABS. At $t = 2.5$ h, the ABS gate valve is opened and the total flux into the TGA Φ_{TGA} (3rd graph from top) jumps up to about 10 kHz/mA . At the same time, the signal rates for mass 3 (HD) and mass 4 (D_2) increase to $\simeq 1 \text{ kHz}$ and 3 kHz respectively. During the next 2 hours, the increase of the mass 4 rate indicates, that a part of the hydrogen atoms of the Drifilm coating are replaced by deuterium atoms. As the temperature is reduced to about 100 K , the beam signal of mass 3 vanishes as the atoms cannot overcome the activation barrier for recombination at the lower temperatures. α^{TGA} is still raising after cooling due to the water layer, which starts to build up on the surface and protects it from further chemical attack of the deuterium radicals. (The jumps in Φ_{TGA} are caused by the ramping of the spectrometer magnet resp. the target magnet.)

If the assumption of surface diffusion is correct, then it follows, that the recombination probability γ_r^{L-H} is increased relative to γ_r^{E-R} by the number of visited sites N_v ⁸³. With the average jump frequency $\nu_j = 1/\tau_c$ one obtains with eq. 5.10 and eq. 5.11:

$$N_v = \tau_s \nu_j = \frac{\tau_s}{\tau_c} = \frac{\nu_d}{\nu} \exp\left(\frac{E_b - E_j}{k_b T}\right). \quad (5.16)$$

and therefore:

$$\gamma_r^{L-H} = \gamma_r^{E-R} \tau_s / \tau_c. \quad (5.17)$$

5.4.1 The Density Dependent Contribution to Recombination

If one assumes, that an impinging atom will always recombine, if it meets a surface site, which is already occupied by a physisorbed atom, then $\sigma_r = a$. In case of hydrogen resp. deuterium, one has to take into account, that atoms with parallel electron spin can not recombine, which yields a factor of $\frac{1}{2}$ ⁸⁴:

$$\gamma_r^{E-R} = \frac{1}{2} a Z_0 \tau_s = \frac{1}{2} a Z_0 \tau_s^0 \exp\left(\frac{E_b}{k_b T}\right) \quad (5.18)$$

$$\gamma_r^{L-H} = \frac{1}{2} a Z_0 \tau_s N_v = \frac{1}{2} a Z_0 \frac{\tau_s^2}{\tau_c} = \frac{1}{2} a Z_0 \frac{(\tau_s^0)^2}{\tau_c^0} \exp\left(\frac{2E_b - E_j}{k_b T}\right). \quad (5.19)$$

⁸³Several authors report of this number to be in the order of a few hundred to some thousands [Tom 78, Rob 93].

⁸⁴The recombination probability is then expected to be reduced by factor $\frac{1}{2}(1 - P_e^2)$ [Bau 96], but as P_e was in the temperature range, where a significant recombination rate of physisorbed atoms occurs (e.g. below about 60 K) - typically low (10...15%), $P_e^2 \ll 1$ holds and only a factor $\frac{1}{2}$ remains.

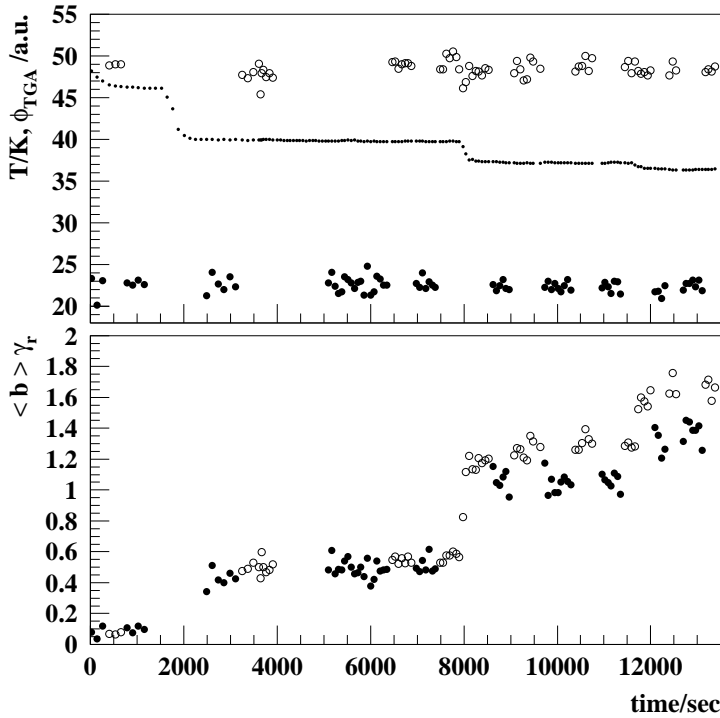


Fig. 5.6: Measurement concerning the density dependence of surface recombination with deuterium. The upper graph shows the storage cell temperature (dots) and Φ_{TGA} vs. time. The injection mode P_e with 3 hyperfine states is indicated by open and the modes with only one hyperfine state by filled circles. The lower graph shows the corresponding recombination probability, calculated by $\langle b \rangle \gamma_r = 1/\alpha_r^{TGA} - 1$. One can clearly identify the density dependence of the reaction rate at low temperatures, which is expected for reactions between the physisorbed reactants. The cell surface was kept cold ($T_{cell} \leq 120 K$) for about 2 weeks before the measurement.

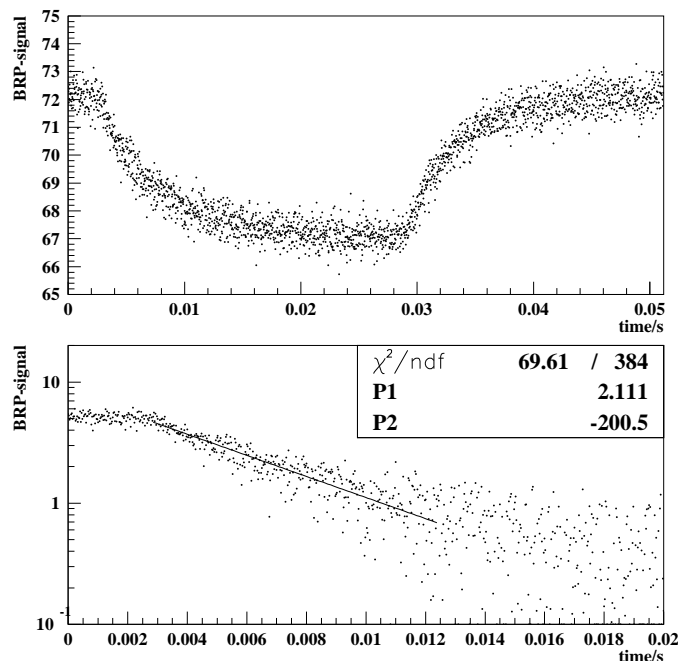


Fig. 5.7: Measured signal rate in the BRP detector versus time for a switched atomic beam intensity of the ABS (for a detailed explanation refer to sec 4.1). The lower graph shows the same signal, now reduced by 67 kHz background and plotted logarithmically. The solid line represents a fitted exponential decay $S_{BRP} \propto \exp(-t/\tau_d)$. The resulting diffusion time is 5 ms (the inverse of the parameter P1 shown in the inset). The storage cell temperature is 37 K , which results in an average thermal velocity of the deuterium atoms of $\langle v \rangle = 626\text{ m s}^{-1}$. The atomic fraction - measured at the same temperature - was $\alpha_r^{TGA} = 0.77$.

From eq. 5.13 and eq. 5.18 one may directly calculate the total sticking time $\langle b \rangle \tau_s$, that the atoms have to spend on the surface in order to produce a certain molecular fraction, *if recombination happens exclusively via the E-R mechanism between physisorbed atoms and atoms impinging from the gas phase*:

$$\langle b \rangle \tau_s = \frac{2 \langle b \rangle \gamma_r}{a Z_0} = \frac{2}{a Z_0} \left(\frac{1}{\alpha_r^{TGA}} - 1 \right). \quad (5.20)$$

The average value of Z_0 can be calculated by eq. 5.8. If one takes the temperature dependence of the density due to the conductance of the storage cell into account⁸⁵, one finds, that Z_0 is temperature independent. With an average atomic density⁸⁶ of $\langle n \rangle = 1.311 \cdot 10^{12}\text{ cm}^{-3}$ at 100 K one obtains $Z_0 \simeq 3.4 \cdot 10^{16}\text{ cm}^{-2}\text{ s}^{-1}$. For a typical size of an adsorption site of $a = 10^{-15}\text{ cm}^2$, one obtains an average rate of impingement per site of about $a Z_0 \simeq 34\text{ s}^{-1}$ for the HERMES storage cell. The average diffusion time of the atoms, that are surviving recombination, is reduced by recombination, so that the right side of eq. 5.20 would have to be multiplied by α_r^{TGA} . This is however compensated by the fact, that Z_0 is - in case of recombination - reduced by the same factor.

For a measured value of $\alpha_r^{TGA} = 0.77$ one finds by eq. 5.20 $\langle b \rangle \tau_s \simeq 17.5\text{ ms}$. The first term in eq. 4.8 is for a storage cell temperature of 37 K and $L_d = 417\text{ cm}$ for deuterium equal to $L_d / \langle v \rangle \alpha_r^{TGA} = 5.13\text{ ms}$. The measured diffusion time τ_d is $5 \pm 0.3\text{ ms}$, as shown in fig. 5.7, which is in good agreement with the expected size of the first term of eq. 4.8, so that the second term may not contribute significantly and the estimated value of $\langle b \rangle \tau_s$ is far too high. Hence the amount of recombination can not be explained by an E-R mechanism - even though this mechanism might of course exist.

This is a strong indication, that density dependent recombination γ_r is - at the HERMES target - caused by L-H type reactions between physisorbed atoms. The ratio of τ_s/τ_c

⁸⁵The conductance of a tube for molecular flow is given by eq. C.25.

⁸⁶A measurement for the determination of the average density in case of deuterium is described in sec. 6.10.5.

results - at 37 K - easily a factor of 100⁸⁷, so that the L-H mechanism can likely explain the amount of recombination without conflict to the measured diffusion time.

Physisorbed atoms are diffusing over the surface and physisorption can be described by the adsorption isotherm of a mobile layer of low coverage. Another strong argument - as will be shown in the next section - is the measured temperature dependence, which is in good agreement with a the factor τ_s^2/τ_c , that enter γ_r^{L-H} of the L-H type process⁸⁸.

5.4.2 The Density Independent Contribution of Recombination

Besides the measurement of fig. 5.6 - most measurements of $\alpha(T)$ resulted a negligible density dependence. An example is shown in fig. 5.8. One can conclude that a precursor mediated process contributes to γ_r and is in most cases dominant at low temperatures. This are presumably reactions between physisorbed atoms H_{ph} and the chemically bond atoms of the Drifilm coating H_{ch} , which are possibly caused by tunneling of the physisorbed atoms through the potential barrier as illustrated by fig. 5.3⁸⁹. The transmission

⁸⁷See sec. 5.5.

⁸⁸The E-R process leads only to a factor τ_s .

⁸⁹Another scenario is a heterogeneous surface, e.g. additional species of surface sites, where atoms can get trapped for longer times, so that the coverage of these sites is already saturated at low gaseous densities. Stepped or rough surfaces are known to increase surface catalytic reactions - even if the binding energy of these sites is higher than on flat surfaces [Som 93]. If the trapped atoms are bond weakly enough to be reactive, the measured density independent recombination rate at low temperatures can also be explained in this way. Investigations of the influence of the geometrical surface structure on the catalytic behavior of the surface are usually performed on stepped surfaces. The measurements show reaction rates, which are typically increased by orders of magnitude on stepped surfaces compared to flat monocrystalline surfaces [Ber 73, Wac 76, Chr 76, Wag 79]. A completely different and new mechanism was proposed by Eilmsteiner, Walkner and Winkler with H and D on Ni(110), which they called *collision induced recombinative Langmuir-Hinshelwood desorption* [Eil 96]. The collision energy of an impinging atom induces a reaction between two chemically bond atoms, followed by the desorption of the so formed molecule. It is nevertheless unclear, what temperature dependence has to be expected for this sort of process.

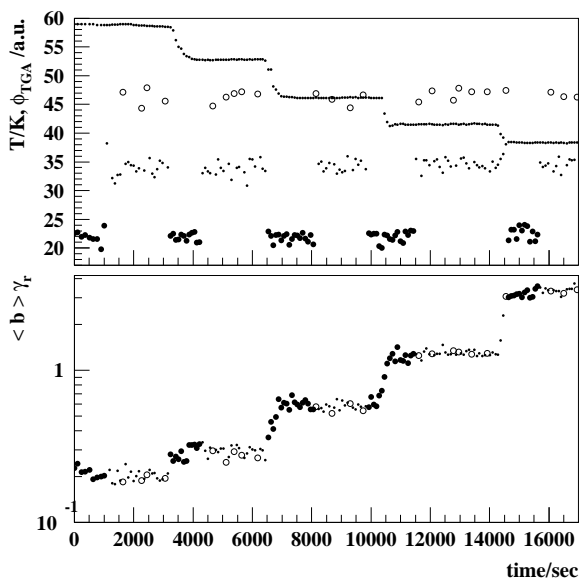


Fig. 5.8: Measurement of the density dependence of deuterium surface recombination as described in fig. 5.6. The dots represent ABS injection modes with two injected hyperfine states ($P_{z\pm}$ and $P_{zz\pm}$). A density dependence of the recombination coefficient γ_r - as shown in fig. 5.6 is not visible. It can be assumed, that the storage cell walls were - in contrast to the situation displayed in fig. 5.6 - at the time of the measurement not yet water covered.

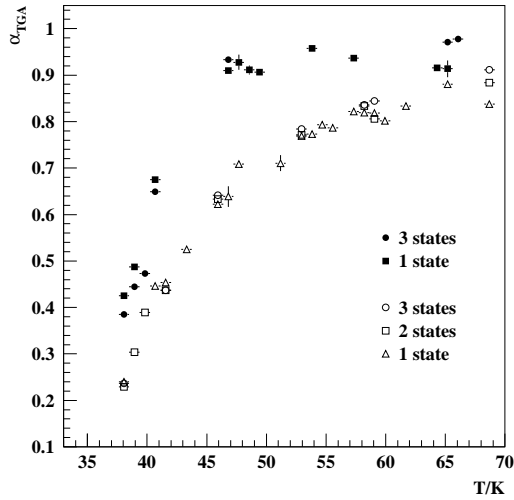


Fig. 5.9: Change of the temperature dependence of surface recombination in case of density dependent γ_r (filled symbols) and density independent γ_r (open symbols), measured with deuterium in the data taking period of 1999. The data are the same as shown in fig. 5.6 and fig. 5.8 resp., but rebinned by the temperature. The density dependent process evidently requires lower temperature (higher coverage) and was measured with a storage cell, which was kept cold ($\leq 120 K$) and exposed to the HERA beam for about 2 weeks and presumably water covered. The density independent process (open symbols) was measured with a new storage cell shortly after installation.

probability T_t for tunneling of an atom with the kinetic energy E through a potential barrier $V(x)$ is approximately given by⁹⁰:

$$T_t \simeq \exp\left(-2 \int dx \sqrt{2m(V(x) - E)/\hbar^2}\right), \quad (5.21)$$

where the integration has to be taken over the range l , where $V(x) > E$. For typical values of $l \simeq 1 \dots 2 \text{ \AA}$ and $V(x) - E \simeq 50 \text{ meV}$ and $m = 1 \text{ amu}$ one finds of $10^{-4} \dots 10^{-8}$. If the physisorbed atom, which is oscillating at frequency ν_{vib} vertical to the surface, has the chance to transmit the potential well at every cycle, then the recombination probability γ_r^{PM} for this process is for $T_t \ll 1$ - using eq. 5.10 - approximately

$$\gamma_r^{PM} \simeq T_t \tau_s \nu_{vib} = T_t \exp\left(\frac{E_b}{k_b T}\right). \quad (5.22)$$

In any case, the low temperature recombination probability can not be described by a single mechanism, but requires at least two different processes. One of these processes is recombination between physisorbed atoms, the other process is likely the reaction between a physisorbed atom and a hydrogen atom, which is chemically bonded to the surface. These binding sites have a high enough binding energy to prevent thermal evaporation, so that their coverage is saturated and the reaction probability independent on the atomic density in the gas phase.

5.5 The Effect of the HERA Beam and of Water on Recombination

As shown in fig. 5.2, the low temperature slope in the Arrhenius plot - represented by T_1 - was determined to be $271.1 K$ for a fresh Drifilm coating and $450.7 K$ after a longer time of target operation in the HERA storage ring. The origin of this significant difference was not discussed so far. It will be argued in this section, that it can be understood, if the

⁹⁰See any standard text book of Quantum Mechanics as for instance [Tow 92]. A survey of reaction-rate theories including activated and tunneling processes is given in [HTB 90].

recombination probability γ_r^{PM} of the density independent process of precursor mediated reactions is assumed to be proportional to the sticking time τ_s as given by eq. 5.10⁹¹

$$\gamma_r^{PM} = \text{const } \tau_s = \gamma_r^0 e^{\frac{E_b}{k_b T}}. \quad (5.23)$$

Fig. 5.9 compares the results of fig. 5.6 and fig. 5.8 versus the storage cell temperature. The results show a strong correlation between the temperature and the density dependence: Weak and density dependent recombination is observed after long exposure of the storage cell to the HERA beam, while the recombination process on the relatively fresh surface is stronger and shows no measurable density dependence.

It is known, that the ABS injects ballistically a small amount of water⁹² into the storage cell, which sticks to the surface and collects there as long as the storage cell temperature is kept below about 140 K. The bond strength of a $H - OH$ of 498 kJ/mol is above the $H - H$ bond strength, so that an ice coverage of the surface prevents from recombination with chemically bond atoms - at least in the temperature range of interest. On a water covered surface, the only possible reaction mechanism is the mentioned L-H type reaction between physisorbed atoms. The behavior of α directly after a HERA beam loss is shown in fig. 3.11. The water coverage grows up (resp. recovers) within a few 10 hours. Fig. 5.10 shows the long term change of the temperature dependence of recombination, measured with hydrogen in 1997. Between the left and the right graph, a new storage cell was installed. The long term change seems to require weeks and is surprisingly reproducible.

The changes in the measured temperature dependences can be understood, if the Drifilm coating is continuous irradiated by the HERA beam. The irradiation leads to a change in the chemical structure at the surface⁹³, causing the Drifilm to be less hydrophobic. A growing fraction of the surface gets covered by water - but the time constant for this change is given by the radiation dose "seen" by the storage cell and is not limited by the amount of the available water in the injected beam. The increasing water coverage leads to a reduction of the direct chemical attack of the surface due to the high binding energy of $H - OH$ and the only remaining possible recombination process is the L-H type reaction between physisorbed atoms - with the described effects, that the recombination rate is reduced and has a stronger temperature dependence, increased by the factor $\tau_s/\tau_c \propto \exp\left(\frac{E_b - E_i}{k_b T}\right)$. In fact, it was observed, that the Drifilm coating is no more hydrophobic after long exposure to the HERA beam [Stw 98].

Alternatively one could suspect, that the binding energy itself changes slowly with time - eventually influenced by irradiation and/or the water coverage. Nevertheless - this explanation can be excluded by the spin relaxation measurements. It will be shown

⁹¹Which is in case of tunneling by eq. 5.21 equivalent to $T_t = \gamma_r^0 \simeq \text{const}$. This is of course only a working assumption and not literally true, as $E = E(T)$ is also temperature dependent. Nevertheless, it can be expected, that the change of the average thermal kinetic energy of the physisorbed atom perpendicular to the surface is only weakly temperature dependent in the measured temperature range. In addition, the main contribution to the potential height is - especially in case of deuterium - given by the activation barrier E_a . In addition, only the root of the energy difference E enters the exponent. The sticking time varies between 40 K and 100 K by about two orders of magnitude and is therefore the dominant factor for the temperature dependence.

⁹²The origin of the water is the oxygen admixture in the discharge of the dissociator [Koc 99].

⁹³For instance by the removal of Methyl groups.

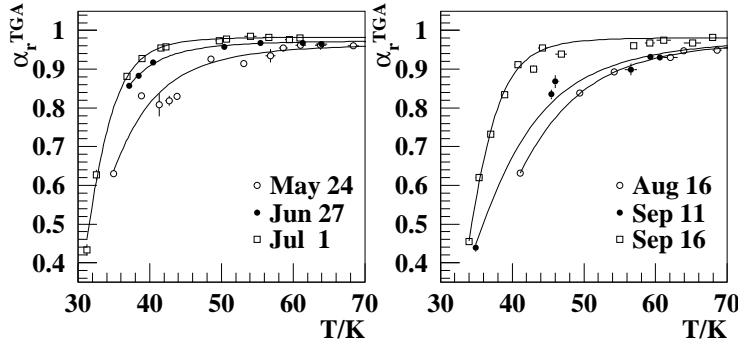


Fig. 5.10: Change of the low temperature behavior of surface recombination with the target running time during the data taking period in 1997. A new storage cell was installed between the first (left) and the second (right) half of the running period.

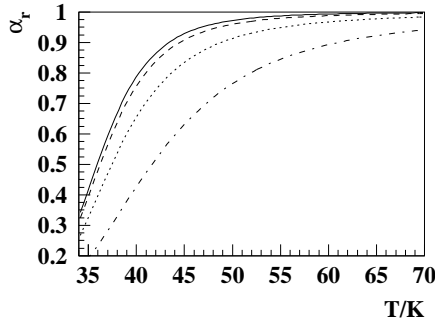


Fig. 5.11: Expected change of the temperature dependence of surface recombination as described by eq. 5.25 for $\langle b \rangle \frac{n}{n_0} = 2 \cdot 10^{-6}$ and $\langle b \rangle \gamma_r^0$ equal (top to bottom) $2 \cdot 10^{-5}$, $8 \cdot 10^{-5}$, $2.4 \cdot 10^{-4}$ and $9.6 \cdot 10^{-4}$ for $E_b = 23 \text{ meV}$ and $E_j = 6 \text{ meV}$.

in sec. 6.7, that the temperature dependence of the wall depolarization strength γ_z of hydrogen can be expressed by

$$\gamma_z(T) \propto \tau_s \tau_c = \gamma_z^0 \exp\left(\frac{E_b + E_j}{k_b T}\right). \quad (5.24)$$

As shown in fig. 6.9, the spin relaxation measurements result, that the energy values change only marginally with time. The observed weak change in the binding energy can not explain the strong change of T_1 . But it can be understood, if the low temperature part of γ_r is composed in the following way:

$$\gamma_r = \frac{n}{n_0} \exp\left(\frac{2E_b - E_j}{k_b T}\right) + \gamma_r^0 \exp\left(\frac{E_b}{k_b T}\right). \quad (5.25)$$

The first term represents the density dependent L-H reaction rate given by eq. 5.19, the second part the density independent process of eq. 5.23. The expected behavior of α_r^{TGA} for varying γ_r^0 is shown in fig. 5.11.

With this model, one obtains an interpretation for the fitted exponent T_r of the water covered surface (right graphs of fig. 5.2),

$$T_1^{(a)} = \frac{2E_b - E_j}{k_b} = 462.7 \text{ K} = 39.9 \text{ meV}/k_b, \quad (5.26)$$

and for the fresh Drifilm coated surface (left graphs of fig. 5.2):

$$T_1^{(b)} = \frac{E_b}{k_b} = 271.3 \text{ K} = 23.4 \text{ meV}/k_b, \quad (5.27)$$

Then the activation energy E_j for surface jump diffusion is⁹⁴

$$E_j = \frac{2T_1^{(b)} - T_1^{(a)}}{k_b} = \frac{79.9 \text{ K}}{k_b} = 6.86 \text{ meV} .$$

It will be shown in sec. 6.7, that the temperature dependence of spin relaxation delivers an estimation for the sum $E_b + E_j$. The relaxation measurements yield values for this sum of about $28 \dots 32 \text{ meV}$, which is in good agreement with this interpretation of the recombination data.

Besides the temperature dependence, one may also ask, whether the absolute value of γ_r meets the expectation. The value of γ_r^{L-H} is given by eq. 5.19 and eq. 5.26:

$$\gamma_r^{L-H} = \frac{1}{2} a Z_0 \frac{(\tau_s^0)^2}{\tau_c^0} e^{T_r^{(a)}/T} , \quad (5.28)$$

so that one obtains at a surface temperature of 37 K with the estimated values of $a Z_0 = 34 \text{ s}^{-195}$ and $\tau_s^0 = \frac{1}{\nu} \simeq 2.2 \cdot 10^{-13}$ and the assumption, that $\tau_s^0 \simeq \tau_c^0$:

$$\gamma_r^{L-H} \simeq 10^{-6} .$$

This value is by a factor of about 460 below a typical value⁹⁶ of $\gamma_r \simeq 4.6 \cdot 10^{-4}$ from the measured recombination data, which is an indication, that $\tau_s^0 \simeq 21 \tau_c^0$ or $\nu \simeq \frac{\nu_d}{22}$ respectively. The spin relaxation measurements (see sec. 6.7) will indicate a ratio of the frequency factors of about the same size.

Abnormal frequency factors (deviating by up to 10^8 from expectation) were found in the physisorption of some substances on tungsten surfaces. Several explanations were given in terms of transition-state theory or partition functions⁹⁷.

5.6 Summary

With the help of the measured temperature and density dependence of recombination it is possible to distinguish three different reaction mechanisms: The first mechanism dominates for temperatures above 120 K and can be interpreted as an activated Eley-Rideal process with activations energies of 31.6 meV and 68 meV in case of hydrogen and deuterium respectively. At low storage cell temperatures two different processes are dominant, a density dependent process that can be understood by reactions between physisorbed atoms and a density independent process, that is likely caused by reactions of the physisorbed atoms with the hydrogen atoms in the methyl groups of the Drifilm coating. It has been shown, that these processes differ also by their temperature dependence. The reaction rate of both processes is proportional to the mean sticking time on the surface, but the density dependent process is additionally proportional to the average number of visited surface sites. This interpretations are consistent with a binding energy of physisorption of about 23 meV and an activation energy for jump diffusion of about 8 meV . Additionally, it has been found, that the storage cell surface is changed by the influence of the HERA beam in such a way, that the density independent process dominates in case of a relatively new storage cell and the density dependent process in case of an aged cell.

⁹⁴Under the assumption, that neither E_b nor E_j significantly depend on the mentioned changes of the surface properties.

⁹⁵See sec. 5.4.1.

⁹⁶The calculation is based on eq. 5.13 for $\alpha_r^{TGA} \simeq 0.77$ and $\langle b \rangle \simeq 650$.

⁹⁷See for example [Tom 78] and references therein.

6 Analysis of Spin Relaxation Measurements

6.1 Introduction

Early measurements of wall and spin exchange relaxation of atomic hydrogen in storage cells with different kinds of wall coatings have been performed in context of hydrogen maser research [Gol 61, Klp 62, Brg 65], but these measurements have been limited to low holding fields. Further studies of the nuclear polarization in dependence on the storage cell temperature have been made by Price and Haeberli [Pri 93, Pri 94] and by Braun [Br 95], who investigated the magnetic field dependence of spin relaxation with a setup similar to the setup of the HERMES target. Kolster has given a description of the hydrogen spin relaxation measurements at HERMES as a function of the storage cell temperature [Ko 98]. Measurements of the spin relaxation of other atomic species have for example been performed by Bouchiat and Brossel for Rb on paraffin [Bou 63, Bou 65], by Levy and Schmor with sodium on Drifilm [Lev 88], by Camparo with Rubidium on Drifilm [Ca 87a], by Stephens, Rhodes and Wieman with alkalis on Pyrex, Drifilm and sapphire [Ste 94], and by Swenson and Anderson with sodium on different materials including Drifilm [Swe 88].

In case of the HERMES hydrogen/deuterium targets, there are three known causes for spin relaxation:

- Wall collisions: During the diffusion process inside the storage cell, the atoms injected by the ABS experience a certain number of wall collisions. Wall collisions can be described by the Van-der-Waals interaction; an attractive potential between the wall and the adsorbed atom causes the atoms to stay for a certain time close to the surface. During this time, the magnetic moment of the unpaired electron of the adsorbed atom interacts with magnetic moments on the surface by means of dipolar coupling and/or with other unpaired electrons by means of exchange interaction. Since the adsorbed atoms are involved in a diffusion process and since the strength of the interaction changes from site to site of the surface, the strength of these interactions is time dependent. From the rest frame of the diffusing atom one can say, that the local magnetic field at the position of the atom fluctuates statistically. Considerable research has been done in order to understand the relaxation rates of the *nuclear* polarization of chemisorbed atoms in liquids and solids for a variety of materials and physical conditions. The group of Fick in Marburg has demonstrated the benefit of nuclear spin relaxation studies of polarized Li chemisorbed on various surfaces⁹⁸ with respect to surface physics.

Bouchiat and Brossel found a reduced relaxation strength with a cell coating of deuterated paraffin compared to conventional paraffin [Bou 65]. As the nuclear magnetic moment of deuterons is smaller compared to protons, they concluded, that the major part of the spin relaxation is caused by dipole-dipole interaction with the

⁹⁸See for example [Chu 90]

nuclear dipoles of the coating⁹⁹. The Van-der-Waals interaction will also change the hyperfine splitting energy, but this should be small¹⁰⁰.

Another contribution to spin relaxation on surfaces results, if unpaired electron spins - so-called *dangling bonds* - are present on the surface. Due to the Pauli principle, electrons with parallel spins may not share the same quantum configuration. This can lead to an energetic difference for parallel and antiparallel spins - the exchange energy¹⁰¹, which is in the Heisenberg model given by $V_{ex} = -J \vec{S}_i \vec{S}_k$, where J is a coupling constant.

Relaxation by wall collisions can be described with a transition probability matrix $W_{b \rightarrow a}$, which represents the probability to find an atom in state $|a\rangle$, which was in state $|b\rangle$ prior to the collision. In case of interactions between the adsorbed atoms, the formalism has to be extended.

- Spin exchange collisions: In the gas phase atoms collide with each other and undergo spin exchange in collision. The effect was first described by E.M. Purcell and G.B. Fields [Pur 56] for interstellar gas collisions and is based on the dependence of the electron interaction potential for the singlet and triplet states. The number of spin exchange collisions per unit time and unit volume \dot{N}_{se} in a gas with the particle density n is given by $\dot{N}_{se} = n^2 \langle \sigma_{se} v_r \rangle$, where σ_{se} is the cross section for spin exchange collisions and v_r is the relative velocity of the atoms¹⁰². Calculations of this cross section were done for example by Purcell and Fields [Pur 56], Allison [All 72], Koelman et. al. [Koe 88] and others. A measurement has for instance been performed by Desaintfusion and Audoin [Des 76], which found σ_{se} to be $23.1 \cdot 10^{-16} \text{ cm}^2$ over a temperature range of $80 \dots 350 \text{ K}$ for H-H and D-D collisions, which is in good agreement with Allison's calculations (see fig. D.2). The effect of spin exchange collisions on the hyperfine population is given by a tensor M_{ab}^c , which describes the probability to find an atom in state $|c\rangle$ after a collision of two atoms, being in state $|a\rangle$ and $|b\rangle$ prior to the collision [Wal 93].
- Bunch field induced resonant depolarization: The beam current of the HERA electron/positron storage ring is strongly bunched to provide optimized luminosity in

⁹⁹The reduction of the relaxation strength was nevertheless below the expectation and they concluded, that the results could only be understood in conjunction with a second relaxation process. They were not sure about the nature of this process and assumed a sort of spin-orbit-coupling of the Rb electrons. This second process was not necessary to explain the measurements of Swenson and Anderson [Swe 88] and was not confirmed by other experiments. A contribution of spin-orbit-coupling can be expected due to the nature of the Van-der-Waals interaction. The induced electrical dipole moment of physisorbed atoms can be understood as a shift of the electron cloud relative to the nucleus. The attractive force is caused by the attraction between the electrical dipoles, resulting in a R^{-6} dependence on the interatomic distance R [Cha 67, Dal 67]. S-orbitals are symmetric and cannot describe an induced atomic electrical dipole moment. The electron wave function of a sticking atom must therefore contain a P-orbital contribution with a non vanishing orbital angular momentum. This contribution could result in a fluctuating LS-coupling with the spin of the electron.

¹⁰⁰A calculation was performed by Margenau *et al* [Mar 59, Her 61, Gol 61]. The result is, that $\frac{\Delta E_{HFS}}{E_{HFS}} = E_b \left(\frac{1}{\Delta E + E_{ion}^{surf}} + \frac{2}{E_{ion}} \right)$, where E_b is the Van-der-Waals interaction energy, E_{ion} and E_{ion}^{surf} the ionization potential of the adsorbed atom and the surface respectively and ΔE the energy difference between the S and P level of the adsorbed atom. With an assumed ionization potential of 4 eV and a binding energy of 20 meV one expects a relative change in E_{HFS} of less than 1%.

¹⁰¹See for example the article of P.W. Anderson in [Rad 63].

¹⁰²The mean relative velocity can be calculated using Maxwell's velocity distribution. It is for two atoms of same mass $\langle v_r \rangle = \sqrt{2} \langle v \rangle$.

the collider experiments H1 and ZEUS. The revolution time τ_{rev} of a certain bunch is $21.14 \mu s$ and the distance between two bunches $\tau_{bunch} = 96 ns$. The frequency ν_{rev} is then given by the revolution time $\nu_{rev} = \frac{1}{\tau_{rev}} = 47.3 KHz$. Since typically most of the 220 bunch positions are filled, the frequency ν_{bunch} is defined by the time gap between two bunches: $\nu_{bunch} = \frac{1}{\tau_{bunch}} = 10.4097 MHz$. As the bunches are very short, a large number of harmonics contributes to the induced magnetic high frequency field near to the HERA beam. If the transition frequencies between different hyperfine states, which are given by the target holding field, match one or several of these harmonics, resonant depolarization occurs. Measurements of hydrogen bunch field induced depolarization at the HERMES target have been presented in [Ko 98, HER 98b], some new measurements with deuterium will be presented in sec. 6.11.

Similar to the treatment of recombination, the description of spin relaxation can be subdivided into two parts. The first part delivers a prediction of the expected behavior of the observables - the hyperfine population numbers - in dependence on the transition probabilities between the hyperfine states for single wall and spin exchange collisions. The (approximate) solution of this problem is given by a master or rate equation. Consequently, the first part of this section investigates the reliability of the predictions of the master equation. The second part deals with the dependence of the transition probabilities on temperature and magnetic holding field.

6.2 The Master Equation

The basic equation, which is used to describe the change of the measured hyperfine population numbers N_a by spin relaxation processes, is called *master equation* (a "derivation" is given in app. C.6.1) [St 95a, Br 95, St 95b]:

$$\dot{N}_a = \frac{1}{\tau_d} \left(N_a^{inj} - N_a + \langle b_{eff} \rangle \sum_b R_{ab} N_b + \langle c_{eff} \rangle \sum_{bc} M_{bc}^a N_b N_c \right), \quad (6.1)$$

where depolarization by bunch field induced transitions is not taken into account¹⁰³ and recombination is represented by the effective wall and spin exchange collision ages $\langle b_{eff} \rangle$ and $\langle c_{eff} \rangle$ instead of the geometrical ones $\langle b \rangle$ and $\langle c \rangle$ (for details see app. C.6.1). The time constant τ_d is the average time, that the atoms stay within the storage cell, which will be called *diffusion time*. The first and the second term on the right side represent the incoming and outgoing flux, the third term depolarization by wall collisions and the last term the influence of spin exchange collisions described in sec. D.4.

Abraham formulated the way, how transition probabilities can be used in a master equation [Abr 61]:

$$\dot{N}_a \propto \sum_b W_{b \rightarrow a} N_b - N_a \sum_b W_{b \rightarrow a} = \sum_b W_{b \rightarrow a} (N_b - N_a). \quad (6.2)$$

One can write this term also in the following way:

$$\dot{N}_a \propto \sum_b \left[W_{b \rightarrow a} - \left(\sum_c W_{c \rightarrow a} \right) \delta_{ab} \right] N_b, \quad (6.3)$$

¹⁰³During data taking, the magnetic holding field value is in between bunch field induced resonances. The relaxation studies have been performed between HERA fills, so that bunch field induced transitions can not occur.

with the Kronecker symbol δ_{ab} . The matrix R_{ab} of eq. 6.1 can therefore be calculated by

$$R_{ab} = W_{b \rightarrow a} - \delta_{ab} \sum_c W_{c \rightarrow a}. \quad (6.4)$$

If both the spin relaxation terms are neglected, eq. 6.1 reduces to:

$$\dot{N}_a = \frac{N_a^{inj} - N_a}{\tau_d}, \quad (6.5)$$

which can for example be solved by a Laplace transformation. The solution is

$$N_a(t) = N_a(0) e^{-t/\tau_d} + N_a^{inj} (1 - e^{-t/\tau_d}). \quad (6.6)$$

For times, that are large compared to τ_d , the hyperfine population converges towards a dynamical equilibrium, which is called the *steady state*. The time dependence was measured with deuterium at the HERMES target as described in sec. 4.1. Besides this special measurement, the steady state population only is of practical interest, as the polarization measurement with the BRP requires the stability of the hyperfine population for the time of the measurement. Mathematically, the steady state is defined by the condition $\dot{N}_a = 0$ and the calculation of the steady state population is given by the solution of the nonlinear algebraic equation system formed by the right side of eq. 6.1, which can be obtained numerically by an iteration algorithm. For hydrogen the master equation can also be solved directly as described in app. D.5.

The *effective wall collision age* $\langle b_{eff} \rangle$ of the sample, which is - without recombination ($\rho_a = 1$) - identical to the *geometrical collision age* $\langle b \rangle$, is given by:

$$\langle b_{eff} \rangle = \rho_a \langle b \rangle = \frac{\langle b \rangle}{1 + \langle b \rangle \gamma_r}, \quad (6.7)$$

which can also be expressed by the average time of flight between two wall collisions τ_f :

$$\langle b_{eff} \rangle = \frac{\tau_d}{\tau_f} = \rho_a \frac{\tau_d^0}{\tau_f} \quad (6.8)$$

In case of recombination, atoms with a high wall collision age - and thus a long diffusion time - have a higher probability to be recombined. This reduces effectively the average number of wall and spin exchange collisions in the atomic sample and therefore the strength of these effects as it will be shown in sec. 6.4. Also τ_d is reduced, as shown by the measurements in sec. 4.1. The *effective spin exchange collision age* $\langle c_{eff} \rangle$ is given by

$$\langle c_{eff} \rangle = \frac{\tau_d}{\tau_{se}} = \rho_a \tau_d^0 \rho_c \sigma_{se} \langle v_r \rangle \langle n \rangle, \quad (6.9)$$

where σ_{se} is the spin exchange cross section, $\langle n \rangle$ the average density of atoms in the storage cell¹⁰⁴, $\langle v_r \rangle = \sqrt{2} \langle v \rangle$ the average relative velocity of the atoms and τ_d^0 the diffusion time without recombination. The factor ρ_c describes the correlation of diffusion time and atomic density and is defined by eq. C.105 in app. C.6.2.

¹⁰⁴The average density of atoms $\langle n \rangle$ itself depends also on recombination, so that one would in principle expect, that $\langle c_{eff} \rangle \propto \rho_a^2$. The measurement of P_z vs. $\rho_a \simeq \alpha_r^{TGA}$ (see sec. 6.4) however shows, that the spin exchange effect is proportional to α_r^{TGA} . The reason for this linearity is, that the correlation factor ρ_c depends strongly on the distribution of atoms along z inside the beam tube of the storage cell and the sample and extension tube. The measurements in sec. 6.4 result, that the actual conditions of the HERMES target are such, that $\langle n \rangle$ (in eq. 6.9) has to be taken as the nominal average atomic density in case of no recombination. This difficulty arises from the fact, that the master equation is only an approximation of the *rate equation*, which replaces the special geometrical form of the storage cell by a simple volume, as described in app. C.6.

6.2.1 The Depolarization Probabilities

In case of hydrogen and a strong magnetic holding field the master equation can be transformed by an orthogonal transformation as described in app. D.5. In this special case, only 3 different wall transition terms contribute, that are W_e for electron transitions, W_z for nuclear transitions and W_σ for the 2-4 transition. Depolarization by wall collisions can then be described by the depolarization coefficients γ_e for the electron polarization and γ_z for the nuclear polarization. Spin exchange collisions can be described by an additional depolarization coefficient γ_{se} as described in sec. D.5.1. The depolarization probabilities are given by:

$$\begin{aligned}\gamma_e &\simeq W_{14} + W_{23} + W_\sigma \simeq 2W_e + W_\sigma \\ \gamma_z &\simeq W_{12} + W_{34} + W_\sigma \simeq 2W_z + W_\sigma \\ \gamma_{se} &= \frac{\tau_f}{\tau_{se}} \sin^2 2\theta,\end{aligned}\tag{6.10}$$

where τ_f is the mean time of flight between two wall collisions. The polarization of electrons P_e and protons P_z is then given by

$$P_{e,z} = \frac{P_{e,z}^{inj}}{1 + \langle b_{eff} \rangle (\gamma_{e,z} + \gamma_{se})}.\tag{6.11}$$

6.3 The Dependence of Spin Exchange Relaxation on Density

The density dependence of spin exchange relaxation as indicated by eq. 6.9 may directly be used to determine the atomic density of the target, as it will be demonstrated for hydrogen in this section.

As derived in app. D.5.1, spin exchange collisions cause a decay of the difference of the polarization of electrons and nucleons. In the strong field limit the transfer of polarization from the nucleons to the electrons is equivalent to a loss of nuclear polarization, as the electrons depolarize fast by wall collisions, while the nuclear depolarization by wall collisions is suppressed because of the decoupling of electrons and nucleons. The relative loss ΔP_z in nuclear polarization by spin exchange collisions (for $P_e^{inj} = 0$) is given by eq. D.69:

$$\Delta P_z = \frac{(P_z)_0 - P_z}{(P_z)_0} = \frac{1}{2} \frac{1}{1 + \tau_{se}/\tau_d (1 + x^2)},\tag{6.12}$$

where $x = B/B_C^H$. The ratio τ_d/τ_{se} is given by eq. 6.9. The spin exchange term in eq. 6.1 is proportional to the number density of atoms n inside the storage cell. It is therefore possible to determine the influence of spin exchange collisions by a variation of the atomic flux of the ABS. Fig. 6.1 shows the measured polarization versus the flux into the TGA ϕ_{tot} , which is proportional to the atomic density. The extrapolated values for $\phi_{tot} \rightarrow 0$ are:

$$\begin{aligned}P_e(P_{z+}, n = 0) &= 0.030 \pm 0.006 & P_z(P_{z+}, n = 0) &= 0.961 \pm 0.006 \\ P_e(P_{z-}, n = 0) &= 0.015 \pm 0.006 & P_z(P_{z-}, n = 0) &= -0.949 \pm 0.005,\end{aligned}\tag{6.13}$$

which corresponds to an average polarization loss of about 3.3% caused by spin exchange collisions at nominal ABS flux¹⁰⁵. As ΔP_z is much smaller than one, one has due to eq. 6.9 and eq. 4.10 approximately

$$\Delta P_z \simeq \frac{\rho_c \langle n \rangle L_d \sigma_{se}}{\sqrt{2}(1+x^2)}, \quad (6.14)$$

so that the average number density of atoms in the storage cell $\langle n \rangle$ can be calculated by

$$\langle n \rangle = \frac{\Delta P_z \sqrt{2}(1+x^2)}{L_d \rho_c \sigma_{se}}. \quad (6.15)$$

At a storage cell temperature of about 100 K, a magnetic holding field of 335 mT ($x = 6.61$), a diffusion length of $L_d = 4.2$ m and a spin exchange cross section of $\sigma_{se} = 23.4 \cdot 10^{-16}$ cm², one obtains for $\langle n \rangle$:

$$\langle n \rangle = 1.942 \cdot 10^{12} \text{ cm}^{-3},$$

corresponding to a central target pressure of about $5.46 \cdot 10^{-5}$ mbar and an injected atomic flux of

$$\Phi^{inj} = 9.3 \cdot 10^{-4} \text{ mbar l s}^{-1} = 6.7 \cdot 10^{16} \text{ atom.s}^{-1}.$$

The statistical uncertainty of ΔP_z is about 0.5%, so that the error on the density and injected flux is about 15% for this measurement. A significantly higher precision will be achieved with the measurement of the magnetic field dependence of spin relaxation as shown in sec. 6.8.

6.4 The Effect of Recombination on Spin Relaxation

The spin relaxation processes are influenced by recombination in several ways. First of all, the average collision age of the atoms is reduced, which can be described by the

¹⁰⁵The asymmetry in the electron polarization can be explained by the lack of the ABS transitions (WFT 1-3 and SFT 2-4). Both inefficiencies lead to a small amount of positive injected electron polarization $(P_e)_0 \geq 0$.

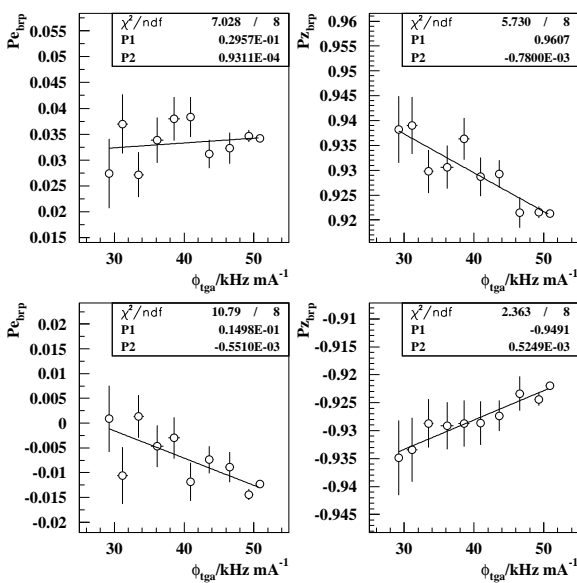


Fig. 6.1: Measurement of the density dependence of spin exchange depolarization. The figures shows the measured values of P_e (left) and P_z (right) for the hydrogen injection modes P_{z+} (upper) respectively P_{z-} (lower) plotted versus the flux into the TGA in kHz/mA. The holding field was 335 mT and the storage cell temperature 105 K.

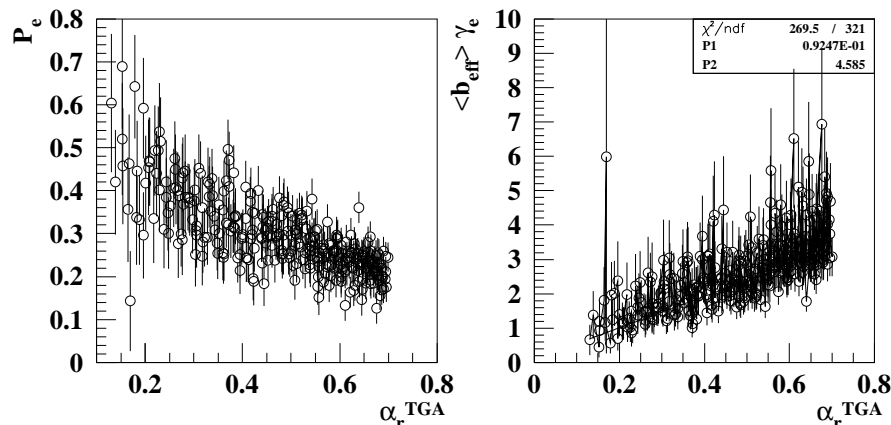


Fig. 6.2: Measured influence of recombination on wall depolarization, measured with hydrogen in injection mode P_e . The left graph shows the measured electron polarization, the right graph $\langle b_{eff} \rangle \gamma_e$ vs. the measured atomic fraction α_r^{TGA} .

effective collision age $\langle b_{eff} \rangle$. The reduction of the effective diffusion time of the atoms at low temperatures delivers a direct measurement of this effect, as shown in fig. 4.6. The high field approximation used in the transformed master equation as given by eq. 6.11 predicts a dependence of the relaxation on the *effective* collision age $\langle b_{eff} \rangle$, which can be proved in the situation of an accidental HERA beam loss. The beam loss comes along with a strong reduction of the atomic fraction inside the storage cell (see fig. 3.11). After the beam loss, the measured atomic fraction α_r^{TGA} recovers with the ABS operation time [Ko 98], and the dependence of the polarization on the atomic fraction can be studied. As the recombination probability of sample- and injection tube does not change during the measurement¹⁰⁶, one can conclude, that the atomic fraction of the TGA α_r^{TGA} is proportional to the normalized atomic density in the center of the storage cell: $\alpha_r^{TGA} \simeq \rho_a(0)$. In this case, one expects by eq. 6.11 and eq. 6.7 for the injection mode P_e of hydrogen, where the spin exchange effect can be neglected compared to wall relaxation, that

$$P_e \simeq \frac{P_e^{inj}}{1 + \langle b \rangle \alpha_r^{TGA} \gamma_e} \quad (6.16)$$

holds and therefore:

$$\frac{P_e^{inj}}{P_e} - 1 \simeq \langle b \rangle \gamma_e \alpha_r^{TGA}. \quad (6.17)$$

Fig. 6.2 shows a plot of P_e and $\langle b_{eff} \rangle \gamma_e$ versus the measured atomic fraction α_r^{TGA} . The beam loss influences the polarization also directly, but the recovery time of the polarization is much longer than for the atomic fraction¹⁰⁷. In case of the nuclear polarization P_z , the spin exchange effect is - at the nominal holding field of 335 mT - of the same strength as wall depolarization or even stronger. As spin exchange relaxation is proportional to the atomic density *and* the diffusion time, one might suspect, that the relaxation constant for the protons γ_z is proportional to α_r^{TGA} squared. But this is an artifact of the master equation, which approximates the geometry of the storage cell by a simple volume. A more

¹⁰⁶This statement is verified by the measured proportionality of the total atomic intensity I_{tot} to the BRP vs. the atomic signal in the TGA as shown in fig. 4.3.

¹⁰⁷Fig. 6.4 contains a time graph of $P_e(P_e^{inj})$ for the year 1997, that shows several sudden drops of $P_e(P_e^{inj})$, followed by periods of slow recovery. The time constant for this slow recovery is in the order of several weeks, while the recovery time for α is in the order of a few ten hours. It is therefore reasonable to assume, that the depolarization coefficient is practically constant for the time of the measurement shown in fig. 6.2

careful analysis results, that the correlation factor ρ_c , which represents the geometrical properties of the density distribution, depends on recombination. It turns out, that the spin exchange effect is approximately proportional to the measured atomic fraction α_r^{TGA} and hence:

$$\langle b_{eff} \rangle (\gamma_z + \gamma_{se}) = \frac{P_z^{inj}}{P_z} - 1 \propto \alpha_r^{TGA}, \quad (6.18)$$

as shown by fig. 6.3.

6.5 Direct Determination of the Injected Polarization for Hydrogen

In case of the three main injection modes of hydrogen, which are P_e , P_{z+} and P_{z-} , as listed in tab. 3.1, the injected hyperfine population is dominantly determined by the efficiencies ε_{s24} and ε_{w13} of the ABS transitions SFT 2-4 and WFT 1-3. They can be estimated by several different methods. The first one is given by a fit of the master equation to the measured magnetic field dependence of the hyperfine population as shown in fig. 6.10. A more simple method makes use of the symmetry of the spin exchange effect and wall depolarization and the asymmetry caused by the efficiencies of the transitions: The injected electron polarization for the modes P_{z+} and P_{z-} is directly given by $1 - \varepsilon_{s24}$ and $1 - \varepsilon_{w13}$ respectively and is positive in both cases. The polarization transfer from the nucleons to the electrons by spin exchange and the 2-4 transition on the other hand follows the sign of the injected proton polarization. In case of the high holding field limit and for the nearly optimal sextupole transmissions of the HERMES ABS, one has $P_e^{inj} \simeq 1$ and $P_z^{inj} \simeq 0$ for injection mode P_e . With Δ defined by eq. D.78 and $\gamma_e \gg \gamma_{se}$ one obtains from eq. D.77 for the measured value of P_e :

$$P_e \simeq \frac{P_e^{inj}}{1 + \langle b_{eff} \rangle \gamma_e} + \Delta P_z^{inj} = \delta P_e^{inj} + \Delta P_z^{inj} \quad (6.19)$$

with the same constants δ and Δ in all injection modes. The constant δ represents the reduction of the injected electron polarization by wall depolarization $\delta \simeq P_e(P_e^{inj})$ and Δ the transfer of polarization from P_z to P_e or vice versa by spin exchange relaxation. One obtains for $P_e(P_{z\pm}^{inj})$:

$$\begin{aligned} P_e(P_{z+}^{inj}) &\simeq \delta (1 - \varepsilon_{s24}) + \Delta P_z(P_{z+}^{inj}) \\ P_e(P_{z-}^{inj}) &\simeq \delta (1 - \varepsilon_{w13}) + \Delta P_z(P_{z-}^{inj}). \end{aligned} \quad (6.20)$$

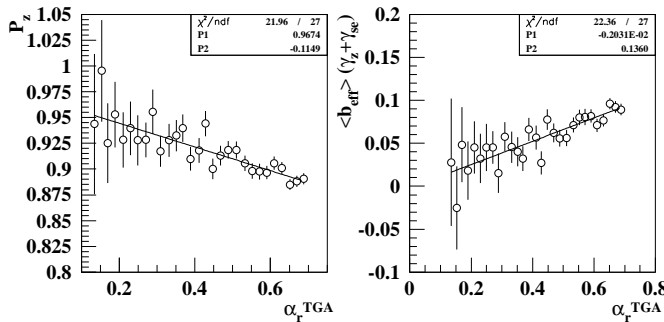


Fig. 6.3: Nuclear spin relaxation vs. atomic fraction, measured with hydrogen in injection mode P_{z+} . The left graph shows P_z and the right $\langle b_{eff} \rangle (\gamma_z + \gamma_{se})$ vs. α_r^{TGA} . In contrast to the relaxation of the electron spins, the contribution of spin exchange is not negligible - but also proportional to α_r^{TGA} in the measured range. The measurement was done after an accidental HERA beam loss in Oct. 1997. The data are rebinned with respect to α_r^{TGA} .

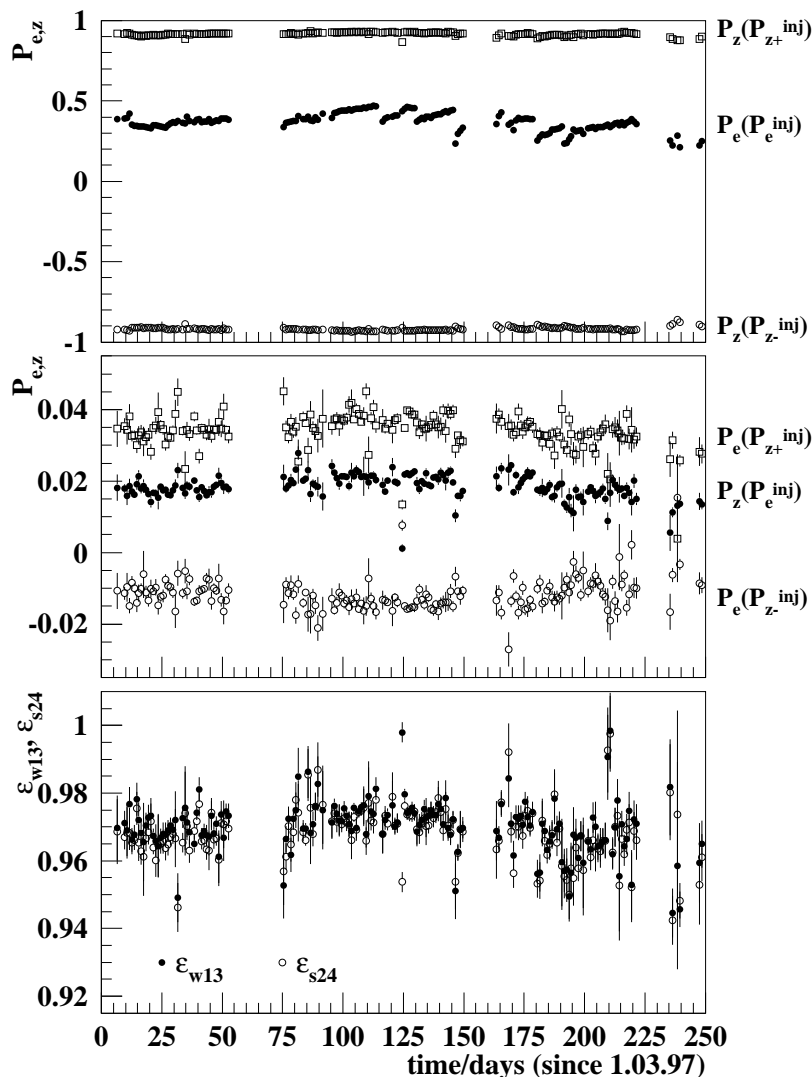


Fig. 6.4: Upper figures: Averaged polarization vs. time during the 1997 polarized data taking periods (between HERA fills). The lower graph shows the calculated efficiencies ε_{w13} (filled symbols) and ε_{s24} (open symbols). The obtained efficiencies are in agreement with the results of tab. 6.1 and were reasonably stable over the data taking period. The systematic uncertainty of this method can be estimated by the variations of the efficiencies and is about 0.25...0.5%. The value of $P_e(P_e^{inj})$ is not stable with time - the sudden drops are related to bad HERA beam conditions respectively beam losses. P_e recovers typically within a few weeks. The recovery time of the atomic fraction is much shorter, as shown in fig. 3.11. The calculated efficiencies are to some extent correlated with these events, which is likely an artifact of the approximations.

As $P_z(P_{z+}^{inj}) + P_z(P_{z-}^{inj}) \simeq 0$ holds, one can extract the sum of both efficiencies directly from the measured polarization values:

$$\varepsilon_{w13} + \varepsilon_{s24} = 2 - \frac{P_e(P_{z+}^{inj}) + P_e(P_{z-}^{inj})}{P_e(P_e^{inj})}. \quad (6.21)$$

As the proton depolarization is reasonably low at the working point, one may approximate eq. 6.11 by:

$$\begin{aligned} P_z(P_{z+}^{inj}) &\simeq \varepsilon_{s24} - (\Delta P)_{se} - (\Delta P)_{wd} \\ P_z(P_{z-}^{inj}) &\simeq -\varepsilon_{w13} + (\Delta P)_{se} + (\Delta P)_{wd}, \end{aligned} \quad (6.22)$$

where $(\Delta P)_{se}$ is the polarization loss by spin exchange collisions and $(\Delta P)_{wd}$ by wall depolarization. One obtains for the difference of the efficiencies:

$$P_z(P_{z+}^{inj}) + P_z(P_{z-}^{inj}) \simeq \varepsilon_{s24} - \varepsilon_{w13}. \quad (6.23)$$

The efficiencies of the ABS transitions can now be obtained by the combination of eq. 6.21 and eq. 6.23. Fig. 6.4 shows an overview over the measured polarization values and calculated efficiencies for the 1997 data taking period.

6.6 Theory of Wall Depolarization

The Hamilton operator \mathcal{H}_d for dipolar interaction of the magnetic moment μ_S of the electron of the adsorbed atom¹⁰⁸ with a magnetic moment μ_J on the surface is given by [Blo 48, Abr 61, Sli 64]:

$$\mathcal{H}_d = \frac{\mu_0}{4\pi} \frac{\vec{\mu}_S \vec{\mu}_J - 3(\vec{\mu}_S \vec{r})(\vec{\mu}_J \vec{r})/r^2}{r^3}, \quad (6.24)$$

where $r = |\vec{r}|$ is the relative distance of the moments. With the gyromagnetic ratios γ_S and γ_J one has the relations $\vec{\mu}_S = \gamma_S \hbar \vec{S}$ and $\vec{\mu}_J = \gamma_J \hbar \vec{J}$. One may represent the different contributions of \mathcal{H}_d by a *local magnetic field*¹⁰⁹ \vec{B}_{loc}^{dd} at the position of the adsorbed atom [Blo 48, Bou 65, Bou 63].

Also the possibility of exchange interaction between the electron of the adsorbed atom with unpaired electrons of the surface has to be taken into account. Exchange interaction involves typically much higher energies than dipolar interaction as it is an electronic effect, based on the Pauli principle¹¹⁰. Nevertheless, it is often represented by an equivalent 'magnetic field', the so-called *exchange field*. In the Heisenberg model, exchange interaction can be described by a Hamilton operator of the form

$$\mathcal{H}_{ex}^{(i)} = -J \sum_k \vec{S}_i \vec{S}_k, \quad (6.25)$$

where J is the *exchange integral* and \vec{S}_i are the spins of the unpaired electrons. It is positive in case of ferromagnetism and negative in case of antiferromagnetism. The local exchange field can then be represented by

$$B_{loc}^{ex} = -\frac{J\hbar}{g_s \mu_B} \sum_k \vec{S}_k. \quad (6.26)$$

The formalism is then analogue to dipolar interaction. The exchange field in iron - where the exchange integral is large - can reach up to 1000 T, corresponding to about 11 meV interaction energy [Kit 86]. Both 'fields' may fluctuate randomly due to the surface diffusion and vibrations of the adsorbed atom. The resulting perturbation of the hyperfine Hamiltonian can be represented in a term

$$\mathcal{H}_p = \frac{g_S \mu_B}{\hbar} \vec{S} \vec{B}_{loc}(t), \quad (6.27)$$

where the total local field $\vec{B}_{loc}(t)$ is the sum of dipolar and exchange contributions.

¹⁰⁸As the interaction strength is proportional to the magnetic moment, direct interaction with the nuclear spin of the adsorbed atom is much weaker and can be neglected.

¹⁰⁹The double d stands for dipole-dipole interaction.

¹¹⁰Between hydrogen atoms for example, only the singlet state with antiparallel spins is attractive - which is the cause of the surprisingly strong effect of the spin exchange collisions. While in the theory of spin exchange collisions, the angular momentum is conserved, this is not required in case of exchange interactions with the 'thermal bath' of a surface.

The average transition probability $W_{ab}(\tau)$ of a random fluctuating perturbation of eq. 6.27 is in first order perturbation theory given by¹¹¹:

$$W_{b \rightarrow a}(\tau) = W_{a \rightarrow b} = \frac{1}{\hbar^2} |V_{ba}|^2 2\pi \tau j(\omega_{ab}), \quad (6.28)$$

where $V_{ab} = \langle a | \mathcal{H}_p | b \rangle$ and τ is the interaction time. The function $j(\omega)$ is the normalized *spectral density* of the fluctuating process, which is proportional to the Fourier cosine transform of the *auto-correlation function* (ACF) $G(\tau)$ of the random process $\mathcal{H}_p(t)$:

$$G(\tau) = \langle \mathcal{H}_p^\dagger(t) \mathcal{H}_p(t + \tau) \rangle. \quad (6.29)$$

The process is assumed to be stationary¹¹², thus $G(\tau)$ does not depend on the value of t .

For certain types of processes, the ACF can be obtained by simple arguments. If the process is given by a brownian diffusion of an atom (or molecule) from site to site on a surface or in a crystal of arbitrary dimension, where one assumes, that the function $\mathcal{H}_p(t)$ varies randomly from site to site, *and the diffusing atom never returns to a site already visited*, then

$$G(\tau) = G(0) e^{-|\tau|/\tau_c}, \quad (6.30)$$

where τ_c describes the average time, that the atom stays at a site. The spectral density, that results from this type of process, is a Lorentzian distribution with resonance frequency zero:

$$j_{bpp}(\omega) = \int_0^\infty e^{-|\tau|/\tau_c} \cos \omega \tau d\tau = \frac{\tau_c}{1 + \tau_c^2 \omega^2}. \quad (6.31)$$

This form of the spectral density is often called BPP-model, which refers to the publication of Bloembergen, Purcell and Pound [Blo 48]. It has been used for the interpretation of many experiments [Bou 63, Bou 65, Hag 86, Hor 82, Lev 88, Swe 88].

In case of a non vanishing probability to return to an already visited site, the diffusion can approximately be described by a continuum model, where the ACF is given by the conditional probability $P(t)$, that the atom, located at the origin at $t = 0$ returns to this position after a time t [Tor 53, Sho 81]. In case of d-dimensional diffusion, the probability $P(t)$ will converge for reasonably long times to $\lim_{t \rightarrow \infty} P(t) = t^{-d/2}$ (see for example [Ric 73]). A direct analytical calculation of the resulting ACF is not possible, but approximations of the spectral density for the limits of high and low frequencies in several dimensions are available [Sho 81]. In the two-dimensional case, the low frequency behavior ($\omega \tau_c \ll 1$) is given by

$$\lim_{\omega \rightarrow 0} j(\omega) \propto \tau_c \ln \frac{1}{\tau_c \omega}, \quad (6.32)$$

while the high frequency behavior ($\omega \tau_c \gg 1$) is - as is case of the BPP model - given by

$$\lim_{\omega \rightarrow \infty} j(\omega) \propto \frac{1}{\tau_c \omega^2}. \quad (6.33)$$

¹¹¹This equation is equivalent to "Fermi's golden rule". A short derivation is given in app. D.1.

¹¹²Strictly spoken, the process is only stationary in case of infinite sticking time $\tau_s \rightarrow \infty$, but one may neglect the difference for $\tau_s \gg \tau_c$.

The logarithmic dependence of the spectral density as represented by eq. 6.32 was confirmed in a variety of experiments, for example in [Avo 76, Kle 80, Sil 74, Mem 88]. Richards suggested the use of the combined spectral density

$$j(\omega) = \tau_c \ln \left(1 + \frac{1}{\tau_c^2 \omega^2} \right) \quad (6.34)$$

for the 2-dimensional case, which provides the required asymptotic behavior for both, low and high frequencies [Ric 78]. The spectral density of eq. 6.34 is equivalent with the assumption of an ACF of the following form [Ebi 98]:

$$G(\tau) \propto \frac{1 - e^{-\tau/\tau_c}}{\tau}. \quad (6.35)$$

H. Kleine used a Monte Carlo simulation technique to investigate the influence of the interdipolar distance relative to the average hopping distance on the spectral density and found, that the diffusion on a two-dimensional lattice in the presence of a sublattice with a larger unit cell with different dipoles is between the functional behavior of eq. 6.31 and eq. 6.34 for high and intermediate frequencies [Kle 98]¹¹³. Especially he found, that the spectral density does *not* diverge for $\omega \rightarrow 0$ in case of limited interaction times - in contrast to the approximation of eq. 6.34. Instead, both models lead to a constant density in the low frequency limit. Also the correlation time constant τ_c is identical for both models.

The maximal value of a relevant transition frequency of hydrogen and deuterium in holding fields of up to 335 mT is about 10^{10} s^{-1} . For the expected correlation time τ_c in the order of 10^{-12} s ¹¹⁴, the relation $\omega_{ab}\tau_c \ll 1$ is fulfilled and the spectral density is approximately constant under the conditions of the HERMES target.

The Hamilton operator, which represents the magnetic interaction between physisorbed atoms and the surface, is given by eq. 6.27. First order perturbation theory yields with an interaction time (sticking time) distribution of¹¹⁵

$$w(t) = \frac{1}{\tau_s} e^{-t/\tau_s} \quad (6.36)$$

a transition probability of the form of eq. 6.28¹¹⁶. The measurements indicate however, that first order theory is not sufficient for the description of the complete data set. Instead of first order perturbation theory, one can calculate the exact behavior for the two state system and apply the result to the hyperfine transitions. The prediction will still be an approximation, but its range of validity might be extended. The calculation is given in app. D.2 and yields

$$W_{ab} = \frac{\Omega_{ab}^2}{2\Delta\Omega^2} \Delta\Omega j(\omega_{ab}), \quad (6.37)$$

¹¹³More detailed discussions of spectral densities and autocorrelation function can for example be found in [Kor 83, Kor 84, Kor 83, Kor 83, Cam 99, Sho 92].

¹¹⁴See the estimation and references in sec. 5.2.1.

¹¹⁵See for example [Fre 57].

¹¹⁶For details refer to app. D.1.

where the resonance width¹¹⁷ $\Delta\Omega$ is given by $\Delta\Omega^2 = 1/\tau_s^2 + \Delta\omega_0^2$, where $\Delta\omega_0$ is the resonance width for infinite interaction times. As described in app. D.2.1, one may approximately use the relaxation strength Ω_{ab}^2 itself as an estimate for $\Delta\omega_0^2$:

$$\Delta\omega_0^2 \simeq \Omega_{ab}^2. \quad (6.38)$$

To summarize: The spectral density of the BPP-model (eq. 6.31) is in the low frequency limit¹¹⁸ approximately equal to τ_c , so that¹¹⁹:

$$W_{ab} = \frac{\Omega_{ab}^2}{2} \frac{\tau_s \tau_c}{\sqrt{1 + \Omega_{ab}^2 \tau_s^2}}. \quad (6.39)$$

The mean square perturbation Ω_{ab}^2 is given by:

$$\Omega_{ab}^2 = \frac{2}{3} \frac{\omega_{HFS}^2}{B_C^2} \langle \vec{B}_{loc}^2 \rangle |C_{ab}|^2. \quad (6.40)$$

The reduced *matrix elements* $|C_{ab}|^2$ are calculated in app. D.3. The factor $\frac{2}{3}$ represents the fact, that only two of the three directions of the fluctuating field contribute in case of π -transitions¹²⁰.

It should be noted that also this result has a limited range of validity: It can be applied only, if the hyperfine states can be treated as well separated, so only transitions between two states have to be taken into account. Deviations from this behavior will be discussed later.

6.7 The Temperature Dependence of Hydrogen Spin Relaxation

Two different interpretations of the temperature dependence of hydrogen spin relaxation measurements will be presented in this section. The first one covers the data above 50 K only and is unable to describe all aspects of the data. The second one, which is able to describe all data, requires the assumption of a non-vanishing polarization of the electrons in thermal equilibrium with the surface and can only be understood, if permanent magnetized sites are present on the surface at low storage cell temperatures.

All measurements of the temperature dependence of spin relaxation have been performed at high magnetic holding field (335 mT), so that the nuclear spin is strongly decoupled from the electron spin ($\theta \rightarrow 0$). In this case, the approximation of app. D.5 holds and one may use eq. 6.11. In high field, the following relations hold:

$$\begin{aligned} W_{23} &\simeq W_{14} & W_{24} &\ll W_{23} \\ W_{12} &\simeq W_{34} & W_{24} &\simeq 2W_{12}, \end{aligned} \quad (6.41)$$

¹¹⁷Transitions between distinct energy levels are described as resonances with a certain line width. In the simplest case, the line width is given by the inverse interaction time $\Delta\omega = 1/\tau$. But typically there are other broadening effects caused by additional perturbations to the Hamiltonian. The different contributions are added squared if they are uncorrelated.

¹¹⁸More precisely spoken, if $\tau_c \omega_{ab} \ll 1$.

¹¹⁹Eq. 6.39 is explained and discussed in app. D.2 and app. D.2.1 respectively.

¹²⁰For the same reason, the matrix elements of the σ -transitions in tab. D.2 were reduced by another factor $\frac{1}{2}$.

then the depolarization probabilities γ_e and γ_z are:

$$\begin{aligned}\gamma_e &= W_{23} + W_{14} + W_{24} \simeq 2W_e \\ \gamma_z &= W_{12} + W_{34} + W_{24} \simeq 4W_z.\end{aligned}\quad (6.42)$$

W_z and W_e are the transition probabilities for nuclear and electron transitions respectively. In case of hydrogen one obtains¹²¹:

$$W_z \simeq \frac{C}{2} \frac{\tau_s \tau_c \sin^2 \theta}{\sqrt{1 + C \sin^2 \theta \tau_s^2}} \quad (6.43)$$

$$W_e = \frac{C}{2} \frac{\tau_s \tau_c \cos^2 \theta}{\sqrt{1 + C \cos^2 \theta \tau_s^2}}, \quad (6.44)$$

where C is given by

$$C = \frac{2}{3} \frac{\omega_{HFS}^2}{B_C^2} \langle \vec{B}_{loc}^2 \rangle. \quad (6.45)$$

The value of γ_{se} is estimated from the polarization loss due to spin exchange at 100 K - $\Delta P_{se}(100 K)$ - using the following formula:

$$\langle b_{eff} \rangle \gamma_{se} \simeq \Delta P_{se}(100 K) \sqrt{\frac{100 K}{T}} \frac{\sigma_{se}(T)}{\sigma_{se}(100 K)} \alpha_r^{TGA}, \quad (6.46)$$

where $\sigma_{se}(T)$ is the spin exchange cross section as calculated by Allison (see app. D.4). The factor $\sqrt{\frac{100 K}{T}}$ is related to the decrease of the storage cell conductance with decreasing temperature and the corresponding increase in the atomic density. $\Delta P_{se}(100 K)$ was obtained to be about 3.3% (see sec. 6.3), the injected polarization in the mode P_{z+}^{inj} is about 97.3% (see eq. 6.67). The atomic fraction enters by eq. 6.7, as $\langle b_{eff} \rangle \simeq \langle b \rangle \alpha_r^{TGA}$. The determination of γ_z is performed with the injection mode P_{z+} and of γ_e with mode P_e of tab. 3.1:

$$\gamma_z \simeq \frac{1}{\langle b_{eff} \rangle} \left(\frac{P_z^{inj}}{P_z} - 1 \right) - \gamma_{se} \simeq \frac{2C \sin^2 \theta \tau_s \tau_c}{\sqrt{1 + C \sin^2 \theta \tau_s^2}} \quad (6.47)$$

$$\gamma_e \simeq \frac{1}{\langle b_{eff} \rangle} \left(\frac{P_e^{inj}}{P_e} - 1 \right) - \gamma_{se} \simeq \frac{C \cos^2 \theta \tau_s \tau_c}{\sqrt{1 + C \cos^2 \theta \tau_s^2}}. \quad (6.48)$$

In order to compare theory and measurement, we will use the following parameterization:

$$\rho(T) = C \cos^2 \theta \tau_s^2 = \rho_0 \exp\left(\frac{2E_b}{kT}\right) \quad (6.49)$$

$$\eta(T) = \frac{\tau_c}{\tau_s} = \eta_0 \exp\left(\frac{E_j - E_b}{kT}\right), \quad (6.50)$$

so that one may write eq. 6.47 and eq. 6.48 as follows:

$$\gamma_e \simeq \frac{\rho \eta}{\sqrt{1 + \rho}} \quad (6.51)$$

$$\gamma_z \simeq \frac{2\rho \eta \tan^2 \theta}{\sqrt{1 + \rho \tan^2 \theta}}. \quad (6.52)$$

¹²¹ θ is the hydrogen mixing angle and C a constant factor.

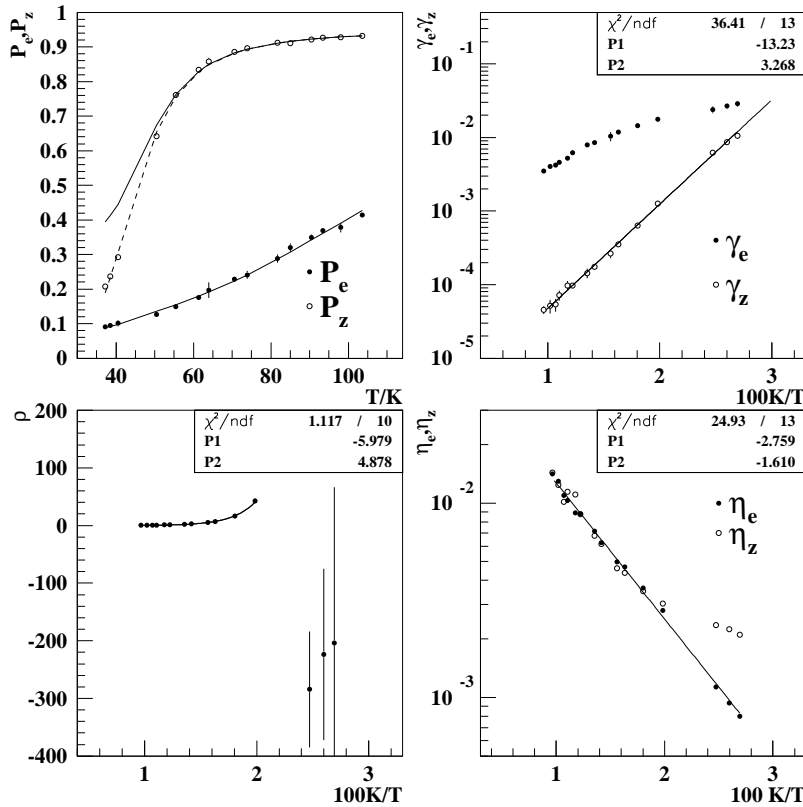


Fig. 6.5: Measurement of the temperature dependence of spin relaxation with hydrogen. The upper left graph shows the measured (symbols) and fitted (lines) polarization values. The meaning of the dashed line in the lower right graph is explained in the text. The extracted relaxation coefficients γ_e and γ_z are shown in the upper right and the extracted value of $\rho(T)$ in the lower left graph. $\rho(T)$ shows the expected theoretical behavior down to a temperature of about 50 K. Below that value, the calculation results unphysical negative values. This corresponds to the results of η_e and η_z , which agree nicely above 50 K - but not below as shown in the lower right figure. The measurement was performed 27th Jun 1997.

A combination of these equations can be used to extract $\rho(T)$ from γ_e and γ_z and to compare with eq. 6.49. The value of η can - for known ρ - be extracted using either γ_e or γ_z , labeled as η_e and η_z respectively. The theory will only describe the data, if both values agree within the uncertainties. With eq. 5.10 and eq. 5.11 one obtains the following equations:

$$\rho = \frac{1}{\tan^2 \theta} \frac{\gamma_z^2 - 4 \tan^4 \theta \gamma_e^2}{4 \tan^2 \theta \gamma_e^2 - \gamma_z^2} \quad (6.53)$$

$$\eta_e = \gamma_e \frac{\sqrt{1 + \rho}}{\rho} \quad (6.54)$$

$$\eta_z = \gamma_z \frac{\sqrt{1 + \rho \tan^2 \theta}}{2 \rho \tan^2 \theta} \quad (6.55)$$

The results of this analysis method are shown in fig. 6.5. It turns out, that the described relaxation model can reproduce the measured data down to storage cell temperatures of about 50 K. The fit results for the exponents¹²²:

$$\begin{aligned} E_b &= \frac{470 \text{ K}}{2k_b} = \frac{235 \text{ K}}{k_b} \simeq 21 \text{ meV} \\ E_j &= \frac{488/2 - 161 \text{ K}}{k_b} = \frac{83 \text{ K}}{k_b} = 7.14 \text{ meV} \end{aligned} \quad (6.56)$$

¹²²For the evaluation of the exponents, only the measured value above 50 K were taken into account.

The analysis of the recombination data delivered $E_b = 23.4 \text{ meV}$ and $E_j = 6.86 \text{ meV}$ (see sec. 5.5), which is in reasonable agreement¹²³ with (6.56).

The fit of $\eta_e = \tau_c/\tau_s$ with eq. 6.50 yields a prefactor, so that

$$\tau_s^0 = 15.7 \tau_c^0. \quad (6.57)$$

The fit yields $\rho_0 = 0.0025$. With $\rho_0 = C (\tau_s^0)^2 \cos^2 \theta$ and eq. 6.45 one can calculate an estimation of the local fluctuating field. In high field $\cos \theta \simeq 1$ holds. With the estimated value (see sec. 5) of $1/\tau_c = \nu_d \simeq 5 \cdot 10^{12} \text{ s}^{-1}$ and eq. 6.57 one obtains $\tau_s^0 \simeq 7.7 \cdot 10^{-12} \text{ s}^{-1}$:

$$\frac{\langle B_{loc}^2 \rangle}{B_C^2} = \frac{3}{2} \frac{\rho_0}{(\tau_s^0 \omega_{HFS})^2} \simeq 0.8,$$

which corresponds to fluctuating fields of about 45 mT . This seems to be a realistic value for a situation with a relatively high density of uncoupled electrons on the surface¹²⁴. Levy and Schmor came up with a similar value. They estimated the local fluctuating field using results of spin relaxation measurements of optically pumped Na vapor on Drifilm and found a value of 48 mT [Lev 88]. One can therefore conclude, that eq. 6.57 is indeed a reasonable assumption for the conditions of the HERMES hydrogen target. It is in its order of magnitude also supported by the absolute value of the recombination probability γ_r (see sec. 5.5). The estimated values of the high temperatures limits τ_s^0 and τ_c^0 then are

$$\tau_s^0 \simeq 7.7 \cdot 10^{-12} \text{ s} \quad \tau_c^0 \simeq 2 \cdot 10^{-13} \text{ s}. \quad (6.58)$$

At lower temperatures, the extracted values η_e and η_z do not agree any more and ρ becomes negative. Kolster interpreted the disagreement between theory and measurement as an indication for a non-constant spectral density. If the assumption, that the data can be described by the constant low frequency limit of the spectral density fails, then the falloff of $j(\omega)$ at high frequencies could explain the measured results, as the transition frequencies differ significantly for electron transitions and nuclear transitions in high holding field [Ko 98]. Nevertheless, it will be shown in sec. 6.8, that the assumption of a non-constant spectral density disagrees with the measured magnetic field dependence of the hyperfine population. Another possible interpretation is, that the line width factor C in the denominator of eq. 6.47 is overestimated. Indeed, if this factor is simply skipped, one obtains the dashed line (in the upper left graph of fig. 6.5) as a prediction for P_z , which describes the data fairly well. Nevertheless - the measurement of the magnetic field dependence (sec. 6.8) supports the presence and about the size of the line width term. A possible explanation of the low temperature behavior will be given in the following section.

6.7.1 Interpretation of the Measurements by Exchange Interaction

A different interpretation of the data is favored by the measured residual and transferred¹²⁵ polarization values as shown fig. 6.6. Especially the measured value of P_e in the injection

¹²³The exact values of the fitted exponents are sensitive to the assumed injected polarization and spin exchange strength. The systematic uncertainty of the exponents is therefore in the order of 10... 15 %.

¹²⁴The magnetic field caused by the magnetic moment of an electron is about 100 mT in a distance of 2 \AA . The dipolar field of a proton in the same distance is 0.176 mT .

¹²⁵The transferred polarization is the fraction of the polarization, that is transferred between electron and nucleus by spin exchange collisions and the σ -transition.

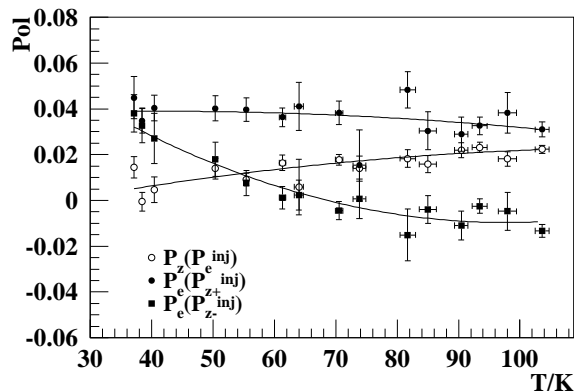


Fig. 6.6: Residual polarizations for the hydrogen injection modes P_e and $P_{z\pm}$. The solid lines are guides for the eye only. The value of $P_z(P_e^{inj})$ (open circles) - which is non zero due to the polarization transfer by spin exchange collisions - reduces as expected to nearly zero at low temperatures. The situation is different for the measured values of $P_e(P_{z\pm}^{inj})$. While $P_e(P_{z+}^{inj})$ (filled circles) stays surprisingly high below 50 K, the value of $P_e(P_{z-}^{inj})$ (filled squares) changes its sign and becomes positive. Neither spin exchange collisions nor (first order) wall relaxation can explain this effect.

modes $P_{z\pm}$ is of special interest. The ABS injects a small fraction $\simeq 2\%$ of positive electron polarization in both injection modes $P_{z\pm}$ due to non-ideal transition efficiencies. Spin exchange collisions tend to reduce the difference of P_e and P_z , which results in a transfer of a small fraction of the injected polarization of the nucleons to the electrons (resp. vice versa in mode P_e^{inj}). One expects therefore a positive residual electron polarization for the states P_{z+}^{inj} and a (smaller) negative one for P_{z-}^{inj} . At low temperatures, where $P_e(P_e^{inj})$ drops to about 10 %, also the residual polarization $P_e(P_{z\pm})$ should decrease. Since also the spin exchange cross section (as calculated by Allison [All 72]) reduces below 100 K, one expects, that $P_e(P_{z\pm}^{inj}) \rightarrow 0$ at low temperatures.

The measured values at about 100 K are in agreement with the expectation, but

- the value of $P_e(P_{z+}^{inj})$ does not decrease with decreasing temperature, even though $P_e(P_e^{inj})$ decreases by a factor of 4.
- the value of $P_e(P_{z-}^{inj})$ first decreases, but then changes sign below 50 K and becomes positive.

Wall depolarization - as far as the referred theory goes - cannot explain this behavior. The only high frequency transition of hydrogen, which is able to transfer polarization between electron and nucleon, is the 2 – 4 transition. But this transition yields the opposite effect in case of $P_e(P_{z-}^{inj})$: It leads to a small fraction of negative electron polarization for P_{z-}^{inj} . It was found, that all measurements of the temperature dependence with hydrogen show this behavior, independent on the measured atomic fraction, which varies strongly from measurement to measurement (see fig. 5.10). It was carefully checked, that the measured values can - to this extend - not be explained by any known artifact of the measurement of the BRP, such as wrong transition efficiencies, transmissions in the sextupole system or offsets of the measured beam rates etcpp.

Up to now, it was assumed, that the polarization should vanish in case of infinitely strong wall depolarization. This is nevertheless only correct, if the polarization vanishes in thermal equilibrium. The thermal equilibrium is defined by the Boltzmann distribution and yields the following equilibrium population N_a^{eq} :

$$N_a^{eq} = \frac{e^{-E_a/k_bT}}{\sum_b e^{-E_b/k_bT}}. \quad (6.59)$$

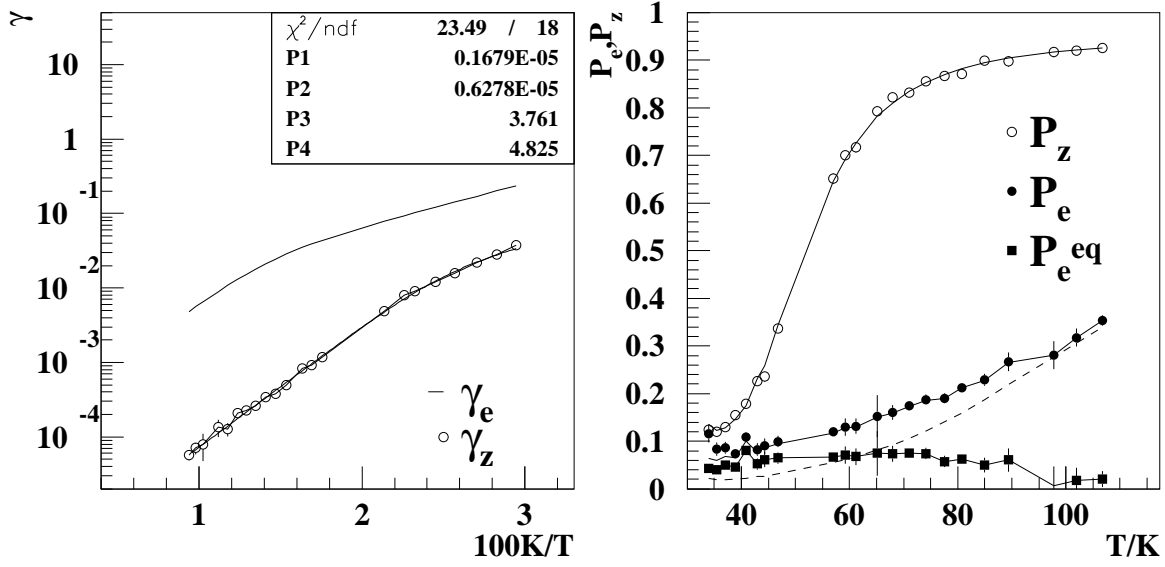


Fig. 6.7: Left: Fitted values of $\gamma_z(T)$ (symbols) and the corresponding prediction for $\gamma_e(T)$ (upper solid line). Right: Measured values of $P_z(P_z^{inj})$ (open circles) and $P_e(P_e^{inj})$ (filled circles). The electron polarization of thermal equilibrium P_e^{eq} , derived using γ_z and γ_e is shown as filled squares. The dashed line is the prediction for $P_e^{eq} = 0$. P_e^{eq} is approximately constant between 35 K and 80 K and vanishes at about 100 K.

One expects a value of P_e (in high field, where $\cos 2\theta \rightarrow 1$ and for $\mu_B B \ll k_b T$) given by

$$P_e^{eq} = -\tanh\left(\frac{\mu_B B}{k_b T}\right) \simeq -\frac{\mu_B B}{k_b T}. \quad (6.60)$$

This yields for a holding field of 335 mT a value of $P_e^{eq} = -0.56\%$ and can practically be neglected. Only in case of exchange interactions of the hydrogen radicals with the surface, much higher interaction energies E_{ex} and exchange fields $B_{ex} = \frac{E_{ex}}{gS\mu_B}$ are possible¹²⁶. If one takes the non-vanishing polarization in thermal equilibrium into account, the master equation has to be modified in the following way:

$$\dot{N}_a = \frac{1}{\tau_d} \left(N_a^{inj} - N_a + \rho_a \langle b \rangle \left(\sum_b W_{ab} (N_b - N_b^{eq}) - W_{ab} (N_a - N_a^{eq}) \right) + \dots \right), \quad (6.61)$$

The high field approximation yields in this case:

$$P_{e,z} = \frac{P_{e,z}^{inj} + \langle b_{eff} \rangle \gamma_{e,z} P_{e,z}^{eq}}{1 + \langle b_{eff} \rangle (\gamma_{e,z} + \gamma_{se})} \quad (6.62)$$

With the assumption, that $P_z^{eq} \simeq 0$ one can derive P_e^{eq} from the data of P_z and P_e , if one assumes, that the referred relaxation model delivers a correct description of the transition probabilities:

$$P_e^{eq} = \frac{P_e (1 + \langle b_{eff} \rangle (\gamma_e + \gamma_{se})) - P_e^{inj}}{\langle b_{eff} \rangle \gamma_e}. \quad (6.63)$$

¹²⁶The exchange interaction energy reaches several meV corresponding to several hundred Tesla in ferro magnets [Kit 86].

The result is shown in fig. 6.7. The measurement of $P_e(T)$ and $P_z(T)$ can be consistently described, if $P_e^{eq} \simeq 0.05$ at low temperatures. The obtained energy values are $E_b = 241 K/k_b = 20.8 meV$ and $E_j = 135 K/k_b = 11.6 meV$ ¹²⁷. One also obtains $\tau_c^0 \simeq 14.9\tau_s^0$ and with the estimated value of τ_c^0 in eq. 6.58 one obtains $\tau_s^0 \simeq 3.3 \cdot 10^{-12} sec$ and an average fluctuating field of $\sqrt{B_{loc}^2} \simeq 70.9 mT$.

The value of P_e^{eq} is in good agreement with the measured residual polarizations and delivers an estimation of the exchange field at 40 K: $|B_{ex}| = P_e^{eq}k_bT/\mu_B \simeq 3 T$. This value may not be interpreted directly as a measure of the fluctuating field - as it can only explain a non-zero P_e^{eq} , if it is basically static. The corresponding exchange energy is $E_{ex} = \mu_B B_{ex} \simeq 0.17 meV$.

This interpretation requires the existence of a magnetic ordering on the surface, which disappears at about 100 K as shown in fig. 6.7. For this ordering there are two potential explanations:

- Ferromagnetic impurities on the surface. In an investigation of pieces of a used cell, it was found, that irregular spots of the Drifilm coating were indeed contaminated with iron [Len 99]. It is therefore not unlikely, that the complete surface contains a dilution by iron of low concentration. These impurities could build ferromagnetic clusters on the surface.
- Blinc and co-workers found *super-paramagnetic clusters* in hydrogenated carbon films ($a - C : H$) [Bli 98]. They were able to measure a hysteresis loop using squids between 4 K and 20 K - the temperature range of the squid. Besides that, they found a deviation of the Curie law with electron spin resonance technique (ESR) below about 50 K. The Drifilm coating of the cell is also a film of hydrocarbons mixed with silicon oxides.

It is known, that thin films and fine particles can show magnetic properties, that differ significantly from the properties of bulk material. Srivastava for instance found strongly

¹²⁷These values are not very precise, as the change in the slope of $\ln \gamma_z$ vs. the reciprocal temperature is not very pronounced. The sum of both values is more precise and agrees reasonably well with the value of 30.26 meV as derived from the recombination measurements.

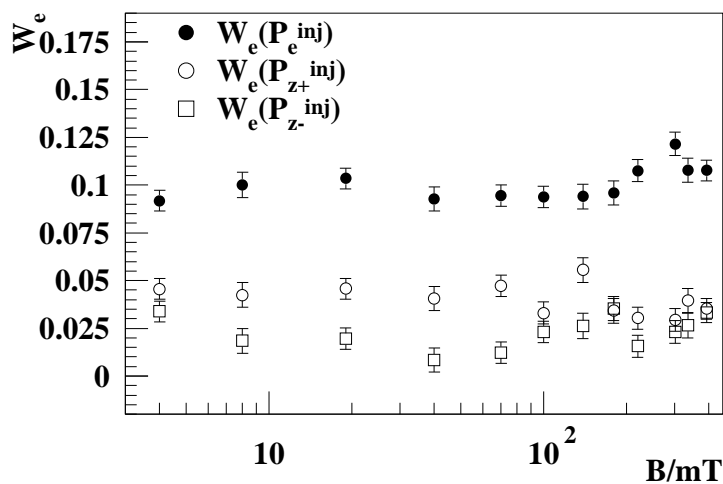


Fig. 6.8: Electronic asymmetry W_e (defined by $W_e = N_1 + N_2 - N_3 - N_4$) at 48 K vs. magnetic holding field for the injection modes P_e and $P_{z\pm}$. The measured data show no significant magnetic field dependence. If the residual asymmetry is caused by normal paramagnetism, it should be proportional to the external field. Only in case of spontaneous magnetization (ferromagnetism) and strong exchange fields, the asymmetry has no significant field dependence.

increased paramagnetic susceptibilities in fine Cr_2O_3 -clusters at low temperatures (below 50 . . . 100 K). The smaller these clusters are, the stronger the measured susceptibility χ_m [Jac 63].

In the verified presence of microscopic iron dust, the assumption of paramagnetic clusters on and/or within the surface is not unlikely. One might of course suspect, that usual paramagnetism can explain the behavior as well, if the exchange coupling is strong enough. But this is not the case. If the surface magnetization would be proportional to the external magnetic field, the asymmetry of the hyperfine population would drop, if the target holding field is ramped down. The measurement as shown in fig. 6.8 shows no significant dependence of the measured asymmetry on the external field. In addition, the measured temperature dependence of P_e^{eq} fits nicely to the expected behavior of the spontaneous magnetization of a ferromagnetic material with a Curie temperature T_c of about 95 K.

Whether the iron dust can already explain this behavior, or if it is reasonable to assume super-paramagnetic clusters within the Drifilm itself, is unclear. But the measurement of a positive electron polarization in case of a negative sum of injected and transferred polarization is a strong indication for a non vanishing equilibrium value P_e^{eq} .

6.7.2 Collection of Hydrogen Temperature Dependence Measurements

It was shown in fig. 6.5, that According to eq. 6.47, the temperature dependence of nuclear wall depolarization of hydrogen is - in high holding field and below saturation - given by the product $\tau_s\tau_c$ and can be written in the form of eq. 5.24:

$$\gamma_z(T) \propto \tau_s\tau_c = \gamma_z^0 \exp\left(\frac{E_b + E_j}{kT}\right). \quad (6.64)$$

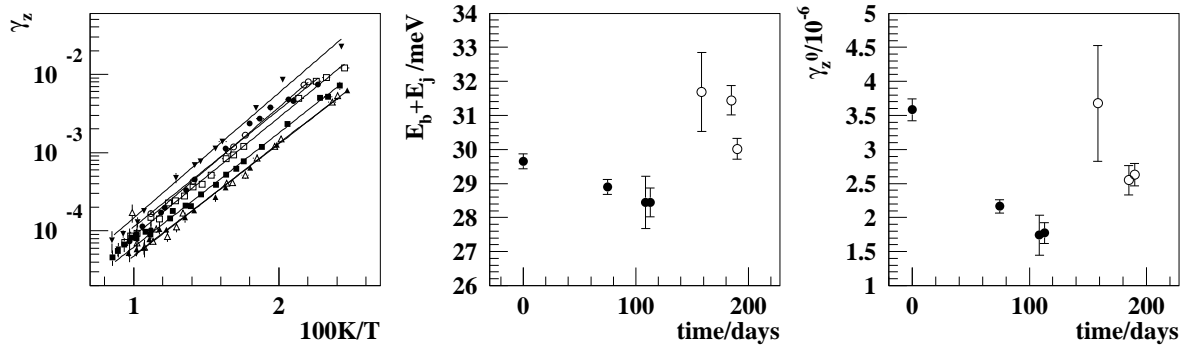
A collection of the measured values of γ_z^0 and $E_b + E_j$ is given in the table associated with fig. 6.9. The values of $E_b + E_j$ are surprisingly constant over a time period of several month, even though a weak drop of about 7% appears after 100 days of running. The new storage cell shows the same tendencies again. The value of γ_z^0 decreases by a factor of about 2 in the same time. This is likely related to the increasing fraction of the surface, that is covered by water, as it was concluded from the recombination measurements. The water layer increases the distance between the physisorbed atoms and the magnetic moments of unpaired electrons within the Drifilm coating.

6.8 The Magnetic Field Dependence of Hydrogen Spin Relaxation

The master equation (eq. 6.1) can - for hydrogen - be transformed in a way, that one obtains direct expressions for the hyperfine populations N_a as a function of the depolarization coefficients. This solution is described in app. D.5.3. Using this set of equations, the relaxation parameters can be fitted directly to the measured hyperfine populations. The transition probabilities are given by eq. 6.39, which can be written as

$$W_{ab} = \frac{A |C_{ab}|^2}{\sqrt{1 + B |C_{ab}|^2}}, \quad (6.65)$$

with the field independent parameters A and B for the assumption of a constant spectral density. Fig. 6.10 shows the result of a fit of eq. 6.1 to the data for the standard injection



Date	$E_b + E_j$ [meV]	$10^6 \cdot \gamma_z^0$
Mar 10	29.65 ± 0.22	3.58 ± 0.16
May 24	28.90 ± 0.22	2.16 ± 0.10
Jun 27	28.45 ± 0.77	1.74 ± 0.29
Jul 1	28.45 ± 0.43	1.77 ± 0.15
Aug 16	31.69 ± 1.16	3.68 ± 0.85
Sep 11	31.44 ± 0.44	2.55 ± 0.22
Sep 16	30.02 ± 0.30	2.63 ± 0.17

Fig. 6.9: Left: Arrhenius plot of $\gamma_z(T)$ for the 7 temperature scans of 1997. The parameters $E_b + E_j$ and γ_z^0 of the fitting model of eq. 5.24 are shown in the central and right graph respectively. Measurements with the first (second) storage cell are indicated by filled (open) symbols. The numerical values are listed in the table on the left.

modes of the ABS and a storage cell temperature of about 100 K. Besides the strength of the wall depolarization and spin exchange effect, also the efficiencies ε_{w13} and ε_{s24} of the ABS appendix transitions could be included into most of the fits. The symbols represent the measured hyperfine population, the lines the fitted results of the master equation. Fig. 6.11 shows the corresponding polarization values vs. the magnetic holding field for the same measurement. The highest measured field value corresponds to the working point of the HERMES target. Fig. 6.12 shows the hyperfine population in dependence on

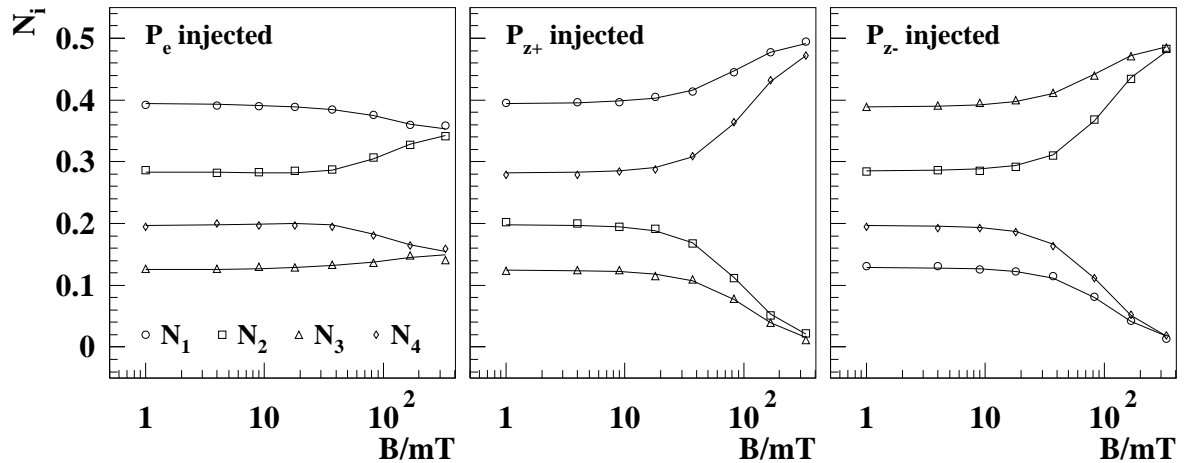


Fig. 6.10: Measured hyperfine population vs. magnetic holding field for hydrogen for the injection modes P_e (left), P_{z+} (middle) and P_{z-} (right). The measured values are given as symbols, while the lines show a fit using the solutions of eq. 6.1. The storage cell temperature was 102 K. The highest field value corresponds to the working point of the HERMES target and is 335 mT. The value of χ^2/N_f of this fit is 1.22 (statistical errors only).

No.	Date	T_{cell}/K	α_r^{TGA}	τ_d/τ_{se}	$\langle b \rangle A$	B	χ^2/N_f
1	May 27	102...105	0.93 ± 0.02	3.03 ± 0.04	1.01 ± 0.03	0.77 ± 0.12	1.22
2	Jul 10	102...104	0.98 ± 0.004	3.03 ± 0.042	1.01 ± 0.02	0.85 ± 0.1	1.53
3	Jul 17	94...96	0.982 ± 0.003	3.22 ± 0.04	0.95 ± 0.03	0.95 ± 0.12	2.1
4	Jul 24	85...95	0.975 ± 0.006	2.76 ± 0.08	1.43 ± 0.07	4.14 ± 0.5	3.16
5	Jul 31	265...250	0.52 ± 0.006	0.94 ± 0.015	0.33 ± 0.01	1.06 ± 0.2	1.65
6	Aug 16	250...255	0.755 ± 0.007	1.77 ± 0.024	0.36 ± 0.02	1.23 ± 0.2	1.47
7	Aug 20	100.65	0.99 ± 0.004	3.23 ± 0.056	1.07 ± 0.04	1.21 ± 0.16	1.73
9	Oct 21	~ 100	$0.5 \dots 0.8$	1.08 ± 0.04	3.48 ± 0.04	4.5 ± 0.15	11.6
11	Oct 23	~ 97	$0.94 \dots 0.97$	1.38 ± 0.03	4.06 ± 0.035	5.16 ± 0.12	14.4
12	Oct 23	~ 75	$0.93 \dots 0.96$	0.31 ± 0.06	10.96 ± 0.096	15.9 ± 0.4	7.6
13	Oct 24	~ 48	$0.82 \dots 0.86$	8.16 ± 0.3	901 ± 40	10780 ± 804	13.9

Tab. 6.1: Results of hydrogen relaxation measurements (magnetic field scans) as shown in fig. 6.10 for the '97 data taking period. The value of χ^2/N_f includes statistical errors only. The listed measurements of Oct. 1997 were performed after the storage cell was seriously damaged by the HERA beam.

the magnetic holding field, measured with a new storage cell at a storage cell temperature of about 250 K. As wall relaxation is relatively weak at higher temperatures (and with a new cell), the behavior is close to the theoretical behavior of pure spin exchange relaxation as shown by fig. D.4. Tab. 6.1 gives an overview of the fit results of the measurements, which were performed in 1997. The first measurement is shown in fig. 6.10 resp. fig. 6.11. The fitted ratio between diffusion time τ_d and the relaxation time τ_{se} allows the calculation of the central target density n_0 as described in sec. 6.8.2. The results of measurement 4 and 5 are less reliable: The temperature stabilization did not work properly during these measurements, so that the change of the magnet current lead to a (correlated) change of the storage cell temperature. Measurement no. 4 has the additional disadvantage, that the lowest magnetic field value was about 65 mT, which is still above the critical field of

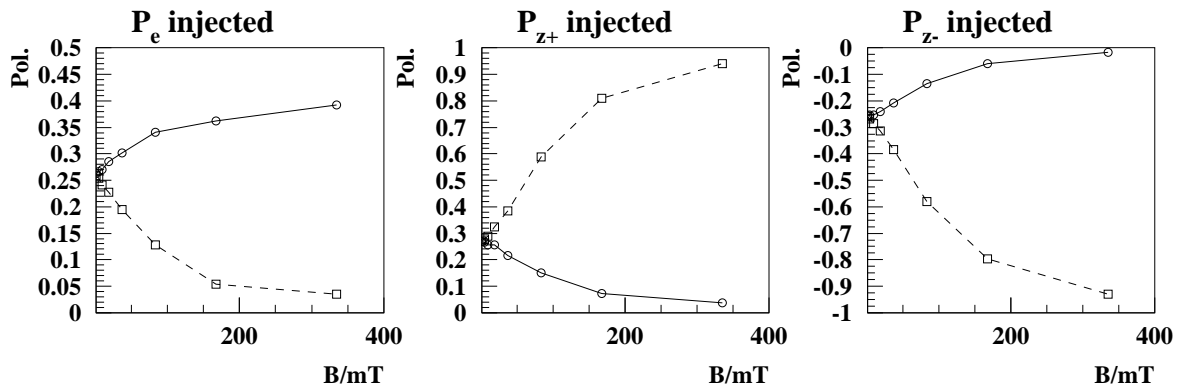


Fig. 6.11: Polarization vs. magnetic holding field for hydrogen for the injection modes P_e (left), P_{z+} (middle) and P_{z-} (right), calculated using the hyperfine population of fig. 6.10. P_e is plotted as a solid line, P_z as dashed line.

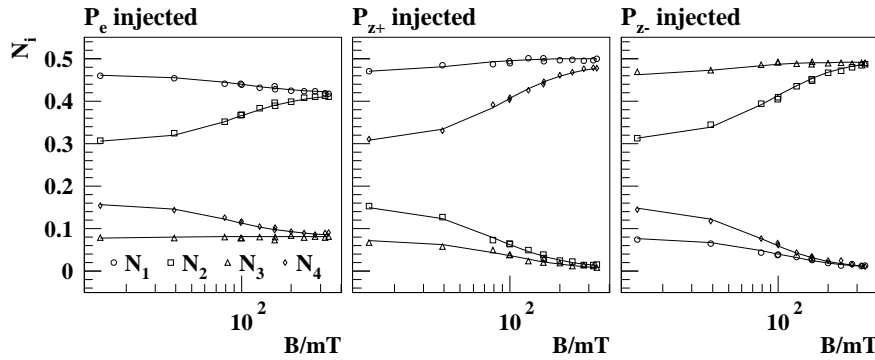


Fig. 6.12: Measured (symbols) and fitted (lines) hyperfine population vs. magnetic holding field for hydrogen with a new storage cell at about 255 K (see meas. no. 6 in tab. 6.1).

hydrogen. This lowers the reliability of the fitted parameters of the relaxation model for this measurement significantly.

After measurement No. 5, the storage cell was exchanged. An accidental HERA beam loss damaged the second storage cell in the end of 1997 and the measurements 9 to 13 were performed with this irradiated cell. The wall relaxation of these measurements is significantly increased at comparable temperatures. The measurements 8 and 10 are not used, as the atomic fraction was unstable during these measurements. The measurement 14, which was performed at low temperature (34 K), could not be fitted with the relaxation model. The measurement 9, 11, 12 and 13 have a bad χ^2/N_f ratio. This is likely to be related to the storage cell damage, which destroys the homogeneity of the wall coating. The corresponding fits are nevertheless informative and the theory describes the qualitative behavior of the relaxation reasonably well, as shown in fig. 6.13 and fig. 6.14. The influence of the saturation factor is given by the fitted value of B , which in this case is much larger than unity and has a strong influence on the functional form of the magnetic field dependence. The parameters A and B , which are listed in tab. 6.1 show¹²⁸ the expected behavior: Both parameters increase, if the temperature is lowered, $B \propto \tau_s^2$ stronger than $A \propto \tau_s \tau_c$. When the relaxation is weak, the hyperfine population of the $P_{z\pm}^{inj}$ states is - at high holding fields - only weakly field dependent. One says, the proton spin is *decoupled* from the electron spin. This changes in case of strong wall relaxation: The magnetic field dependence is stretched to higher field values. This is visible in fig. 6.13 and fig. 6.14, which show the measurements no. 12 and 13, performed at 75 and 48 K respectively: The maximal field of 335 mT is not strong enough to reach the region, where the

¹²⁸As there are only 3 comparable measurements at different (low) temperatures, a precise quantitative analysis is not presented.

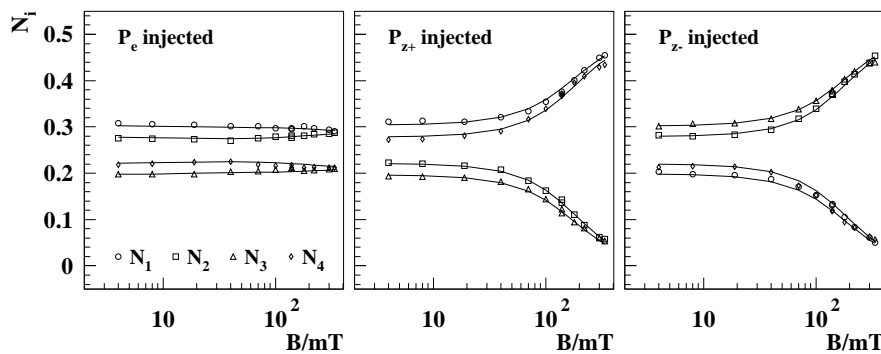


Fig. 6.13: Measured hyperfine population vs. magnetic holding field for hydrogen at a cell temperature of about 75 K (refer meas. no. 12 in tab. 6.1).

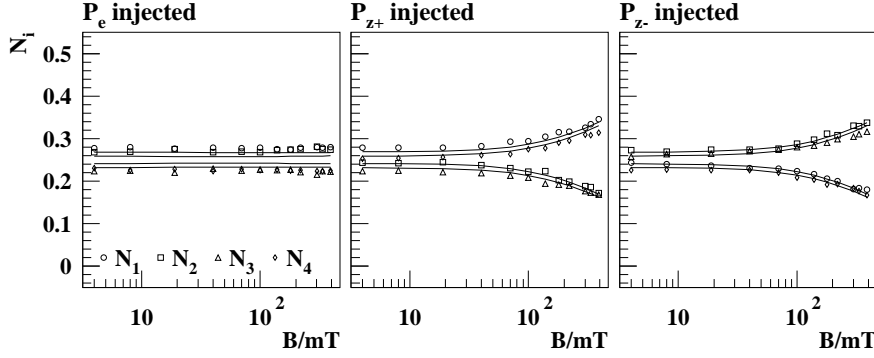


Fig. 6.14: Measured (symbols) and fitted (lines) hyperfine population vs. magnetic holding field for hydrogen at a cell temperature of about 48 K (refer to meas. No. 13 in tab. 6.1).

hyperfine population is (nearly) independent from small variations of the holding field. As a consequence, it is not possible to obtain the ABS efficiencies from these measurements. Both efficiencies were - for measurements no. 9,11,12 and 13 - assumed to be 98 %. The results for ε_{w13} and ε_{s24} of the measurements No. 1 to 7 are listed in tab. 6.2. Even at the lowest temperatures, the good over all agreement with the measured data legitimates the assumption of a constant spectral density.

6.8.1 ABS Efficiencies and Injected Polarization for Hydrogen

If one ignores the measurement no 4, the results of the relaxation measurements as listed in tab. 6.2 yield the following average transitions efficiencies of the ABS:

$$\begin{aligned}\varepsilon_{w13} &= 0.9794 \pm 0.0005 \\ \varepsilon_{s24} &= 0.9780 \pm 0.0007\end{aligned}\tag{6.66}$$

The injected hyperfine population is given by eq. 3.5. The polarization can then be calculated using eq. 2.5 with the formula for $\cos 2\theta$ as given in tab. B.1. The calculation yields for a target holding field of 335 mT:

$$\begin{aligned}P_{z+}^{inj} &= \frac{1}{2}(1 - \cos 2\theta) + \varepsilon_{s24} \cos 2\theta = 0.9726 \pm 0.0005 \\ P_{z-}^{inj} &= \frac{1}{2}(1 - \cos 2\theta) - \varepsilon_{w13} = -0.9738 \pm 0.0007.\end{aligned}\tag{6.67}$$

The uncertainties of ε_{w13} and ε_{s24} have been calculated by the statistical uncertainty of the relaxation measurements only.

6.8.2 Determination of the Hydrogen Density from the Spin Exchange Effect

For strong wall relaxation one expects, that the difference between the pure and the mixed states gets less pronounced. This is visible in fig. 6.13, where the difference almost vanishes. In this case, the determination of τ_{se} is of low precision and the uncertainty reaches values of 20 % and more (see tab. 6.1). A strong difference between mixed and pure states in case of low wall relaxation is shown in fig. 6.12, which was performed with a new storage cell at high temperature (measurement No. 6). The measured magnetic field dependence of the hyperfine populations in this case is close to the theoretical behavior of pure spin exchange interaction as shown in fig. D.4 and the spin exchange relaxation time τ_{se} is obtained by the relaxation model with high precision. If the spin exchange cross section is known, the target atomic density can be derived or vice versa.

No.	ε_{w13} [%]	ε_{s24} [%]	σ_{se}	η_{se}	n_0	ϕ_{TGA}	ρ_a^{BRP}
1	98.1 ± 0.2	97.8 ± 0.35	23.4	3.09 ± 0.05	3.71 ± 0.06	54.0 ± 0.9	0.9 ± 0.02
2	98.1 ± 0.13	98.0 ± 0.17	23.4	3.07 ± 0.04	3.70 ± 0.048	49.9 ± 0.2	0.97 ± 0.014
3	97.9 ± 0.12	97.8 ± 0.15	23.2	3.14 ± 0.04	3.81 ± 0.048	50.4 ± 0.12	0.99 ± 0.014
4	98.9 ± 0.2	99.3 ± 0.28	22.95	2.63 ± 0.1	3.22 ± 0.123	49.8 ± 0.25	0.85 ± 0.034
5	97.6 ± 0.13	97.5 ± 0.16	23.75	1.5 ± 0.03	1.77 ± 0.036	45.1 ± 0.35	0.52 ± 0.012
6	98.3 ± 0.12	98.1 ± 0.15	23.75	2.82 ± 0.04	3.34 ± 0.048	51.8 ± 0.31	0.85 ± 0.013
7	97.7 ± 0.13	97.6 ± 0.16	23.4	3.24 ± 0.06	3.90 ± 0.072	50.6 ± 0.17	1.01 ± 0.018

Tab. 6.2: Results of the hydrogen relaxation measurements: The ABS transition efficiencies and spin exchange parameters. More results of the same measurements are listed in tab. 6.1. The value of σ_{se} is taken from Allison [All 72] in units 10^{-16} cm^2 and η_{se} is defined as τ_d/τ_{se} , normalized to a storage cell temperature of 100 K: $\eta_{se} = \tau_d/\tau_{se} \sqrt{T/100 \text{ K}}$. The atomic density in the storage cell center n_0 (normalized to a storage cell temperature of 100 K) is given in units of $10^{12} \text{ atoms cm}^{-3}$. The error bars are of statistical nature. ϕ_{TGA} is the total flux, measured with the TGA in kHz/mA , which is proportional to the ABS intensity. ρ_a^{BRP} was obtained by the atomic density n_0 , normalized to a flux of $\phi_{TGA} = 50 \text{ kHz/mA}$ and scaled such, that $\rho_a^{BRP} \rightarrow 1$ for $\alpha_{TGA} \rightarrow 1$. The scaling factor is $4.13 \cdot 10^{12} \text{ atoms cm}^{-3}$ at a TGA flux of $\phi^{TGA} = 50 \text{ kHz/mA}$ corresponding to $8.25 \cdot 10^{11} \text{ atoms}$ at $\phi^{TGA} = 1 \text{ kHz/mA}$. The details of the calculation are explained in sec. 6.8.2.

In order to extract the central atomic density by the spin exchange effect, one may use eq. 6.9: The correlation factor ρ_c was introduced in sec. 6.3 and is defined by eq. C.105 in app. C.6.2. For the atomic sample of the BRP, the molecular flow simulation resulted $\rho_c = 1.093 \pm 0.015$. One obtains for the average density of hydrogen atoms:

$$\langle n \rangle = \frac{\tau_d}{\tau_{se}} \frac{1}{\sqrt{2} \rho_c L_d \sigma_{se}}. \quad (6.68)$$

In case of low recombination ($\alpha_{TGA} \geq 0.97$), one can assume, that for the average atomic density $\langle n \rangle = \frac{1}{2} n_0$ holds and the integrated areal proton density¹²⁹ D_t or *target thickness* is then given by:

$$D_t = 2L \langle n \rangle, \quad (6.69)$$

where L is the length of one wing of the storage cell (20 cm). The results for τ_d/τ_{se} and n_0 including the statistical uncertainty are listed in tab. 6.1 and tab. 6.2.

Even though there is no strong reason for this relations, the measurement of fig. 6.3 shows, that the polarization loss by spin exchange is proportional to α_r^{TGA} . The measurement of fig. 4.3 shows under the same conditions, that $\alpha_r^{TGA} \propto \rho_a^{BRP}$, so that it is reasonable to assume, that the normalized atomic density ρ_a^{BRP} is proportional to the atomic density in the storage cell center n_0 as measured by the spin exchange effect.

A measured value of n_0 , that was obtained from a measurement, for which α_r^{TGA} is close to one ($\alpha_r^{TGA} \rightarrow 1 \Rightarrow \rho_a^{BRP} \rightarrow 1$), was used to estimate the normalization of ρ_a^{BRP} . The values of ρ_a^{BRP} obtained by the estimated normalization are listed in tab. 6.2 are compared to the values of α_r^{TGA} of tab. 6.1 in fig. 6.15. The new storage cell (measurements no. 6 and 7) is in agreement with the Monte Carlo (MC) predictions for a homogeneous

¹²⁹More precisely: The areal density of protons in atoms.

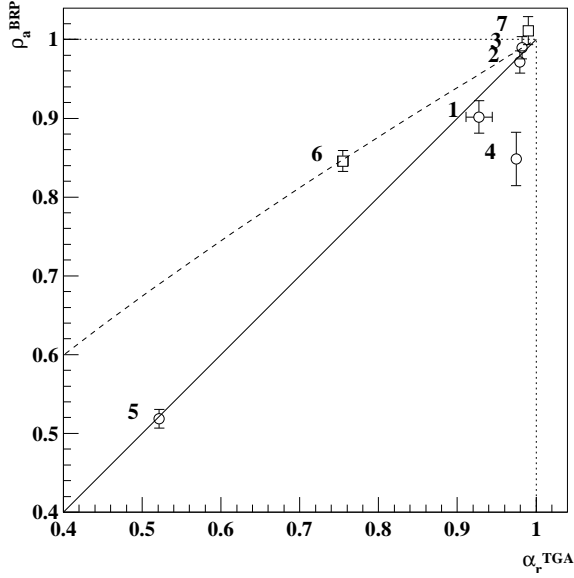


Fig. 6.15: Comparison between the density results of the relaxation measurements and the measured atomic fraction for the measurements No. 1 to 7 from tab. 6.1 and tab. 6.2. The number of the measurement is printed close to the corresponding data point. The solid line is the diagonal, where $\alpha_r^{TGA} = \rho_a^{BRP}$. The dotted lines are the mathematical limits and the dashed line is the a prediction calculated with the results of a molecular flow simulation for a completely homogeneous storage cell surface. The circles represent measurements with the first storage cell in 1997, the squares two measurements shortly after the installation of a new storage cell.

storage cell, while measurement 5, taken after a several weeks of target operation in the HERA ring disagrees with this prediction. The fact, that this data point is located on the diagonal, indicates that most recombination occurs in the beam tube, while recombination in sample- and extension tube - which would have a stronger influence on the TGA sample than on the BRP sample - plays a minor role. As already reasoned above, measurement no. 4 can be ignored. The results are in agreement with the ones shown in fig. 4.4. They indicate again, that - now measured at high temperatures and with a completely different technique - the recombination probability of the sample tube surface γ_r^{ST} is much smaller than for the beam tube γ_r^{BT} ($\gamma_r^{ST} \ll \gamma_r^{BT}$) in case of the first storage cell of the 1997 data taking period, and $\gamma_r^{ST} \simeq \gamma_r^{BT}$ for the second.

Besides the analysis of the sampling properties, the absolute value of the derived atomic density can be compared to the target density measured by the HERMES luminosity monitor. The expected *total* target density at a flux $\phi_{TGA} = 50.4 \text{ kHz}$ (3rd measurement) is $\langle n \rangle = 1.855 \cdot 10^{12} \text{ cm}^{-3}$ (see sec. 3.7). The spin relaxation measurements yields an average *atomic* density of $\langle n \rangle_a = 1.905 \cdot 10^{12} \text{ cm}^{-3}$ as listed in tab. 6.2. As the measurement of the luminosity monitor includes also molecular contributions of ballistic flow and rest gas (see sec. 3.5.4), this value has to be multiplied by $\alpha_0 \simeq 0.96$, if one wants to compare it to the *atomic* density obtained from spin exchange relaxation. The comparison yields with this correction a relative difference of about 7%. As the calibration uncertainty of the Lumi is about 6%, both results are in agreement. However, it can not be used for a significantly improved measurement of σ_{se} . But it should be mentioned, that the statistical precision of the ratio τ_d/τ_{se} is 1.5% only. One can assume, that the systematical uncertainty of the BRP measurement is - in case of low recombination - of about the same size. The value of σ_{se} could therefore be measured to a high precision with the setup of the HERMES target - provided, an independent density measurement of high precision is available.

It is worth mentioning, that measured atomic target density corresponds to a target thickness of $D_t = 7.42 \cdot 10^{13} \text{ nucl cm}^{-2}$. As the conductance of the storage cell for atomic

hydrogen is $17380 \text{ cm}^3 \text{ s}^{-1}$ at a storage cell temperature of 100 K (see tab. F.2), the calculation yields an injected flux of

$$\Phi^{ABS} = 2 \langle n \rangle C_{tot} = 6.62 \cdot 10^{16} \text{ s}^{-1}, \quad (6.70)$$

which is in good agreement to a previous compression tube measurement of $6.4 \cdot 10^{16} \text{ s}^{-1}$ [Stw 97].

6.9 Measurement and Analysis of the Transition Spectra

It will be shown in this section, that the master equation (eq. 6.1) can be used to calculate the individual transition probabilities W_{ab} of each relaxational transition from the measured hyperfine population numbers - if the following assumptions are correct:

- Possible effect of super-paramagnetic clusters can be neglected at higher temperatures. The surface is unpolarized.
- The relaxation is not dominated by the interaction between adsorbed atoms, but by the interaction of the adsorbed atoms with the wall. This can assumed to be true, if the surface coverage is low.
- $\overline{W_{b \rightarrow a}}$ is independent from the injected hyperfine population.
- The transition probabilities are symmetric: $\overline{W_{b \rightarrow a}} = \overline{W_{a \rightarrow b}} = W_{ab}$.
- Correlated multi photon transitions can be neglected.

If these assumptions are - under the typical HERMES conditions - true, then it is possible to use the master equations (eq. 6.1) for several injection modes and magnetic holding field values as a linear (and over-determined) system of equations for the transition probabilities W_{ab} - if the injected hyperfine population is known. At any given value of the magnetic holding field and using the hydrogen injection modes P_e , P_{z+} and P_{z-} (see tab. 3.1), one has 12 equations and 5 unknown transition probabilities. For a simpler analysis, we define the *spectrum* $J_{ab}(\omega_{ab})$ of a relaxational transition. The spectrum is the ratio of the transition probabilities, that are required to match the measured hyperfine populations and the squared reduced matrix elements:

$$J_{ab}(\omega_{ab}) = \frac{W_{ab}}{|C_{ab}|^2}. \quad (6.71)$$

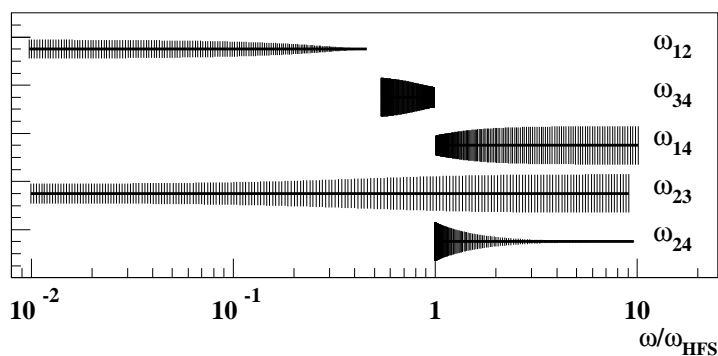


Fig. 6.16: Frequency range of hydrogen relaxation transitions for holding field values within $0.7 \dots 350 \text{ mT}$. The size of the reduced matrix elements C_{ab} is indicated by vertical lines. The 2–3 transition has the widest range and a reasonably large reduced matrix element over the whole range.

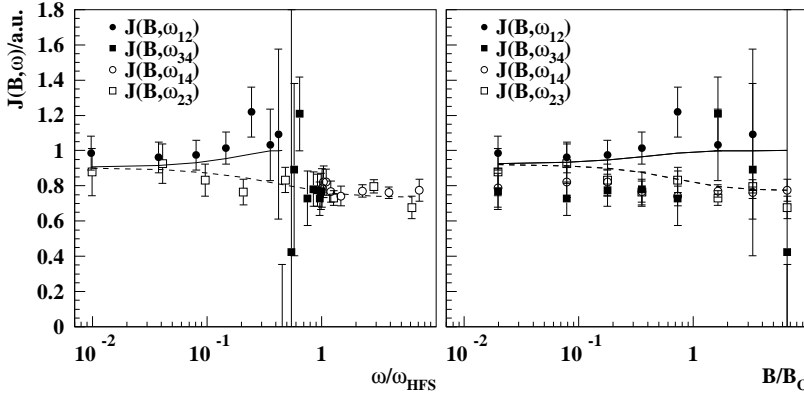


Fig. 6.17: Measured spectra of the hydrogen π -transitions at a storage cell temperature of about 100 K. In the left graph, the spectra are plotted vs. the transition frequency in the right graph vs. the target holding field. The solid line is the prediction by the saturation prefactor for $J(B, \omega_{12})$ and the dashed line for $J(B, \omega_{23})$.

The spectrum is not identical to the spectral density, but it has the advantage, that it can be determined directly from the measured data, as the squared reduced matrix elements $|C_{ab}|^2$ depend on the magnetic holding field only. The spin exchange relaxation time τ_{se} is the same for all magnetic field values, as the magnetic field dependence of the spin exchange reaction is expressed by the (well known) tensor M_{ab}^c in eq. 6.1. Even if one takes the normalization of the hyperfine population into account ($\sum_a N_a = 1$), one has still 9 equations and 5 unknowns per field value. This relation is even better in case of deuterium, as there are 11 different standard injection modes. With the definition

$$\begin{aligned}
 W_{12} &= W_{21} = w_1 & W_{34} &= W_{43} = w_2 \\
 W_{14} &= W_{41} = w_3 & W_{23} &= W_{32} = w_4 \\
 W_{24} &= W_{42} = w_5
 \end{aligned} \tag{6.72}$$

the equations for hydrogen in *one* injection mode are:

$$\begin{aligned}
 0 &= N_1^{inj} - N_1 + \frac{\tau_d}{\tau_{se}} \sum_{b,c} M_{bc}^1 N_b N_c + \frac{\tau_d}{\tau_f} \{w_1(N_2 - N_1) + w_3(N_4 - N_1)\} \\
 0 &= N_2^{inj} - N_2 + \frac{\tau_d}{\tau_{se}} \sum_{b,c} M_{bc}^2 N_b N_c + \frac{\tau_d}{\tau_f} \{w_1(N_1 - N_2) + w_4(N_3 - N_2) + w_5(N_4 - N_2)\} \\
 0 &= N_3^{inj} - N_3 + \frac{\tau_d}{\tau_{se}} \sum_{b,c} M_{bc}^3 N_b N_c + \frac{\tau_d}{\tau_f} \{w_2(N_4 - N_3) + w_4(N_2 - N_3)\} \\
 0 &= N_4^{inj} - N_4 + \frac{\tau_d}{\tau_{se}} \sum_{b,c} M_{bc}^4 N_b N_c + \frac{\tau_d}{\tau_f} \{w_2(N_3 - N_4) + w_3(N_1 - N_4) + w_5(N_2 - N_4)\}
 \end{aligned} \tag{6.73}$$

All values - except w_i and τ_{se} are either known or measured directly, so that the equation system can be solved in case of hydrogen. In case of deuterium, the injected hyperfine populations are less well known, so that an iteration process had to be performed, which will be described in sec. 6.10.2.

6.9.1 The Spectrum of Hydrogen Spin Relaxation

The quality of the determined spectrum depends on whether the corresponding transitions are strong enough to cause a significant change in the hyperfine population. Especially in case of a high holding field and nuclear transitions, which are suppressed by decoupling, this condition is not always fulfilled. Fig. 6.16 shows the scope of the transition frequencies for the HERMES holding field range (0... 350 mT). The measured spectra for all hydrogen transitions at a storage cell temperature of 102 K, which corresponds to meas. no. 1 in

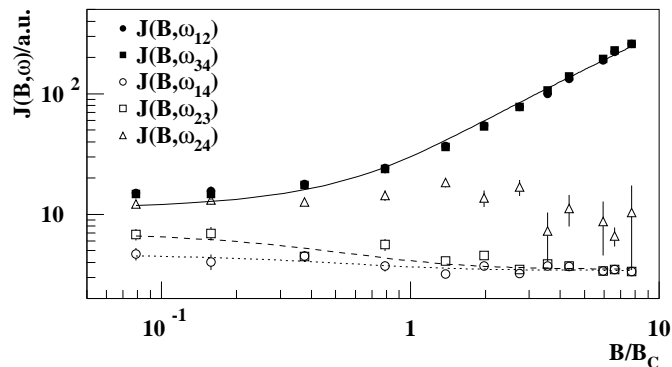


Fig. 6.18: Measured spectra of hydrogen at a storage cell temperature of 48 K. The symbols for the $1 \leftrightarrow 2$ transition and the $3 \leftrightarrow 4$ transition are on top of each other. The lines are fits to the data with the saturation prefactor, the solid line for the 1-2 and 3-4 transitions, the dashed line for the 2-3 transitions and the dotted line for the 1-4 transition. The behavior of the 2-4 transition (triangles) is discussed in the text.

tab. 6.1, are shown in fig. 6.17. The frequency (resp. field) dependence is weak compared to the statistical error and the behavior of the spin relaxation can be described by a constant spectral density, respectively by the constant low frequency limit of it. The remaining weak decrease of the transition probabilities of the electronic transitions at higher holding fields and of the proton transitions at lower holding field is described by the factor $(\sqrt{1 + \Omega_{ab}^2 \tau_s^2})^{-1}$ in eq. 6.39. The agreement between master equation model and the data is shown in fig. 6.10.

Also at lower temperatures, the transition spectra can be reasonably well described by this factor. Fig. 6.18 shows a measurement of the spectra at about 48 K cell temperature. As already presumed in context with the temperature dependence, a measurable frequency dependence of the electron transitions $1 \leftrightarrow 4$ and $2 \leftrightarrow 3$ is not observed. The increase of the nuclear spectra in a high holding field can be described and understood by the saturation factor, which plays only a minor role in case of the electron resonances, as the matrix elements of the electron transitions ($\cos^2 \theta$) are less field dependent.

Besides the fact, that the electron transitions are weaker than the proton transitions¹³⁰, which was already discussed in sec. 6.7, also the 1-4 and 2-3 transition seem to differ by some amount. Especially in low field, the 2-3 transition seems to be slightly stronger than the 1-4 transition. Spin relaxation was up to now treated in analogy to a spin- $\frac{1}{2}$ system, which is expected to be a good approximation in the high field limit, where the spin of proton and electron are decoupled. In the low field limit, this approximation is somewhat unprecise, as the spins are coupled and at least the upper three hyperfine states would in principle require a description as a triplet system. In case of such an ideal triplet, the transition probabilities are increased by a factor of 2 as described in app. D.2.3. But also this treatment is not exact, as an ideal multiplet has equally distanced energy levels - independent of the external field. In case of the hydrogen hyperfine structure, the transition frequencies are even in low fields not equally spaced and the fluctuations of the local field will tend to reduce the effect, as they smear out the position of the resonance over a certain range. This smearing will tend to reduce multiplet effects, as the atom 'sees' only for a fraction of the time a field, which is close enough to zero. One may understand this effect in analogy to the so-called *motional narrowing* of the line width in nuclear magnetic resonance (NMR).

¹³⁰In vanishing field, all π -transitions are expected to have the same strength. As shown in fig. 6.18, the electron transitions are slightly weaker than the proton transitions.

The nearly field independent behavior of the σ -transition $2 \leftrightarrow 4$ can be understood by a second contribution to the resonance width - the jitter of the resonance frequency due to the fluctuations in the z -component of the local fluctuating field. This contribution to the resonance width is given by

$$\Delta\omega = \frac{d\omega_{ab}}{dB} \Delta b_z, \quad (6.74)$$

where Δb_z is the z -component of the local fluctuating field. For the nuclear transitions of hydrogen the calculation yields $\Delta\omega = \omega_{HFS} \sin^2 \theta \Delta b_z / B_C$ and for electron transitions $\Delta\omega = \omega_{HFS} \cos^2 \theta \Delta b_z / B_C$. For the σ -transition, one obtains $\Delta\omega = \omega_{HFS} \cos 2\theta \Delta b_z / B_C$. If this contribution is added squared to the total width, it leads to a field independent resonance width of the σ -transition and therefore to a field independent saturation factor and spectrum as it was measured (see fig. 6.18).

But even though this is a possible explanation of the measurement, it should be taken into account, that the determination of the σ -transition probability is less reliable than for other transitions, as its effect is similar to the effect of spin exchange collisions, which also tend to reduce the difference in the hyperfine population of the states $|2\rangle$ and $|4\rangle$. Also the magnetic field dependence is the same: Both effects are proportional to $\sin^2 2\theta$, so that it is difficult to distinguish between them. Another problem is the referred possibility of a positive electron polarization in thermal equilibrium, which would likely influence the determination of the 2-4 transition spectrum. In all other measurements, this additional contribution to the resonance width was negligible. If it is included into the analysis of the relaxation measurements of sec. 6.8, some fits result a slightly lower, others a slightly higher χ^2 -value. The ratio τ_d/τ_{se} would be about 1% higher, if this additional contribution to the line width is taken into account.

6.10 Measurements of Deuterium Spin Relaxation

The spin relaxation theory of deuterium is in all items analogue to the hydrogen theory, represented by eq. 6.1 - if it is still allowed to treat the relaxation by the analogy to a two state system. This of course is questionable - at least in case of the nuclear transitions, as they have to be understood as transitions within a triplet in the high field limit. In the low field limit, the upper 4 states build a quadruplet and the lower 2 states a duplet. Additionally, there are (in contrast to hydrogen) 2 pairs of hyperfine transitions, which have exactly the same transition frequency, which are the 2-3 and 5-6 transition and consequently also the 2-5 and 3-6 transition. One therefore can not expect, that the analogy to a two state system will work without modifications. This difference can be measured by the analysis of the spectrum, which is by definition proportional to the ratio of the measured and the calculated transition probabilities, as they are given by first order perturbation theory. This will be done in sec. 6.10.3.

6.10.1 The Temperature Dependence of Deuterium Relaxation Measurements

Fig. 6.19 shows the first measurement of the temperature dependence of the deuterium polarization, measured at a holding field of 111 mT . It was performed with the first storage cell of 1997 in march 1998 and delivered approximately the same behavior of γ_e and γ_z , as it was shown in fig. 6.5 for hydrogen. From the slope of γ_z and $\gamma_{zz\pm}$ in the Arrhenius plot

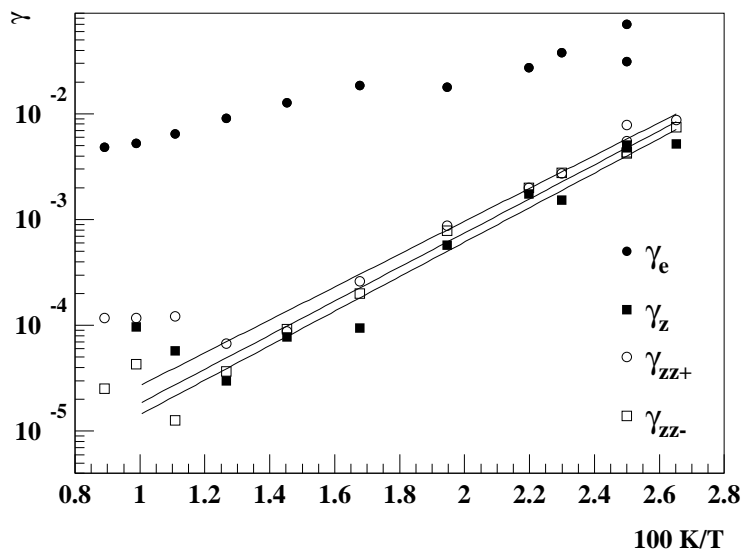


Fig. 6.19: First measurement of the temperature dependence of deuterium spin relaxation with the first storage cell of 1997, which had already been used for the hydrogen measurements. The error bars are not shown. The global behavior of γ_e , γ_z and $\gamma_{zz\pm}$ corresponds surprisingly well to the hydrogen measurements as shown in fig. 6.5. The lines show the Arrhenius fits to γ_z and $\gamma_{zz\pm}$. The slope delivers the sum of E_b and E_j .

one obtains $E_b + E_j \simeq 31 \text{ meV}^{131}$. This measurement gives confidence, that the binding energy E_b and the activation energy for jump diffusion E_j do not differ significantly between hydrogen and deuterium for the same surface.

Later deuterium relaxation measurements were performed with a new storage cell, which had a thicker Drifilm coating [Wise 99]. Tab. 6.3 shows some results for the 1998 storage cell. The energy sum $E_b + E_j$ was found to be typically around 20 meV and is significantly reduced compared to the value obtained in fig. 6.19. Fig. 6.20 shows the value of γ_e of measurement No. 4 of tab. 6.3. The difference to the measurements of fig. 6.5 and fig. 6.19 is obvious: As soon, as γ_e starts to saturate, it stays practically constant. This can be understood by a temperature independent value of τ_c and therefore a vanishing activation energy for surface jump diffusion $E_j \simeq 0$. If this interpretation is correct, then one finds a binding energy of about $E_b \simeq 22 \text{ meV}$, which is a value close to the hydrogen results. The difference between the storage cells of 1997 and 1998 with respect to spin relaxation is then given by a different value of E_j^{132} . This means, that the Drifilm coating of the 1998 storage cell is not only thicker, but is in that sense more 'flat', that there are much smaller barriers between neighboring sites. Narrower potential valleys with an increased oscillation frequency and ground state levels close to the barrier height between neighboring sites would lead to a situation, in which essentially no localized states exist.

¹³¹The evaluation is just a rough estimate, as the results are neither corrected for spin exchange nor for the influence of the atomic fraction.

¹³²And potentially by a difference in the strength of the fluctuating field $\sqrt{\langle B_{loc}^2 \rangle}$.

No	Date	T_e [K]	$E_b + E_j$ [meV]
1	Aug 8 '98	256 ± 9	22 ± 0.8
2	Aug 12 '98	223 ± 8	19.2 ± 0.7
3	Aug 27 '98	209 ± 18	18 ± 1.55
4	Oct 31 '98	252 ± 2.5	21.7 ± 0.2

Tab. 6.3: Results of spin relaxation measurements with deuterium vs. temperature. The energy sum $E_b + E_j$ for the storage cell of 1998 is reduced by about 30 % compared to the storage cell of 1997.

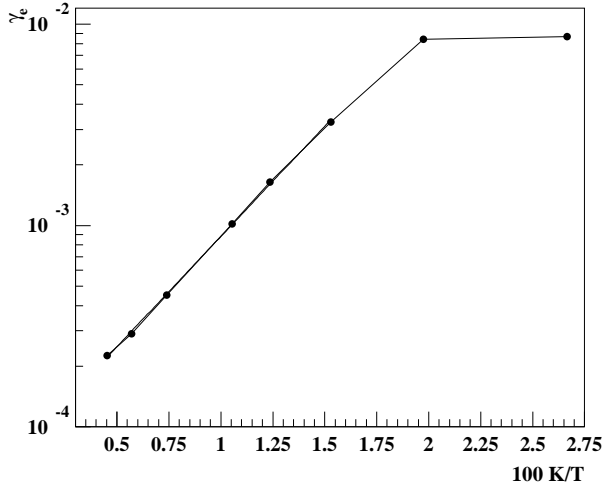


Fig. 6.20: Measurement of the temperature dependence of γ_e with the storage cell of 1998 (Arrhenius plot). The slope of $\ln \gamma_e$ vs. the inverse temperature delivers $E_b + E_j \simeq 21.7 \text{ meV}$. As γ_e stays constant as soon as the saturation starts, one can conclude, that $\tau_c \simeq \text{const}$ and therefore $E_j \simeq 0$ holds.

Under such circumstances the correlation time is given by the average velocity of the atoms parallel to the surface and by the distance between neighboring sites.

The depolarization strength as shown in fig. 6.20 can - at higher temperatures - be parameterized as

$$\gamma_e = 0.7 \cdot 10^{-4} e^{253 K/T}, \quad (6.75)$$

so that at the extrapolated value at the lowest measured temperature of $T = 37.4 \text{ K}$ would be $\gamma_e = 0.062$. Instead, the measurement delivers $\gamma_e = 0.0087$, so that the saturation must have reduced γ_e by a factor of about $\sqrt{1 + \Omega^2 \tau_s^2} = 7.16$. From this, one finds, that

$$\Omega^2 \tau_s^2 = \frac{\omega_{HFS}^2 (\tau_s^0)^2 \langle B_{loc}^2 \rangle}{B_C^2} e^{506 K/37.4 K} \simeq 50. \quad (6.76)$$

If one assumes again a high temperature limit $\tau_s^0 = 7.7 \cdot 10^{-12} \text{ s}$ (see eq. 6.58), one obtains for the average square of the local fluctuating field $\frac{\langle B_{loc}^2 \rangle}{B_C^2} \simeq 0.265$ and therefore

$$\sqrt{\langle B_{loc}^2 \rangle} \simeq 6 \text{ mT}. \quad (6.77)$$

This value is much smaller than the estimated value obtained by the hydrogen measurements and it indicates either a surface with significantly less unpaired electrons or with a smaller high temperature limit τ_s^0 for the storage cell of 1998 than for the storage cells of 1997.

6.10.2 The Injected Polarization in Deuterium Running

In contrast to the hydrogen relaxation measurements, a complete data set of spin relaxation measurements vs. holding field for all 11 injection modes is available at temperatures between 37.5 and 212 K, measured within three days in October 1998. The hyperfine population was measured three times at each temperature and magnetic holding field value for all injection modes. The atomic fraction kept well above 0.9 during these measurements at all temperatures. No HERA beam was injected over this period. The values of γ_e shown in fig. 6.20 were obtained in this way. A least square fit algorithm, which is described in

ε_{s26}	$97.3 \pm 0.14 \%$	ε_{t26}	$91.4 \pm 0.12 \%$
ε_{s35}	$97.3 \pm 0.20 \%$	ε_{v14r13}	$98.0 \pm 0.13 \%$
ε_{t35}	$93.7 \pm 0.14 \%$	ε_{v14r24}	$100 \pm 2.9 \%$
ε_{w14r56}	$98.2 \pm 2.58 \%$	ε_{v14r14}	$91.2 \pm 0.16 \%$
ε_{m14r12}	$98.8 \pm 0.28 \%$	ε_{v14r56}	$100 \pm 1.2 \%$
ε_{m14r23}	$99.3 \pm 0.27 \%$	ε_{m34r34}	$96.1 \pm 0.15 \%$
ε_{m14r34}	$98.2 \pm 0.39 \%$		

Tab. 6.4: Left table: Fitted transition efficiencies of deuterium for the first five injection modes of tab. 3.2. The claimed uncertainties were calculated using the statistical uncertainties of the measured hyperfine populations. The table on the right side lists fitted efficiencies for the 6 single state injection modes of tab. 3.2 under the assumption, that the efficiencies of the left table are correct.

app. H, was used to match the hyperfine population in dependence of the holding field separately for each temperature. The dependence of the injected hyperfine population on the transition efficiencies of the ABS was part of each fit. The transmission probabilities σ_{ab} of the ABS sextupole system were assumed to match the simulated results of tab. 3.3. The modeling of the ABS WFT units was performed using 6 separate efficiencies as described in app. B.2.5, where the efficiencies of the single-photon transitions were assumed to be 100% ¹³³. The spin exchange collision rate, respectively $1/\tau_{se}$ was balanced between the different injection modes scaled with the measured total intensity I_{tot} of the BRP¹³⁴. For wall collisions, the spectral density was first assumed to be constant over the complete frequency range. But it was found, that the hyperfine populations at low holding fields could not be described properly by the relaxation model as shown in fig. A.1. A measurement of the spectrum of the transitions was therefore required to investigate the behavior of the transition probabilities. This measurement had to be worked out iteratively, as the determination of the injected polarization is more complex for deuterium than for hydrogen. This is a consequence of the transition units between the ABS sextupole subsystems as well as of the fact, that several transition units have to be operated simultaneously for most injection modes listed in tab. 3.2. The knowledge of the injected hyperfine population however is required for a precise determination of the spectrum. Insofar, the injected polarization had first to be estimated. The general difficulties in the analysis of both - the injected hyperfine population and the wall depolarization - results of course a certain systematical uncertainty respectively correlation in the determination of both results.

The next step after the determination of the injected hyperfine population was the investigation of the spectrum, as it was found, that the assumption of a constant spectrum does not lead to a satisfactory agreement between the measured and modeled hyperfine populations. As already mentioned, this had to be expected, as the transition probabilities were calculated for a two state system. But the deuteron spin is $I = 1$ ¹³⁵ and the structure of the the Hamilton operator is - with respect to the nuclear transitions and including the perturbing terms - similar to the tridiagonal form of a multiplet operator. This structure is explicitly used for the operation of HFT units as weak field transitions (see sec. B.2.5). The

¹³³The reason for this assumption is the convergence of the fit algorithm. It is legitimated by the measurement, which is explained in app. B.2.5, which shows that the single-photon transitions are first to saturate, so that one can assume, that their efficiency is high.

¹³⁴This is only necessary, if transitions between the two sextupole subsystems of the ABS are operated, which are used to reject one or two hyperfine states from the injected atomic beam. This was not the case for hydrogen.

¹³⁵Respectively for the deuterium atom $F = \frac{3}{2}$ for the upper and $F = \frac{1}{2}$ for the lower states in limit of low holding field.

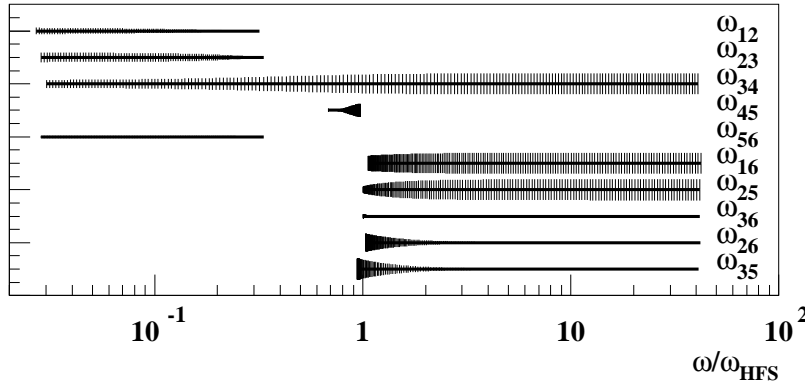


Fig. 6.21: Frequency range of deuterium transitions for holding field values within $0.7 \dots 350 \text{ mT}$. The size of the matrix elements is indicated by vertical lines. The 3 – 4 transition has the widest range and a reasonably high matrix element over the whole range.

simplest assumption, which can be made for the spectrum with respect to this expectation is, that all transitions, which have matrix elements directly above and below the diagonal, have about twice the value of the transition probabilities of eq. 6.39. Even though this assumption is not hardly rejected by all data, a better agreement with a constant spectral density could be achieved with the two state theory¹³⁶. Only at very low fields ($B \leq 3 \text{ mT}$), a significant¹³⁷ deviation from the two state theory was found. The effect will be analyzed in more detail in sec. 6.10.3.

The fits of the relaxation model to the measured data for the first 5 injection modes of tab. 3.2 were then performed with the a relatively short list of free parameters: Wall depolarization strength, spin exchange strength, injected intensity and the efficiencies from tab. 6.4¹³⁸. The remaining efficiencies, which are only relevant for the single state injection modes in tab. 3.2, were fitted exclusively with the data of these modes and with the averaged efficiencies of the previous fit of the left side of tab. 6.4. The resulting injected hyperfine populations and polarization values are listed in tab. E.3 and tab. E.4 respectively.

Concerning the saturation factor $\left(\sqrt{1 + \Omega_{ab}^2 \tau_s^2}\right)^{-1}$ in eq. 6.39 it was expected from fig. 6.20, that it can be neglected for temperatures above 50 K .

6.10.3 The Spectrum of Deuterium Spin Relaxation

After reasonable estimations of the ABS efficiencies had been derived in the described way, they were kept fixed and all 11 injection modes were fitted by the relaxation model. The result is shown in fig. A.1. Most data points are described reasonably well by the two state relaxation model - only at very low holding fields, a deviation is visible.

Deuterium transitions with large matrix elements, that are most useful for a determination of the spectrum, are especially the “electron” transitions 1 – 6, 2 – 5 and 3 – 4. The 3 – 4 transition has the widest frequency range of them, as shown in fig. 6.21. A plot of the spectrum evaluated with the 3-4 transition is shown in fig. 6.22 for a storage cell temperature of 212 K .

¹³⁶With the hydrogen like relaxation theory it was possible to match the magnetic field dependence at 95 K with $\chi^2/N_f = 1.94$. Using the discussed factor of 2, $\chi^2/N_f = 2.74$ was obtained.

¹³⁷Significant means in this context, that practically *all* measurements show the same tendency at low field, which indicates increased relaxation.

¹³⁸All other efficiencies of the WFT in the ABS appendix were comparable to unity.

The spectrum shows an increase at low frequency resp. low fields in two steps. The first step increases the transition probability by a factor of about 2 and the second step again by in total about 5...6. The first step can be interpreted by the expected multiplet enhanced relaxation. Also the magnitude of the enhancement matches the expectation, which predicts a factor of 2 in case of a triplet and a factor of 3 for a quadruplet. But this factors are expected for ideal multiplets with identical transition frequencies. For different frequencies, one expects a reduction of the effect, which depends on the overlap of the resonances and therefore on the characteristic width and the frequency difference for the transitions of the multiplet. The second step is likely related to a partial zero-field. If the energy difference between the hyperfine states is smaller than the width $\Delta E \leq h\Delta\nu$, the hyperfine states are only distinguished by their magnetic quantum number m_F . But in the presence of a random fluctuating field or a 'thermal reservoir', this quantum number is 'less good', so that the degeneracy enters the transition probabilities as a factor.

Fig. 6.23 gives an overview over the transition frequencies and frequency differences of deuterium multiplet transitions. The transition probabilities will have multiplet character, if the *differences* between the transition frequencies is below the width. Degeneracy starts, if the if the differences between the energies and therefore the transition *frequencies* are small compared to the width. One can assume for both cases the same characteristic width $\Delta\nu$. As the second step appears at a field of about $B < 0.1 B_C \simeq 1 mT$, the width must be about $10 MHz$ (left graph of fig. 6.23). One should then expect multiplet transitions for $B \simeq 0.5 B_C$ (right graph of fig. 6.23). This is in good agreement with the measured spectrum as shown in fig. 6.22. A value of $\Delta\nu \simeq 10 MHz$ is much smaller than the resonance width, which was estimated in context with the saturation factor (see sec. 6.10.1), where already the contribution of $\sqrt{\Omega^2}$ should be in the order of $\Delta B = \sqrt{\langle B_{loc}^2 \rangle} \simeq 6 mT$, which corresponds to $\Delta\nu = \frac{g\mu_B}{h} \Delta B \simeq 170 MHz$. As only one direction of the fluctuating field is involved, this value has to be reduced by $1/\sqrt{3}$. Another reduction of the line width by about $\frac{1}{2}$ is expected by the matrix elements, so that one would expect a value of about $\Delta\nu \simeq 50 MHz$. The contribution of the sticking time to the total resonance width would be even larger by orders of magnitude. But these quantities can not be compared directly, as the physical context is different. Narrowing effects¹³⁹ of resonance lines have been excluded for the resonance width, that enters the saturation prefactor, but they may enter in the calculation of *correlated* transitions, when the sum of holding field and local fluctuating field determines the exact position of the resonances. Measurements at lower temperatures - where the line width is reduced due to the longer sticking time - show, that the effect is still present, but weaker. Fig. 6.24 shows a measurement of the

¹³⁹Like motional narrowing or exchange narrowing [Abr 61, Kit 69].

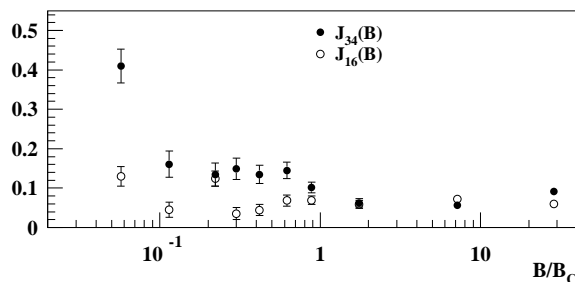


Fig. 6.22: Measured spectrum of the deuterium 3–4 transition in dependence of the holding field at a storage cell temperature of 212 K. The 1-6 spectrum is shown for comparison.

spectrum of the 3-4 transition at 95 K. At even lower temperatures, the increase is nearly hidden under the error bars as shown in fig. 6.25, which was measured at 50.7 K. The same increase was also measured with the 1-2 transition and the 2-3 transition. But the matrix elements of these transitions are small at field values, which are large compared to the critical field, so that the shape of the spectrum cannot be measured with the required precision at high fields.

A slightly different interpretation is favored by the fact, that also the 5-6 transition spectrum shows the stepwise increase at low holding fields respectively low frequencies. This transition is - at low holding fields - not part of the upper multiplet, but of the $F = \frac{1}{2}$ duplet. Nevertheless it shows a very similar behavior as the other transitions, as shown in fig. 6.26. One can describe the increase in the transition probabilities within multiplets and other transitions with sufficiently close transition frequencies by internal *cross-relaxation*. Cross-relaxation appears in systems, where correlated transitions can appear, which yield a total change in the energy of the spin system, which is close to zero. Bloembergen and co-authors argue, that the conservation of angular momentum appears to be less strict in the presence of the 'lattice' (or surface) than the conservation of energy. Correlations between a $6 \rightarrow 5$ and a $1 \rightarrow 2$ transition for instance then are possible, even though the total change in angular momentum is $\Delta m_F = -2$ [Blo 59]. This explanation of the increased transition probabilities is close to the argumentation with multiplets, but not identical, as cross-relaxation does not require, that the matrix elements of the transitions have to be tridiagonal. The only requirement is the overlap of the line shape functions of the involved transitions, respectively, that the total energy change ΔE is close to the total resonance width $\Delta\omega$: $\Delta E \simeq \hbar\Delta\omega$. This type of transitions is only possible, because the atoms are not in *eigenstates* of the Hamilton operator, but in mixed states. If this fact is accepted, then it is clear, that a state $\psi = \frac{1}{\sqrt{2}}(|1\rangle + e^{i\phi}|6\rangle)$ can be transferred into a state $\Psi = \frac{1}{\sqrt{2}}(|2\rangle + e^{i\Phi}|5\rangle)$ without a change of the expectation value of the energy in low fields. Cross-relaxation effects between electron and σ -transitions have also to be taken into account. But in the low field limit, a correlated transition $3 \rightarrow 6$ and $5 \rightarrow 2$ for

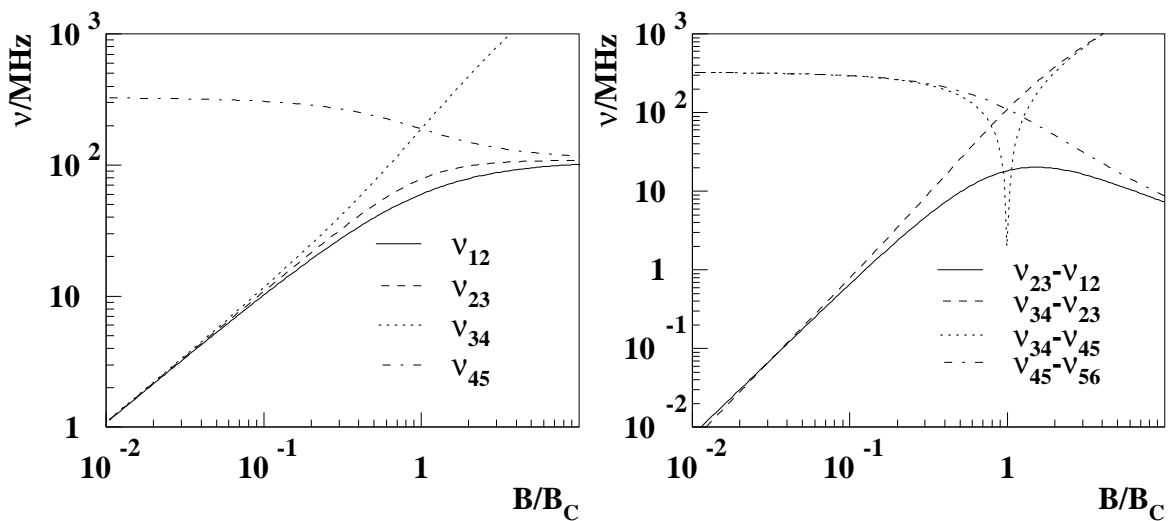


Fig. 6.23: Left: Transition frequencies of multiplet transitions of deuterium in dependence of the holding field. Right: Differences between neighboring transition frequencies of deuterium vs. holding field.

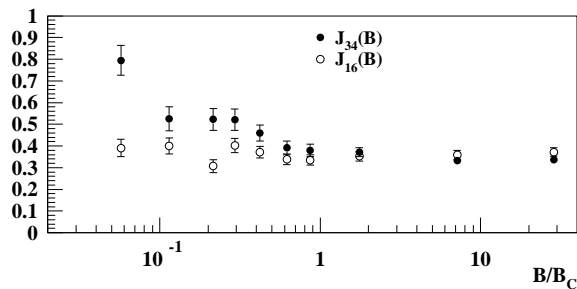


Fig. 6.24: Measured spectrum of the deuterium 3 – 4 transition (filled circles) in dependence of the holding field at a storage cell temperature of 95 K. The 1-6 spectrum is shown for comparison.

instance can not be distinguished from a correlated $3 \rightarrow 2$ and $5 \rightarrow 6$ transition. It will then depend on the set of injection modes and the details of the fit algorithm, where the increased transition probability appears. In any case, the relaxation theory as represented in the master equation is not able to properly describe this kind of cross-relaxation, as it depends on the quantummechanical mixtures within the spin system. A tensor formalism as used to describe spin-exchange relaxation would be required.

Both arguments for the stepwise increase are still valid: The first step appears at the holding field value, where the difference between the transition frequencies equals the width $\Delta\nu$, the second step, where the energy difference between the levels equals $h \Delta\nu$.

One may in contrary to these presented arguments assume, that the spectral density itself is increasing at low frequencies. Even though this interpretation can not be rejected with hard arguments, there are at least three good reasons to believe, that it is wrong. The first argument is, that the frequency, where the increase appears, must be explained by a time constant associated to it. This time constant would have to be in the order of 10^{-7} s. As the typical sticking times on the surface are by at least two orders of magnitude below this value, a process with such a long time constant should not appear during a wall collision. The second argument against this interpretation is, that the effect should not get weaker at lower temperatures without changing its typical time constant, if it was related to the spectral density. The third argument is, that one would expect to find the same effect in case of hydrogen, if it was related to the spectral density. This is not the case with the presented explanation, as the number of possible candidates for cross-relaxation is much higher for deuterium than for hydrogen. In case of hydrogen, only two transitions, namely the 1-2 and the 2-3 transition, have similar transition frequencies in the low field limit¹⁴⁰. In case of deuterium, there are already 4 transitions with $\Delta F = 0$ in low field, namely the 1-2, the 2-3, the 3-4 and the 5-6 transitions. Each pair of them

¹⁴⁰The 1-4 and the 2-4 transition can not be correlated, as there belong to different (uncorrelated) directions of the fluctuating field.

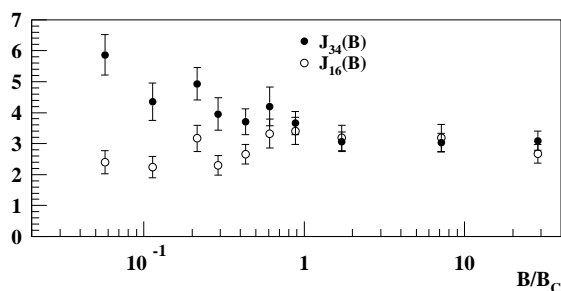


Fig. 6.25: Measured spectrum of the deuterium 3 – 4 transition in dependence of the holding field at a storage cell temperature of 50.7 K. The 1-6 spectrum is shown for comparison.

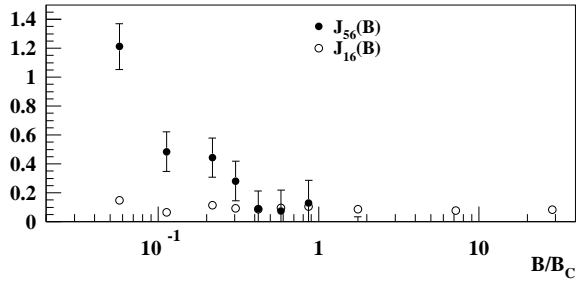


Fig. 6.26: Measured spectrum of the deuterium 5–6 transition in dependence of the holding field at a storage cell temperature of 175 K. The 1-6 spectrum is shown for comparison.

may contribute, so that we obtain 6 possible pairs of transitions. The only weakness of this argument is the limited number of hydrogen measurements, which were extended to low field values. Most hydrogen measurements were performed with a holding field range of about 10...335 mT, as there was no indication for a change at low fields and the parameters of the master equation can be determined without measurements at very low fields. Typically, measurements at holding field values well below the critical field are sufficient.

6.10.4 The Magnetic Field Dependence of Deuterium Spin Relaxation

Besides the fact, that a quantitative theory of wall depolarization including multiplet effects, energy degeneracy and cross-relaxation is not at hand, also the statistical precision of the measurements is under the actual conditions not high enough, that one can expect to verify or falsify such a theory. But an ad hoc treatment was found, that enables to compare the data with the relaxation model. Even though it is not believed, that the increase of the transition probabilities is caused by an increase of the spectral density at low frequencies, it can approximately be modeled with the help of a non-constant spectral density, that increases stepwise at low frequencies. With a spectral density of the form

$$j(\omega_{ab}) = \tau_c \left(1 + A \frac{\omega_1^4}{\omega_1^4 + \omega_{ab}^4} + B \frac{\omega_2^4}{\omega_2^4 + \omega_{ab}^4} \right) \quad (6.78)$$

one obtains a reasonable agreement¹⁴¹ of the master equation and the data - also at low magnetic fields - as shown in fig. A.2. A fit of the relaxation model to the measured polarization values at a storage cell temperature of 95 K is shown in fig. A.3. The frequency values of the steps were kept fixed at $\omega_1/2\pi = 7 \text{ MHz}$ and $\omega_2/2\pi = 80 \text{ MHz}$ respectively. The results for the parameters $A(T)$ and $B(T)$ are shown in fig. 6.27. The wall depolarization strength $C \propto \Omega_{ab}^2 \tau_s \tau_c$ that one obtains by the fitting routine, was already shown in fig. 6.20. Unfortunately, it was found, that the obtained values of τ_d/τ_{se} and therefore the spin-exchange relaxation strength varied relatively strong¹⁴², depending on the assumed spectral density, so that they are not analyzed in further detail. Instead, it will be shown in sec. 6.10.5, that the spin-exchange relaxation strength and consequently the atomic density can be determined in case of deuterium without a change in the magnetic holding field.

¹⁴¹One may use different forms, also of second order in the frequency.

¹⁴²By about 5...10% of the absolute value with a statistical uncertainty of less than 2%.

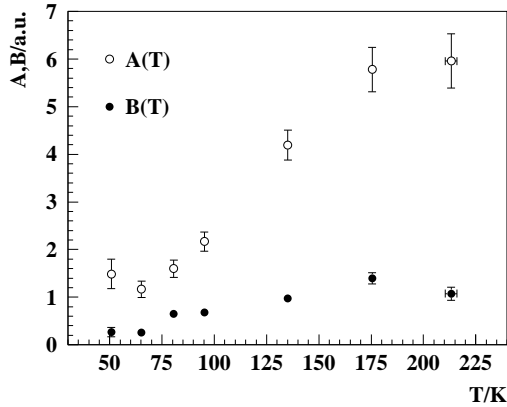


Fig. 6.27: Temperature dependence of the parameters A and B of the phenomenological spectral density of eq. 6.78 obtained by the fitted relaxation model (see fig. A.2 for an example of the fitted hyperfine population).

6.10.5 Relaxation of $\langle \vec{I}\vec{S} \rangle$, Spin-Exchange and Target Density

As described in app. D.6.1, spin exchange relaxation does not change the polarization values P_e , P_z and P_{zz} in the high holding field limit. It may however still modify the hyperfine populations and therefore the value of the asymmetry A_{IS} , which is in the high field limit given by

$$\lim_{B \rightarrow \infty} A_{IS} = N_1 + N_4 - N_3 - N_6. \quad (6.79)$$

The value of A_{IS}^{inj} is high in case of the injection mode P_{zz+} and one may use the measured change in the hyperfine populations to measure the atomic target density - or the spin exchange cross section. The calculation with the master equation in the high field limit¹⁴³ yields, that

$$A_{IS} = \frac{A_{IS}^{inj}}{1 + \langle b \rangle \gamma_e + \tau_d / \tau_{se}}. \quad (6.80)$$

The reduction of A_{IS} by wall depolarization can be measured in the high field limit using the measured value of $P_e(P_e^{inj})$ as in case of hydrogen (eq. 6.11):

$$P_e(P_e^{inj}) = \frac{P_e^{inj}}{1 + \langle b \rangle \gamma_e}, \quad (6.81)$$

so that:

$$\frac{\tau_d}{\tau_{se}} = \frac{A_{IS}^{inj}(P_{zz+}^{inj})}{A_{IS}(P_{zz+}^{inj})} - \frac{P_e^{inj}}{P_e(P_e^{inj})}. \quad (6.82)$$

The advantage of this method is the simplicity of the analysis - especially compared to the complex modeling of the magnetic field dependence¹⁴⁴. Fig. 6.28 shows the result of a temperature scan with deuterium performed 27th Aug. 1998, where the normalized density $\langle n_{norm} \rangle = \langle n \rangle \sqrt{\frac{T}{100K}}$ was calculated by

$$\langle n_{norm} \rangle = \frac{\tau_d}{\tau_{se}} \sqrt{\frac{T}{100K}} \frac{1}{\sqrt{2} \rho_c L_d \sigma_{se}}. \quad (6.83)$$

¹⁴³The *high field limit* can also be defined by the condition of decoupled nucleons: The approximation requires, that wall relaxation does not change the nuclear spin. In case of low target temperatures ($T < 50K$) one finds, that a holding field of 335 mT is not always enough to fulfill this requirement.

¹⁴⁴Of course the injected asymmetry A_{IS}^{inj} has to be known and is obtained by the analysis of the magnetic field dependence of spin relaxation.

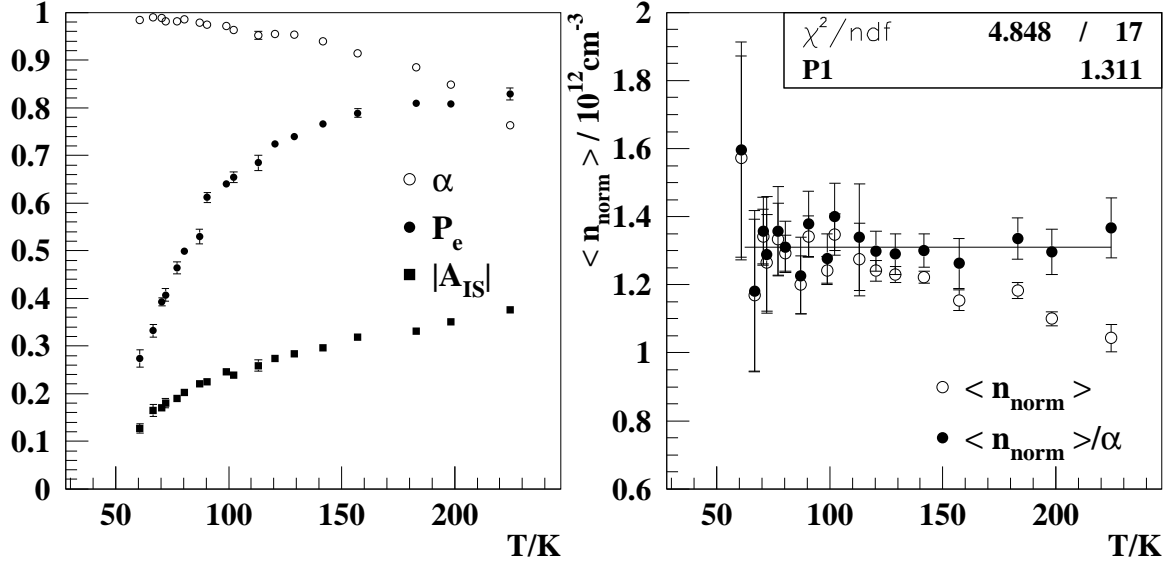


Fig. 6.28: Results of the $\langle \vec{I}\vec{S} \rangle$ relaxation measurement with deuterium in dependence of storage cell temperature T . Left: Measured atomic fraction α_r^{TGA} , P_e and $|A_{IS}|$ versus storage cell temperature T . Right: Calculated normalized density $\langle n_{norm} \rangle$ (open circles) and its ratio to the measured atomic fraction (filled circles) for two injected hyperfine states. The measurement was performed 27th Aug. 1998 at a holding field of $B = 335 mT$. A_{IS}^{inj} was assumed to be -0.8614 (see tab. E.4). Data below 60 K are not shown, since the statistical precision was unsatisfactory.

The atomic flux into the TGA was $\phi_a \simeq 53.6 kHz/mA$ with 2 injected hyperfine states. The resulting atomic target density $\langle n \rangle$ at 100 K in injection mode P_{zz+}^{inj} - assuming $\sigma_{se} = 24 \cdot 10^{-16} cm^2$ - is then:

$$\langle n \rangle = 1.311 \pm 0.019 \cdot 10^{12} cm^{-3}. \quad (6.84)$$

The target areal nucleon density is $1.05 \cdot 10^{14} nucl/cm^2$. The number of injected atoms is $3.2 \cdot 10^{16} s^{-1}$ for two injected hyperfine states. The intensity with 3 injected hyperfine states is then about $4.5 \cdot 10^{16} s^{-1}$ and thus about 30 % lower than for hydrogen (eq. 6.70).

Unfortunately, a direct comparison with the lumi calibration of sec. 3.7 is not possible, as the TGA sensitivity changed between both measurements. But a luminosity measurement of 13th of August 1998 delivered a target density of $1.292 \cdot 10^{12} cm^{-3}$ at a TGA-flux of $57 kHz/mA$, a storage cell temperature of 100 K and an atomic fraction α_r close to unity. If one compares both values scaled by the atomic flux ϕ_a into the TGA, one finds again a deviation of about 6.3 % in the same direction as for hydrogen. This is still covered by the systematic uncertainty of the luminosity monitor, which is estimated to be about 5...7 % and by the uncertainty of σ_{se} , which is about 10 %. Other systematic uncertainties - like BRP calibration and precision of the molecular flow simulation - might of course also play a role, but the contribution of these errors is expected to be $\leq 2\%$. Another uncertainty is of course the exact value of α_r within the beam tube. Its size will be discussed in sec. 7.

6.11 Bunch Field Induced Resonant Depolarization

The beam current of the HERA electron/positron storage ring is bunched to provide high luminosity for the collider experiments H1 and ZEUS. The revolution time τ_{rev} of a certain bunch at $27.5 GeV$ beam energy is $21.14 \mu s$ and the distance between two bunches $\tau_{bunch} = 96 ns$. The basic frequency ν_{rev} is then given by the revolution time $\nu_{rev} = \frac{1}{\tau_{rev}} = 47.3 KHz$. Since typically most of the 220 bunches are filled, the time gap between two bunches defines the basic frequency, which is $\nu_{bunch} = \frac{1}{\tau_{bunch}} = 10.4097 MHz$. It is assumed, that the bunches have a Gaussian shape with a length σ_z of a few mm , corresponding to a duration in time of σ_t a few ten ps . The envelope of the Fourier spectrum should then also have a Gaussian shape with $\sigma_\nu = (2\pi\sigma_t)^{-1}$, of a few GHz . The frequency spectrum contains dominantly harmonics of ν_{bunch} . The resonance condition for a transition $|a\rangle \leftrightarrow |b\rangle$ is given by:

$$(E_a - E_b)/h = n_{harm}\nu_{bunch}. \quad (6.85)$$

As the magnetic high frequency field surrounds the electron beam, only π -transitions are induced, as the RF-field contains no component parallel to the longitudinal holding field of the target. Measurements of hydrogen bunch field induced depolarization at the HERMES target were presented in [Ko 98, HER 98b]. The present work therefore contains only measurements on the bunch field induced depolarization of deuterium.

Fig. 6.29 shows in the left graph the depolarizing resonance positions for nucleon transitions ($1 \leftrightarrow 2$, $2 \leftrightarrow 3$, $5 \leftrightarrow 6$, $4 \leftrightarrow 5$, and $3 \leftrightarrow 6$) and in the right graph for the first 50 beam harmonics of the electron transitions ($1 \leftrightarrow 6$, $2 \leftrightarrow 5$ and $3 \leftrightarrow 4$). At the working point the electron resonances are very tight and the single resonances can not be resolved with the given homogeneity of the longitudinal magnet, as there are always several resonances inside the length of the storage cell. All nuclear resonances besides the $3 \leftrightarrow 6$ -resonance are located below $\sim 60 mT$. The target can hence be operated at any higher field. The resonances around $5 \dots 50 mT$ can be observed separately as shown in fig. 6.30 and fig. 6.31. The measurement of fig. 6.30 is performed using the *flip-in*-technique. This means, that the BRP measures the atomic beam rate with a constant HFT status, which is selected in a way, that bunch field resonance increases the signal. For the injection mode P_{z+} , the MFT 1-4 of the BRP was switched on, so that the BRP-signal is in first order proportional to the sum $N_2 + N_3 + N_4$ - none of them being injected by the ABS. The 1-2 resonance and the 5-6 resonance, (followed by a 2-5 electron resonance) increase the signal

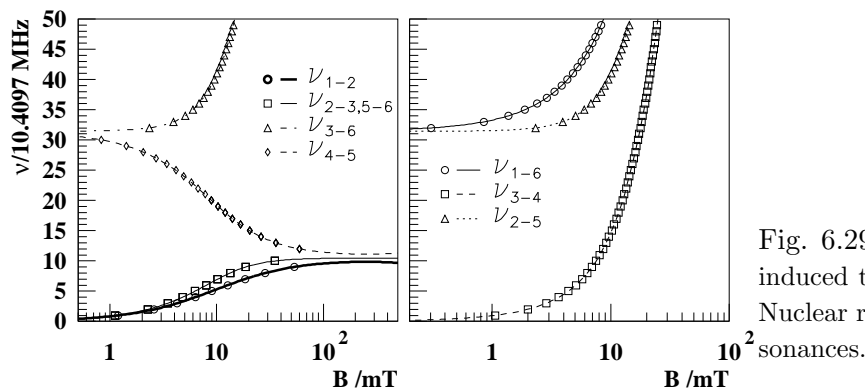


Fig. 6.29: Resonances for bunch field induced transitions of deuterium. Left: Nuclear resonances. Right: Electron resonances.

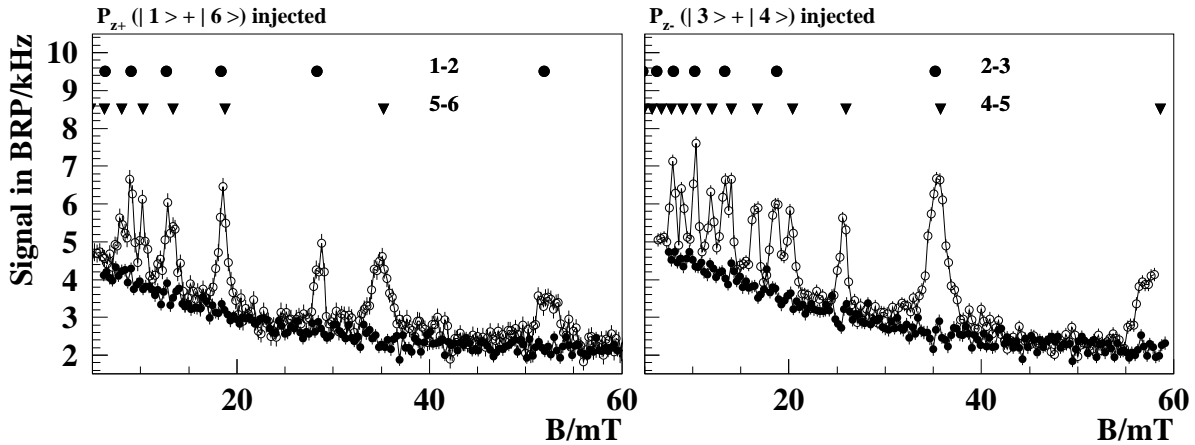


Fig. 6.30: Bunch field resonances of deuterium, measured with the flip-in-technique. The open/closed circles represent the beam rate into the BRP with/without HERA beam for the injection mode P_{z+} and P_{z-} in the left and right plot. The calculated resonance positions are indicated by symbols above the graph.

by filling state $|2\rangle$. The nuclear resonances 2-3 and 4-5 are not visible in this mode. For the injection mode P_{z-} (lower graph), the SFT 3-5 in the BRP was switched on, so that the count rate in the BRP represents the sum $N_1 + N_2 + N_5$. In this mode, the resonances 2-3 and 4-5 cause an increase of the signal. Fig. 6.31 shows the result of measurements, which were performed as complete polarization measurements. The resonances have the same shape as measured with hydrogen. The form can be explained by a combination of the magnetic field shape of the longitudinal target magnet, the acceptance of the BRP and the frequency spectrum of the bunch field [Ko 98, HER 98b].

Besides measurements of the resonance form, also the resonant strength was measured in dependence of the beam current. The results indicate, that the resonances are - under certain conditions - saturated or at least close to saturation. A small fraction of atoms enters the BRP (respectively the sample tube) without any passage through a resonance. The saturation value of the polarization is therefore not zero. If p is the number of passages through a resonant region, γ_d the depolarization coefficient for one passage and $N(p)$ the

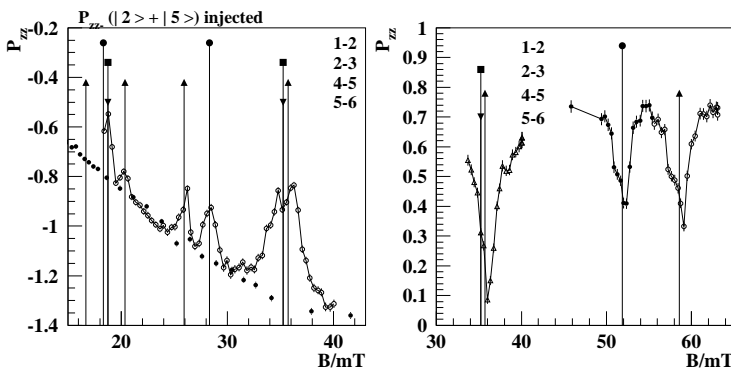


Fig. 6.31: Measurement of bunch field induced depolarization of deuterium for the injection modes P_{zz-} (left figure). The filled circles correspond to a measurement without HERA beam. The right figure shows resonance details for 3 different resonances and three different injection modes collected in one plot. The calculated resonance positions are again indicated by symbols.

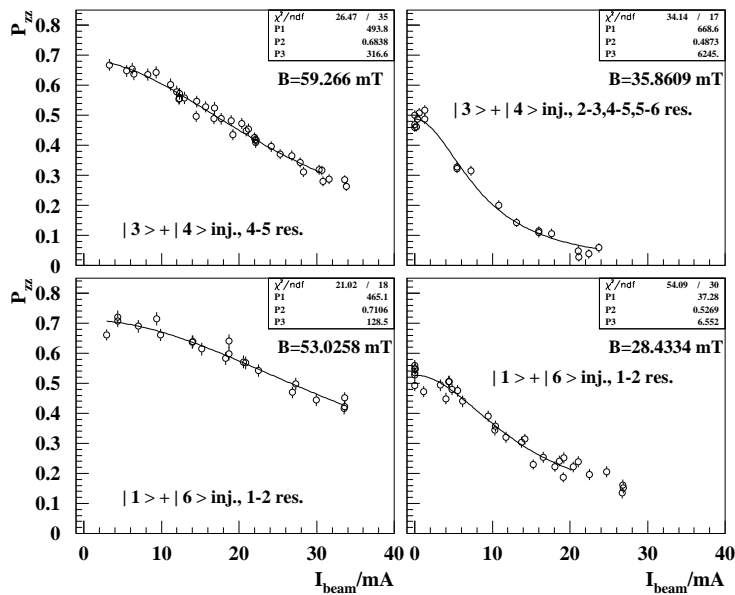


Fig. 6.32: Resonances strength for bunch field induced nuclear transitions of deuterium vs. HERA beam current for four different resonances. The data points represent the measured polarization and the line a fit with eq. 6.88. The fitted parameters are shown in the inlet. P1 corresponds to the saturation current I_0 , P2 to $P(I_b = 0)$ and P3 to $\langle p \rangle$. The numbers of

probability distribution for the atoms entering the BRP, then the polarization can be described by:

$$P^{BRP} = P(I_b = 0) \int_0^{\infty} N(p) e^{-\gamma_d p} dp, \quad (6.86)$$

where I_b is the HERA beam current. Similar to the collision ages, one can assume that $N(p)$ is exponentially distributed and one obtains:

$$P^{BRP} = \frac{P(I_b = 0)}{1 + \langle p \rangle \gamma_d}. \quad (6.87)$$

The depolarization coefficient γ_d is given by eq. D.19, where $\Omega\tau_s$ can be replaced by I_b/I_0 :

$$P^{BRP} = \frac{P(I_b = 0)}{1 + \langle p \rangle \frac{I_b^2}{I_0^2 + I_b^2}}. \quad (6.88)$$

Eq. 6.88 indicates saturation for $I_b \geq I_0$. Fig. 6.32 shows a fit of this equation to four

meas.	I_0/mA	$P(I_b = 0)$	$\langle p \rangle$
1	494 ± 179	0.6838 ± 0.0072	317 ± 228
2	669 ± 528	0.4873 ± 0.005	6244 ± 9722
3	465 ± 258	0.7106 ± 0.0064	128 ± 139
4	37.3 ± 5	0.527 ± 0.006	6.55 ± 1.395

Tab. 6.5: Measured bunch field induced resonant depolarization vs. HERA beam current.

different measurements of the polarization vs. the HERA beam current. The fitted results are listed in tab. 6.5. Only the last measurement resulted values with acceptable error bars. It shows, that the average number of passages can be fairly low. The saturation effect has of course an influence on measurements of the resonance shape: the peak height is reduced by saturation.

6.12 Summary

The analysis of the spin relaxation measurements allowed not only the determination of the relaxation parameters but also of the injected polarization and of the transition efficiencies of the hyperfine transitions of the ABS respectively. The measurements yielded an injected polarization of about ± 0.973 , a polarization loss of about 3.3 % by spin exchange collisions and of about 2 % by wall collisions in case of hydrogen. The target areal nucleon density could be determined as $7.4 \cdot 10^{13} \text{ cm}^{-2}$ corresponding to an injected atomic flux of $6.62 \cdot 10^{16} \text{ s}^{-1}$ from the ABS. The measurements with deuterium delivered a typical density of $1.05 \cdot 10^{14} \text{ nucl/cm}^2$ corresponding to $4.5 \cdot 10^{16} \text{ s}^{-1}$ injected atoms for an injection mode with 3 injected hyperfine states. This is about 30 % less than for hydrogen. The temperature dependence of the deuterium measurements verifies, that the nucleons are at the target working point of 335 mT strongly decoupled from the electrons and that any relaxational loss of $P_{z\pm}$ is too weak to be significant down to temperatures below 50 K .

The measurements concerning wall depolarization are consistent with a spectral density that is constant within the relevant frequency range, so that the high temperature limit τ_c^0 of the correlation time has to be less than $2.3 \cdot 10^{-12} \text{ s}$. The wall depolarization showed saturation much below a spin flip probability of $\frac{1}{2}$, which was not found in literature but can be described by a simple extension of the known theory. The hydrogen measurements showed an increase of the residual electron polarization at low storage cell temperatures, that could only be explained by exchange interaction of the physisorbed atoms with a permanent magnetized cell surface.

The deuterium measurements show an increase of depolarization at low holding fields, that indicates multiplet relaxation and/or so-called *cross-relaxation*. Other differences in the relaxational behavior between both isotopes can be related to the differences in the properties of the cell coatings.

It was also shown for deuterium, that the spin exchange relaxation strength - and therefore the atomic target density - can be measured with high precision and a simple evaluation scheme by the measurement of $\langle \vec{S}\vec{I} \rangle$ -relaxation compared with the measured $\langle \vec{S} \rangle$ -relaxation in high fields. This is also possible for hydrogen, if a corresponding injection mode is prepared and used¹⁴⁵.

Since the electron/positron beam of HERA is bunched, the beam current induces an electromagnetic high frequency field, that may cause significant depolarization of the target atoms in case of resonance. The measurements of this effect with the deuterium target showed saturation already at relatively low beam currents. The magnetic holding field values of the resonances were found to be in agreement with the expectations and the resonances could be identified with the corresponding hyperfine transitions.

¹⁴⁵This could be either $|1\rangle$ and $|3\rangle$ or $|2\rangle$ and $|4\rangle$.

7 Target Polarization and Sampling Corrections

The calculation of the target polarization, which is given by eq. 1.1

$$P^T = \alpha_0 \cdot (\alpha_r + (1 - \alpha_r) \cdot \beta) \cdot P_a, \quad (7.1)$$

requires the knowledge of the average atomic fraction α_r and polarization P_a in the beam tube of the storage cell. They are related to the measured values α_r^{TGA} and P^{BRP} by the sampling corrections c_α and c_P , which are defined by eq. 1.2 and eq. 1.3:

$$\begin{aligned} \alpha_r &= c_\alpha \alpha_r^{TGA} \\ P_a &= c_P P^{BRP}. \end{aligned} \quad (7.2)$$

The knowledge of the sampling corrections is therefore crucial for the calculation of the target polarization.

If the storage cell is not yet exposed to the HERA beam, one can assume, that the recombination and depolarization probability per wall collision are constant all over the surface of the storage cell - or at least, that possible microscopic inhomogeneities by different types of surface sites are equally distributed. Under normal running conditions, an influence of the HERA beam on the target performance is not observed. Only during certain limited periods of non-optimal beam tune or after an accidental beam loss near the HERMES target region, the target - and especially the values of α_r^{TGA} and P_e - were affected¹⁴⁶. During this periods, increased charged and/or synchrotron rates are measured by the HERMES hodoscopes, and increased vacuum pressures have been observed, which indicate an unusual increase of the heat load at certain points of the beam pipe. Typically, α_r recovers after hours up to some ten-hours of polarized running. Several mechanism are able to explain, why the HERA beam changes the surface properties, as

- radiation damage of the Drifilm coating by synchrotron light.
- removal of the water layer of a predamaged Drifilm coating by micro wave energy deposition into the target chamber.
- ion bombardment of the storage cell walls: the ions are (partly) confined by the longitudinal target field, which makes a localization of the influence very difficult.
- chemical reactions of ionized hydrogen radicals with the cell coating.
- contamination of the storage cell surface by sputtered material from collimator C_2 .

The exact influence of the beam on the storage cell surface and the distribution of this influence within the beam tube is unknown, but since the storage cell almost always recovered within reasonable time scales, the experimental program of HERMES was not seriously affected.

In this section, the calculation (or better: limitation) of the sampling corrections will be presented. The problem of the sampling corrections c_α and c_P can be divided into two separate questions: The fact, that the atom sample for both - BRP and TGA - is formed in the storage cell center, defines the questions:

¹⁴⁶The increase of the storage cell temperature and the decrease of P_e due to bunch field depolarization during injection are not taken into account.

1. What is the relation between the atomic fraction respectively the polarization in the storage cell center and the (density weighted) average value over the complete length?
2. What is the influence of the sample and extension tube on the sampled beam?

It is convenient to distinguish certain scenarios of special interest:

Homogeneous cell (HC): The natural assumption, when the cell has not (yet) been exposed to the HERA beam.

Homogeneous beam tube (HBT): A beam tube, homogeneously affected by the beam, the side tubes unaffected.

Inhomogeneous beam tube (IBT): Beam tube inhomogeneously affected by the beam, the side tubes unchanged. This scenario does not lead to a single sampling corrections, but it can be used to calculate a lower limit for α_r (P_a) at a given measured value α_r^{TGA} (P^{BRP}).

It is assumed in all scenarios, that for the recombination probabilities in the sample tube γ_r^{ST} and beam tube γ_r^{BT} the relation $\gamma_r^{ST} \leq \gamma_r^{BT}$ holds at any time¹⁴⁷. Proofs for this assumption were given in sec. 4 and sec. 6.8.2.

All scenarios are dedicated to the target working conditions, if nothing else is said, since the target is operated under these conditions for polarized data taking. Systematic investigations like measurements of the dependence of polarization and atomic fraction on the magnetic holding field or the storage cell temperature were performed between the HERA positron/electron fills or during machine studies of HERA. During luminosity run, the target is operated between 80...120 K and at a holding field of 335 mT. As an exception, there were some fills of dedicated systematic studies, which are excluded for the HERMES physics analysis.

It should also be stressed, that all calculations for the sampling correction c_α are based on the assumption of the density independence of γ_r . As discussed in sec. 5, this is the dominant case. In a more general sense, a density dependent γ_r is in any case less critical, as it leads to a situation, where most recombination happens in the center of the storage cell.

The scenarios **HC** and **HBT** can either be calculated with the *model of distributed sources* as described in app. C.7 - or be obtained from collision age distributions of the molecular flow simulation. For the **IBT** scenario, the *model of localized sources* was developed. This model is able to deliver a lower limit for α_r (α_r^{TGA}) for any possible distribution of γ_r with mathematical precision. It is described in app. C.8.

7.1 The Sampling Corrections c_α and c_P

The calculation of the sampling correction c_α requires the calculation of normalized densities. For the TGA, it was already discussed, that $\alpha_r^{TGA} = \rho_a^{TGA}$ holds (eq. 3.27), since α_r^{TGA} is defined using fluxes instead of densities. The atomic fraction inside the beam tube of the storage cell is (of course) defined by the densities, so that eq. 2.40 has to be

¹⁴⁷The validity of this assumption is of some importance, as α_r could otherwise - even in the limiting case $\alpha_r^{TGA} \rightarrow 0$ - be still high, if $\gamma_r^{ST} \gg \gamma_r^{BT}$.

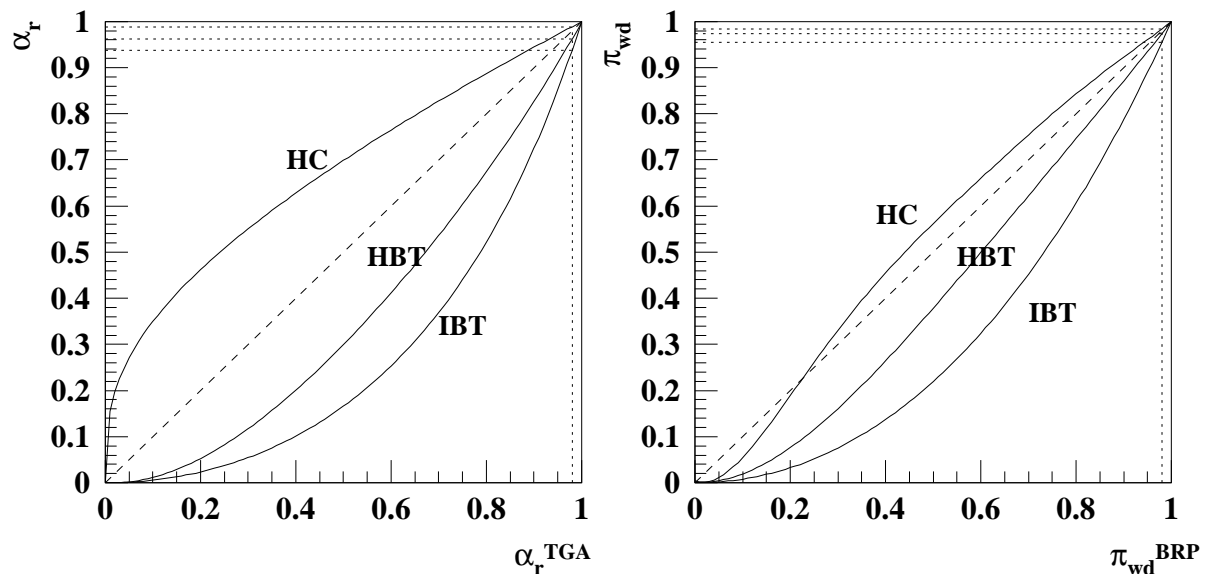


Fig. 7.1: Left: Relations between α_r in the beam tube and the measured value α_r^{TGA} for a homogeneous storage cell **HC**, a homogeneous beam tube **HBT** and the lower limit of the inhomogeneous beam tube scenario **IBT** a for large storage cell. Right: The same relations for wall depolarization as measured with the BRP. Examples of the corrections are given by the dotted lines. For a measured value $\alpha_r^{TGA} = 0.98$, one obtains a value $\alpha_r \simeq 0.96 \pm 0.025$ and for $\pi_{wd}^{BRP} = 0.98$ one obtains $\pi_{wd} \simeq 0.97 \pm 0.013$. For low values of α_r^{TGA} and π_{wd}^{BRP} , the uncertainty becomes large, if none of the scenarios can be excluded by measurements.

used to calculate atomic fractions with the normalized densities, as the relative density of molecules is increased by the lower conductance for mass 2. This transformation is not required, if the formulas are used for c_P . Typically c_P is less critical, as the wall depolarization of the nucleons is reduced by the strong holding field. Another reason, why the sampling correction c_P can assumed to be less critical, is given by the fact, that the BRP sample beam contains about 38 % atoms from the storage cell center. The influence of the properties of the sample and extension tube on the measured polarization is smaller than for the TGA.

In case of hydrogen, the sampling correction c_P has to be subdivided into two different corrections - one for the wall depolarization and a second one for spin exchange relaxation, as both processes have different corrections. If all depolarizing effects are small (a few percent), the polarization can be described by depolarization factors π_{wd} and π_{se} for wall depolarization and spin exchange depolarization respectively:

$$\begin{aligned} P_a &= \pi_{wd} \pi_{se} P^{inj} \\ P^{BRP} &= \pi_{wd}^{BRP} \pi_{se}^{BRP} P^{inj}. \end{aligned} \quad (7.3)$$

The depolarization factor $\pi_{wd}(\pi_{wd}^{BRP})$ is shown in the right part of fig. 7.1. The factor π_{se}^{BRP} can be written as

$$\pi_{se}^{BRP} = \frac{1}{1 + \Delta P_{se}^{BRP}}. \quad (7.4)$$

and the corresponding depolarization factor for the beam tube is:

$$\pi_{se} = \frac{1}{1 + c_{se} \Delta P_{se}^{BRP}}, \quad (7.5)$$

where c_{se} is defined by the density weighted ratio of the average trajectory length $\langle l_\rho \rangle$ (see eq. C.103) for beam tube sample and BRP sample respectively:

$$c_{se} = \frac{\langle l_\rho \rangle^{BT}}{\langle l_\rho \rangle^{brp}} \simeq 1.06. \quad (7.6)$$

As c_{se} is close to one, the difference of π_{se} and π_{se}^{BRP} may - compared to other error contributions - be neglected, and the sampling correction c_P is defined by wall depolarization only:

$$c_P = \frac{P_a}{P^{BRP}} \simeq \frac{\pi_{wd}}{\pi_{wd}^{BRP}}. \quad (7.7)$$

Fig. 7.1 shows the results of the calculations. The resulting relations are given (or can be approximated) by:

$$\mathbf{HC:} \quad \alpha_r = (0.3665x + 0.63233x^2)^{\frac{1}{3}} \quad (7.8)$$

$$\mathbf{HBT:} \quad \alpha_r = -0.054x + 1.836x^2 - 1.334x^3 + 0.55x^4 \quad (7.9)$$

$$\mathbf{IBT:} \quad \alpha_r \geq x^2 \left(\sqrt{2}(1 + \frac{1}{2}\varepsilon(1-x)) - (\sqrt{2}-1)x^2 \right)^{-1} \quad (7.10)$$

$$\mathbf{HC:} \quad \pi_{wd} = 0.00463 - 0.36731y + 11.736y^2 - 35.374y^3 + 51.51y^4 - 36.874y^5 + 10.365y^6 \quad (7.11)$$

$$\mathbf{HBT:} \quad \pi_{wd} = 0.00123 - 0.054y + 2.577y^2 - 2.309y^3 + 0.78456y^4 \quad (7.12)$$

$$\mathbf{IBT:} \quad \pi_{wd} \geq 2y^2(2 + \varepsilon(1-y))^{-1}, \quad (7.13)$$

where $x = \alpha_r^{TGA}$ and $y = \pi_{wd}^{BRP}$ respectively. The factor ε is defined by eq. C.145 and is for the large storage cell $\varepsilon \simeq 0.55$.

Since it is basically unknown, which sampling correction is correct, the complete range between the scenario **HC** and **IBT** has to be considered. The value α_r is then given by the average of eq. 7.8 and eq. 7.10 and the systematic uncertainty by the half difference¹⁴⁸.

¹⁴⁸It should be stressed, that this is a very conservative estimation of the uncertainty.

	a	b
HC:	0.443	0.225
HBT:	-0.75	-1.138
IBT:	-1.81	-0.29
$\bar{x} = (x^{HC} + x^{IBT})/2$	-0.683	-0.456
$\Delta x = (x^{HC} - x^{IBT})/2$	1.126	0.681

Tab. 7.1: Values of a and b for the linear approximations of c_α and c_P by eqs. 7.14. The average \bar{x} of the **HC** and **IBT** scenario is given by the 4th line from top and the uncertainty by Δx by the bottom line. The results are calculated for the large storage cell geometry.

As the measurements of α_r^{TGA} and π_{wd}^{BRP} have almost always¹⁴⁹ been well above 0.9, one may use linear approximations for the sampling corrections, which are given by:

$$\begin{aligned}\alpha_r &= \bar{a} + (1 - \bar{a})\alpha_r^{TGA} = \alpha_r^{TGA} + \bar{a}(1 - \alpha_r^{TGA}) \\ \pi_{wd} &= \bar{b} + (1 - \bar{b})\pi_{wd}^{BRP} = \pi_{wd}^{BRP} + \bar{b}(1 - \pi_{wd}^{BRP}).\end{aligned}\quad (7.14)$$

with the constants \bar{a} and \bar{b} listed in the 4th row of tab. 7.1. The linear approximations 7.14 are smarter to use than eq. 1.2 and eq. 1.3 and they allow to express the uncertainty of the sampling corrections by the uncertainty of \bar{a} and \bar{b} , which are Δa and Δb . Due to the huge uncertainties Δa and Δb in the last row of tab. 7.1, a reasonably small error in α_r and P_a can only be achieved, if the values of α_r^{TGA} and π_{wd}^{BRP} are close to unity. This becomes clear by the rightmost expressions of eqs. 7.14.

7.2 The Atomic Polarization P_a

By the combination of eq. 7.3, eq. 7.14 and eq. 7.4 one obtains for the atomic polarization P_a :

$$P_a \simeq P^{BRP} + \bar{b}(\pi_{se} P^{inj} - P^{BRP}) = P^{BRP} + \bar{b} \left(\frac{P^{inj}}{1 + \Delta P_{se}} - P^{BRP} \right). \quad (7.15)$$

In case of hydrogen, the calculation yields $\Delta P_{se} \simeq 0.033$, which is much smaller than one, so that the (small) uncertainty in ΔP_{se} can be neglected, when eq. 7.15 is used. Also the uncertainty in the injected polarization (eq. 6.67) is fairly small¹⁵⁰, so that the main uncertainties, that enter into the atomic polarization P_a , are Δb and $\Delta_{sys} P^{BRP}$, which are independent. For a value $\Delta_{sys} P^{BRP} = 0.009$ and $\pi_{wd}^{BRP} \simeq 0.98$ one obtains a total systematic uncertainty of

$$\Delta_{sys} P_a = \left((1 - \bar{b})^2 (\Delta_{sys} P^{BRP})^2 + (1 - \pi_{wd})^2 \pi_{se}^2 (P^{inj})^2 \Delta b^2 \right)^{\frac{1}{2}} \simeq 0.0183. \quad (7.16)$$

The obtained value for P_a itself is in average for the hydrogen data taking period of 1997: $P_a \simeq \pm 0.907$.

In case of Deuterium running, the target holding field of 335 mT during data taking is by a factor of 29 higher than the critical field B_C^D . Hence the spins of the deuterons and electrons are strongly decoupled. As shown in fig. 7.2, no nuclear relaxation can be measured above a storage cell temperature of about 55 K. Other measurements did not even show a decrease of P_z at the lowest possible temperature of 37 K. One can therefore neglect the sampling correction for wall depolarization. Also spin exchange relaxation is suppressed by the holding field with $1/x^2$, which is in case of deuterium by a factor of $\simeq 20$ smaller than for hydrogen and therefore below 0.2%. Hence the sampling correction of the measured polarization values equals unity in case of deuterium, as long as the temperature during data taking is well above a value, where relaxation is measurable.

¹⁴⁹During the periods of HERMES data taking.

¹⁵⁰Eq. 6.67 refers to the statistical uncertainty only. But since the relaxation measurements deliver high confidence, that the polarization loss by spin exchange and wall depolarization are well understood at the target working point, one has to assume, that the systematic uncertainty of P^{inj} and P^{BRP} are strongly positively correlated, so that it would be wrong to treat both as independent error contributions.

7.3 The Reduction of the Target Polarization by Recombination

The second factor besides P_a entering the target polarization is the total atomic fraction α_{tot} , which is defined by

$$\alpha_{tot} = \alpha_0 (\alpha_r + (1 - \alpha_r) \beta). \quad (7.17)$$

The calculation of the systematic uncertainty of α_{tot} is more difficult than for the atomic polarization, as a lot of covariances have to be taken into account. α_0 and α_r^{TGA} are given by eq. 3.35 and eq. 3.21 respectively¹⁵¹. Both values depend on the measured values of ϕ_a and ϕ_m and the determined calibration values of c_{rg} , ϕ_{ball} and β . Unfortunately one finds in eq. 3.25, that even ϕ_{ball} depends on ϕ_{rg} and therefore by eq. 3.23 on the calibration constant c_{rg} . It is therefore necessary to know the covariance of ϕ_{ball} and ϕ_{rg} or to use the independent values in eq. 3.25 and eq. 3.23, which are $\phi_m^{(i)}$, $\phi_a^{(i)}$, $p_{tc}^{(i)}$ and c_{rg} . Besides these values, the systematic uncertainty $\Delta_{sys}\alpha_{tot}$ depends on the measured values, that enter α_{tot} and on the values and uncertainties of κ , β and \bar{a} . If the matrix T is defined by

$$T = \left(\frac{\partial \alpha_{tot}}{\partial \phi_m^{(i)}}, \dots, \frac{\partial \alpha_{tot}}{\partial \bar{a}} \right) \quad (7.18)$$

and C is the (diagonal) covariance matrix of all calibration constants, then $\Delta_{sys}\alpha_{tot}$ is given by¹⁵²:

$$\Delta_{sys}\alpha_{tot} = (T C T^T)^{\frac{1}{2}}. \quad (7.19)$$

The matrix T contains a derivation for all independent determined calibration constants, as there are κ , β , \bar{a} , c_{rg} and all values entering into the calculation of ϕ_{ball} as there are $\phi_{a,m}^{(i)}$ and $p_{tc}^{(i)}$, which are in total 10. The calculation can to some extent be simplified, if

¹⁵¹As it was already presumed, that $\alpha_r^{TGA} \geq 0.9$ holds, one may also use eq. 3.36 instead of eq. 3.35.

¹⁵²One may also calculate the uncertainty in several steps, if one takes care to include always all non-diagonal elements of the covariance matrix.

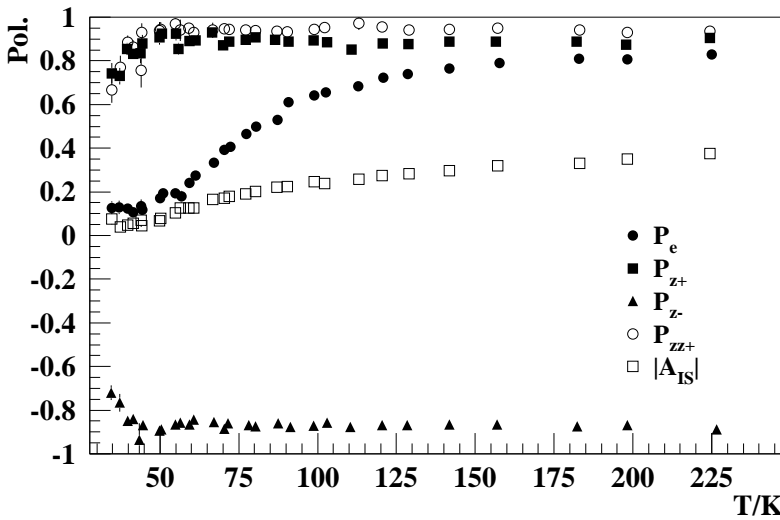


Fig. 7.2: Measured polarization values P_e of the corresponding injection modes and $|A_{IS}|$ for P_{zz+}^{inj} vs. storage cell temperature.

one uses the following formula for α_{tot} , that can be derived from eq. 7.17, eq. 3.21, eq. 7.14 and eq. 3.36:

$$\alpha_{tot} = \frac{\phi_a + (\bar{a}(1 - \beta) + \beta)(\phi_m - \phi_{ball} - \phi_{rg})}{\phi_a + \phi_m + (\sqrt{2} - 1)\phi_{ball} + (2\sqrt{2} - 1)\phi_{rg}}. \quad (7.20)$$

The influence of the values of $\phi_{a,m}^{(i)}$ and $p_{tc}^{(i)}$ enters exclusively the calculation of ϕ_{ball} , so that one may collect their uncertainties in a reduced uncertainty $\tilde{\Delta}\phi_{ball}$, which excludes the uncertainty of the rest gas calibration c_{rg} . The remaining derivatives, that are required, are:

$$\frac{\partial\alpha_{tot}}{\partial\kappa} = [(\bar{a}(1 - \beta) + \beta - \alpha_{tot})\phi_r - \alpha_{tot}\sqrt{2}(2\phi_{rg} + \phi_{ball})] / (\kappa N) \quad (7.21)$$

$$\frac{\partial\alpha_{tot}}{\partial c_{rg}} = - \left[(\bar{a}(1 - \beta) + \beta + (\sqrt{2} - 1)\alpha_{tot})(p_{tc} + \frac{\partial\phi_{ball}}{\partial c_{rg}}) + \alpha_{tot}\sqrt{2}p_{tc} \right] / N \quad (7.22)$$

$$\frac{\partial\alpha_{tot}}{\partial\phi_{ball}} = - [\bar{a}(1 - \beta) + \beta + (\sqrt{2} - 1)\alpha_{tot}] / N \quad (7.23)$$

$$\frac{\partial\alpha_{tot}}{\partial\bar{a}} = (1 - \beta)\phi_r / N \quad (7.24)$$

$$\frac{\partial\alpha_{tot}}{\partial\beta} = (1 - \bar{a})\phi_r / N, \quad (7.25)$$

where $N = \phi_a + \phi_m + (\sqrt{2} - 1)\phi_{ball} + (2\sqrt{2} - 1)\phi_{rg}$ is the denominator of eq. 7.20 and is proportional to the total amount of nucleons in the storage cell. The flow of molecules into the TGA caused by recombination ϕ_r is defined by eq. 3.20. The value of $\tilde{\Delta}\phi_{ball}$ and of the derivative $\frac{\partial\phi_{ball}}{\partial c_{rg}}$ can be derived from eq. 3.25:

$$\begin{aligned} \frac{\partial\phi_{ball}}{\partial c_{rg}} &= -(\phi_a^{(1)}p_{tc}^{(2)} - \phi_a^{(2)}p_{tc}^{(1)}) / (\phi_a^{(1)} - \phi_a^{(2)}) \\ \tilde{\Delta}\phi_{ball}^2 &= [(\phi_r^{(2)}\Delta\phi_a^{(1)})^2 + (\phi_r^{(1)}\Delta\phi_a^{(2)})^2 + (\phi_a^{(2)}\Delta\phi_m^{(1)})^2 + (\phi_a^{(1)}\Delta\phi_m^{(2)})^2 \\ &\quad + (\phi_a^{(2)}c_{rg}\Delta p_{tc}^{(1)})^2 + (\phi_a^{(1)}c_{rg}\Delta p_{tc}^{(2)})^2] / (\phi_a^{(1)} - \phi_a^{(2)})^2. \end{aligned} \quad (7.26)$$

For the fill in the night between 21st and 22nd sep. '97, the average measured and calculated results are listed as an example in tab. 7.2, that also lists the used calibration values.

For the 1997 running period, the analysis yielded for the estimated β -value of $\beta \simeq 0.6 \pm 0.4$ [Ko 98] the following average results and systematic uncertainties [Sto 2000]:

$$\begin{aligned} \alpha_0 &= 0.964 \pm 0.003 & \alpha_r &= 0.939 \pm 0.039 \\ P_{a+} &= 0.9050 \pm 0.0167 & P_{a-} &= -0.9072 \pm 0.0158 \\ P_{+}^T &= 0.8515 \pm 0.03 & P_{-}^T &= -0.8536 \pm 0.03 \end{aligned} \quad (7.27)$$

For the deuterium running period of 1999, some preliminary results are:

$$\begin{aligned} \alpha_0 &= 0.936 \pm 0.0057 & \alpha_r &= 0.966 \pm 0.006 \\ P_{a+} &= 0.892 \pm 0.018 & P_{a-} &= -0.893 \pm 0.011 \end{aligned} \quad (7.28)$$

Measurement		Calculation			value	$\Delta_{sys}\alpha_{tot}$
ϕ_a	46.63 ± 0.034	α^{TGA}	0.9674	\bar{a}	-0.683 ± 1.126	0.0042
ϕ_m	1.571 ± 0.025	α_r^{TGA}	0.99	β	0.6 ± 0.4	0.0063
p_{tc}	1.402 ± 0.0015	α_0	0.9573	κ	0.572 ± 0.0026	0.0002
ϕ_{rg}	0.373	α_r	0.9836	c_{rg}	0.2663 ± 0.0107	0.0054
		α_{tot}	0.951 ± 0.0094	ϕ_{ball}	0.739 ± 0.112	0.0016

Tab. 7.2: Left table: Measured values and statistical uncertainties during the fill (left column) and the calculated atomic fractions and the resulting systematical uncertainty of α_{tot} . The right table lists the used calibration constants, their uncertainties and the contributions to the uncertainty in α_{tot} . The fluxes are given in units of kHz/mA , the values of p_{tc} in 10^{-7} mbar and of c_{rg} in units of 10^{-7} mbar $kHz mA^{-1}$. The results show, that $\Delta_{sys}\alpha_{tot}$ is significantly lower for this HERA fill than in average for the complete data taking period (7.27). In combination with the estimated value of P_a one obtains $P^T = 0.8626 \pm 0.0206$ for the time of this fill.

The target polarization is about $P^T \simeq 0.82$ with a systematic uncertainty of $\Delta_{sys}P^T \simeq 0.02$. Due to the better quality of the storage cell surface and the higher decoupling, the factors, that lead to a reduction of the target polarization are α_0 and P^{inj} . For both, the sampling corrections are well known, so that the systematic uncertainty is dominated by the BRP calibration uncertainty in case of deuterium. As this uncertainty is basically of statistical nature¹⁵³, it can be reduced by improvements of the signal-to-background-ratio of the BRP signals in the future.

7.4 Summary

The sampling corrections of the atomic fraction c_α and polarization c_P have been discussed by the introduction of three different scenarios. The calculations, that are explained in detail in the appendix, delivered predictions for $\alpha_r(\alpha_r^{TGA})$ and $P_a(P_a^{BRP})$ for these scenarios. All scenarios have been approximated by first order expressions in case of low recombination and wall depolarization. An expression for the systematic uncertainty of P_a for hydrogen and for α_{tot} for both target gases has been derived. Arguments were given, that the systematical uncertainty of P_a in case of the deuterium target is dominated by the calibration of the BRP.

For the hydrogen data taking period of 1997, the analysis resulted a target polarization of ± 0.852 with a systematical uncertainty of ± 0.03 . The preliminary results for 1999 with deuterium are a target polarization of ± 0.82 and a systematical uncertainty of ± 0.02 .

¹⁵³The limiting factor of the precision is the time required for a calibration measurement.

8 Discussion and Outlook

The presented work gives an overview of the main technical and physical items of the HERMES target with special attention for those questions, that have consequences for the target polarization and its uncertainty.

The calibration of the Breit-Rabi type polarimeter has been discussed not only with respect to its polarization measurement, but also to the possibility to use it as an absolute monitor of the atomic beam intensity. For this purpose, the new technique of pulse modulated high frequency transitions has been developed, which enables to perform TOF measurements without a mechanical chopper. Effectively, it was shown, that the high frequency transitions can be used as a beam chopper. The results show, that the sextupole system of the BRP can be improved in order to obtain a higher absolute transmission - especially for measurements at storage cell temperatures below 100 K.

The same technique applied to a HFT of the ABS delivered a measurement of the diffusion time distribution of the atoms on their way through the storage cell, which was found to be in excellent agreement with the results of a molecular flow simulation. This measurement was the first direct verification of the simulated results and gives some confidence, that the assumption of diffusive desorption is correct. If this measurement is repeated using six or more different states of the BRP transitions, the time dependence of the hyperfine population after a flip of the injection mode can be measured with the resolution of a few *ms*. A measurement of this type was not presented, as it does not match into the frame of this work. A second option of this technique would require lower storage cell temperatures than possible with the current setup: The measurement of the sticking/correlation time at low temperatures. In fact, a possibility to measure the high temperature limits of the sticking and correlation time would close a huge lack of knowledge and would deliver very useful information - even though there is no strong indication, that the estimated values are unrealistic.

A detailed analysis of the recombination and spin relaxation processes has been presented, that is able to consistently describe the measurements within the range of physical conditions, that can be realized at the HERMES target.

The recombination process at the HERMES target has been analyzed and modeled before by Kolster [Ko 98] on the basis of the recombination theory of Gelb and Kim [Gel 71]. Some aspects had to be reinterpreted: The theory of Gelb and Kim neglects the possibility of reactions between physisorbed atoms with the surface (precursor mediated reaction) and of L-H type reactions between physisorbed atoms. The missing density dependence of recombination at low temperatures and fresh surfaces requires however an explanation by a different process than E-R reactions of atoms from the gas phase with physisorbed atoms. This process was found to be likely reactions of physisorbed atoms with the atoms of the Drifilm by tunneling. Additionally, it was found that an E-R process can only explain the amount of density dependent recombination at low temperatures, if much higher sticking times are assumed, which is in contradiction to the diffusion time measurement. The density dependent process was therefore identified with L-R type reactions between physisorbed atoms, which get in contact by surface diffusion. Nevertheless, the interpretation of the high temperature behavior by an E-R process with a covered monolayer was found to be in agreement with the data. The covered monolayer was identified with the hydrogen atoms in the methylgroups of the Drifilm coating.

The change in the temperature dependence of the recombination rate at low temperatures could be explained by a change of the surface coating due to continuous irradiation of the target cell by the HERA beam, causing the Drifilm to lose more and more its hydrophobic properties. The surface gets then covered by water, that prevents tunneling reactions of physisorbed atoms with the Drifilm coating.

It turned out, that the conventional first order theory [Bou 63, Bou 65, Br 95] of wall depolarization had to be modified in order to describe the low temperature data for both - electron and nuclear polarization. Instead of an interpretation in terms of the spectral density [Ko 98], which is in disagreement with the magnetic field dependence at low temperatures, it was shown, that the data are reasonably consistent with a modified relaxation theory based on the formula of Rabi.

In case of hydrogen indications have been found for a non-zero electron polarization in thermal equilibrium at low temperature, that might be explained by unexpected (ferro-) magnetic properties of the surface. These effects are likely caused by the (verified) iron contamination of the surface. Another possibility is the existence of super-paramagnetic clusters within the Drifilm itself. In case of deuterium, clear evidence for such effects was not found, but this can also be related to a reduced signal to noise ratio within the BRP detector, which is caused by residual H_2 gas, that is continuously evaporated by the titanium sublimation pump.

A ratio of $\tau_s^0/\tau_c^0 \gg 1$, which was indicated by the measurements of both - recombination and spin relaxation, can be understood, if desorption - the transition from a bound state into an unbound state - is most probable for atoms in excited bound states. Even though it is questionable, if the concept of a constant oscillator frequency makes sense, if the potential is far from being harmonic for the excited states - one can expect an increased period of oscillation τ_s^0 , if one focuses on the reduction of attractive part of the potential slope in larger distances to the surface, that is only relevant for excited atoms. The potential barrier for jump diffusion on the other side is only relevant for atoms in the lower energy states, where the potential slope and therefore the driving force of oscillation is high. This is illustrated by fig. 5.1. If this argument is valid, then $\tau_s^0 \geq \tau_c^0$ seems to be a plausible consequence.

One of the questions, that arises naturally from the measurements and their interpretation is, why Drifilm (or other hydrocarbons) should be the favorite material for surface coatings of storage cells. The recombination measurements indicate, that Drifilm is not that radiation resistant, that it is not damaged by the HERA beam. In addition, the binding energy of the hydrogen atoms in methyl groups is below the binding energy of the H_2 bond, so that it is possible for the hydrogen radicals to break surface bonds and thus to produce unpaired electrons, which increase spin relaxation by their strong magnetic moments. With respect to recombination and spin relaxation, ionic crystals like LiF have promising properties. The binding energy of LiF for physisorbed hydrogen/deuterium was determined by Finzel *et al* [Fin 75] to be $12.2\text{ meV}/14.0\text{ meV}$ and only about half of the measured value for Drifilm of 23 meV . The bond strength of (diatomic) $Li - F$ is above the bond strength of $H - F$, $H - Li$ and $H - H$ [Lid 98], so that hydrogen radicals are at low temperatures not able to react with a LiF surface. If one takes these factors into account, it seems reasonable to propose tests with LiF (or similar ionic crystals) as a coating material.

A Results of Deuterium Spin Relaxation

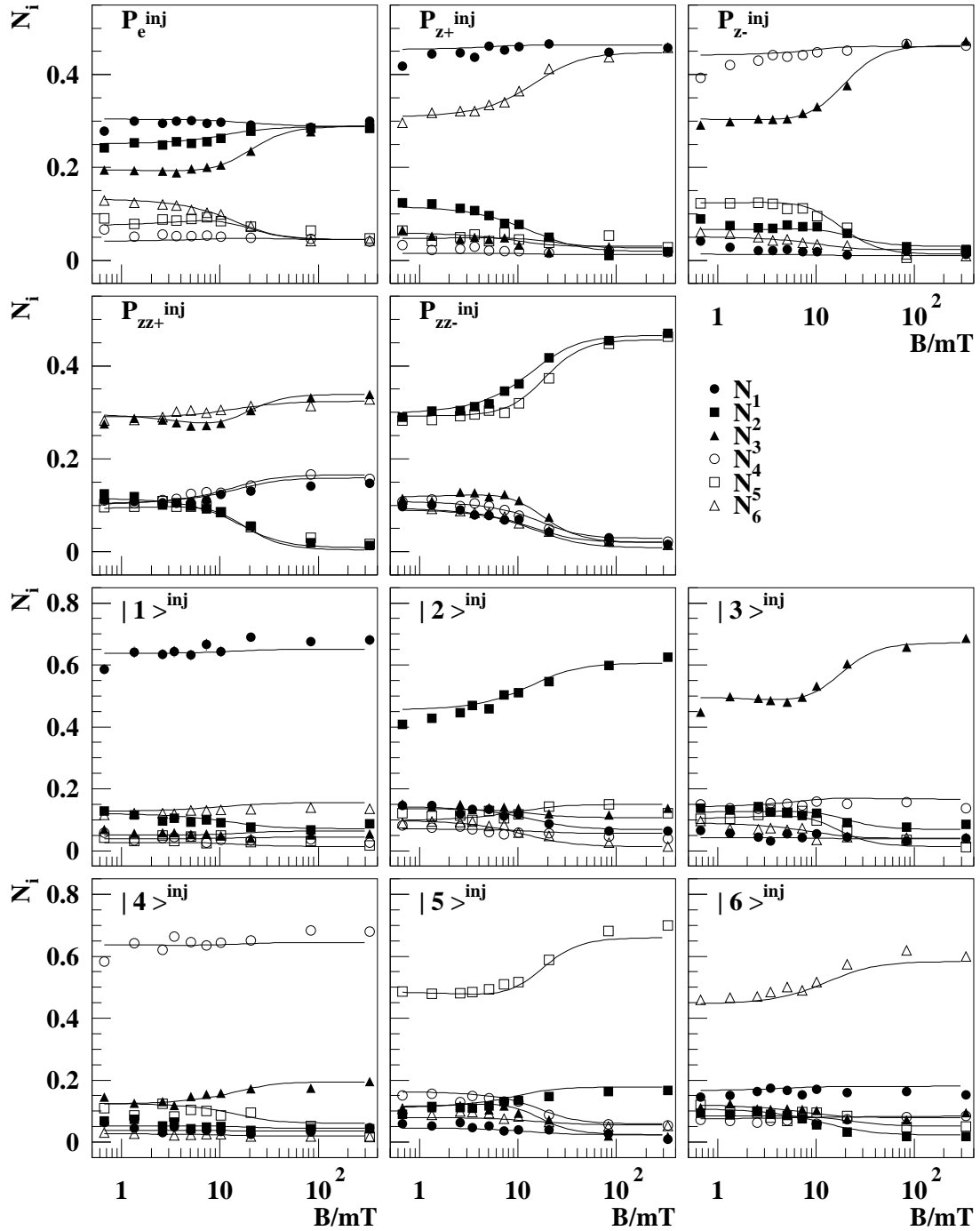


Fig. A.1: Hyperfine population of deuterium vs. magnetic holding field for the injection modes of tab. 3.2. The symbols represent the measured results and the lines the fit with the spin relaxation model of eq. 6.1. The storage cell temperature of this measurement was 135 K.

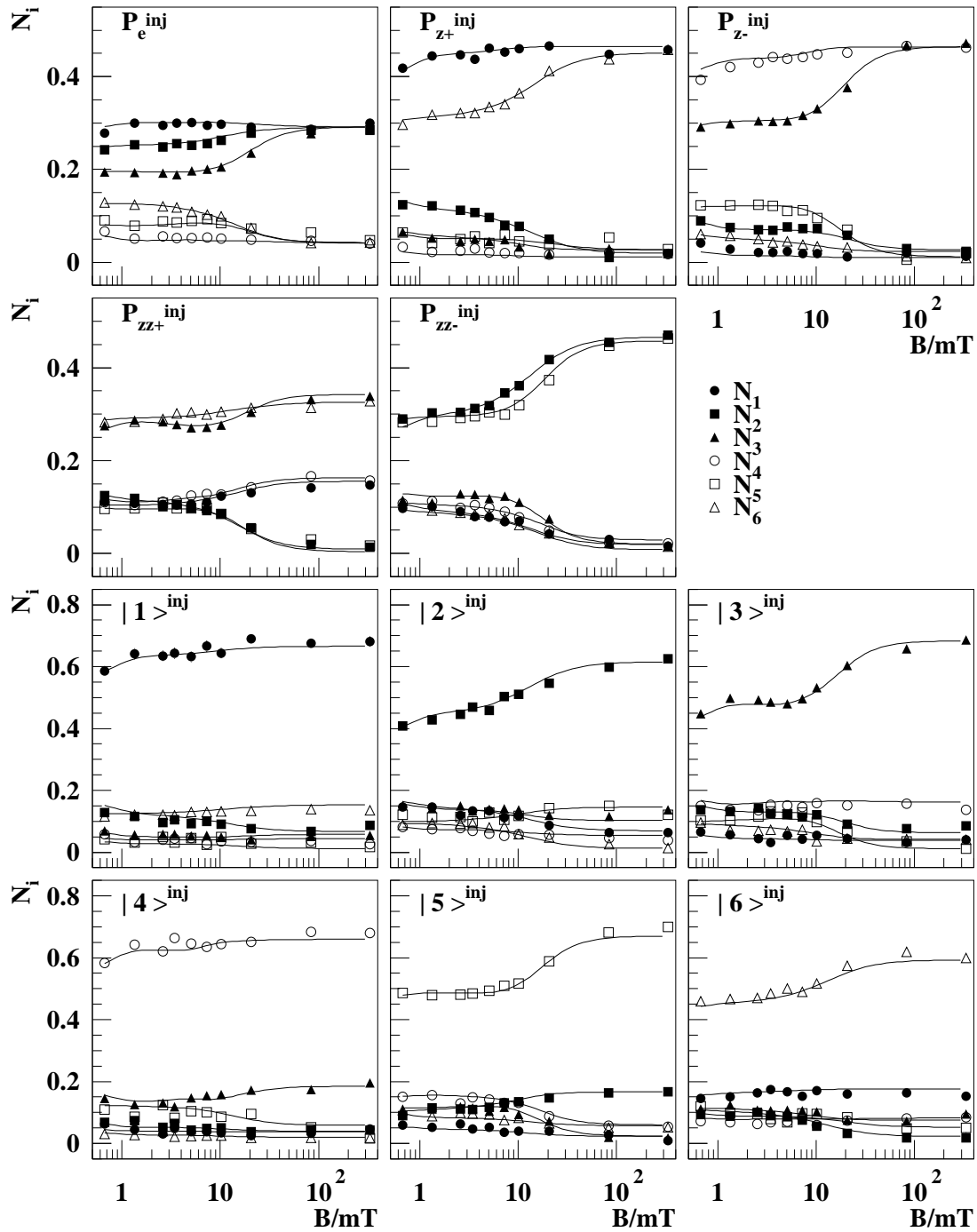


Fig. A.2: Same measurement as shown in fig. A.1. An artificially stepwise increased spectral density was used to describe the behavior at low fields (see sec. 6.10.4).

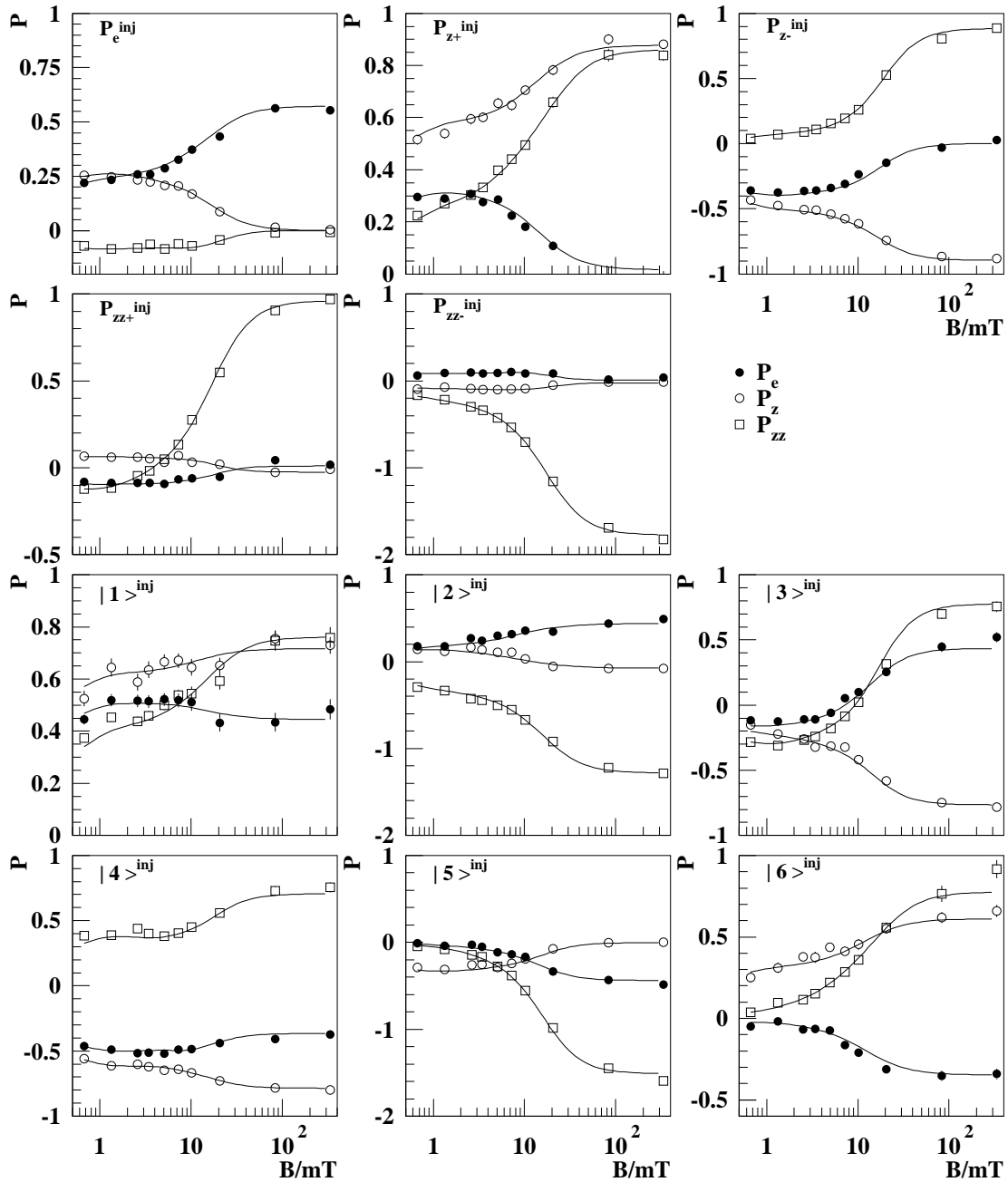


Fig. A.3: Measured and fitted polarization values P_e , P_z and P_{zz} vs. magnetic holding field for a storage cell temperature of 95 K. An artificially stepwise increased spectral density was used to describe the behavior at low fields (see sec. 6.10.4).

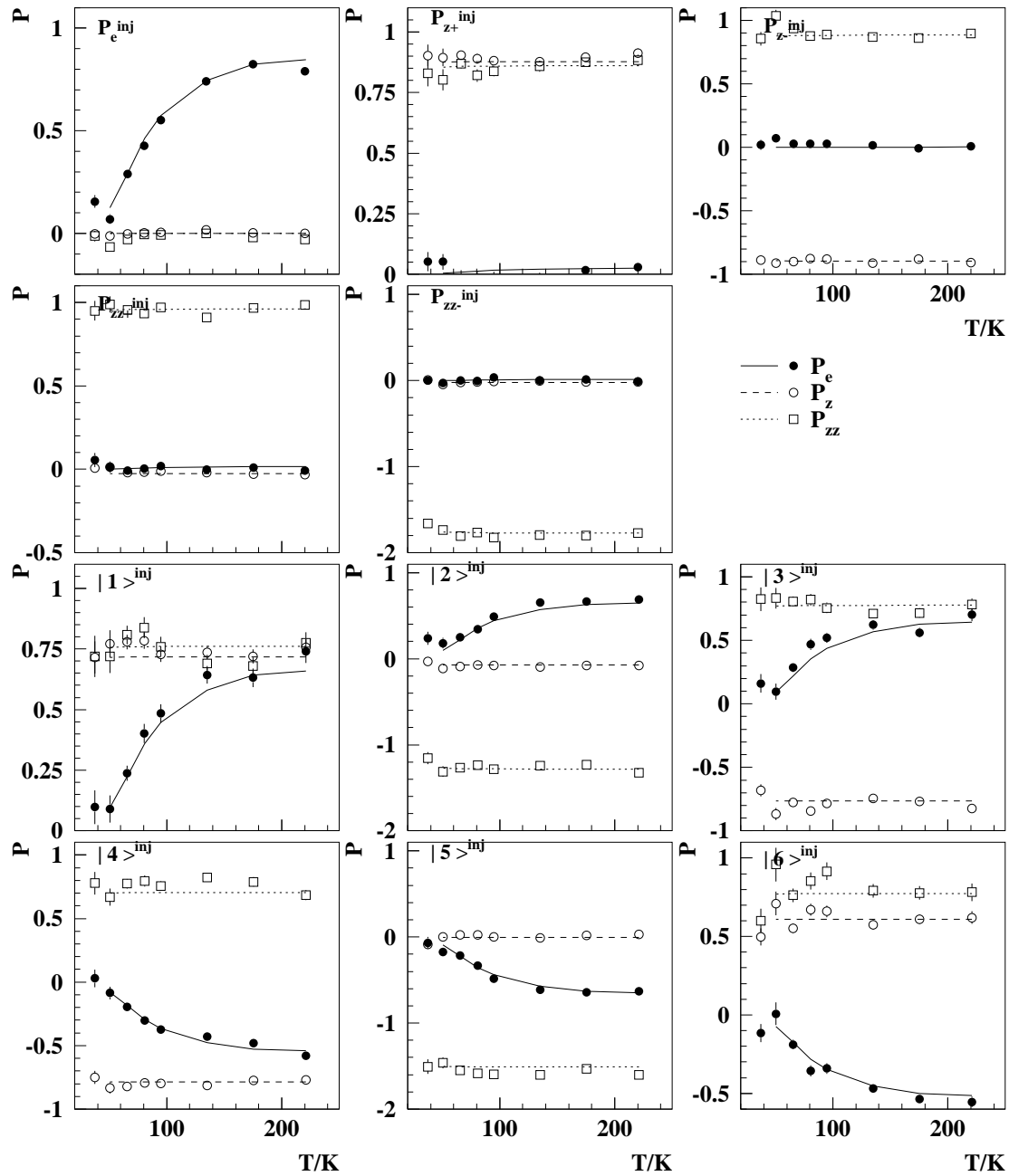


Fig. A.4: Polarization values P_e , P_z and P_{zz} of deuterium at a magnetic holding field of 335 mT vs. storage cell temperature for the injection modes of tab. 3.2. The symbols represent the measured results and the lines the fit with the spin relaxation model of eq. 6.1.

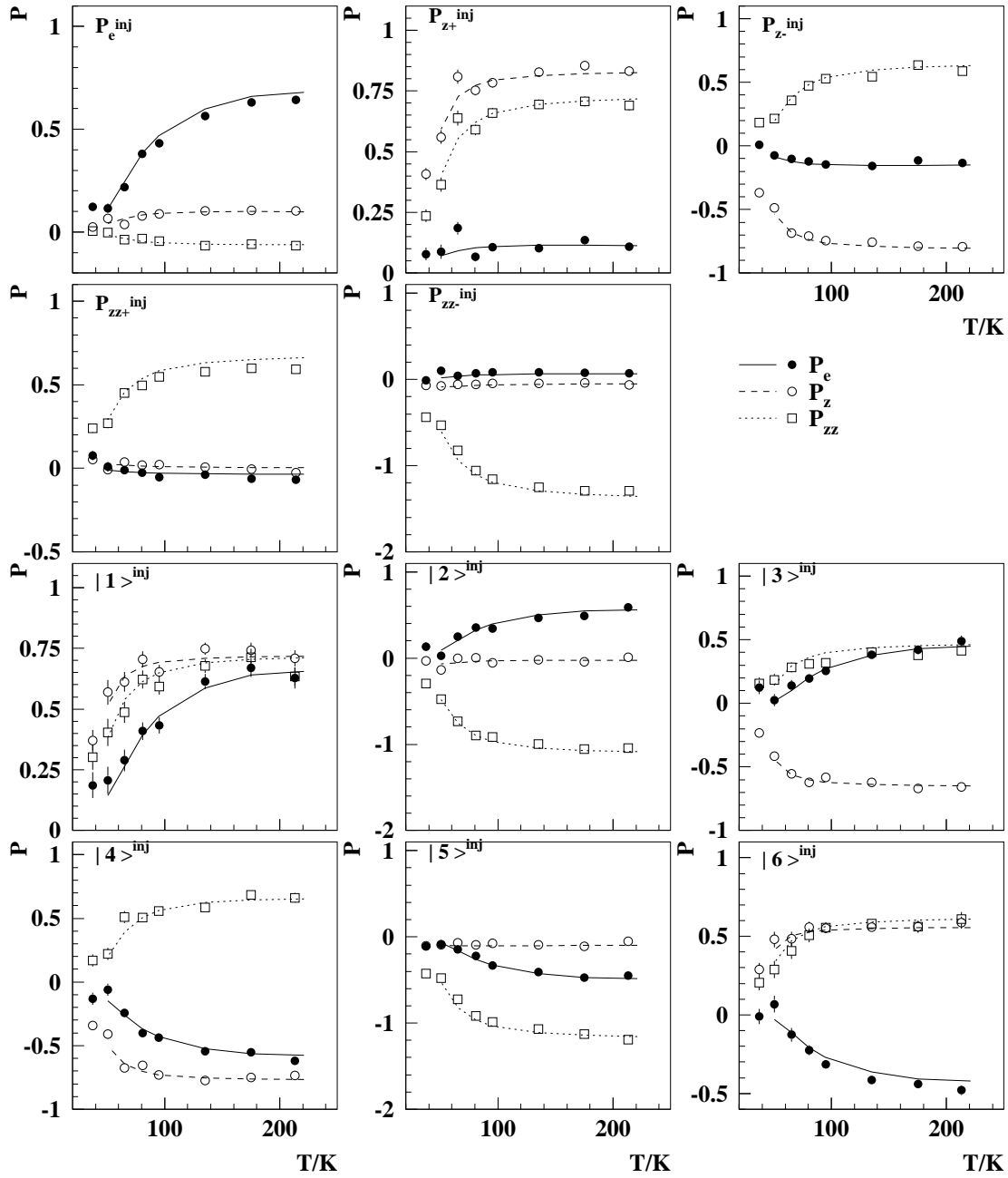


Fig. A.5: Polarization values P_e , P_z and P_{zz} of deuterium at a magnetic holding field of 20.6 mT vs. storage cell temperature.

B The Hyperfine Structure of Hydrogen and Deuterium

B.1 The Diagonalization of the Static Hamiltonian

The product $\vec{I}\vec{S}$, which appears as the first term in eq. 2.1, can be written as

$$\vec{I}\vec{S} = I_z S_z + \frac{1}{2}(I_+ S_- + I_- S_+), \quad (\text{B.1})$$

where $I_{\pm} = I_x \pm iI_y$ and $S_{\pm} = S_x \pm iS_y$. In matrix representation this product can be written in the following way:

$$\vec{I}\vec{S} = \frac{\hbar^2}{4} \begin{pmatrix} \text{Hydrogen} \\ 1 & 0 & 0 & 0 \\ 0 & -1 & 0 & 2 \\ 0 & 0 & 1 & 0 \\ 0 & 2 & 0 & -1 \end{pmatrix} \quad \vec{I}\vec{S} = \frac{\hbar^2}{2} \begin{pmatrix} \text{Deuterium} \\ 1 & & & 0 \\ & 0 & & \sqrt{2} \\ & & -1 & 0 \\ & & 0 & 1 \\ & 0 & \sqrt{2} & 0 \\ 0 & \sqrt{2} & & -1 \end{pmatrix}. \quad (\text{B.2})$$

For the terms, which represent the interaction with the external field, one finds:

$$\vec{S}\vec{B} = S_z B_z + \frac{1}{2}S_+(B_x - iB_y) + \frac{1}{2}S_-(B_x + iB_y). \quad (\text{B.3})$$

In case of a static magnetic field in z -direction, the static Hamiltonian \mathcal{H}_0^{ST} for \vec{H} is given by:

$$\mathcal{H}_0^{ST} = \frac{\mathcal{A}_H \hbar^2}{4} \begin{pmatrix} 1 + 2x(1 - \epsilon) & 0 & 0 & 0 \\ 0 & -1 + 2x(1 + \epsilon) & 0 & 2 \\ 0 & 0 & 1 - 2x(1 - \epsilon) & 0 \\ 0 & 2 & 0 & -1 - 2x(1 + \epsilon) \end{pmatrix},$$

and for \vec{D} :

$$\mathcal{H}_0^{ST} = \frac{\mathcal{A}_D \hbar^2}{2} \begin{pmatrix} 1 + \frac{3}{2}x(1 - 2\epsilon) & 0 & 0 & 0 & 0 & 0 \\ 0 & \frac{3}{2}x & 0 & 0 & 0 & \sqrt{2} \\ 0 & 0 & -1 + \frac{3}{2}x(1 + 2\epsilon) & 0 & \sqrt{2} & 0 \\ 0 & 0 & 0 & 1 - \frac{3}{2}x(1 - 2\epsilon) & 0 & 0 \\ 0 & 0 & \sqrt{2} & 0 & 0 & -\frac{3}{2}x \\ 0 & \sqrt{2} & 0 & 0 & 0 & -1 - \frac{3}{2}x(1 + 2\epsilon) \end{pmatrix}.$$

Where x is defined by $x = \frac{B_z}{B_C}$ with the *critical field* B_C defined by eq. 2.3. ϵ is the correction term for the energy of the nucleus, given by $\epsilon = \frac{Sg_I \mu_K}{I g_S \mu_B}$. The diagonalisation of the static Hamiltonian \mathcal{H}_0^{ST} is performed with an orthogonal transformation:

$$\mathcal{H}_1^{ST} = U_0^T \mathcal{H}_0^{ST} U_0, \quad (\text{B.4})$$

where the transformation matrix U_0 is given by:

Hydrogen	Deuterium
$\cos \theta = \sqrt{\frac{1}{2}(1 + \cos 2\theta)}$ $\sin \theta = \sqrt{\frac{1}{2}(1 - \cos 2\theta)}$ $\cos 2\theta = \frac{x(1 + \epsilon)}{\sqrt{x^2(1 + \epsilon)^2 + 1}}$ $\sin 2\theta = \frac{1}{\sqrt{x^2(1 + \epsilon)^2 + 1}}$	$\cos \theta_{\pm} = \sqrt{\frac{1}{2}(1 + \cos 2\theta_{\pm})}$ $\sin \theta_{\pm} = \sqrt{\frac{1}{2}(1 - \cos 2\theta_{\pm})}$ $\cos 2\theta_{\pm} = \frac{3x(1 + 2\epsilon) \pm 1}{\sqrt{(3x(1 + 2\epsilon) \pm 1)^2 + 8}}$ $\sin 2\theta_{\pm} = \frac{\sqrt{8}}{\sqrt{(3x(1 + 2\epsilon) \pm 1)^2 + 8}}.$
$E_1 = \frac{E_{HFS}^H}{4} (1 + 2x(1 - \epsilon))$ $E_2 = \frac{E_{HFS}^H}{4} \left(-1 + 2\sqrt{x^2(1 + \epsilon)^2 + 1} \right)$ $E_3 = \frac{E_{HFS}^H}{4} (1 - 2x(1 - \epsilon))$ $E_4 = \frac{E_{HFS}^H}{4} \left(-1 - 2\sqrt{x^2(1 + \epsilon)^2 + 1} \right)$ $E_{HFS}^H = \mathcal{A}_H \hbar^2$	$E_1 = \frac{E_{HFS}^D}{3} \left(1 + \frac{3}{2}x(1 - 2\epsilon) \right)$ $E_2 = \frac{E_{HFS}^D}{6} \left(-1 + \sqrt{9x^2(1 + 2\epsilon)^2 + 6x(1 + 2\epsilon) + 9} \right)$ $E_3 = \frac{E_{HFS}^D}{6} \left(-1 + \sqrt{9x^2(1 + 2\epsilon)^2 - 6x(1 + 2\epsilon) + 9} \right)$ $E_4 = \frac{E_{HFS}^D}{3} \left(1 - \frac{3}{2}x(1 - 2\epsilon) \right)$ $E_5 = \frac{E_{HFS}^D}{6} \left(-1 - \sqrt{9x^2(1 + 2\epsilon)^2 - 6x(1 + 2\epsilon) + 9} \right)$ $E_6 = \frac{E_{HFS}^D}{6} \left(-1 - \sqrt{9x^2(1 + 2\epsilon)^2 + 6x(1 + 2\epsilon) + 9} \right)$ $E_{HFS}^D = \frac{3}{2} \mathcal{A}_D \hbar^2$

Tab. B.1: Mixing coefficients and eigenenergies of the hyperfine states of hydrogen and deuterium.

$$\begin{array}{c}
 \text{Hydrogen} \\
 U_0 = \begin{pmatrix} 1 & 0 & 0 & 0 \\ 0 & \cos \theta & 0 & -\sin \theta \\ 0 & 0 & 1 & 0 \\ 0 & \sin \theta & 0 & \cos \theta \end{pmatrix}
 \end{array}
 \quad
 \begin{array}{c}
 \text{Deuterium} \\
 U_0 = \begin{pmatrix} 1 & 0 & 0 & 0 & 0 & 0 \\ 0 & \cos \theta_+ & 0 & 0 & 0 & -\sin \theta_+ \\ 0 & 0 & \cos \theta_- & 0 & -\sin \theta_- & 0 \\ 0 & 0 & 0 & 1 & 0 & 0 \\ 0 & 0 & \sin \theta_- & 0 & \cos \theta_- & 0 \\ 0 & \sin \theta_+ & 0 & 0 & 0 & \cos \theta_+ \end{pmatrix}.
 \end{array}
 \quad (\text{B.5})$$

The mixing coefficients and the eigenvalues are listed in tab. B.1. Fig. 2.1 shows the graphs of the energy levels of hydrogen and deuterium versus the static holding field.

As U_0 is orthogonal and thus $U_0^T U_0 = \mathbf{1}$ holds, the Schrödinger equation for the system

$$i\hbar \dot{\Psi} = H \Psi \quad (\text{B.6})$$

transforms by multiplication with U_0^T from the left side into

$$i\hbar \left(\dot{U}_0^T \Psi + U_0^T \dot{\Psi} \right) = \left(U_0^T \mathcal{H} U_0 + i\hbar \dot{U}_0^T U_0 \right) U_0^T \Psi; \quad (\text{B.7})$$

and by the usage of a new basis, which is given by $\chi = U_0^T \Psi$, one gets:

$$i\hbar \dot{\chi} = \left(\mathcal{H}_1^{ST} + i\hbar \dot{U}_0^T U_0 \right) \chi. \quad (\text{B.8})$$

\mathcal{H}_1^{ST} denotes the diagonal static Hamiltonian. As the field is assumed to be constant in time $\dot{B}_z = 0$, also the *mixing angles* θ or θ_{\pm} are constant in time. In this case the term $\dot{U}_0^T U_0$ vanishes and the vectors of the new basis, which is called *Breit-Rabi-Basis*, are the eigenstates of the static Hamiltonian \mathcal{H}_1^{ST} . This vectors, which are also eigenstates of the operator $F_z = S_z + I_z$ (and for $B \rightarrow 0$ of $\vec{F}^2 = (\vec{S} + \vec{I})^2$), are given in sec. 2.1.

B.2 Hyperfine Transitions

Using the eigen energies of tab. B.1, one can calculate the field values, that match the resonance condition (eq. 2.11.). The results are listed in tab. B.2.

B.2.1 σ -Transitions

If the holding field changes with time, the second term of eq. B.8, does not vanish as it represents the distortion of the eigenstates, if they experience a change in the value of B_z . We will call this term the *sigma*-term or \mathcal{H}_1^σ as it is responsible for σ -transitions, where the field is parallel to the static holding field. The matrix multiplication results, that only the following elements of the term $i\hbar\dot{U}_0^T U_0$ remain¹⁵⁴ in case of Hydrogen:

$$\begin{aligned}\{\mathcal{H}_1^\sigma\}_{ab} &= \{i\hbar\dot{U}_0^T U_0\}_{ab} \\ \{\mathcal{H}_1^\sigma\}_{24}^H &= -\{\mathcal{H}_1^\sigma\}_{42}^H = i\hbar(c\dot{s} - \dot{c}s) = -i\hbar\frac{\sin^2 2\theta}{2} \frac{\dot{B}_z}{B_C^H},\end{aligned}$$

where $c = \cos\theta$ and $s = \sin\theta$. In case of deuterium, where $c_\pm = \cos\theta_\pm$ and $s_\pm = \sin\theta_\pm$ is used, the following matrix elements are non-zero:

$$\begin{aligned}\{\mathcal{H}_1^\sigma\}_{35}^D &= -\{\mathcal{H}_1^\sigma\}_{53}^D = i\hbar(c_- \dot{s}_- - \dot{c}_- s_-) \\ \{\mathcal{H}_1^\sigma\}_{26}^D &= -\{\mathcal{H}_1^\sigma\}_{62}^D = i\hbar(c_+ \dot{s}_+ - \dot{c}_+ s_+) \\ c_\pm \dot{s}_\pm - \dot{c}_\pm s_\pm &= -\frac{3}{4\sqrt{2}} \sin^2 2\theta_\pm \frac{\dot{B}_z}{B_C}.\end{aligned}$$

¹⁵⁴The terms, which are proportional to ϵ , are neglected in the following calculations as $\epsilon \ll 1$. For the same reason, factors $1 + \epsilon$ are replaced by 1.

Hydrogen	Deuterium
$y = 4 \frac{E_a - E_b}{E_{HFS}}$	$y = 3 \frac{E_a - E_b}{E_{HFS}}$
$r_\pm = \sqrt{(y \pm 2)^2 (1 - \epsilon)^2 + 4\epsilon y (y \pm 4)}$	$r_\pm = \sqrt{(y - 2\epsilon(y - 2) \pm 1)^2 + 8\epsilon y (y \pm 3)}$
$x_{12} = \frac{1}{8\epsilon} (2 + \epsilon(y - 2) - y - r_-)$	$x_{12} = \frac{1}{12\epsilon} (1 + 2\epsilon(y - 2) - y - r_-)$
$x_{34} = \frac{1}{8\epsilon} (-2 - \epsilon(y - 2) + y - r_-)$	$x_{45} = \frac{1}{12\epsilon} (-1 - 2\epsilon(y - 2) + y - r_-)$
$x_{23} = \frac{1}{8\epsilon} (-2 + \epsilon(y + 2) - y + r_+)$	$x_{16} = \frac{1}{12\epsilon} (1 + 2\epsilon(y - 2) - y + r_-)$
$x_{14} = \frac{1}{8\epsilon} (2 + \epsilon(y - 2) - y + r_-)$	$x_{25} = x_{36} = \frac{y}{3} \sqrt{\frac{y^2 - 9}{(1 + 2\epsilon)^2 (y^2 - 1)}}$
$x_{24} = \frac{1}{4} \frac{\sqrt{y^2 - 16}}{1 + \epsilon}$	$x_{26} = \frac{1}{3} \frac{\sqrt{y^2 - 8 - 1}}{1 + \epsilon}$
	$x_{35} = \frac{1}{3} \frac{\sqrt{y^2 - 8 + 1}}{1 + \epsilon}$
	$x_{34} = \frac{1}{12\epsilon} (-1 + 2\epsilon(y + 2) - y + r_+)$

Tab. B.2: Magnetic holding field values of hyperfine transitions of hydrogen and deuterium.

Where $\dot{c}c + \dot{s}s = 0$ (and correspondingly for \vec{D}) causes all diagonal terms to vanish. If B_z is given by $B_z = B_z^0 + b_z \cos \omega t$, and one defines $y_\sigma = \frac{b_z}{B_C}$, one obtains for \mathcal{H}_1^σ :

$$\begin{aligned} \{\mathcal{H}_1^\sigma\}_{24}^H &= -\{\mathcal{H}_1^\sigma\}_{42}^H = i\hbar\omega \frac{\sin^2 2\theta}{2} y_\sigma \sin \omega t \\ \{\mathcal{H}_1^\sigma\}_{35}^D &= -\{\mathcal{H}_1^\sigma\}_{53}^D = i\hbar\omega \frac{3}{\sqrt{8}} \frac{\sin^2 2\theta_-}{2} y_\sigma \sin \omega t \\ \{\mathcal{H}_1^\sigma\}_{26}^D &= -\{\mathcal{H}_1^\sigma\}_{62}^D = i\hbar\omega \frac{3}{\sqrt{8}} \frac{\sin^2 2\theta_+}{2} y_\sigma \sin \omega t. \end{aligned} \quad (\text{B.9})$$

There are two σ -transitions in case of \vec{D} , namely $|3\rangle \leftrightarrow |5\rangle$ and $|2\rangle \leftrightarrow |6\rangle$, and one in case of \vec{H} , which is the $|2\rangle \leftrightarrow |4\rangle$ transition. The matrix elements are given by eq. B.9. Obviously, σ -transitions are only possible between the corresponding mixed states. In a strong holding field, the spins of electron and nucleus are more and more decoupled, and the matrix element of the σ -transition are in this case of the same size as the matrix element for pure nuclear transitions.

B.2.2 π -Transitions

In order to describe π -transitions, it is necessary to go back to eq. 2.1 and calculate the terms, which result in case, that either $B_x \neq 0$ or $B_y \neq 0$. If one choses $B_x \neq 0$, the Hamilton operator \mathcal{H}_0 is given by

$$\mathcal{H}_0 = \mathcal{H}_0^{ST} + \mathcal{H}_0^\pi. \quad (\text{B.10})$$

Correspondingly, the π -operator has to be transformed into the Breit-Rabi basis:

$$\mathcal{H}_1^\pi = U_0^T \mathcal{H}_0^\pi U_0. \quad (\text{B.11})$$

If one neglects again the terms, which contain a factor ϵ , the calculation yields with $\frac{B_x}{B_C} = y_\pi \cos \omega t = \tilde{y}_\pi$ for \vec{H} :

$$\mathcal{H}_1^\pi = \frac{E_{HFS}^H}{2} \tilde{y}_\pi \begin{pmatrix} 0 & \sin \theta & 0 & \cos \theta \\ \sin \theta & 0 & \cos \theta & 0 \\ 0 & \cos \theta & 0 & -\sin \theta \\ \cos \theta & 0 & -\sin \theta & 0 \end{pmatrix} \quad (\text{B.12})$$

and in case of \vec{D} :

$$\mathcal{H}_1^\pi = \frac{E_{HFS}^D}{2} \tilde{y}_\pi \begin{pmatrix} 0 & s_+ & 0 & 0 & 0 & c_+ \\ s_+ & 0 & s_- c_+ & 0 & c_- c_+ & 0 \\ 0 & s_- c_+ & 0 & c_- & 0 & -s_+ s_- \\ 0 & 0 & c_- & 0 & -s_- & 0 \\ 0 & c_- c_+ & 0 & -s_- & 0 & -s_+ c_- \\ c_+ & 0 & -s_- s_+ & 0 & -s_+ c_- & 0 \end{pmatrix} \quad (\text{B.13})$$

If the situation can be described by a particle in a static holding field B_z , which experiences a periodic high frequency field $B_x \cos \omega t$ for a certain time period τ , then the transition probability $W_{a \rightarrow b}$ is in first order given by [Mes 90]:

$$W_{a \rightarrow b} \simeq y_{\pi, \sigma}^2 |V_{ab}|^2 f(\omega_{ab} - \omega, \tau), \quad (\text{B.14})$$

where V_{ab} is defined by

$$V_{ab} = \frac{\{\mathcal{H}_1^{\pi, \sigma}\}_{ab}}{\tilde{y}_{\pi, \sigma}}, \quad (\text{B.15})$$

and the function $f(\omega, t)$ by:

$$f(\omega, t) = \left| \int_0^t d\tau \exp(i\omega\tau) \right|^2 = 2 \frac{1 - \cos(\omega t)}{\omega^2}. \quad (\text{B.16})$$

For a long interaction time $\tau \gg \frac{1}{\nu}$, the function $f(\omega, t)$ can be replaced by Dirac's δ -function times the interaction time τ squared. This is equivalent to the requirement of exact resonance $\omega = \omega_{ab}$:

$$W_{a \rightarrow b} \simeq y_{\pi, \sigma}^2 \tau^2 \omega_{HFS}^2 |V_{ab}|^2. \quad (\text{B.17})$$

The resonance condition results in case of the σ -transitions:

$$\begin{aligned} \omega_{24} &= \frac{E_2 - E_4}{\hbar} = \frac{\omega_{HFS}^H}{\sin 2\theta} \\ \omega_{35} &= \frac{E_3 - E_5}{\hbar} = \frac{\sqrt{8}}{3} \frac{\omega_{HFS}^D}{\sin 2\theta_-} \\ \omega_{26} &= \frac{E_2 - E_6}{\hbar} = \frac{\sqrt{8}}{3} \frac{\omega_{HFS}^D}{\sin 2\theta_+}. \end{aligned}$$

The transition probability matrix W_{ab}^{155} is then for \vec{H} given by:

$$W_{ab}^H = \frac{\tau^2 (\omega_{HFS}^H)^2}{4} \begin{pmatrix} 0 & y_\pi^2 \sin^2 \theta & 0 & y_\pi^2 \cos^2 \theta \\ y_\pi^2 \sin^2 \theta & 0 & y_\pi^2 \cos^2 \theta & y_\sigma^2 \sin^2 2\theta \\ 0 & y_\pi^2 \cos^2 \theta & 0 & y_\pi^2 \sin^2 \theta \\ y_\pi^2 \cos^2 \theta & y_\sigma^2 \sin^2 2\theta & y_\pi^2 \sin^2 \theta & 0 \end{pmatrix}. \quad (\text{B.18})$$

The calculation results for deuterium transitions:

$$W_{ab}^D = \frac{\tau^2 (\omega_{HFS}^D)^2}{4} \begin{pmatrix} 0 & y_\pi^2 s_+^2 & 0 & 0 & 0 & y_\pi^2 c_+^2 \\ y_\pi^2 s_+^2 & 0 & y_\pi^2 s_-^2 c_+^2 & 0 & y_\pi^2 c_-^2 c_+^2 & y_\sigma^2 \sin^2 2\theta_+ \\ 0 & y_\pi^2 s_-^2 c_+^2 & 0 & y_\pi^2 c_-^2 & y_\sigma^2 \sin^2 2\theta_- & y_\pi^2 s_+^2 s_-^2 \\ 0 & 0 & y_\pi^2 c_-^2 & 0 & y_\pi^2 s_-^2 & 0 \\ 0 & y_\pi^2 c_-^2 c_+^2 & y_\sigma^2 \sin^2 2\theta_- & y_\pi^2 s_-^2 & 0 & y_\pi^2 s_+^2 c_-^2 \\ y_\pi^2 c_+^2 & y_\sigma^2 \sin^2 2\theta_+ & y_\pi^2 s_-^2 s_+^2 & 0 & y_\pi^2 s_+^2 c_-^2 & 0 \end{pmatrix}. \quad (\text{B.19})$$

B.2.3 Adiabatic High Frequency Transitions

Adiabatic high frequency transitions are used to exchange the hyperfine population of typically two hyperfine states¹⁵⁶. They can reach exchange efficiencies close to 100%. An adiabatic transition is realized, if atoms pass a high frequency transition by the slow passage through an increasing or decreasing magnetic field $B_z(x) = B_z(0) + B_{gr} v_x t$, which is superposed to the magnetic high frequency field B_{hf} . Fig. B.1 shows the resonance frequencies for hydrogen transitions as a function of the static field. In order to obtain a precise understanding of the way

¹⁵⁵The first order approximation is symmetric: $W_{a \rightarrow b} = W_{b \rightarrow a}$.

¹⁵⁶Multiple MFTs can also effectively *rotate* the hyperfine population of 3 or more states.

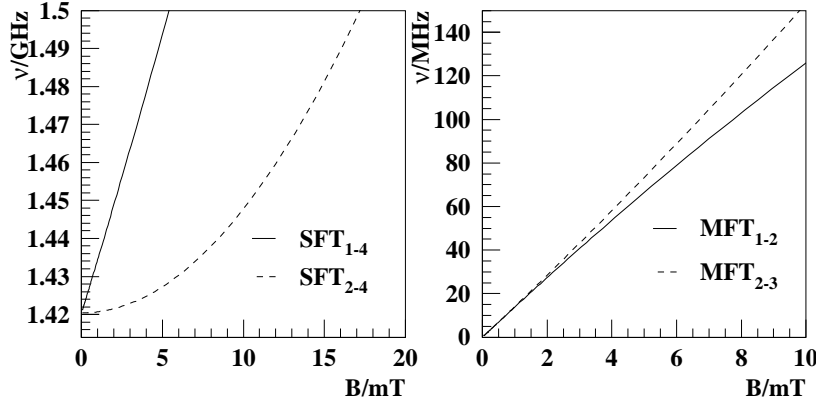


Fig. B.1: Hydrogen transition frequencies as a function of the static magnetic field for the $SFT_{1\leftrightarrow 4}$ and $SFT_{2\leftrightarrow 4}$ (left) and the $MFT_{1\leftrightarrow 2}$ and $MFT_{2\leftrightarrow 3}$ (right).

this transitions work, it is useful take a look at the adiabatic passage¹⁵⁷. For the diagonalization of the Hamiltonian $\mathcal{H}_1^{ST} + \mathcal{H}_1^\pi$ one can apply a second transformation, given by the matrix

$$U_1 = \{u_{jk}\} = \delta_{jk}e^{-i\omega_j t} \quad (\text{B.20})$$

with certain frequencies ω_j for each hyperfine state. The reverse transformation is given by $U_1^{-1} = \delta_{jk}e^{i\omega_j t}$. The static Hamiltonian is diagonal and therefore unchanged. The high frequency Hamiltonian $\mathcal{H}_1^\pi = \{h_{jk}\}$ is transformed to

$$\{\mathcal{H}_2^\pi\}_{jk} = \{U_1^{-1}\}_{jl}\{\mathcal{H}_1^\pi\}_{lm}\{U_1\}_{mk} = \delta_{jl}e^{i\omega_l t}\{\mathcal{H}_1^\pi\}_{lm}\delta_{mk}e^{-i\omega_k t} = \{\mathcal{H}_1^\pi\}_{jk}e^{i(\omega_j - \omega_k)t}. \quad (\text{B.21})$$

The term $i\hbar\dot{U}_1^{-1}U_1$ results:

$$i\hbar\dot{U}_1^{-1}U_1 = -\hbar\omega_j\delta_{jk}, \quad (\text{B.22})$$

which causes a *shift* of the energy value of state $|j\rangle$ with respect to the eigenvalues of \mathcal{H}_1^{ST} . The new - phaseshifted - basis is given by $\phi = U_1^{-1}\chi$. If one neglects \mathcal{H}_1^π , the Schrödinger equation is now given by:

$$i\hbar\dot{\phi}_j = \left(\{\mathcal{H}_1^{ST}\}_{jk} - \hbar\omega_j\delta_{jk} + \{\mathcal{H}_1^\pi\}_{jk}e^{i(\omega_j - \omega_k)t} \right) \phi_k. \quad (\text{B.23})$$

The next step is given by averaging the Hamiltonian over a sufficient long time period. While the first two terms are stable with time, rapidly oscillating terms disappear from the Hamiltonian:

$$i\hbar\dot{\phi}_j = \left(\{\mathcal{H}_1^{ST}\}_{jk} - \hbar\omega_j\delta_{jk} + \langle \{\mathcal{H}_1^\pi\}_{jk}e^{i(\omega_j - \omega_k)t} \rangle_t \right) \phi_k. \quad (\text{B.24})$$

\mathcal{H}_1^π contains a factor $\cos(\omega t) = \frac{1}{2}(e^{i\omega t} + e^{-i\omega t})$. If the frequencies ω_j of the transformation are chosen such, that $\omega = |\omega_j - \omega_k|$ for the selected transition $|j\rangle \leftrightarrow |k\rangle$, a constant term results by the time averaging, while all terms, where the frequencies do not fit, vanish. Tab. B.3 lists a convenient set of frequencies for WFT and SFT transitions. Obviously, the WFT/MFT shifts are given by $\omega_j = \langle j | m_F | j \rangle \omega$, while the SFT shifts are given by $\omega_j = \frac{E_j(0)}{E_{HFS}}\omega$

¹⁵⁷The calculation follows the paper of Philpott [Phi 87]

Transition	Hydrogen				Deuterium					
	$ 1\rangle$	$ 2\rangle$	$ 3\rangle$	$ 4\rangle$	$ 1\rangle$	$ 2\rangle$	$ 3\rangle$	$ 4\rangle$	$ 5\rangle$	$ 6\rangle$
WFT/MFT	ω	0	$-\omega$	0	$\frac{3}{2}\omega$	$\frac{1}{2}\omega$	$-\frac{1}{2}\omega$	$-\frac{3}{2}\omega$	$-\frac{1}{2}\omega$	$\frac{1}{2}\omega$
SFT	$\frac{1}{4}\omega$	$\frac{1}{4}\omega$	$\frac{1}{4}\omega$	$-\frac{3}{4}\omega$	$\frac{1}{4}\omega$	$\frac{1}{4}\omega$	$\frac{1}{4}\omega$	$\frac{1}{4}\omega$	$-\frac{3}{4}\omega$	$-\frac{3}{4}\omega$

Tab. B.3: Frequency shifts for the calculation of the adiabatic eigenstates for hydrogen and deuterium transitions.

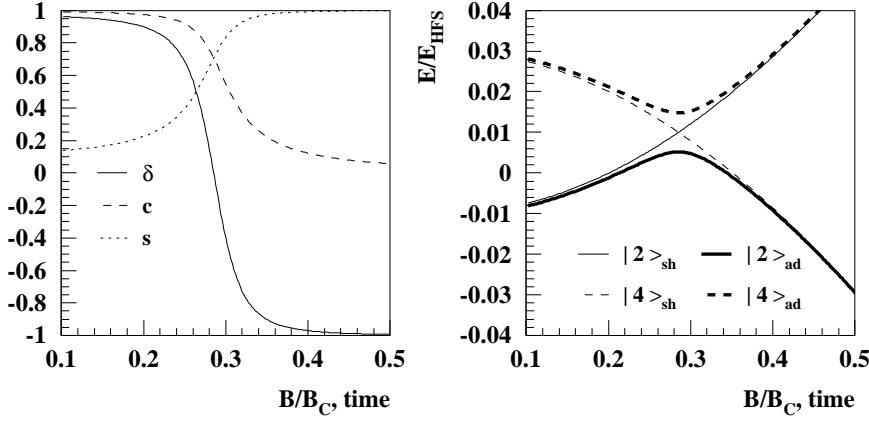


Fig. B.2: Left: The functions $\delta(B)$, $c(B)$ and $s(B)$ of the transformation into the adiabatic basis. Right: Eigen energies of the shifted eigenstates $|2\rangle$ and $|4\rangle$ in the Breitabi basis and of the adiabatic eigenstates in presence of a high frequency field vs. magnetic field - for the adiabatic passage - vs. time.

B.2.4 Strong Field Transitions

In a SFT unit, which is designed for σ -transitions only¹⁵⁸, the hydrogen hamiltonian for the adiabatic passage has the following form:

$$\mathcal{H}_2^{SFT} = \begin{pmatrix} E_1 - \frac{1}{4}\hbar\omega & 0 & 0 & 0 \\ 0 & E_2 - \frac{1}{4}\hbar\omega & 0 & \hbar A \\ 0 & 0 & E_3 - \frac{1}{4}\hbar\omega & 0 \\ 0 & \hbar A & 0 & E_4 + \frac{3}{4}\hbar\omega \end{pmatrix}, \quad (\text{B.25})$$

with $A = y_\sigma \frac{\omega_{HFS}}{2} \sin(2\theta)$. As expected, only the states $|2\rangle$ and $|4\rangle$ are involved in the transition and have to be diagonalized by a new orthogonal transformation U_2 . Ignoring the unaffected states, the Schrödinger equation can be written as:

$$i \begin{pmatrix} \dot{\phi}_2 \\ \dot{\phi}_4 \end{pmatrix} = \begin{pmatrix} \omega_2 - \frac{1}{4}\omega & A \\ A & \omega_4 + \frac{3}{4}\omega \end{pmatrix} \cdot \begin{pmatrix} \phi_2 \\ \phi_4 \end{pmatrix} \quad (\text{B.26})$$

The orthogonal transformation U_2 is given by

$$U_2 = \begin{pmatrix} c & s \\ -s & c \end{pmatrix}, \quad c = \sqrt{\frac{1}{2}(1 + \delta)} \\ s = \sqrt{\frac{1}{2}(1 - \delta)}, \quad \delta = \frac{\omega - \omega_{24}}{\sqrt{(\omega - \omega_{24})^2 + 4A^2}}. \quad (\text{B.27})$$

¹⁵⁸This is the case for the SFT units of the HERMES ABS, while the SFT unit of the BRP has tilted resonators, that allow to run σ and π transitions simultaneously.

The adiabatic eigenstates $\phi_2^{(a)}$ and $\phi_4^{(a)}$ are given by

$$\begin{aligned}\phi^{(a)} &= U_2^T \phi, \\ \phi_2^{(a)} &= c\phi_2 + s\phi_4, \quad \phi_4^{(a)} = -s\phi_2 + c\phi_4.\end{aligned}\tag{B.28}$$

The new - adiabatic - Hamilton operator is given by:

$$\begin{aligned}\mathcal{H}_{ad} &= U_2^T \mathcal{H}_2^{SFT} U_2 + i\hbar \dot{U}_2^T U_2 = \hbar \begin{pmatrix} \tilde{\omega}_2 & 0 \\ 0 & \tilde{\omega}_4 \end{pmatrix} + i\hbar \dot{U}_2^T U_2, \\ \tilde{\omega}_2 &= (\omega_2 - \frac{1}{4}\omega)c^2 - 2Asc + (\omega_4 + \frac{3}{4}\omega)s^2, \\ \tilde{\omega}_4 &= (\omega_2 - \frac{1}{4}\omega)s^2 + 2Asc + (\omega_4 + \frac{3}{4}\omega)c^2.\end{aligned}\tag{B.29}$$

As shown in fig. B.1, the transition frequency $\omega_{24} = \omega_2 - \omega_4$ increases monotonically with the static field. If the atom passes the resonance $\omega = \omega_{24}$ within the high frequency resonator by means of travelling along an increasing static field, the values of δ , c and s change with time as shown in the left graph of fig. B.2. The right graph shows the eigenenergies without high frequency field (thin lines) and with the high frequency field switched on (thick lines). If the passage through the resonance is slow enough¹⁵⁹, the atoms stay on the thick lines and the population of the hyperfine states is exchanged. As the other hyperfine states $|1\rangle$ and $|3\rangle$ are not involved, the effect can be described by one parameter - the exchange efficiency ε_{24} ¹⁶⁰.

The efficiency of an adiabatic transition is given by $\varepsilon = 1 - e^{-2\pi\kappa}$ with κ given by [Phi 87]:

$$\kappa = \left| \frac{\mu B_{HF}^2}{2\hbar \dot{B}_{stat}} \right|.\tag{B.30}$$

Hence, a high efficiency requires most of all sufficient high frequency amplitude¹⁶¹:

$$\mu B_{HF}^2 \gg |2\hbar \dot{B}_{stat}|.\tag{B.31}$$

B.2.5 Weak/Medium Field Transitions

Weak and medium field transitions are in contrast to strong field transitions not single, well separated transitions between two hyperfine states, but more complex multiple transitions. Their effect on the hyperfine population depends on the selected frequency, the amplitude of the high frequency, the strength and sign of the gradient field and is very sensitive on the selected static field. For hydrogen, the Hamilton operator \mathcal{H}_2^{WFT} is given by:

$$\mathcal{H}_2^{WFT} = \begin{pmatrix} E_1 - \hbar\omega & A \sin(\theta) & 0 & 0 \\ A \sin(\theta) & E_2 & A \cos(\theta) & 0 \\ 0 & A \cos(\theta) & E_3 + \hbar\omega & 0 \\ 0 & 0 & 0 & E_4 \end{pmatrix},\tag{B.32}$$

¹⁵⁹The condition is given by the requirement, that the distortion term $\hbar \dot{U}_2^T U_2$ is small compared to the adiabatic eigenenergies.

¹⁶⁰Due to the symmetry of the eigenenergies as a function of time/field as shown in fig. B.2, the efficiency should be symmetric: $\varepsilon_{2 \rightarrow 4} = \varepsilon_{4 \rightarrow 2} = \varepsilon_{24}$.

¹⁶¹The equation could also be interpreted in the way, that \dot{B}_{stat} should be as low as possible. This interpretation has to be rejected due to the following reasons: With the average velocity of the atoms $\langle v \rangle$ and the field gradient B_{grad} , one obtains: $\dot{B}_{stat} = B_{grad} \langle v \rangle$. The velocity of the atoms as well as the effective length Δl of the high frequency resonator (resp. coil) are given by the experimental circumstances. The requirement of a high efficient exchange is, that δ ranges from $\sim 1 \dots \sim -1$ within the high frequency field, which requires, that $\Delta B = B_{grad} \cdot \Delta l \geq |B(\delta \sim 1) - B(\delta \sim -1)|$. A reduction of the gradient is possible, if the high frequency amplitude is a smooth function along the path of the atoms.

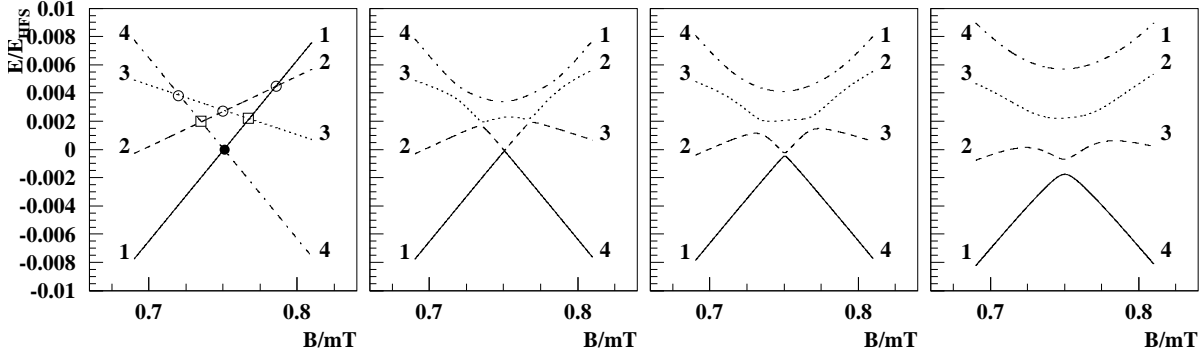


Fig. B.3: Eigen energies of the shifted eigenstates $|1\rangle \dots |4\rangle$ in the adiabatic basis for a high frequency amplitude of - from left to right - 0, 0.01, 0.02 and 0.04 times the critical field and a frequency of 7 MHz . Cross points of the shifted energy levels are marked in the leftmost graph. Open circles represent single-photon, open squares double-photon and the filled circle the three-photon transition points.

with $A = \frac{E_{HFS}^H}{4} y$. For deuterium one finds:

$$\mathcal{H}_2^{WFT} = \begin{pmatrix} E_1 - \frac{3}{2}\hbar\omega & As_+ & 0 & 0 & 0 & 0 \\ As_+ & E_2 - \frac{1}{2}\hbar\omega & As_{-c_+} & 0 & 0 & 0 \\ 0 & As_{-c_+} & E_3 + \frac{1}{2}\hbar\omega & Ac_- & 0 & 0 \\ 0 & 0 & Ac_- & E_4 + \frac{3}{2}\hbar\omega & 0 & 0 \\ 0 & 0 & 0 & 0 & E_5 - \frac{1}{2}\hbar\omega & -As_+c_- \\ 0 & 0 & 0 & 0 & -As_+c_- & E_6 + \frac{1}{2}\hbar\omega \end{pmatrix}, \quad (\text{B.33})$$

with $A = \frac{E_{HFS}^D}{4} y$. Again the resulting Hamilton operators are symmetric and real and can be diagonalized by an orthogonal transformation. Fig. B.3 shows the resulting eigenenergies for a deuterium weak field transition at a frequency of 7 MHz for the states $|1\rangle \dots |4\rangle$. The resonance condition is matched for single-photon transitions at 3 points, indicated by open circles, at two points for two-photon transitions (open squares) and at one point for a three-photon transition. One can see, that the separation of the eigenenergies and hence the efficiency depends on the multiplicity of the transition. A *medium* field transition is based on the single photon transitions only, while one usually speaks only of a *weak* field transition, if multiple photon transitions take place. The second graph from the left in fig. B.3 indicates, that only the single-photon transitions $1 \leftrightarrow 2$, $2 \leftrightarrow 3$ and $3 \leftrightarrow 4$ will effectively run at this low amplitude. With a positive gradient, the transition will have the following effect on the hyperfine population (state $|5\rangle$ and $|6\rangle$ can be analyzed separately):

$$\begin{pmatrix} N_1 \\ N_2 \\ N_3 \\ N_4 \end{pmatrix} \xrightarrow{3 \leftrightarrow 4} \begin{pmatrix} N_1 \\ N_2 \\ N_4 \\ N_3 \end{pmatrix} \xrightarrow{2 \leftrightarrow 3} \begin{pmatrix} N_1 \\ N_4 \\ N_2 \\ N_3 \end{pmatrix} \xrightarrow{1 \leftrightarrow 2} \begin{pmatrix} N_4 \\ N_1 \\ N_2 \\ N_3 \end{pmatrix}$$

This is effectively a rotation of the hyperfine population, which is typical for a MFT $1 \leftrightarrow 4$. Clearly the effect would be different, if the gradient would be negative (still called MFT $1 \leftrightarrow 4$):

$$\begin{pmatrix} N_1 \\ N_2 \\ N_3 \\ N_4 \end{pmatrix} \xrightarrow{1 \leftrightarrow 2} \begin{pmatrix} N_2 \\ N_1 \\ N_3 \\ N_4 \end{pmatrix} \xrightarrow{2 \leftrightarrow 3} \begin{pmatrix} N_2 \\ N_3 \\ N_1 \\ N_4 \end{pmatrix} \xrightarrow{3 \leftrightarrow 4} \begin{pmatrix} N_2 \\ N_3 \\ N_4 \\ N_1 \end{pmatrix}$$

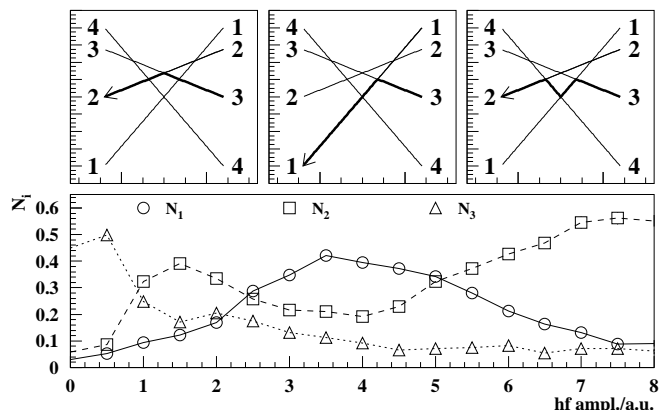


Fig. B.4: Lower figure: Amplitude dependence of WFT operation (with negative field gradient), measured with the deuterium WFT in the appendix of the ABS. The transitions between the sextupoles were used to reject state $|1\rangle$ and $|2\rangle$. As indicated in the upper schemes, state $|3\rangle$ enters the WFT unit (from high to low field) and is transferred to state $|2\rangle$ by a single-photon transition at an amplitude of ~ 1.5 , to state $|1\rangle$ with the double-photon transition at an ampl. of ~ 3.5 and again to state $|2\rangle$ at full ampl., where the 3-photon transition runs.

A MFT $2 \leftrightarrow 4$ would have to be adjusted such, that the high frequency amplitude is already low at the position of the $1 \leftrightarrow 2$ resonance, respectively, that the gradient stops before this resonance. A MFT is usually operated at higher frequencies compared to a WFT in order to realize a better separation of the different transitions, so that the optimal settings for the static and gradient field can be found easier.

The rightmost figure shows a real weak field transition, even though the efficiency of the 3 photon transition $1 \leftrightarrow 4$ might not yet reach 100%. The effect of a deuterium WFT on the hyperfine population can not be described by the transitions $1 \leftrightarrow 4$ and $2 \leftrightarrow 3$. Instead, the following description is suggested, which is more general and allows the usage of symmetric exchange efficiencies:

$$\begin{pmatrix} N_1 \\ N_2 \\ N_3 \\ N_4 \end{pmatrix} \xrightarrow{1 \leftrightarrow 2} \begin{pmatrix} N_2 \\ N_1 \\ N_3 \\ N_4 \end{pmatrix} \xrightarrow{2 \leftrightarrow 4} \begin{pmatrix} N_2 \\ N_4 \\ N_3 \\ N_1 \end{pmatrix} \xrightarrow{2 \leftrightarrow 3} \begin{pmatrix} N_2 \\ N_3 \\ N_4 \\ N_1 \end{pmatrix} \xrightarrow{1 \leftrightarrow 4} \begin{pmatrix} N_1 \\ N_3 \\ N_4 \\ N_2 \end{pmatrix} \xrightarrow{1 \leftrightarrow 3} \begin{pmatrix} N_4 \\ N_3 \\ N_1 \\ N_2 \end{pmatrix} \xrightarrow{3 \leftrightarrow 4} \begin{pmatrix} N_4 \\ N_3 \\ N_2 \\ N_1 \end{pmatrix}$$

In this case, one needs 3 efficiencies to describe a hydrogen weak field transition and 6 in case of deuterium. If the HF amplitude is sufficient, one can assume, that the single-photon transitions operate close to 100%. This reduces the required number of efficiencies to one for hydrogen and 3 for deuterium.

Fig. B.4 shows the result of a polarization measurements for different amplitudes of a deuterium WFT, that illustrates the mentioned WFT/MFT behavior. This analysis of the WFT behavior is necessary for optimization and analysis of the injected polarization.

The optimal conditions for the operation of a WFT/MFT transition therefore depend on the intended effect on the hyperfine population and the location of the transition. If, as in case of the HERMES setup for deuterium, the sextupole subsystems (see sec. 3.4) in combination with a SFT 3-5 prepare a hyperfine population with atoms only in state $|1\rangle$ and $|2\rangle$, and the WFT behind the sextupoles is supposed to deliver state $|3\rangle$ and $|4\rangle$ for P_z^- injection, then a negative gradient has to be chosen. In this case, the three photon transition is not required to run at all, as the intended population of hyperfine states $|3\rangle$ and $|4\rangle$ can also be realized with a $1 \rightarrow 3/2 \rightarrow 4$ transition instead of a $1 \rightarrow 4/2 \rightarrow 3$ transition.

In the limiting case of high rf-amplitude and low rf-frequency¹⁶², the single photon transitions of a WFT can be assumed to run at full efficiency, so that a hydrogen WFT can be described

¹⁶²14 MHz in case of a hydrogen and 7 MHz in case of a deuterium WFT.

by the efficiency ε_{13} and a deuterium WFT by 3 transition efficiencies ($\varepsilon_{13}, \varepsilon_{14}, \varepsilon_{24}$). In case of MFT operation, higher rf-frequencies¹⁶³ are chosen and multi-photon transitions are assumed to be negligible, so that a hydrogen MFT can be described by 2 and a deuterium MFT by 3 efficiencies.

B.3 The Stern-Gerlach-Force of Sextupole Magnets

The Stern-Gerlach force [Stn 21] results from the field dependence of the eigenenergies of the hyperfine states, which is given the relations in tab. B.1. The Lagrange function \mathcal{L} for an atom in hyperfine state $|a\rangle$ is given by:

$$\mathcal{L} = \frac{m}{2}(\dot{x}^2 + \dot{y}^2 + \dot{z}^2) - E_{|a\rangle}(|\vec{B}|). \quad (\text{B.34})$$

The absolute value of the magnetic field inside a sextupole magnet, which is aligned along the z -axis, is given by the following formula [Hal 80]:

$$B(r) = B_{pt} \left(\frac{r}{r_{pt}} \right)^2, \quad (\text{B.35})$$

with the radius $r = \sqrt{x^2 + y^2}$ and the field B_{pt} given by

$$B_{pt} = \frac{3 J \cdot \sin(4\pi\varepsilon/M)}{2 \cdot 4\pi/M} \left(1 - \frac{r_{pt}^2}{r_a^2} \right), \quad (\text{B.36})$$

J is the *magnetization* of the sextupole material, M the number of segments, r_a the outer and r_{pt} the inner radius of the magnet, while ε is the so-called *filling factor* ($0 < \varepsilon < 1$).

The magnetic moment $\mu_{|a\rangle}$ of hyperfine state $|a\rangle$ is defined by:

$$\mu_{|a\rangle} = \frac{dE_{|a\rangle}}{d\mathbf{B}} = \frac{dE_{|a\rangle}}{d\mathbf{x}} \frac{1}{B_C}, \quad (\text{B.37})$$

where the bold printed \mathbf{x} is defined by $\mathbf{x} = \frac{\mathbf{B}}{B_C}$. The resulting equations of motion are then given by:

$$m\ddot{x} = -\frac{dE_{|a\rangle}}{dB} \frac{dB}{dr} \frac{x}{r} = -\mu_{|a\rangle} \frac{2B_{pt}}{r_{pt}^2} x \quad (\text{B.38})$$

$$m\ddot{y} = -\frac{dE_{|a\rangle}}{dB} \frac{dB}{dr} \frac{y}{r} = -\mu_{|a\rangle} \frac{2B_{pt}}{r_{pt}^2} y \quad (\text{B.39})$$

$$m\ddot{z} = 0, \quad (\text{B.40})$$

¹⁶³ > 50 MHz in case of a hydrogen and > 25 MHz in case of a deuterium MFT.

Hydrogen	Deuterium
$\mu_1^H = \frac{dE_1}{dB} = \frac{1}{2}g_S\mu_B$	$\mu_1^D = \frac{dE_1}{dB} = \frac{1}{2}g_S\mu_B$
$\mu_2^H = \frac{dE_2}{dB} = \frac{1}{2}g_S\mu_B \cos(2\theta)$	$\mu_2^D = \frac{dE_2}{dB} = \frac{1}{2}g_S\mu_B \cos(2\theta_+)$
$\mu_3^H = \frac{dE_3}{dB} = -\frac{1}{2}g_S\mu_B$	$\mu_3^D = \frac{dE_3}{dB} = \frac{1}{2}g_S\mu_B \cos(2\theta_-)$
$\mu_4^H = \frac{dE_4}{dB} = -\frac{1}{2}g_S\mu_B \cos(2\theta)$	$\mu_4^D = \frac{dE_4}{dB} = -\frac{1}{2}g_S\mu_B$
	$\mu_5^D = \frac{dE_5}{dB} = -\frac{1}{2}g_S\mu_B \cos(2\theta_-)$
	$\mu_6^D = \frac{dE_6}{dB} = -\frac{1}{2}g_S\mu_B \cos(2\theta_+)$

Tab. B.4: Magnetic moments of the hyperfine states for hydrogen and deuterium. The formulas of tab. B.1 have been used with $\varepsilon \simeq 0$.

The magnetic moments $\mu_{|a\rangle}$ are listed in tab. B.4. The pure states have a constant magnetic moment, while the moments of the mixed states depend on the mixing angles. Atoms in state $|1\rangle$ perform harmonic oscillations around the axis of the sextupole magnet in both coordinates - x and y . A calculation of the frequency ω of this oscillation yields:

$$\omega^2 = \frac{E_{HFS}}{m r_{pt}^2} \frac{B_{pt}}{B_C} = \frac{g_s \mu_B B_{pt}}{m r_{pt}^2}. \quad (\text{B.41})$$

As $\ddot{z} = \dot{v}_z = 0$, the time can be replaced by the axial coordinate z by $t = z/v_z$. The motion can then be described by

$$\begin{aligned} x(z) &= \frac{v_x(0)}{\omega} \sin\left(\frac{\omega}{v_z} z\right) + x(0) \cos\left(\frac{\omega}{v_z} z\right) \\ y(z) &= \frac{v_y(0)}{\omega} \sin\left(\frac{\omega}{v_z} z\right) + y(0) \cos\left(\frac{\omega}{v_z} z\right) \\ v_x(z) &= v_x(0) \cos\left(\frac{\omega}{v_z} z\right) - x(0) \omega \sin\left(\frac{\omega}{v_z} z\right) \\ v_y(z) &= v_y(0) \cos\left(\frac{\omega}{v_z} z\right) - y(0) \omega \sin\left(\frac{\omega}{v_z} z\right). \end{aligned} \quad (\text{B.42})$$

The solution for atoms in state $|3\rangle$ ($|4\rangle$ in case of deuterium) is given by:

$$\begin{aligned} x(z) &= \frac{v_x(0)}{\omega} \sinh\left(\frac{\omega}{v_z} z\right) + x(0) \cosh\left(\frac{\omega}{v_z} z\right) \\ y(z) &= \frac{v_y(0)}{\omega} \sinh\left(\frac{\omega}{v_z} z\right) + y(0) \cosh\left(\frac{\omega}{v_z} z\right) \\ v_x(z) &= v_x(0) \cosh\left(\frac{\omega}{v_z} z\right) + x(0) \omega \sinh\left(\frac{\omega}{v_z} z\right) \\ v_y(z) &= v_y(0) \cosh\left(\frac{\omega}{v_z} z\right) + y(0) \omega \sinh\left(\frac{\omega}{v_z} z\right). \end{aligned} \quad (\text{B.43})$$

The solutions indicate an exponential increase of the radius $r = \sqrt{x^2 + y^2}$, which means, that these states are defocussed. The solutions for the mixed states can be calculated numerically. They show a similar behavior in some distance to the sextupole axis, where $B(r) \geq B_C$ and therefore $\cos(2\theta) \simeq 1$, whereas their behavior differs close to the sextupole axis¹⁶⁴. In case of deuterium, where the critical field B_C is only about $11.7 mT$, the difference between the pure and the mixed states is less pronounced compared to hydrogen.

¹⁶⁴The difference is not very large, as the sextupole force is weak in low field.

C Diffusion by Molecular Flow

For the diffusion constant D the following relation can be derived from eq. 2.17 [Bec 85] for the one-dimensional case:

$$\frac{\partial \langle \delta z^2 \rangle}{\partial t} = 2D \quad (\text{C.1})$$

or

$$\langle \delta z^2 \rangle = 2Dt, \quad (\text{C.2})$$

respectively, where $\delta z(t)$ is the particle's displacement along z as a function of time. In the case under study, this can be replaced by $\langle \delta l \rangle$, the mean length of the particle's trajectory between two wall collisions, if one takes into account, that $\langle \delta z^2 \rangle = \frac{1}{3} \langle \delta l^2 \rangle$ holds for isotropic diffusion. With τ_f being the mean time of flight between two wall collisions, one may write:

$$\langle \delta l^2 \rangle = 6 D \tau_f. \quad (\text{C.3})$$

Hence the conductance of the tube is given by

$$C = \frac{S}{L} \frac{\langle \delta l^2 \rangle}{6\tau_f}. \quad (\text{C.4})$$

C.1 Wall Collisions

Wall collisions are the driving mechanism for gas diffusion in tubes in the molecular flow regime and are important for the understanding and modeling of relaxation processes. In the present context, the details of the particles interaction with the wall are of low importance, as long as the particles velocities follow approximately a maxwellian distribution and desorption is about isotropic, so that the distribution of the desorption angle is not too far from a $\cos \Theta$ distribution¹⁶⁵.

In statistical mechanics the pressure on a wall by means of gas particle collisions is defined as:

$$p = \frac{\langle \dot{N}_b \rangle 2m \langle v_\rho \rangle}{A}, \quad (\text{C.5})$$

where $\langle \dot{N}_b \rangle$ is defined as the mean number of particle collisions¹⁶⁶ on the surface area A per unit time, m is the mass of the particles and $\langle v_\rho \rangle$ the mean normal velocity. The factor $2m \langle v_\rho \rangle = \sqrt{2\pi m k T}$ equals the mean momentum transfer to the wall per collision. The average pressure can be calculated using

$$\langle p \rangle = \frac{1}{2} \Delta p, \quad (\text{C.6})$$

and one obtains with eq. 2.29 and eq. 2.23:

$$\langle p \rangle = \frac{\Phi}{2C} = \frac{\langle \dot{N} \rangle k T}{2C}, \quad (\text{C.7})$$

¹⁶⁵ θ is the angle between the surface normal vector and the direction of desorption.

¹⁶⁶The quotient $Z_0 = \frac{\langle \dot{N} \rangle}{A}$ is called *rate of impingement* [Tom 78] or *collision frequency*[Gel 71] and eq. C.5 is equivalent to the Herz-Knudsen Equation [Tom 78].

where $\langle \dot{N} \rangle$ is the mean number of particles flowing through the tube per unit time. The mean number of wall collisions $\langle b \rangle(L)$, that a particle experiences by flowing through a tube of circumference U and length L , is given by¹⁶⁷:

$$\langle b \rangle(L) = \frac{\langle \dot{N}_b \rangle}{\langle \dot{N} \rangle} = \frac{UL}{\sqrt{8\pi C}} \sqrt{\frac{kT}{m}} = \frac{UL}{8C} \langle v \rangle, \quad (\text{C.8})$$

where the mean velocity $\langle v \rangle$ of the particle - given by the Maxwell distribution - is $\langle v \rangle = \sqrt{\frac{8kT}{\pi m}}$. As the particle flow through the tube is constant in time and along the z -axis, one may also make use of the gas equation

$$\langle p \rangle V = \langle N \rangle kT, \quad (\text{C.9})$$

where V is the volume given by $V = SL$, and $\langle N \rangle$ the average number of particles in the tube. If τ_d is the mean total time a particle spends inside the tube, one may also write

$$\begin{aligned} \langle N \rangle &= \langle \dot{N} \rangle \tau_d = \frac{\Phi}{kT} \tau_d \\ \langle N \rangle &= \frac{V \langle p \rangle}{kT} = \frac{V \Phi}{2C kT}, \end{aligned} \quad (\text{C.10})$$

and therefore:

$$\tau_d = \frac{SL}{2C}. \quad (\text{C.11})$$

With $\tau_d = \langle b \rangle \tau_f$ one may calculate the mean time of flight τ_f between two wall collisions by:

$$\tau_f = \frac{\tau_d}{\langle b \rangle} = \frac{S}{U} \sqrt{\frac{2\pi m}{kT}} = 4 \frac{S}{U} \frac{1}{\langle v \rangle}. \quad (\text{C.12})$$

The mean length $\langle \delta l \rangle$ of the particle's trajectory between two wall collisions is then given by

$$\langle \delta l \rangle = \tau_f \langle v \rangle = 4 \frac{S}{U}, \quad (\text{C.13})$$

which is - in case of a circular tube - exactly the diameter $\langle \delta l \rangle = 2R$. As a result it turns out, that neither the time of flight τ_f nor the mean pathlength $\langle \delta l \rangle$ between two wall collisions depend on the details of the tube's profile. The same can be expected for the conductance C , which is given by eq. C.4.

A diffusion process can usually be described by a free pathlength distribution

$$w(\delta z) = \frac{1}{\delta z_0} \exp\left(\frac{-\delta z}{\delta z_0}\right), \quad (\text{C.14})$$

with the expectation values $\langle \delta z^n \rangle = n! \delta z_0^n$. The ratio $\frac{\langle \delta z^2 \rangle}{\langle \delta z \rangle^2}$ then equals 2 and one obtains for the conductance of a long tube¹⁶⁸:

$$C = \frac{S}{L} \frac{\langle \delta l \rangle^2}{3\tau_f} = \frac{4}{3} \frac{S^2}{UL} \langle v \rangle = \frac{16}{3\sqrt{2\pi}} \frac{S^2}{UL} \sqrt{\frac{kT}{m}}. \quad (\text{C.15})$$

¹⁶⁷The surface area is given by $A = UL$.

¹⁶⁸The distribution $w(z)$ is different in case of thin gases, when the particle-particle interaction can be neglected. The correct calculation for a circular tube, which can be found in appendix C.2, results the same ratio $\frac{\langle \delta z^2 \rangle}{\langle \delta z \rangle^2}$. The effect of the opening at the end of the tube is also cited there.

The average number of wall collisions of particles at the end of the tube $\langle b \rangle (L)$ can be calculated with eq. C.8:

$$\langle b \rangle (L) = \frac{3}{32} \left(\frac{UL}{S} \right)^2. \quad (\text{C.16})$$

Tab. C.1 gives an overview over the relevant equations.

Volume of tube	V	$= SL$	
Cross section	S		
Circumference	U		
Length	L		
Mean length of traj.	$\langle \delta l \rangle$	$= 4 \frac{S}{U}$	
	$\langle \delta l^2 \rangle$	$= 32 \frac{S^2}{U^2}$	
Mean velocity	$\langle v \rangle$	$= \sqrt{\frac{8kT}{\pi m}}$	
Mean time of flight	τ_f	$= 4 \frac{S}{U} \frac{1}{\langle v \rangle}$	
Mean total time	τ_d	$= \frac{SL}{2C}$	
Number of wall coll.	$\langle b \rangle (L)$	$= \frac{3}{32} \left(\frac{UL}{S} \right)^2 = \frac{L^2}{\langle \delta z^2 \rangle}$	
Mod. diff. constant	\tilde{D}	$= \frac{16}{3} \frac{S^2}{U^2} = \frac{\langle \delta z^2 \rangle}{2}$	
Conductance	C	$= \frac{4}{3} \frac{S^2}{UL} \langle v \rangle = \frac{V}{2\tau_d}$	

Tab. C.1: List of relations of diffusive molecular flow through tubes of arbitrary crosssection.

C.2 Calculation of the Diffusion Constant for Long Tubes

For a cylindrical tube one can calculate the value for $\langle \delta z^2 \rangle$ by direct integration. If (Φ, Θ) are the angles relative to the normal vector at some point on the surface inside a circular tube with radius R , the value for δz is then given by

$$\delta z = 2R \frac{\cos \Theta \sin \Theta \cos \Phi}{1 - \sin^2 \Theta \cos^2 \Phi}. \quad (\text{C.17})$$

As one assumes a $\cos \Theta$ -distribution for the desorption from the surface, one obtains:

$$\langle \delta z^2 \rangle = \frac{1}{\pi} \int_0^{2\pi} \int_0^{\pi/2} d\Phi \sin \Theta d\Theta P(\Theta) \delta z^2. \quad (\text{C.18})$$

$$\langle \delta z^2 \rangle = \frac{4}{\pi} \int_0^{\pi/2} \int_0^{\pi/2} d\Phi d\Theta 4R^2 \frac{\cos^3 \Theta \sin^3 \Theta \cos^2 \Phi}{(1 - \sin^2 \Theta \cos^2 \Phi)^2}. \quad (\text{C.19})$$

With the substitution $t = \sin \Theta$, $dt = \cos \Theta d\Theta$ this results:

$$\langle \left(\frac{\delta z}{2R} \right)^2 \rangle = \frac{4}{\pi} \int_0^{\pi/2} d\Phi \int_0^1 dt \frac{(1-t^2) t^3 \cos^2 \Phi}{(1-t^2 \cos^2 \Phi)^2}. \quad (\text{C.20})$$

The integration yields

$$\langle \left(\frac{\delta z}{2R} \right)^2 \rangle = \frac{2}{3}, \quad (\text{C.21})$$

and with eq. C.13 $2R = \langle \delta l \rangle$ and $\langle \delta z^2 \rangle = \frac{1}{3} \langle \delta l^2 \rangle$ one obtains the confirmation, that

$$\frac{\langle \delta z^2 \rangle}{\langle \delta z \rangle^2} = 2. \quad (\text{C.22})$$

The diffusion constant for one-dimensional gas diffusion in long tubes is then obtained by

$$D = \frac{1}{2} \frac{\langle \delta z^2 \rangle}{\tau_f} = \frac{1}{3} \frac{\langle \delta l \rangle^2}{\tau_f} = \frac{4}{3} \frac{S}{U} \langle v \rangle. \quad (\text{C.23})$$

For tubes of finite length, the conductance of the opening C_{op} at the end of the tube has to be taken into account [Rot 90]:

$$C_{op} = \frac{S}{\sqrt{2\pi}} \sqrt{\frac{kT}{m}}, \quad (\text{C.24})$$

so that the complete conductance of a tube of finite length L is

$$C = \frac{1}{\frac{1}{C_{op}} + \frac{1}{C_{tube}}} = \frac{16}{3\sqrt{2\pi}} \frac{S^2}{UL + \frac{16}{3}S} \sqrt{\frac{kT}{m}}. \quad (\text{C.25})$$

C.3 Diffusion and Wall Collision Ages

Based on eq. 2.20 molecular flow in vacuum vessels like the HERMES storage cell can be understood as a diffusion process with the diffusion constant given by eq. C.23. The smallest time constant for this diffusion process is the mean time of flight τ_f given by eq. C.12. Time can then be expressed by the number of wall collisions b using $t = \tau_f b$, and eq. 2.20 can be modified to

$$\frac{\partial n}{\partial b} = \dot{n} \tau_f = D \tau_f \frac{\partial^2 n}{\partial z^2} = \tilde{D} \frac{\partial^2 n}{\partial z^2}, \quad (\text{C.26})$$

with a modified diffusion constant $\tilde{D} = D \tau_f$ given by $\tilde{D} = \frac{16}{3} \frac{S^2}{U^2}$. The Fourier transformed equation is

$$\frac{\partial \tilde{n}(b, k)}{\partial b} = \tilde{D} (ik)^2 \tilde{n}(b, k), \quad (\text{C.27})$$

with the Fourier transformed particle density $\tilde{n}(b, k)$. Integration yields $\tilde{n}(b, k) = N e^{-\tilde{D} k^2 b}$ and the backtransformation is then given by

$$n(z, b) = \frac{N}{\sqrt{2\tilde{D}b}} e^{-\frac{z^2}{4\tilde{D}b}}, \quad (\text{C.28})$$

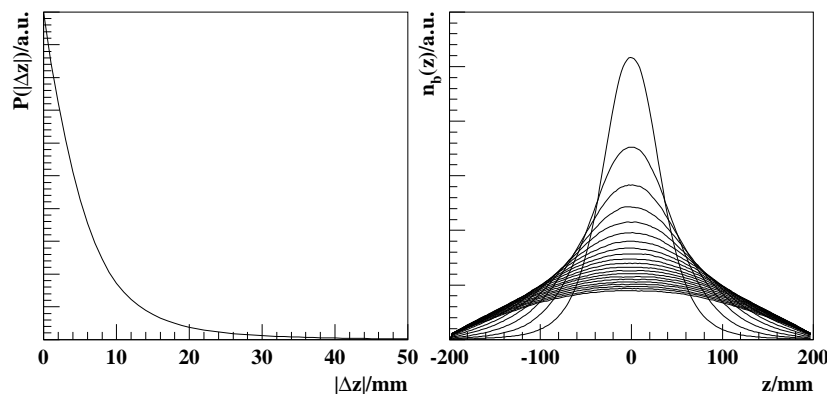


Fig. C.1: Left: Probability distribution $P(|\Delta z|)$ for particle movement in HERMES storage cell, obtained by Monte Carlo simulation. Right: Distribution of particles with a collision age $b = 10, 20 \dots 200$ in the storage cell.

which describes the density distribution of N particles in one dimension, which are located at $z = 0$ with $b = 0$ as a function of collision age b and position z . If the probability to find a particle, which desorbes off the wall at z , has its next wall collision between z and $z + \Delta z$, is $P(|\Delta z|)$ with $\langle \Delta z^2 \rangle < \infty$, then the central limiting theoreme predicts a Gaussian probability distribution in the limiting case $b \rightarrow \infty$, while eq. C.28 predicts it already for the first collision. Nevertheless the convergence with a Gaussian distribution is usually fast in case of a random walk and a small number of collisions $b \simeq 10$ are enough to describe the process with eq. C.26.

A more general solution of eq. C.26 can be derived using the technique of separation of variables:

$$u(z, b) = \sum_k \left[a_k \exp\left(-\tilde{D}\omega_k^2 b\right) \cos(\omega_k z) + b_k \exp\left(-\tilde{D}\Omega_k^2 b\right) \sin(\Omega_k z) \right]. \quad (\text{C.29})$$

As a boundary condition for the storage cell it is required, that the density at the end of the tube vanishes ($u(L, b) = u(-L, b) = 0$), so that the coefficients have to fulfill the following relations:

$$\begin{aligned} \omega_k &= \frac{\pi}{2} \frac{2k+1}{L} \\ a_{2k} &= 0 \\ \Omega_k &= \frac{k\pi}{L}. \end{aligned} \quad (\text{C.30})$$

Without relaxation, which might in general give reason for an asymmetry, the solution is symmetric in z and the coefficients b_k vanish¹⁶⁹:

$$u(z, b) = \sum_{k=0}^{\infty} a_k \exp\left(-\frac{\pi^2 \tilde{D}}{4L^2} (2k+1)^2 b\right) \cos\left(\frac{(2k+1)\pi z}{2L}\right). \quad (\text{C.31})$$

With eq. C.16 it follows, that

$$\frac{L^2}{2\tilde{D}} = \langle b \rangle. \quad (\text{C.32})$$

Setting $a_k = \frac{u_0}{\langle b \rangle}$, eq. C.31 can be written as¹⁷⁰:

$$u(z, b) = \frac{u_0}{\langle b \rangle} \sum_{k=0}^{\infty} \exp\left(-\frac{\pi^2}{8} (2k+1)^2 \frac{b}{\langle b \rangle}\right) \cos\left(\frac{(2k+1)\pi z}{2L}\right). \quad (\text{C.33})$$

The solution $u(z, b)$ is - provided a correct normalization - the *collision age distribution* (CAD) $N_{CAD}(z, b)$ of the atoms at position z :

$$N_{CAD}(z, b) = \frac{u(z, b)}{\int_0^{\infty} u(z, b) db}. \quad (\text{C.34})$$

The denominator is the atomic density:

$$u(z) = \int_0^{\infty} u(z, b) db = u_0 \sum_{k=0}^{\infty} \frac{8}{\pi^2} \frac{\cos\left(\frac{\pi(2k+1)z}{2L}\right)}{(2k+1)^2}. \quad (\text{C.35})$$

¹⁶⁹Sommerfeld presents a detailed discussion of solutions of eq. C.26 in the context of thermal transport under a variety of boundary conditions [Som 47]. The sum in eq. C.31 is closely related to the θ -functions and can also be described as an infinite sum of Gaussian functions, which corresponds to the sum of mirrored solutions in [Ko 98].

¹⁷⁰The sum on the right side of eq. C.33 represents a linear combination of θ -functions and can not be expressed in a simple analytical form.

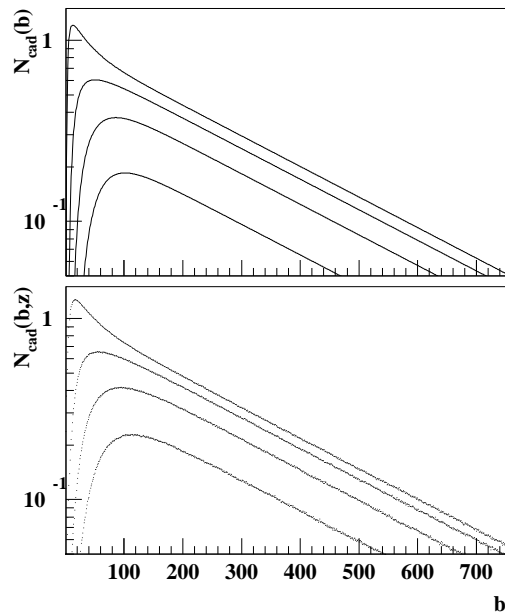


Fig. C.2: Comparison of theoretical calculations and results obtained by a molecular flow Monte Carlo simulation [Bau 96]. The top figure shows function $u_z(b)$ of eq. C.35 vs. the collision age b for several positions z in the cell in steps of 4 cm . The calculation used the first 20 terms of the sum in eq. C.35. The upper curves belong to lower values of z . The lower figure shows the same curves obtained with a molecular flow Monte Carlo simulation [Bau 96]. The agreement is reasonable (but not perfect, as eq. C.35 neglects the effect of injection- and sample tube as well as the effect of a non-zero conductance at the end of the tube). For $b \geq 160$, the behavior is equivalent to an exponential decay.

The right side of eq. C.35 is nothing but the Fourier series of a triangular shaped density distribution, which reaches u_0 at $z = 0$ and vanishes at $z = \pm L$. The sum on the right side of eq. C.33 is - for sufficiently high values of b - rapidly converging. For $b \geq \frac{1}{2} \langle b \rangle$, the sum can to a precision of better than 1% be replaced by the first summand. The conclusion is, that any CAD at any position in the storage cell drops exponentially for high enough collision ages. Fig. C.1 shows the particle distribution in the storage cell after $b = 10, 20 \dots 100$ wall collisions. While the distribution is practically Gaussian after 10 collisions, it has the shape of a cos-function after a high number of wall collisions.

Fig. C.2 shows a comparison of the function $u(z, b)$ from eq. C.35 with the results obtained by a Monte Carlo simulation. The results agree within the expected systematic differences¹⁷¹. The only significant difference can be found for low values of the collision age $b \leq 10$ and higher values of z . This can be explained by the fact, that the diffusion equation holds in strength only for the limiting case $b \rightarrow \infty$, where a Gaussian particle distribution is predicted by the central limiting theorem. The low values of b play a minor role in the calculation of the relaxation process, as their statistical weight is small.

C.3.1 Moments of Collision Age Distributions (CAD)

The m -th moment $\beta_m = \langle b^m \rangle$ of a CAD is defined by

$$\beta_m(z) = \frac{1}{u(z)} \int_0^{\infty} b^m u(z, b) db, \quad (\text{C.36})$$

with the density $u(z)$ defined by

$$u(z) = \int_0^{\infty} db u(z, b). \quad (\text{C.37})$$

¹⁷¹The Monte Carlo simulation includes sample and injection tube, while the calculations do not.

The first partial derivation of β_m is

$$\frac{\partial \beta_m}{\partial z} = \frac{1}{u(z)} \int_0^\infty b^m \frac{\partial u(z, b)}{\partial z} db - \frac{\beta_m}{u(z)} \int_0^\infty \frac{\partial u(z, b)}{\partial z} db, \quad (\text{C.38})$$

and the second (using the result of the first):

$$\frac{\partial^2 \beta_m}{\partial z^2} = \frac{1}{\bar{D} u(z)} \int_0^\infty b^m \frac{\partial u(z, b)}{\partial b} db - 2 \frac{\partial \beta_m}{\partial z} \frac{\partial \eta}{\partial z} - \beta_m \left\{ \left(\frac{\partial \eta}{\partial z} \right)^2 + \frac{\partial^2 \eta}{\partial z^2} \right\}, \quad (\text{C.39})$$

where $\eta(z)$ is defined by $\eta(z) = \log u(z)$. For a linear density distribution of the form $u(z) = u_0 \left(1 - \frac{|z|}{L}\right)$ one finds, that

$$\left(\frac{\partial \eta}{\partial z} \right)^2 + \frac{\partial^2 \eta}{\partial z^2} = 0.$$

By partial integration one obtains:

$$\int_0^\infty b^m \frac{\partial u(z, b)}{\partial b} db = b^m u(z, b) \Big|_0^\infty - m \int_0^\infty b^{m-1} u(z, b) db = -m \beta_{m-1} u(z), \quad (\text{C.40})$$

where the left terms vanish for any m due to the limiting exponential behavior of $u(z, b)$. Hence the result is:

$$\frac{\partial^2 \beta_m}{\partial z^2} + \frac{m}{\bar{D}} \beta_{m-1} + 2 \frac{\partial \beta_m}{\partial z} \frac{\partial \eta}{\partial z} = 0. \quad (\text{C.41})$$

With $\beta_0 = 1$ and $\frac{\partial \eta}{\partial z} = \frac{1}{z-L}$ for $z \geq 0$ one can solve the differential equation for the first moment by a polynomial of 2nd order:

$$\beta_1 = a + \frac{L}{3\bar{D}} z - \frac{1}{6\bar{D}} z^2. \quad (\text{C.42})$$

With the boundary condition $\beta_1(L) = \langle b \rangle(L) = \frac{L^2}{2\bar{D}}$ one obtains:

$$\beta_1 = \langle b \rangle(z) = \frac{L^2}{3\bar{D}} \left(1 + \frac{z}{L} - \frac{1}{2} \frac{z^2}{L^2} \right). \quad (\text{C.43})$$

In a long storage cell, the average collision age in center is therefore about¹⁷² $\frac{2}{3}$ of the average collision age at the end. It is worth noting, that the collision age distribution itself was not used for this calculation, but only the triangular shaped density distribution and the diffusion equation.

C.4 Diffusion and Recombination

If the probability to recombine during one wall collision is γ_r , the probability, that an atom survives b wall collisions is $(1 - \gamma_r)^b$. If $\gamma_r \ll 1$, this is approximately equal to a factor $\exp -b \gamma_r$, so that sol. C.33 has to be replaced by

$$u_\gamma(z, b) = \frac{u_0}{\langle b \rangle} \sum_{k=0}^{\infty} \exp \left(-\frac{\pi^2}{8} (2k+1)^2 \frac{b}{\langle b \rangle} - \gamma_r b \right) \cos \left(\frac{(2k+1)\pi z}{2L} \right). \quad (\text{C.44})$$

¹⁷²The effect of the ends and the sample and injection tube are neglected, so that the result is only an approximation for a *real* storage cell.

Again, the total atomic density is obtained by integration over all collision ages:

$$u_\gamma(z) = \int_0^\infty u(z, b) db = u_0 \sum_{k=0}^\infty \frac{8}{\pi^2} \frac{\cos\left(\frac{\pi(2k+1)z}{2L}\right)}{(2k+1)^2 + \frac{8}{\pi^2} \langle b \rangle \gamma_r}. \quad (\text{C.45})$$

One can also subtract the number of recombined atoms $\gamma_r n$ from the left side of eq. C.26 to take recombination into account:

$$\frac{\partial n}{\partial b} = \dot{n}\tau_f = \tilde{D} \frac{\partial^2 n}{\partial z^2} - \gamma_r n, \quad (\text{C.46})$$

The solution is again given by eq. C.44, if γ_r does not depend on the atomic density n . One can obtain an ordinary differential equation by defining the atomic density $n(z)$

$$n(z) = \int_0^\infty n(z, b) db. \quad (\text{C.47})$$

For eq. C.46 one obtains:

$$n(z, \infty) - n(z, 0) = 0 = \tilde{D} \frac{d^2 n}{dz^2} - \gamma_r n, \quad (\text{C.48})$$

which is equivalent to eq. 6.21 in [Bau 96]. A solution of eq. C.48, which fulfills the boundary condition $n(L) = 0$, is

$$n(z) = n(0) \frac{\sinh\left(\sqrt{\frac{\gamma_r}{\tilde{D}}} |L - z|\right)}{\sinh\left(\sqrt{\frac{\gamma_r}{\tilde{D}}} L\right)} = n(0) \frac{\sinh\left(\sqrt{2 \langle b \rangle \gamma_r} \frac{|L - z|}{L}\right)}{\sinh\left(\sqrt{2 \langle b \rangle \gamma_r} \frac{L}{L}\right)}. \quad (\text{C.49})$$

This is identical to sol. C.45, which is a Fourier serie of the sinh-function.

With the *recombination length* λ defined by

$$\lambda = \sqrt{\frac{\tilde{D}}{\gamma_r}} \quad (\text{C.50})$$

this can be written as:

$$n(z) = n(0) \frac{\sinh\left(\frac{|L - z|}{\lambda}\right)}{\sinh\left(\frac{L}{\lambda}\right)}. \quad (\text{C.51})$$

Eq. C.51 fulfills the boundary condition of a given fixed central density $n(0)$. If - as in case of the HERMES target - the boundary condition is given as a constant atomic flux into the storage cell center, the atomic density $n(0)$ depends on recombination. The *effective conductance* C_{eff} for atoms at the entrance of a tube is given by:

$$C_{eff} = - \frac{\dot{n}_{inj}}{L \left. \frac{dn_a}{dz} \right|_{z=0}} = \frac{\dot{n}_{inj}}{n_a(0) \frac{L}{\lambda} \frac{1}{\tanh\left(\frac{L}{\lambda}\right)}}, \quad (\text{C.52})$$

so that one can derive an expression for the central atomic density:

$$n_a(0) = \frac{\dot{n}_{inj}}{C_{eff}}, \quad (\text{C.53})$$

and C_{eff} of a tube with a reactive surface is¹⁷³:

$$C_{eff} = C \frac{\frac{L}{\lambda}}{\tanh \frac{L}{\lambda}}. \quad (\text{C.54})$$

The calculation of the atomic density in the storage cell with the boundary condition of a constant injected atomic flux yields¹⁷⁴:

$$n_a(z) = \frac{\dot{n}_{inj}}{C} \frac{\sinh \frac{L-|z|}{\lambda}}{\frac{L}{\lambda} \cosh \frac{L}{\lambda}}. \quad (\text{C.55})$$

C.4.1 Moments of the CAD by Laplace Transformation

Eq. 2.43 has the form of a Laplace transformation:

$$\rho_a(z, \gamma_r) = \int_0^{\infty} N_{CAD}(b) e^{-\gamma_r b} db. \quad (\text{C.56})$$

The moments β_m of the CAD can therefore also be obtained by:

$$\beta_m = \langle b^m \rangle = \int_0^{\infty} b^m N_{CAD}(b) db = \int_0^{\infty} N_{CAD}(b) (-)^m \frac{d^m}{d\gamma_r^m} \Big|_{\gamma_r=0} e^{-\gamma_r b} db = (-)^m \frac{d^m \rho_a}{d\gamma_r^m} \Big|_{\gamma_r=0}. \quad (\text{C.57})$$

If one compares this equation to the Taylor serie of ρ_a , one finds:

$$\rho_a = \sum_{m=0}^{\infty} \frac{d^m \rho_a}{d\gamma_r^m} \Big|_{\gamma_r=0} \frac{\gamma_r^m}{m!} = 1 - \beta_1 \gamma_r + \frac{1}{2} \beta_2 \gamma_r^2 - \frac{1}{6} \beta_3 \gamma_r^3 + \dots \quad (\text{C.58})$$

The normalized atomic density $\rho_a(z)$ can be calculated analytically with $n(z)$ using eq. C.55:

$$\rho_a(z, \gamma_r) = \frac{n(z, \gamma_r)}{n(z, 0)}. \quad (\text{C.59})$$

If one substitutes $\frac{L}{\lambda}$ by $\varepsilon \sqrt{\gamma_r}$ with ε defined by

$$\varepsilon = \frac{\sqrt{3} UL}{4 S} = \frac{L}{\sqrt{\tilde{D}}}, \quad (\text{C.60})$$

one obtains with eq. C.55:

$$n_a(z) = \frac{\dot{n}_{inj}}{C} \frac{\sinh \left(\varepsilon \frac{L-|z|}{L} \sqrt{\gamma_r} \right)}{\varepsilon \sqrt{\gamma_r} \cosh \left(\varepsilon \sqrt{\gamma_r} \right)}. \quad (\text{C.61})$$

With x and y defined by $x = \varepsilon^2 \gamma_r$ and $y = \frac{L-|z|}{L}$ respectively, one can expand nominator and denominator into series, use the formula for division of series [Ab 84] and normalize by division through $n(z, \gamma_r = 0) = \frac{\dot{n}_{inj}}{C} \frac{L-|z|}{L}$. $\rho_a(z, \gamma_r)$ can then be written in the following way¹⁷⁵:

$$\rho_a = \left[1 + \frac{y^2 - 3}{6} x + \frac{y^4 - 10y^2 + 25}{120} x^2 + \frac{y^6 - 21y^4 + 175y^2 - 427}{5040} x^3 + \dots \right], \quad (\text{C.62})$$

¹⁷³More precisely: With a density and position independent recombination probability γ_r .

¹⁷⁴A proper calculation has to take the conductances of sample and injection tube into account. It can be found in [Bau 96]. The conductance C is here the conductance of both wings of the storage cell.

¹⁷⁵It should be mentioned, that it is possible to write $n_a(z)$ using the generating function of the Euler polynomials, which represent in this case the Taylor coefficients of the series.

which is a Taylor series and can be compared to eq. C.58:

$$\begin{aligned}
 \beta_1 &= \langle b \rangle = \frac{\varepsilon^2}{6}(3 - y^2) \\
 \beta_2 &= \frac{\varepsilon^4}{60}(25 - 10y^2 + y^4) = \frac{\varepsilon^4}{60}(5 - y^2)^2 \\
 \beta_3 &= \frac{\varepsilon^6}{840}(427 - 175y^2 + 21y^4 - y^6) \\
 &\dots
 \end{aligned}
 \tag{C.63}$$

For the first moment one finds the same expression as before (eq. C.43).

The advantage of the usage of the Laplace transformation turns out, if the tube is connected to additional side tubes - as in case of the HERMES storage cell. Eqs. C.63 are not accurate, if the total conductance of all side tubes C_{side} does not fulfill the requirement $C_{side} \ll C_{cell}$. As the atomic density $n(z, \gamma_r)$ can indeed be calculated in the presence of side tubes [Bau 96], one can calculate the average collision age using eq. C.57.

If C_i are the single conductances, that are connected to the storage cell center (with ε_i defined correspondingly), then the atomic density of the j-th tube is given by¹⁷⁶:

$$n^{(j)}(z, \gamma_r) = n_0 \frac{\sum_i C_i}{\sum_i C_i^{eff}} \frac{\sinh \varepsilon_j \sqrt{\gamma_r} y}{\sinh \varepsilon_j \sqrt{\gamma_r}}, \tag{C.64}$$

where $y = 1 - \frac{z}{L}$. The average collision age $\langle b \rangle_j(z)$ in the j-th tube is then given by:

$$\langle b \rangle_j(z) = \frac{1}{3} \frac{\sum_i C_i \varepsilon_i^2}{\sum_i C_i} + \frac{\varepsilon_j^2}{6}(1 - y_j^2). \tag{C.65}$$

C.4.2 First Order Approximation of Collision Age Distributions

The function $u(z, b)$ of eq. C.44 can - for collision ages $b \geq 100$ or low values of z - be approximated by an exponential function of the form:

$$N_{CAD}(b) = \frac{1}{\langle b \rangle} \exp\left(-\frac{b}{\langle b \rangle}\right). \tag{C.66}$$

¹⁷⁶This relation holds only for tubes of constant cross section.

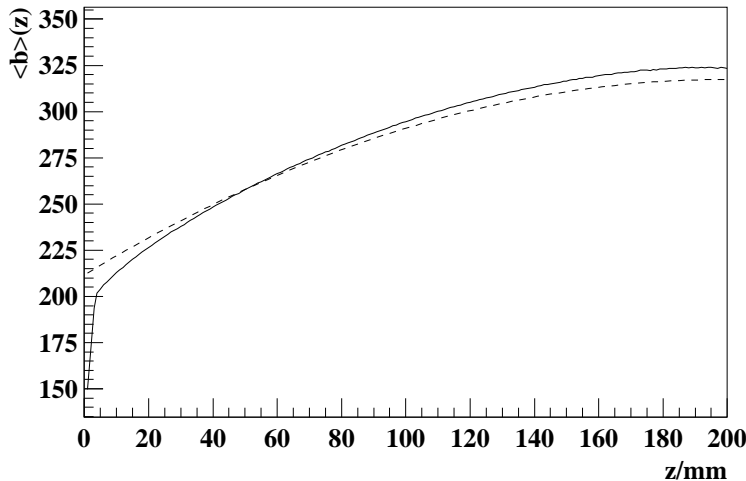


Fig. C.3: Average collision age $\langle b \rangle(z)$ in the beam tube of the HERMES storage cell obtained by the molecular flow simulation (solid line) and eq. C.65 (dashed line). The drop of $\langle b \rangle(z)$ in the storage cell center is caused by the injected jet. Besides this jet, the difference between calculation and simulation is $\leq 4\%$. The causes for this remaining difference are likely the effect of the conductance of the openings at the end of the storage cell and the uncertainty of the conductance formula.

For an exponential CAD one obtains¹⁷⁷:

$$\rho_a(\gamma_r) = \frac{1}{\langle b \rangle} \int_{b=0}^{\infty} \exp\left(-\frac{b}{\langle b \rangle} - \gamma_r b\right) = \frac{1}{1 + \langle b \rangle \gamma_r}. \quad (\text{C.67})$$

If the surface is not uniform in the sense, that there are different adsorption sites or different adsorption channels like physisorption and chemisorption, eq. 2.43 has to be modified. If f_i is the relative fraction of collisions of type i , leading with a probability $\gamma_r^{(i)}$ to recombination, one obtains:

$$\rho_a(\gamma_r^{(1)}, \dots, \gamma_r^{(N)}) = \frac{1}{1 + \langle b \rangle \sum_{i=1}^N f_i \gamma_r^{(i)}}. \quad (\text{C.68})$$

Using eq. C.58 one can derive, that the next order approximation for recombination is given by:

$$\rho_a(\gamma_r) = \frac{1}{1 + \langle b \rangle \gamma_r + \left(\langle b \rangle^2 - \frac{\langle b^2 \rangle}{2}\right) \gamma_r^2}, \quad (\text{C.69})$$

respectively by:

$$\rho_a(\gamma_r^{(1)}, \dots, \gamma_r^{(N)}) = \frac{1}{1 + \langle b \rangle \sum_{i=1}^N f_i \gamma_r^{(i)} + \left(\langle b \rangle^2 - \frac{\langle b^2 \rangle}{2}\right) \sum_{i=1}^N (f_i \gamma_r^{(i)})^2}. \quad (\text{C.70})$$

In the case, that the atoms diffuse through a cascade of tubes or volumes with different surface properties/materials, the total collision age distribution is a composition of the partial collision age distributions. In case of the HERMES target, one has to distinguish between the collisions in the beam tube, which is exposed to the HERA beam and the sample/extension tube (and injection tube). If $N_{CAD}^{BT}(b)$ is the CAD of the atoms in the cell center - counting only collisions with the surface of the beam tube - and N_{CAD}^{ST} is the CAD of the atoms entering the

¹⁷⁷A pure exponential CAD is a proper description for globular storage cells with small sampling exit (no tube connected).

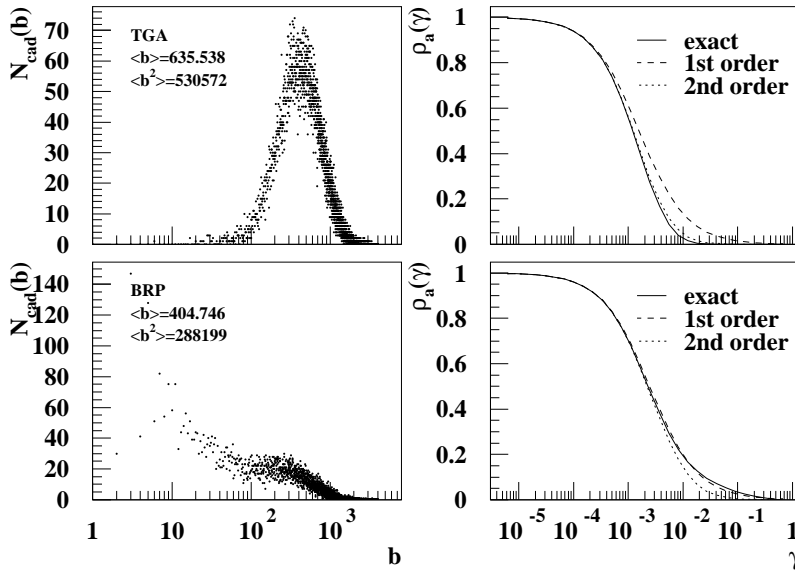


Fig. C.4: Collision age distributions (left) of atoms entering BRP (lower graphs) and TGA (upper graphs). The corresponding normalized densities $\rho_a(\gamma_r)$ are plotted in the right graph vs. γ_r (solid lines in the right graphs). The first (second) order approximation, given by eq. 2.45 (eq. 2.43) is plotted as a dashed (dotted) line. The CADs are obtained by a molecular flow Monte Carlo simulation [Bau 96].

TGA or BRP detector - counting only collisions in the sample/extension tube, the total collision age of the detected atoms is given by the convolution of the single CADs, as this processes are statistically independent:

$$N_{CAD}(b) = \int_0^{\infty} N_{CAD}^{BT}(\tilde{b}) N_{CAD}^{ST}(b - \tilde{b}) d\tilde{b}. \quad (C.71)$$

As $\rho_a(\gamma_r)$ is the Laplace transform of N_{CAD} , it is - assumed, the situation can be described by a common value γ_r - given by the product of the Laplace transform of N_{CAD}^{BT} and N_{CAD}^{ST} :

$$\rho_a(\gamma_r) \simeq \frac{1}{1 + \langle b_{BT} \rangle \gamma_r} \cdot \frac{1}{1 + \langle b_{ST} \rangle \gamma_r}. \quad (C.72)$$

If one has to distinguish between the recombination probability in the beam tube γ_r^{BT} and sample/ext. tube γ_r^{ST} , one still obtains a product:

$$\rho_a(\gamma_r) \simeq \frac{1}{1 + \langle b_{BT} \rangle \gamma_r^{BT}} \cdot \frac{1}{1 + \langle b_{ST} \rangle \gamma_r^{ST}}. \quad (C.73)$$

C.4.3 Expected Effect of the Density Dependence of Recombination

In order to estimate the expected effect of a density dependent γ_r , one may use eq. 2.45 with $\gamma_r = k \rho_a$, where $k = \frac{n^{inj}}{n_0} \langle b \rangle$:

$$\rho_a = \frac{1}{1 + \langle b \rangle \gamma_r} = \frac{1}{1 + \langle b \rangle k \rho_a}. \quad (C.74)$$

The solution of this equation is

$$\rho_a = \frac{\sqrt{4k + 1} - 1}{2k}, \quad (C.75)$$

which is shown by fig. C.5. If a competing reaction is present, a precise determination of the change in the value of α_{TGA} requires reasonably low values of $\alpha_{TGA} \simeq 0.5$ and low statistical

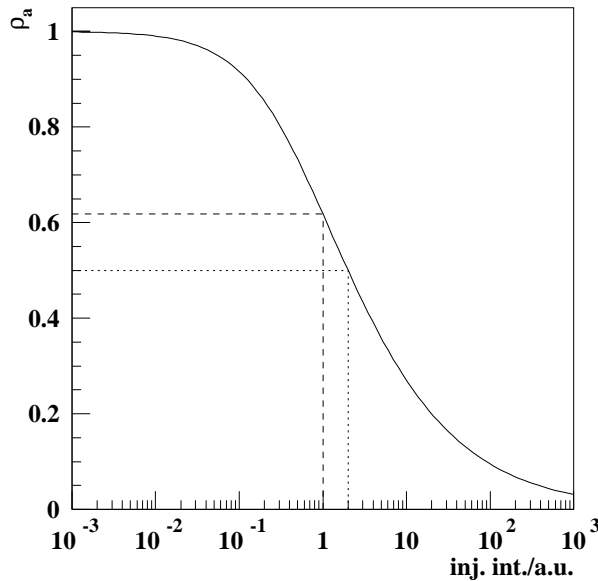


Fig. C.5: Expected measurement $\alpha_{TGA} \simeq \rho_a$ as a function of the injected intensity in case of a density dependent recombination probability γ_r . The expected change of α_{TGA} for a change in the intensity by a factor of 2 is indicated by the dashed and dotted lines. For $\alpha_{TGA} = 0.62$, an increase of the injected intensity by a factor of 2 results in a drop of α_{TGA} of about 20 %.

uncertainties¹⁷⁸. In case of the measurement, which is shown in fig. 5.8, this requirements are certainly fulfilled.

C.5 Differential Collision Ages

Besides the question, what the average collision age within a certain atomic sample is, one is also interested in the question, how many collisions the atoms of a sample had within a certain region, which can be called the *differential collision age*. It is for example interesting to know, how many wall collisions the atoms of the TGA and BRP sample had in average in the beam tube of the storage cell - and how these collisions are distributed over the length of the beam tube. The calculation may start with the calculation of the atomic density in the storage cell center, if $\gamma_r^{ST} = 0$ and γ_r^{BT} is non-zero only for parts of the beam tube, where $|z| > L_0$. The effective conductance C^{eff} of the beam tube is then

$$C^{eff} = \frac{C_{<L_0} C_{>L_0}}{C_{<L_0} + C_{>L_0}}. \quad (C.76)$$

The conductance of the non-recombining inner part $C_{<L_0}$ is $C_{<L_0} = C_{BT} \frac{L}{L_0}$ and the effective conductance of the recombining outer part is

$$C_{>L_0} = C_{BT} \frac{L}{L - L_0} \frac{\frac{L-L_0}{\lambda}}{\tanh \frac{L-L_0}{\lambda}}. \quad (C.77)$$

The calculation of the combined conductance yields:

$$C^{eff} = C \frac{\frac{L}{\lambda}}{\frac{L_0}{\lambda} + \tanh \frac{L-L_0}{\lambda}}. \quad (C.78)$$

The central normalized density can be obtained from eq. C.64:

$$\rho_a(0) = \frac{\sum_i C_i}{\sum_i C_i^{eff}}. \quad (C.79)$$

If the conductances of injection and sample tube are neglected, one finds:

$$\rho_a(0) = \frac{L_0}{L} + \frac{\lambda}{L} \tanh \frac{L - L_0}{\lambda}. \quad (C.80)$$

The first terms of the Taylor serie are:

$$\rho_a(0) = 1 - \frac{1}{3} \left(1 - \frac{L_0}{L}\right)^3 \frac{L^2}{\tilde{D}} \gamma_r \dots \quad (C.81)$$

The average number of collisions $\langle b \rangle_0(L_0)$, that atoms in the storage cell center had in the region $z > L_0$ is therefore:

$$\langle b \rangle_0(L_0) = \frac{1}{3} \left(1 - \frac{L_0}{L}\right)^3 \frac{L^2}{\tilde{D}}. \quad (C.82)$$

The average number of collisions $\delta \langle b \rangle_0(z)$ between z and $z + \delta z$ is just the derivative with respect to L_0 :

$$\delta \langle b \rangle_0(z) = \left(1 - \frac{z}{L}\right)^2 \frac{L^2}{\tilde{D}} \frac{\delta z}{L}. \quad (C.83)$$

Fig. C.6 shows a comparison between the second order dependence in z of eq. C.83 and the differential collision age of the sample beam into the TGA chamber.

¹⁷⁸In addition, a reasonable correction for the ballistic flow and the restgas contribution is required.

C.6 Diffusion and Spin Relaxation - the Rate Equation

If R_{ab} is the probability, that an atom in hyperfine state $|b\rangle$ is after the next wall collision in hyperfine state $|a\rangle$, then eq. C.46 has to be modified in the following way, if wall depolarization is taken into account:

$$\frac{\partial n_a}{\partial b} = \tilde{D} \frac{\partial^2 n_a}{\partial z^2} - \gamma_r n_a + (1 - \gamma_r) \sum_b R_{ab} n_b, \quad (\text{C.84})$$

where n_a is the number density of atoms in hyperfine state $|a\rangle$ ¹⁷⁹. As discussed in chapter D.4, spin-exchange collisions between atoms in the gas phase also lead to a change in the hyperfine states of the colliding atoms. The rate of change in the number density of atoms in state $|a\rangle$ is given by eq. D.51 and eq. C.84 has to be modified accordingly:

$$\frac{\partial n_a}{\partial b} = \tilde{D} \frac{\partial^2 n_a}{\partial z^2} - \gamma_r n_a + (1 - \gamma_r) \sum_b R_{ab} n_b + \sigma_{se} \langle v_r \rangle \tau_f \sum_{bc} M_{bc}^a n_b n_c, \quad (\text{C.85})$$

where σ_{se} is the cross section for spin exchange collisions and $\langle v_r \rangle$ the mean relative velocity of the atoms with $\langle v_r \rangle = \sqrt{2} \langle v \rangle$.

Usually, it is difficult to solve partial differential equations. As one is mainly interested in the steady state solution - one may simplify eq. C.85 by the integration over all collision ages, as already described before. The result is an ordinary non-linear differential equation of second order:

$$0 = \tilde{D} \frac{d^2 n_a}{dz^2} - \gamma_r n_a + (1 - \gamma_r) \sum_b R_{ab} n_b + \sigma_{se} \langle v_r \rangle \tau_f \sum_{bc} M_{bc}^a n_b n_c, \quad (\text{C.86})$$

where $n_a = n_a(z)$. Eq. C.86 is called the *rate equation* and is supposed to give a description of all relevant relaxation processes inside the storage cell in the steady state. Only bunch field induced depolarization - which is negligible with carefully chosen operation conditions (resp. at the target working point) - is not included. The equation can be solved numerically.

¹⁷⁹The factor $(1 - \gamma_r)$ in the wall depolarization term represents the fact that atoms can either depolarize or recombine during a wall collision. If they recombine, they are taken away from the sampled beam entering the BRP. The measured polarization is the polarization of atoms.

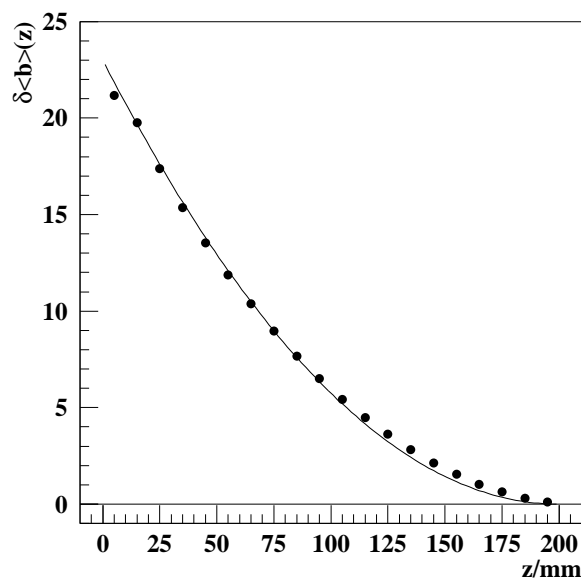


Fig. C.6: Average differential collision age of TGA/BRP sample beam as obtained by molecular flow simulation (symbols) and by eq. C.83 (line).

C.6.1 The Master Equation

If eq. C.86 is averaged over z , one obtains:

$$0 = \frac{\tilde{D}}{L} \left(\left. \frac{dn_a}{dz} \right|_{z=L} - \left. \frac{dn_a}{dz} \right|_{z=0} \right) - \gamma_r \langle n_a \rangle + (1 - \gamma_r) \sum_b R_{ab} \langle n_b \rangle + \sigma_{se} \langle v_r \rangle \tau_f \sum_{bc} M_{bc}^a \langle n_b n_c \rangle, \quad (\text{C.87})$$

The density gradient is related to the net particle flux¹⁸⁰ $\dot{N}_a = \int \vec{j} d\vec{S}$ by:

$$\frac{dn_a}{dz} = -\frac{1}{DS} \dot{N}_a, \quad (\text{C.88})$$

so that

$$\frac{\tilde{D}}{L} \frac{dn_a}{dz} = -\frac{\tau_f}{SL} \dot{N}_a, \quad (\text{C.89})$$

and hence

$$0 = \frac{\tau_f}{SL} \left(\dot{N}_a^{inj} - \dot{N}_a^{exit} \right) - \gamma_r \langle n_a \rangle + (1 - \gamma_r) \sum_b R_{ab} \langle n_b \rangle + \sigma_{se} \langle v_r \rangle \tau_f \sum_{bc} M_{bc}^a \langle n_b n_c \rangle. \quad (\text{C.90})$$

The hyperfine populations N_a are given by $N_a = \frac{\langle n_a \rangle}{\langle n \rangle}$ with the average atomic density $\langle n \rangle = \frac{N}{SL}$ and the total number of atoms N in the storage cell. The product $\langle n_b n_c \rangle$ has to be treated in a different way. If one assumes in zero order approximation, that

$$\langle n_b n_c \rangle = N_b N_c \langle n^2 \rangle, \quad (\text{C.91})$$

one finds, that

$$\langle n^2 \rangle = \frac{1}{L} \int_0^L n^2(z) dz = \frac{4}{3} \langle n \rangle^2. \quad (\text{C.92})$$

This holds within the beam tube in case of no recombination and low relaxation, but if the equation is thought to describe the BRP measurement, then more effort is required for the evaluation. With the definition of a *correlation factor* ρ_c by

$$\rho_c = \frac{\langle n^2 \rangle}{\langle n \rangle^2} \quad (\text{C.93})$$

one may write:

$$0 = \frac{\dot{N}_a^{inj} - \dot{N}_a^{exit}}{N} - \frac{\gamma_r}{\tau_f} N_a + \frac{1 - \gamma_r}{\tau_f} \sum_b R_{ab} N_b + \frac{1}{\tau_{se}} \sum_{bc} M_{bc}^a N_b N_c, \quad (\text{C.94})$$

where $\frac{1}{\tau_{se}} = \rho_c \sigma_{se} \langle v_r \rangle \langle n \rangle$. The total number of atoms inside the storage cell is equivalent to the number of injected atoms per unit time times the mean residence time inside the storage cell τ_d^0 times the normalized atomic density: $N = \rho_a \tau_d^0 \sum_a \dot{N}_a^{inj}$, so that

$$\frac{\dot{N}_a^{inj}}{N} = \frac{N_a^{inj}}{\rho_a \tau_d^0}, \quad (\text{C.95})$$

¹⁸⁰More precisely speaking: The average net number of particles passing through a defined surface area per unit time.

where N_a^{inj} is the hyperfine population of the injected atomic beam. The number of atoms exiting the storage cell per unit time is equal to the number of atoms inside the storage cell divided by their mean residence time:

$$\dot{N}_a^{exit} = N \frac{N_a}{\tau_d^0}, \quad (\text{C.96})$$

so that:

$$0 = \frac{N_a^{inj}}{\rho_a \tau_d^0} - \left(\frac{1}{\tau_d^0} + \frac{\gamma_r}{\tau_f} \right) N_a + \frac{1 - \gamma_r}{\tau_f} \sum_b R_{ab} N_b + \frac{1}{\tau_{se}} \sum_{bc} M_{bc}^a N_b N_c. \quad (\text{C.97})$$

The average collision age can be written as $\langle b \rangle = \frac{\tau_d^0}{\tau_f}$, so that the summation over a delivers:

$$0 = \frac{1}{\rho_a} - 1 - \langle b \rangle \gamma_r, \quad (\text{C.98})$$

as $\sum_{a,b} R_{ab} = 0$ and $\sum_a M_{bc}^a = 0$. The recombination probability is usually small compared to unity $\gamma_r \ll 1$, so that one obtains eq. 6.1

$$0 = N_a^{inj} - N_a + \langle b_{eff} \rangle \sum_b R_{ab} N_b + \langle c_{eff} \rangle \sum_{bc} M_{bc}^a N_b N_c, \quad (\text{C.99})$$

where $\langle b_{eff} \rangle = \langle b \rangle \rho_a$ is the effective average number of wall collisions and $\langle c_{eff} \rangle = \tau_d / \tau_{se} \rho_a$ is the effective average number of spin exchange collisions of the sample beam. Eq. 6.1 is called the *master equation*.

C.6.2 Spin Exchange Collisions and The Correlation Factor

Similar to the description of the effects of wall collisions by a *collision age distribution* (CAD) $N_{CAD}(b)$ and the average collision age $\langle b \rangle$ of an atomic sample, a *spin exchange collision age distribution* (SCAD) $N_{scad}(c)$ may be used to describe spin exchange relaxation by the master equation. The number \dot{N}_{se} of spin exchange collisions per atom and unit time is:

$$\dot{N}_{se} = \langle n \rangle \sigma_{se} \langle v_r \rangle = \sqrt{2} n \sigma_{se} \langle v \rangle. \quad (\text{C.100})$$

If the atom with index i , injected into the storage cell at time $t = 0$, is at a position $\vec{x}_i(t)$ at time t , then the length l of its trajectory (its *diffusion length*) is in average given by $l_i = \langle v \rangle t$. The number c_i of exchange collisions after a diffusion length L_i is:

$$c_i = \sqrt{2} \sigma_{se} \langle n \rangle (l_\rho)_i, \quad (\text{C.101})$$

with the total length of its tranjectory L_i , the average atomic density $\langle n \rangle$ along the beam tube and $(l_\rho)_i$ defined by

$$(l_\rho)_i = \frac{1}{\langle n \rangle} \int_0^{L_i} n(l_i) dl_i. \quad (\text{C.102})$$

The mean value $\langle l_\rho \rangle$ is given by

$$\langle l_\rho \rangle = \frac{1}{M} \sum_{i=1}^M (l_\rho)_i. \quad (\text{C.103})$$

The ratio between $\langle l_\rho \rangle$ and the diffusion length $\langle l \rangle$ is the *correlation factor* ρ_c of the atomic sample as introduced in sec. C.6.1. The factor is defined as the correlation between atomic density and the residence time of the atoms¹⁸¹:

$$\rho_c = \frac{\langle l_\rho \rangle}{\langle l \rangle}. \quad (\text{C.104})$$

The average number of spin exchange collisions $\langle c \rangle$ of an atom is:

$$\langle c \rangle = \sqrt{2} \sigma_{se} \rho_c \langle l \rangle \langle n \rangle. \quad (\text{C.105})$$

For the beam tube itself, eq. C.92 delivers already a reasonable approximation: $\rho_c^{BT} \simeq \frac{4}{3}$. The exact value is - due to the effect of the non-zero conductance of the cell ends - slightly higher. Especially the values of ρ_c^{BRP} and ρ_c^{BT} are required for the interpretation of the BRP measurement and for the evaluation of the target polarization respectively. The molecular flow simulation was used to obtain the numerical values, that are listed in tab. F.6. The polarization loss by spin exchange collisions is - in first order - proportional to c_i and therefore to $\langle l_\rho \rangle = \rho_c \langle l \rangle$. The difference in the value of $\langle l_\rho \rangle$ between the atomic sample of the beam tube and the BRP is small (about 6%), so that the polarization loss by spin exchange is in the beam tube about 6% higher than measured by the BRP.

C.7 The Model of Distributed Sources

The model of distributed sources assumes, that the recombination or depolarization probabilities are - at least piecewise - constant. The calculation of the atomic density follows basically the treatment of sec. C.4 and was in some detail developed in [Bau 96]. Hence only a short summary will be given in the present work. The purpose of this model is the calculation of the sampling corrections for scenarios, where the recombination probability is constant within each tube of the storage cell, but may differ between the beam tube and the side tubes. One has therefore two different values of γ_r , as there are γ_r^{BT} and $\gamma_r^{IT} = \gamma_r^{ST} = \gamma_r^{ET}$, as a distinction between the side tubes is possible, but of low practical use. The geometrical factors ε_{xx} were defined by eq. C.60 and are listed in tab. F.1 for all tubes of the large and small storage cell.

The atomic density in the beam tube of the storage cell is given by eq. C.64:

$$n^{BT}(z) = n(0) \frac{\sinh\left(\varepsilon_{BT} \sqrt{\gamma_r^{BT}} y\right)}{\sinh\left(\varepsilon_{BT} \sqrt{\gamma_r^{BT}}\right)}, \quad (\text{C.106})$$

where $y = 1 - \frac{|z|}{L_{BT}}$. The central atomic density $n(0)$ is given by

$$n(0) = n_0 \frac{2C_{BT} + C_{IT} + C_{STET}}{2C_{BT}^{eff} + C_{IT}^{eff} + C_{STET}^{eff}}. \quad (\text{C.107})$$

The effective conductance of a tube is defined by eq. C.52. The combined value C_{STET}^{eff} of sample and extension tube is:

$$C_{STET}^{eff} = \frac{C_{ST}^{eff} C_{ET}^{eff}}{C_{ST}^{eff} + C_{ET}^{eff}}. \quad (\text{C.108})$$

¹⁸¹As the density is proportional to the mean residence time, this definition is equivalent to the one given in app. C.6.1.

The atomic density along z in the sample tube is¹⁸²:

$$n^{ST}(z) = \frac{n(0)}{C_{ST}^{eff} + C_{ET}^{eff}} \left(C_{ST}^{eff} \frac{\cosh\left(\varepsilon_{ST}\sqrt{\gamma_r^{ST}}y\right)}{\cosh\left(\varepsilon_{ST}\sqrt{\gamma_r^{ST}}\right)} + C_{ET}^{eff} \frac{\sinh\left(\varepsilon_{ST}\sqrt{\gamma_r^{ST}}y\right)}{\sinh\left(\varepsilon_{ST}\sqrt{\gamma_r^{ST}}\right)} \right). \quad (C.109)$$

For the extension tube one finds¹⁸³:

$$n^{ET}(z) = \frac{n(0)}{\cosh\left(\varepsilon_{ST}\sqrt{\gamma_r^{ST}}\right)} \frac{C_{ST}^{eff}}{C_{ST}^{eff} + C_{ET}^{eff}} \frac{\sinh\left(\varepsilon_{ET}\sqrt{\gamma_r^{ET}}y\right)}{\sinh\left(\varepsilon_{ET}\sqrt{\gamma_r^{ET}}\right)}. \quad (C.110)$$

The normalized atomic densities are given by $\rho_a = \frac{n(z, \gamma_r)}{n(z, 0)}$ - only for the calculation of α_r as a density weighted average along the beam tube one has:

$$\langle \rho_a^{BT} \rangle = \frac{2}{n_0} \int_{y=0}^1 n(z, \gamma_r) dy = \frac{n(0)}{n_0} \frac{C_{BT}}{C_{BT}^{eff}} \frac{2 \cosh\left(\varepsilon_{BT}\sqrt{\gamma_r^{BT}}\right)}{1 + \cosh\left(\varepsilon_{BT}\sqrt{\gamma_r^{BT}}\right)}. \quad (C.111)$$

For the TGA measurement, one may approximate the sampling distribution by a polynomial of 2nd order as shown in fig. 4.2. This polynomial is approximately given by $w(y) = (y_0 - y)y$ and α_r^{TGA} is then given by:

$$\alpha_r^{TGA} = \frac{\int_{y=0}^{y_0} \rho_a^{ET}(y)w(y) dy}{\int_{y=0}^{y_0} w(y) dy}, \quad (C.112)$$

where $\rho_a^{ET}(y)$ is:

$$\rho_a^{ET}(y) = \rho_a^{BT}(0) \frac{C_{ST}^{eff}}{C_{ST}} \frac{C_{ST} + C_{ET}}{C_{ST}^{eff} + C_{ET}^{eff}} \frac{\sinh\left(\varepsilon_{ET}\sqrt{\gamma_r^{ET}}y\right)}{y \cosh\left(\varepsilon_{ST}\sqrt{\gamma_r^{ST}}\right) \sinh\left(\varepsilon_{ET}\sqrt{\gamma_r^{ET}}\right)}. \quad (C.113)$$

The integration yields:

$$\alpha_r^{TGA} = 6 \rho_a^{BT}(0) \frac{C_{ST}^{eff}}{C_{ST}} \frac{C_{ST} + C_{ET}}{C_{ST}^{eff} + C_{ET}^{eff}} \frac{\sinh\left(\varepsilon_{ET}\sqrt{\gamma_r^{ET}}y_0\right) - \varepsilon_{ET}\sqrt{\gamma_r^{ET}}y_0}{\varepsilon_{ET}^2 \gamma_r^{ET} y_0^3 \cosh\left(\varepsilon_{ST}\sqrt{\gamma_r^{ST}}\right) \sinh\left(\varepsilon_{ET}\sqrt{\gamma_r^{ET}}\right)}. \quad (C.114)$$

As visible in fig. 4.2, z_0 is about 20 mm and $y_0 = 1 - \frac{z_0}{L_{ET}} = \frac{5}{6}$. The results of the calculations for several ratios between the recombination probabilities of beam tube and side tubes are collected in fig. C.7.

¹⁸²The meaning of the position z is in this context is the distance to the most central point in the sample tube. $z = L_{ST}$ is the position, where the sample tube is connected to the extension tube. Correspondingly y has to taken as $y = 1 - \frac{z}{L_{ST}}$.

¹⁸³The meaning of z and y is relative to the extension tube in this context.

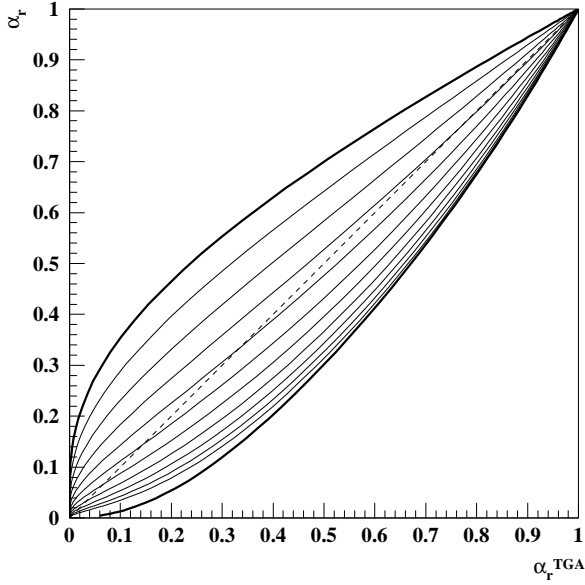


Fig. C.7: The upper thick line is the graph of $\alpha_r(\alpha_r^{TGA})$ for the homogeneous cell model (**HC**), where $\gamma_r^{BT} = \gamma_r^{IT} = \gamma_r^{ST} = \gamma_r^{ET}$. The lower thick line is the graph of $\alpha_r(\alpha_r^{TGA})$ for the extreme case $\gamma_r^{ST} = \gamma_r^{ET} = \gamma_r^{IT} = 0$ and $\gamma_r^{BT} \geq 0$ of the **HBT** scenario. This curve represents the "worst case" of this scenario. All calculations were done for the large storage cell. The thin lines in between represent mixtures of these scenarios, where γ_r^{BT} is by a fixed factor larger than $\gamma_r^{ST} = \gamma_r^{ET} = \gamma_r^{IT}$. The dashed line is the diagonal, where $\alpha_r = \alpha_r^{TGA}$ and is drawn as a guide for the eye.

C.8 The Model of Localized Sources

This section describes a way to study scenarios, where recombination (or depolarization) occurs dominantly in small regions (so-called *hot spots*) inside the storage cell - the *model of localized sources*. The purpose of this model is to describe wall recombination and relaxation in case of an inhomogeneous beam tube (**IBT**) and to draw conclusions for an arbitrary distribution of the recombination probability $\gamma_r(z)$ along the beam tube axis with mathematical precision.

The sample gas leaves the HERMES storage cell in the center through the sample tube. Hence the properties of the sample gas are - besides further recombination and/or spin relaxation on the walls of the sample tube - the properties of the target gas at the center of the storage cell. If the surface is not uniform, there is no unique relation between $\langle \alpha \rangle$ and $\alpha(z=0)$, but there should still be a range $\alpha_{min} \leq \langle \alpha \rangle \leq \alpha_{max}$ for any given $\alpha(z=0)$ and *any* possible surface inhomogeneity. This assumption is reasonable due to the diffusion process: The particle sample, that leaves the cell via the sample tube, contains *all* subsamples of particles, which can be found inside the cell - only the relative weight is different from the storage cell.

The model of localized sources requires a lot of calculations. A simpler argumentation, that leads to the same results, was suggested by Dr. Sergei Pod'yachev and will be explained in advance.

From eq. C.48 it follows that the slope of the atomic density $n(z)$ can (besides the exception at $z=0$, where the ABS injects) never decrease along z :

$$\tilde{D} \frac{d^2 n}{dz^2} = \gamma_r(z) n(z) \geq 0, \quad (\text{C.115})$$

and from eq. 2.17 and eq. 2.30 one can conclude, that the flux $\phi = \int \vec{j} d\vec{S}$ through the cross section of the beam tube is given by

$$\phi^{BT} = -C^{BT} L \frac{\partial n}{\partial z}, \quad (\text{C.116})$$

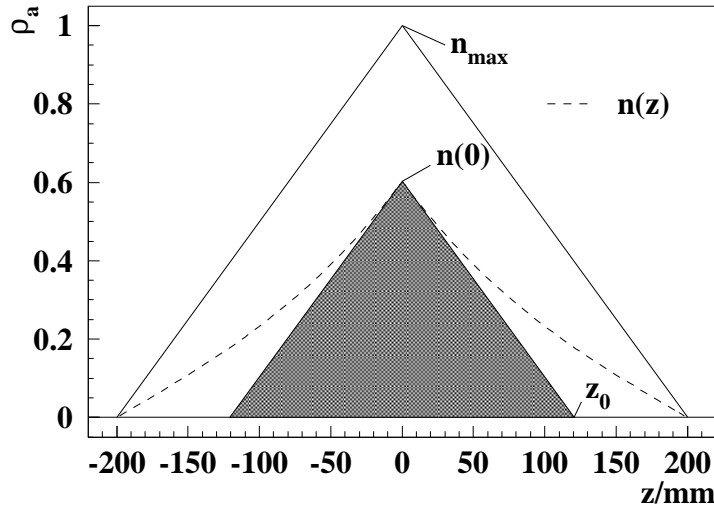


Fig. C.8: The minimal atomic density in case of recombination is given by the colored area. The atomic density for a constant γ_r is indicated by the dashed line. The solid line corresponds to the maximal density in case of $\gamma_r = 0$.

which is negative for positive z along the beam tube. One finds by eq. C.115, that the absolute slope is maximal at the center of the beam tube (see fig. C.8):

$$\left| \frac{\partial n}{\partial z} \right| \leq \left| \frac{\partial n}{\partial z}(0) \right|. \quad (\text{C.117})$$

If one restricts the argumentation to a symmetric situation $\gamma_r(z) = \gamma_r(-z)$, then the average atomic density $\langle n \rangle$ is the area under the dashed line in fig. C.8. This area is for any function $\gamma_r(z)$ greater than or equal to the colored area:

$$\langle n \rangle = \frac{1}{L} \int_{z=0}^L n(z) dz \geq n(0) \frac{z_0}{2L}, \quad (\text{C.118})$$

where L is the length of one half of the beam tube and z_0 is - as shown in fig. C.8 given by

$$n(0) + \frac{\partial n}{\partial z}(0) z_0 = 0. \quad (\text{C.119})$$

On the other hand, the continuity equation delivers

$$\phi^{ABS} = n(0) [C^{IT} + C^{ST}] - 2C^{BT}L \frac{\partial n}{\partial z}(0) = n_{max} C^{TOT}, \quad (\text{C.120})$$

where $C^{TOT} = 2C^{BT} + C^{IT} + C^{ST}$ is the total conductance of the storage cell. Using these equation, one finds:

$$\langle \rho_a \rangle = 2 \frac{\langle n \rangle}{n_{max}} \geq \rho_a^2(0) \frac{2}{2 + \varepsilon - \varepsilon \rho_a(0)}, \quad (\text{C.121})$$

where $\rho_a(0) = n(0)/n_{max}$ and $\varepsilon = (C^{IT} + C^{ST})/C^{BT}$. The model of localized sources yields the same result and will be explained in the following.

The model of localized sources replaces the continuous distribution of recombining sources, represented by the term $-\gamma_r n$ in eq. C.46 by a sum over m localized sources¹⁸⁴:

$$\frac{d^2 n_a}{dz^2} = \sum_{k=1}^m Q_k \delta(z - z_k), \quad (\text{C.122})$$

¹⁸⁴A similar ansatz of argumentation for wall depolarization in storage cells was found in [Gil 93].

with Dirac's δ -function. By integration of eq. C.122 over a single source Q_j , one obtains:

$$\frac{dn_a}{dz}(z_j + \varepsilon) - \frac{dn_a}{dz}(z_j - \varepsilon) = Q_j. \quad (\text{C.123})$$

The model of localized source leads therefore to a piecewise linear function, which can approximate any other function to any precision with the appropriate choice of the Q_k and z_k and a high enough m . The advantage of this picture is its high predictive and explanatory power in combination with mathematical simplicity, as it will be demonstrated in this section.

Fig. C.9 illustrates the situation with a hot spot in one wing of the storage cell for two different recombination probabilities. A recombining hot spot is equivalent to a whole in the surface, where atoms disappear and molecules are injected. The right graph of fig. C.9 shows a hot spot of maximal strength, which is equivalent to a situation, where the outer part of the cell surface has a recombination probability γ_r of 1. An important physical property of the atomic density $\rho_a(z)$ is, that it is positive semidefinite. Therefore it has to be ensured in this model, that the negative densities, which represent recombination, do not exceed the atomic densities. A source located at $z = z_0$ can be described by the density distribution:

$$\rho(z) = Q \left(1 - \frac{z_0}{L^2 - z_0^2}(z - z_0) - \frac{L}{L^2 - z_0^2}|z - z_0| \right). \quad (\text{C.124})$$

Obviously the following relations hold:

$$\rho(z) \leq Q \frac{L+z}{L+z_0} \quad (\text{C.125})$$

$$\rho(z) \leq Q \frac{L-z}{L-z_0} \quad (\text{C.126})$$

$$\rho(z) = Q \text{Min} \left\{ \frac{L+z}{L+z_0}, \frac{L-z}{L-z_0} \right\}. \quad (\text{C.127})$$

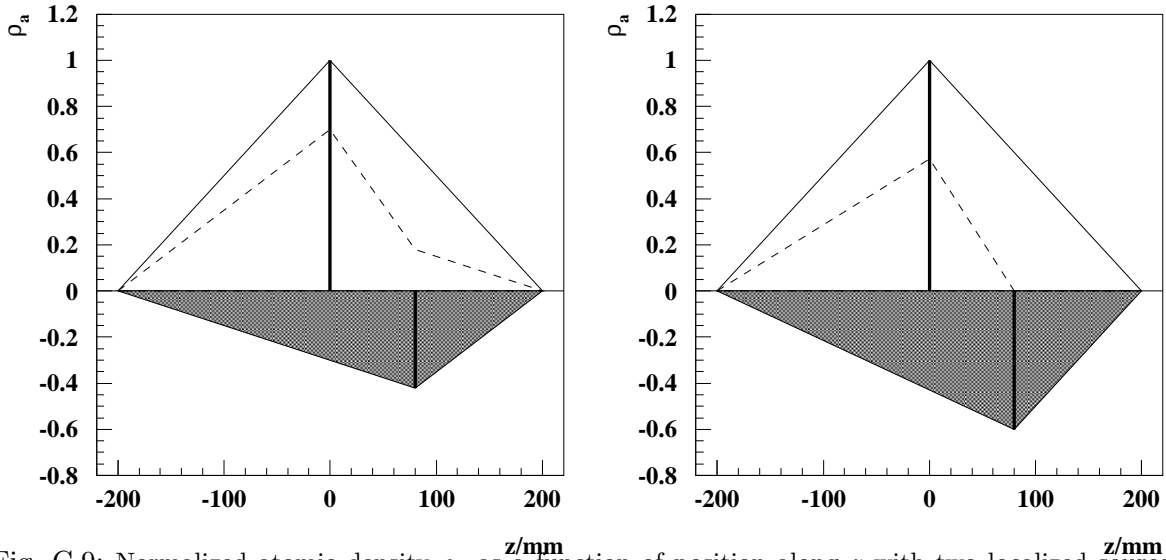


Fig. C.9: Normalized atomic density ρ_a as a function of position along z with two localized sources - the ABS injecting in the center and a hot spot 80 mm off center. The resulting density is given as the sum of both densities and is drawn as a dashed curve. The strength of each source is indicated by a thick vertical line. The hot spot of the left figure has a 70% of the maximal strength. The right figure shows a hot spot with maximal strength. The dashed curve of the right figure drops to zero at $z < L$. A point source of maximal strength is therefore equivalent to a distributed source with $\gamma_r = 1$ for $z > L$.

The picture of localized sources uses for the general case the atomic density, subtracted by a sum of this functions:

$$\rho_a(z) = \frac{L - |z|}{L} - \sum_{k=1}^m \rho_k(z) \geq 0. \quad (\text{C.128})$$

Which can be written as

$$\sum_{k=1}^m \rho_k(z) \leq \frac{L + z}{L} \text{ for } z \leq 0 \quad (\text{C.129})$$

$$\sum_{k=1}^m \rho_k(z) \leq \frac{L - z}{L} \text{ for } 0 \leq z. \quad (\text{C.130})$$

Using the conditions from above this can be written as

$$\sum_{k=1}^m \frac{Q_k}{L + z_k} \leq \frac{1}{L} \quad (\text{C.131})$$

$$\sum_{k=1}^m \frac{Q_k}{L - z_k} \leq \frac{1}{L}, \quad (\text{C.132})$$

or by the combination of both inequalities:

$$\sum_{k=1}^m \frac{Q_k L}{L^2 - z_k^2} + \left| \sum_{k=1}^m \frac{Q_k z_k}{L^2 - z_k^2} \right| \leq \frac{1}{L}. \quad (\text{C.133})$$

It is useful to define $q_k = Q_k \frac{L^2}{L^2 - z_k^2}$ and $\eta_k = \frac{z_k}{L}$. One then obtains as the restriction:

$$\sum_{k=1}^m q_k + \left| \sum_{k=1}^m q_k \eta_k \right| \leq 1. \quad (\text{C.134})$$

The atomic density at the cell center ($z = 0$) is given by:

$$\rho_a(0) = 1 - \sum_{k=1}^m Q_k \frac{L}{L + |z_k|} = 1 - \sum_{k=1}^m q_k (1 - |\eta_k|) \quad (\text{C.135})$$

The average atomic $\langle \rho_a \rangle$ density is given by:

$$\langle \rho_a \rangle = 1 - \sum_{k=1}^m Q_k = 1 - \sum_{k=1}^m q_k (1 - |\eta_k|)(1 + |\eta_k|) = \rho_a(0) - \sum_{k=1}^m q_k (1 - |\eta_k|)|\eta_k|. \quad (\text{C.136})$$

As by definition q_k is positiv or zero, it follows, that the maximal value for $\langle \rho_a \rangle$ is given by $\rho_a(0)$ for $\eta_k = 0$. This result could be expected, as a deviation from $\eta_k = 0$ reduces immediately the effect of the source k located at z_k at the position $z = 0$, as it is illustrated in fig. C.9. In order to find the minimum of $\langle \rho_a \rangle$ for a given value of $\rho_a(0)$ under the boundary condition C.134, one can make use of Lagrange multipliers λ and μ :

$$\frac{d}{dq_k} \left(\langle \rho_a \rangle + \lambda(\rho_a(0) - c_1) + \mu \left(\sum_{k=1}^m q_k + \left| \sum_{k=1}^m q_k \eta_k \right| - c_2 \right) \right) = 0. \quad (\text{C.137})$$

This results:

$$-(1 - |\eta_k|)(1 + |\eta_k|) - \lambda(1 - |\eta_k|) + \mu(1 + |\eta_k|) = 0 \quad (\text{C.138})$$

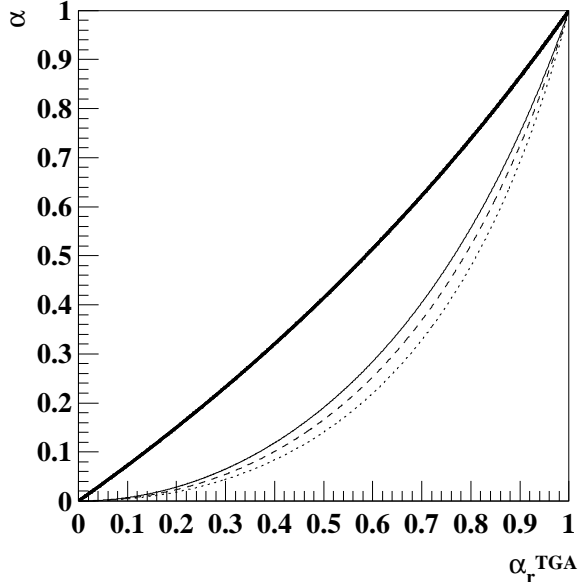


Fig. C.10: Limits of the average atomic fraction α_r in storage cell as a function of measured atomic fraction α_r^{TGA} in case of negligible recombination in sample and extension tube - calculated with the model of localized sources. The solid curve represents a scenario with infinite small conductance of sample and injection tube, the dashed curves a calculated for the large cell geometry and the dotted curve for the small beam tube cross section. The thick solid curve is the (common) upper limit.

It is not necessary to solve this equation - as it is a condition, which is independent on k . Therefore only two sources are relevant for the extreme case - one at $z = L|\eta|$ and one at $z = -L|\eta|$. Using the parameter σ to quantify the difference between the two sources, and a parameter $\kappa \leq 1$ to fulfill the boundary condition C.134, one defines:

$$\begin{aligned} q_1 &= q(1 - \sigma^2) \\ q_2 &= q(1 + \sigma^2) \\ \eta_1 &= \eta \\ \eta_2 &= -\eta \\ 2q(1 + \eta\sigma^2) &= \kappa \leq 1, \end{aligned}$$

and obtains:

$$\begin{aligned} \eta &= \frac{\kappa - 1 + \rho_a(0)}{\kappa + \sigma^2(1 - \rho_a(0))} \\ \rho_a(0) &= 1 - 2q(1 - \eta) \\ \langle \rho_a \rangle &= 1 - 2q(1 - \eta^2). \end{aligned}$$

For the average density one gets:

$$\langle \rho_a \rangle = \rho_a(0) - (1 - \rho_a(0)) \frac{\kappa - 1 + \rho_a(0)}{\kappa + \sigma^2(1 - \rho_a(0))}, \quad (\text{C.139})$$

which is minimal for $\sigma = 0$, that is the symmetric case. The partial derivative $\frac{\partial \langle \rho_a \rangle}{\partial \kappa}$ is negative in the range of interest, therefore the minimal value of $\langle \rho_a \rangle$ is given by $\kappa = 1$ and therefore for the maximal possible values of q . In this extreme cases the following relations hold:

$$\rho_a(0) = \eta \quad (\text{C.140})$$

$$\langle \rho_a \rangle = \eta^2. \quad (\text{C.141})$$

The situation is still idealized as the sample and injection tube, which are connected to the center of the cell, are neglected. This tubes change the situation in two ways: First, they

contribute to the molecular fraction and second, they build an additional conductance at the center, where the injected *and* the recombined particles can leave the cell. This reduces the central density of the 'negative' particles coming from the localized source and changes the relation of $\rho_a(0)$ and $\langle \rho_a \rangle$. If one still neglects recombination on the surface of sample and injection tube, but takes the proper conductances into account, the formulas to calculate $\rho_a(0)$, $\langle \rho_a \rangle$ and the constrain for the sources are - for the symmetric case - given by:

$$\rho_a(0) = 1 - \sum_{k=1}^m \frac{Q_k}{1 + (1 + \varepsilon)|\eta_k|} \quad (\text{C.142})$$

$$\langle \rho_a \rangle = 1 - \sum_{k=1}^m Q_k \frac{1 + |\eta_k|(1 + \frac{\varepsilon}{2})}{1 + (1 + \varepsilon)|\eta_k|} \quad (\text{C.143})$$

$$1 \geq \sum_{k=1}^m Q_k \frac{1 + \frac{\varepsilon}{2}|\eta_k|}{1 + \varepsilon|\eta_k| - (1 + \varepsilon)\eta_k^2}. \quad (\text{C.144})$$

where ε is the ratio of the sum of the conductances of sample and injection tube to the conductance of one wing of the storage cell (beam tube):

$$\varepsilon = \frac{C_{IT} + C_{ST}}{C_{BT}}. \quad (\text{C.145})$$

The minimal value of $\langle \rho_a \rangle$ is then given by:

$$\rho_a(0) = \frac{2 + \varepsilon}{2 + \varepsilon\eta} \quad (\text{C.146})$$

$$\langle \rho_a \rangle = \rho_a(0)\eta = \rho_a^2(0) \frac{2}{2 + \varepsilon - \varepsilon\rho_a(0)}, \quad (\text{C.147})$$

and $\langle \rho_a \rangle$ is limited by the diffusion process within:

$$\rho_a^2(0) \frac{2}{2 + \varepsilon - \varepsilon\rho_a(0)} \leq \langle \rho_a \rangle \leq \rho_a(0). \quad (\text{C.148})$$

$\rho_a(0)$ is related by eq. 3.29 to α_r^{TGA} and α_r is a monoton function of $\langle \rho_a \rangle$, given by tab. 2.2:

$$\alpha_r \geq \frac{(\alpha_r^{TGA})^2}{\sqrt{2} [1 + \frac{\varepsilon}{2}(1 - \alpha_r^{TGA})] - (\sqrt{2} - 1)(\alpha_r^{TGA})^2} \quad (\text{C.149})$$

The second part of the inequality C.148 is only valid with the additional assumption, that the sample- and extension tube causes no significant recombination - which is explicitly wrong in case of low ($< 60 K$) or high ($> 120 K$) temperatures of the storage cell. If this condition can however assumed to be true, one obtains

$$\alpha_r \leq \frac{\sqrt{2} \alpha_r^{TGA}}{1 + (\sqrt{2} - 1) \alpha_r^{TGA}}. \quad (\text{C.150})$$

The model of localized sources delivers a mathematical precise limits for the average atomic fraction inside the beam tube - α_r - as a function of - precisely spoken - the normalized atomic density in the storage cell center. Fig. C.10 shows these limits as a function of the measured value α_r^{TGA} . The lower limit holds under all circumstances as a general lower limit for α_r , while the upper limit is valid only for negligible recombination in sample and extension tube.

D Spin Relaxation

D.1 Theory of Spin Relaxation by a Fluctuating Field

If a system can be described by a Hamilton operator \mathcal{H} of the form

$$\mathcal{H} = \mathcal{H}_0 + V, \quad (\text{D.1})$$

where \mathcal{H}_0 is diagonal with the eigenvectors $|a\rangle$ and V represents a small ($V \ll H_0$) random fluctuating perturbation. The transition probability $W_{a \rightarrow b}$ is given by time dependent perturbation theory [Mes 90]:

$$W_{a \rightarrow b} = |\langle b | U(t, t_0) | a \rangle|^2, \quad (\text{D.2})$$

where

$$U(t, t_0) = \sum_{n=1}^{\infty} U^{(n)}(t, t_0). \quad (\text{D.3})$$

Using $V_{ba}(t) = \langle b | V(t) | a \rangle$, the first two orders of the operator $U(t, t_0)$ are for $t_0 = 0$:

$$\begin{aligned} U^{(1)} &= \frac{1}{i\hbar} e^{-i\omega_b t + i\omega_a t_0} \int_0^t d\tau V_{ba}(\tau) e^{i\omega_{ba}\tau} \\ U^{(2)} &= \frac{1}{(i\hbar)^2} e^{-i\omega_b t + i\omega_a t_0} \sum_k \int_0^t d\tau V_{bk}(\tau) e^{i\omega_{bk}\tau} \int_0^\tau d\tau' V_{ka}(\tau') e^{i\omega_{ka}\tau'}. \end{aligned} \quad (\text{D.4})$$

The fluctuating term $V_{ba}(t)$ can be expressed by its Fourier transform:

$$V_{ba}(t) = \frac{1}{\sqrt{2\pi}} \int_{-\infty}^{+\infty} e^{-i\omega t} V_{ba}(\omega) d\omega, \quad (\text{D.5})$$

so that $W_{a \rightarrow b}$ is in first order given by:

$$W_{a \rightarrow b} = \frac{1}{2\pi\hbar^2} \int_{-\infty}^{+\infty} d\omega \int_{-\infty}^{+\infty} d\omega' V_{ba}(\omega) V_{ba}^*(\omega') g(\omega_{ba} - \omega, t) g^*(\omega_{ba} - \omega', t), \quad (\text{D.6})$$

where $g(\omega, t)$ is defined by:

$$g(\omega, t) = \int_0^t d\tau e^{i\omega\tau} = \frac{e^{i\omega t} - 1}{i\omega}. \quad (\text{D.7})$$

The expectation value $\langle V_{ab}(\omega) V_{ab}^*(\omega') \rangle$ is given by [Str 63]:

$$\langle V_{ab}(\omega) V_{ab}^*(\omega') \rangle = |V_{ab}|^2 2\pi \delta(\omega - \omega') j(\omega), \quad (\text{D.8})$$

with the spectral density $j(\omega)$. The spectral density is the Fourier transform of the autocorrelation function (ACF) $G(\tau) = \langle V_{ab}(t) V_{ab}^*(t + \tau) \rangle$. It follows, that:

$$W_{a \rightarrow b} = \frac{1}{\hbar^2} |V_{ba}|^2 \int_{-\infty}^{+\infty} d\omega j(\omega) f(\omega_{ba} - \omega, t), \quad (\text{D.9})$$

where $f(\omega, t) = |g(\omega, t)|^2$. As illustrated by fig. D.1, $f(\omega, t)$ is a peaked function of the frequency with a width $\Delta\omega = \frac{2\pi}{t}$ and a peak value of t^2 , so that for a slowly varying spectral density, the transition probability is¹⁸⁵:

$$W_{a \rightarrow b} = \frac{1}{\hbar^2} |V_{ba}|^2 2\pi t j(\omega_{ab}). \quad (\text{D.10})$$

¹⁸⁵The factor 2π depends on the normalization of the spectral density and the mean square perturbation.

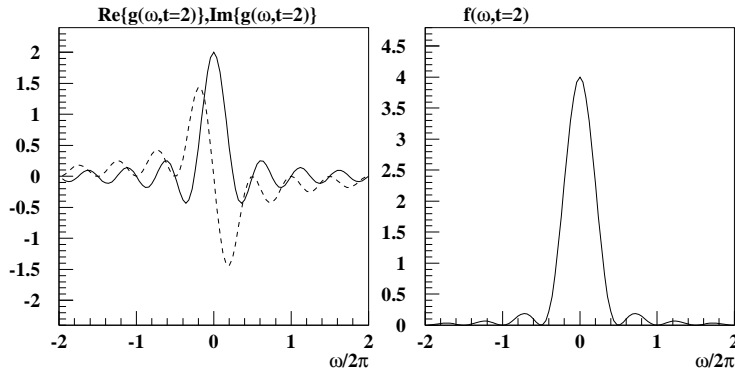


Fig. D.1: Left graph: Real (solid line) and imaginary (dashed line) part of the function $g(\omega, t)$ for $t = 2$ versus ω . Right graph: Graph of the function $f(\omega, t) = |g(\omega, t)|^2$ for $t = 2$ versus ω . The width $\Delta\omega$ is given by $\frac{2\pi}{t}$ and the maximal value is $f(0, t) = t^2$.

D.2 Theory of Resonant Relaxation

If an electron¹⁸⁶, located in the static magnetic field $\vec{B} = \frac{\hbar\omega_0}{gS\mu_B} \vec{e}_z$, experiences a rotating high frequency field of frequency $\nu = \frac{\omega}{2\pi}$ perpendicular to the static field and strength $b = \frac{\hbar\Omega}{gS\mu_B}$, the Hamilton operator can be written as:

$$\mathcal{H}_0 = \frac{gS\mu_B}{\hbar} \vec{S}\vec{B} = \frac{\hbar}{2} \begin{pmatrix} \omega_0 & \Omega e^{-i\omega t} \\ \Omega e^{i\omega t} & -\omega_0 \end{pmatrix}. \quad (\text{D.11})$$

The transformation matrix

$$U_0 = \begin{pmatrix} e^{-i\omega t/2} & 0 \\ 0 & e^{i\omega t/2} \end{pmatrix}$$

can be used to transform into the rotating frame. The (time independent) Hamilton operator in the rotating frame \mathcal{H}_1 is given by

$$\mathcal{H}_1 = U_0^\dagger \mathcal{H}_0 U_0 + i\hbar \dot{U}_0^\dagger U_0 = \frac{\hbar}{2} \begin{pmatrix} \omega_0 - \omega & \Omega \\ \Omega & -\omega_0 + \omega \end{pmatrix}. \quad (\text{D.12})$$

The static transformation matrix

$$U_1 = \begin{pmatrix} \cos \theta & -\sin \theta \\ \sin \theta & \cos \theta \end{pmatrix}$$

can be used to obtain the diagonal $\mathcal{H}_2 = U_1^\dagger \mathcal{H}_1 U_1$. The coefficients of U_1 are defined by

$$\begin{aligned} \cos \theta &= \sqrt{\frac{1+\cos 2\theta}{2}} & \sin \theta &= \sqrt{\frac{1-\cos 2\theta}{2}} \\ \cos 2\theta &= \sqrt{\frac{(\omega_0 - \omega)^2}{(\omega_0 - \omega)^2 + \Omega^2}} & \sin 2\theta &= \sqrt{\frac{\Omega^2}{(\omega_0 - \omega)^2 + \Omega^2}}. \end{aligned} \quad (\text{D.13})$$

The diagonal Hamilton operator \mathcal{H}_2 is given by its Eigenvalues $\pm E$:

$$\frac{E}{\hbar} = \frac{a}{2} = \frac{\sqrt{(\omega_0 - \omega)^2 + \Omega^2}}{2}. \quad (\text{D.14})$$

¹⁸⁶Or more general: a spin- $\frac{1}{2}$ particle.

The Schrödinger equation is solved (in the $|\chi\rangle$ -basis) by the vector $|\chi(t)\rangle = e^{-i\mathcal{H}_2/\hbar t} |\chi(0)\rangle$ and correspondingly in the $|\psi\rangle$ -basis by $|\psi(t)\rangle = U_0(t)U_1(t)|\chi(t)\rangle$. The transition probability $W_{\uparrow\downarrow}(\omega, t)$ is given by the matrix element

$$W_{\uparrow\downarrow}(\omega, t) = |\langle \psi_a(0) | \psi_b(t) \rangle|^2 = |\langle \psi_a(0) | U_0(t) U_1(t) e^{-i\mathcal{H}/\hbar t} U_1^\dagger(0) U_0^\dagger(0) \psi_b(0) \rangle|^2. \quad (\text{D.15})$$

The central matrix product results:

$$U_0(t) U_1 e^{-i\mathcal{H}/\hbar t} U_1^\dagger U_0^\dagger(0) = \begin{pmatrix} e^{-i\frac{\omega}{2}t} (\cos \frac{a}{2}t - i \cos 2\theta \sin \frac{a}{2}t) & -i e^{-i\frac{\omega}{2}t} \sin 2\theta \sin \frac{a}{2}t \\ -i e^{i\frac{\omega}{2}t} \sin 2\theta \sin \frac{a}{2}t & e^{i\frac{\omega}{2}t} (\cos \frac{a}{2}t + i \cos 2\theta \sin \frac{a}{2}t) \end{pmatrix}, \quad (\text{D.16})$$

so that the transition probability is given by:

$$W_{\uparrow\downarrow}(\omega, t) = W_{\downarrow\uparrow}(\omega, t) = \sin^2 2\theta \sin^2 \frac{a}{2}t = \frac{\Omega^2}{a^2} \sin^2 \frac{a}{2}t, \quad (\text{D.17})$$

which is the so-called Rabi formula¹⁸⁷ [Rab 37, Abr 61, Got 66]. If the particle experiences the high frequency field for a limited time t , which can - for example in case of wall collisions - assumed to follow an exponential probability distribution $w(t) = \frac{1}{\tau_s} \exp(-t/\tau_s)$ with an average value of τ_s , one finds¹⁸⁸:

$$W_{\uparrow\downarrow}(\omega, \tau_s) = \int_0^\infty w(t) W_{\uparrow\downarrow}(\omega, t) dt = \frac{1}{2} \frac{\Omega^2 \tau_s^2}{1 + (\Omega^2 + (\omega - \omega_0)^2) \tau_s^2}, \quad (\text{D.18})$$

which is a Lorentzian resonance shape function with a resonance width $\Delta\omega = \sqrt{\frac{1}{\tau_s^2} + \Omega^2}$ and an amplitude at resonance ($\omega = \omega_0$) of

$$W_{\uparrow\downarrow}(\omega_0, \tau_s) = \frac{1}{2} \frac{\Omega^2}{\Delta\omega^2} = \frac{1}{2} \frac{\Omega^2 \tau_s^2}{1 + \Omega^2 \tau_s^2}. \quad (\text{D.19})$$

Eq. D.18 is only valid for a situation, where the atom is in a pure eigenstate of the static Hamiltonian at $t = 0$. This is only a realistic assumption at the first wall collision in the storage cell. At a later point in time, the particle is in a mixed state, which can generally be expressed by $|\psi\rangle = \cos \alpha |\uparrow\rangle + e^{i\phi} \sin \alpha |\downarrow\rangle$, where ϕ is the relative and arbitrary phase of the mixture and α describes the composition of the mixture. After the next wall collision, the mixture and the relative phase will have changed. The phase is of no interest, as any phase correlation will vanish between two wall collisions. For the new mixture, the calculation - including the averaging over ϕ - yields:

$$\begin{aligned} \sin^2 \alpha &\rightarrow \sin^2 \alpha + \frac{\Omega^2}{a^2} (\cos^2 \alpha - \sin^2 \alpha) \sin^2 \frac{a}{2}t \\ \cos^2 \alpha &\rightarrow \cos^2 \alpha - \frac{\Omega^2}{a^2} (\cos^2 \alpha - \sin^2 \alpha) \sin^2 \frac{a}{2}t. \end{aligned} \quad (\text{D.20})$$

The polarization is given by $P = \frac{N_\uparrow - N_\downarrow}{N_\uparrow + N_\downarrow} = \cos^2 \alpha - \sin^2 \alpha$ and therefore:

$$P \rightarrow P \left(1 - 2 \frac{\Omega^2}{a^2} \sin^2 \frac{a}{2}t\right). \quad (\text{D.21})$$

¹⁸⁷Rabi used the wave functions instead of the operators for the calculation [Rab 37].

¹⁸⁸This formula is well-known in the theory of the power absorption of hydrogen masers [Wit 56, Klp 62].

The relative polarization loss ΔP per wall collision $\Delta b = 1$ is then twice the transition probability:

$$\frac{\Delta P}{\Delta b} = -\gamma_p(\omega_0, \tau_s) P, \quad (\text{D.22})$$

where $\gamma_p = 2W_{\uparrow\downarrow}$. For high numbers of wall collisions, this can be written as a differential equation, so that the polarization $P(b)$ after $b \gg 1$ wall collisions is approximately given by:

$$P(b) = P(0) e^{-\gamma_p b}. \quad (\text{D.23})$$

D.2.1 The Transition Probabilities

Eq. D.18 is a Lorentzian resonance curve with a width $\Delta\omega = \sqrt{\frac{1}{\tau_s^2} + \Omega^2}$. The resonance width is a composition of the width given by the 'distortion' and the width, that results from Heisenbergs relation $\Delta\omega \simeq \frac{1}{\tau_s}$. If the spectral density is reasonably flat over the resonance width, then the total transition probability $W_{\uparrow\downarrow}$ is approximately given by

$$W_{\uparrow\downarrow}(\omega) \simeq \langle W_{\uparrow\downarrow}(0) \rangle \Delta\omega j(\omega_0) = \frac{1}{2} \frac{\Omega^2}{\Delta\omega} j(\omega_0) = \frac{1}{2} \frac{\Omega^2 \tau_s}{\sqrt{1 + \Omega^2 \tau_s^2}} j(\omega_0). \quad (\text{D.24})$$

One may have doubts, whether it is legitimate to keep the complete amplitude responsible for the broadening Ω^2 , even though the amplitude of the noise spectrum of the fluctuating field times the resonance width is much smaller in case of a short correlation time. Abragam refers a treatment, where only frequencies of the spectral density can contribute to the (NMR-) line broadening, which are close to zero in the rotating frame [Abr 61]. This leads to the formula for motional narrowing $\Delta\omega = (\Delta\omega)_0^2 \tau_c$. But this treatment would lead to a transition probability according to eq. D.19 and thus to a situation, which is equivalent to the case of exact resonance. However this can not be correct, as eq. D.18 predicts a transition probability $W_{\uparrow\downarrow} \leq \frac{1}{2}$ for $\omega \neq \omega_0$ and the power of the noise spectrum is distributed over the complete frequency range. Insofar, it is believed, that eq. D.24 delivers a better description than eq. D.10 for $\Omega^2 \tau_s^2 > 1$. But it has the somewhat strange consequence, that the transition probability stays below $\frac{1}{2}$ for $\sqrt{\Omega^2 \tau_c} < 1$ - even in the limiting case of $\tau_s \rightarrow \infty$. Hence the formula predicts, that an atom may never depolarize completely by a single wall collision. This might be an artifact of the calculation scheme, which starts up taking a perturbation of only one single frequency into account. Nevertheless eq. D.24 fits well to the measured behavior and thus seems to be a reasonable approximation for the situation under study.

The transition probability $\langle W_{\uparrow\downarrow}(\omega - \omega_0) \rangle$ has - if the spectral density is not "flat" - to be averaged over all frequencies weighted by the spectral density $j(\omega)$:

$$W_{\uparrow\downarrow} = \frac{\int_{-\infty}^{+\infty} W_{\uparrow\downarrow}(\omega - \omega_0) j(\omega) d\omega}{\int_{-\infty}^{+\infty} j(\omega) d\omega}. \quad (\text{D.25})$$

The integral in the denominator is given by the corresponding ACF:

$$\int_{-\infty}^{+\infty} j(\omega) d\omega = \sqrt{2\pi} G(0). \quad (\text{D.26})$$

The convolution integral in the nominator can be solved by the convolution theorem of the Fourier transformation:

$$\int_{-\infty}^{+\infty} W_{\uparrow\downarrow}(\omega_0 - \omega) j(\omega) d\omega = \int_{-\infty}^{+\infty} F(t) G(t) e^{-i\omega_0 t} dt, \quad (\text{D.27})$$

where $F(t)$ and $G(t)$ are the Fourier transforms of $W_{\uparrow\downarrow}(\omega)$ and $j(\omega)$ respectively¹⁸⁹. $G(t)$ is given by the ACF of the process and the calculation yields for $F(t)$:

$$F(t) = \sqrt{\frac{\pi}{2}} \frac{\Omega^2}{2\Delta\omega} e^{-\Delta\omega t}. \quad (\text{D.28})$$

For the BPP-model one obtains:

$$\langle W_{\uparrow\downarrow} \rangle = \frac{\Omega^2 \Delta\omega + \frac{1}{\tau_c}}{2} \frac{1}{(\Delta\omega + \frac{1}{\tau_c})^2 + \omega_0^2} = \frac{\Omega^2}{2} \frac{\tau_s \tau_c}{\sqrt{1 + \Omega^2 \tau_s^2}} \frac{b}{b^2 + \omega_0^2 \tau_c^2}, \quad (\text{D.29})$$

where $b = 1 + \tau_c/\tau_s \sqrt{1 + \Omega^2 \tau_s^2}$. For the transition probability of two-dimensional diffusion one calculates with the ACF of eq. 6.35:

$$\begin{aligned} \langle W_{\uparrow\downarrow} \rangle &= \frac{\Omega^2 \tau_c}{4\Delta\omega} \ln \left(\frac{(\frac{1}{\tau_c} + \Delta\omega)^2 + \omega_0^2}{\Delta\omega^2 + \omega_0^2} \right) \\ &= \frac{\Omega^2 \tau_c \tau_s}{4\sqrt{1 + \Omega^2 \tau_s^2}} \ln \left(1 + \frac{2b - 1}{(\frac{1}{\tau_s} + \Omega^2 + \omega_0^2) \tau_c^2} \right), \end{aligned} \quad (\text{D.30})$$

D.2.2 The Saturation Factor

If $\Omega^2 \tau_s^2 \ll 1$ holds, then $W_{\uparrow\downarrow}$ is proportional to the sticking time, which is identical to the result of a first order perturbation theory. But the factor $\frac{\tau_s}{\sqrt{1 + \Omega^2 \tau_s^2}}$ represents "partial saturation", if $\Omega^2 \tau_s^2 \gg 1$ and hence $b \simeq 1 + \Omega \tau_c$. One finds in this case for the BPP model:

$$\langle W_{\uparrow\downarrow} \rangle \simeq \frac{1}{2} \frac{\Omega \tau_c (1 + \Omega \tau_c)}{(1 + \Omega \tau_c)^2 + \omega_0^2 \tau_c^2}, \quad (\text{D.31})$$

which is independent on the interaction time τ_s and describes the relaxation in partial saturation¹⁹⁰. The saturation is surprising in its functional form, as the transition probabilities do not have to be close to $\frac{1}{2}$. Instead it predicts, that the transition probability will never reach its maximal value of $\frac{1}{2}$ - no matter how long the atom may stick on the wall - if the amplitude Ω of the distortion is too small.

If in addition $\omega_0^2 \tau_c^2 \ll 1$, one finds a "real" saturation:

$$\langle W_{\uparrow\downarrow} \rangle \simeq \frac{1}{2} \frac{\Omega \tau_c}{1 + \Omega \tau_c}, \quad (\text{D.32})$$

which verifies that $\langle W_{\uparrow\downarrow} \rangle \leq \frac{1}{2}$ holds. The factor $\frac{1}{\sqrt{1 + \Omega^2 \tau_s^2}}$ describes the saturation of the transition probability for large interaction times and strong interactions respectively broad resonances. This factor can not be obtained by first order perturbation theory - but is required for the understanding of the behavior of hydrogen and deuterium relaxation below about 100 K.

¹⁸⁹As all functions are even, one may use the Fourier-cosine integral. The integral on the right side is besides a factor $\sqrt{2\pi}$ identical to the inverse Fourier transform.

¹⁹⁰The distortion Ω has in the context of a random fluctuations to be understood as the square root of the average square of the distortion: $\Omega = \sqrt{\langle \Omega^2 \rangle}$.

m, m'	1	0	-1		$\frac{3}{2}$	$\frac{1}{2}$	$-\frac{1}{2}$	$-\frac{3}{2}$
1	c^4	$2c^2s^2$	s^4	$\frac{3}{2}$	c^6	$3c^4s^2$	$3c^2s^4$	s^6
0	$2c^2s^2$	$(c^2 - s^2)^2$	$2c^2s^2$	$\frac{1}{2}$	$3c^4s^2$	$c^2(c^2 - 2s^2)^2$	$s^2(2c^2 - s^2)^2$	$3c^2s^4$
-1	s^4	$2c^2s^2$	c^4	$-\frac{1}{2}$	$3c^2s^4$	$s^2(2c^2 - s^2)^2$	$c^2(c^2 - 2s^2)^2$	$3c^4s^2$
				$-\frac{3}{2}$	s^6	$3c^2s^4$	$3c^4s^2$	c^6

Tab. D.1: Transition probabilities in multiplets with $I = 1$ (left table) and $I = \frac{3}{2}$ (right table) between states with different magnetic quantum numbers m and m' . c and s stand for $\cos \frac{\alpha}{2}$ and $\sin \frac{\alpha}{2}$ respectively. If the transition probabilities are known to be small, one may approximate $c^2 \simeq 1$ and neglect all terms s^n with $n > 2$. One then obtains eq. D.17, but with prefactors of 2 (left table, triplet) and 3 or 4 (right table, quadruplet).

D.2.3 The Spectrum of a Transition

In case of hydrogen or deuterium - atoms with hyperfine structure - the two state theory should be a good approximation for electron transitions in the high field limit, when electron and nucleon are decoupled. In case of hydrogen, also the nuclear transitions should be reasonably well described in the high field limit, as the proton has $I = \frac{1}{2}$. In case of the high field limit for deuterons and generally in case of the low field limit, the question arises, what the influence of the multiplet structure on the transition probabilities will be. In case of deuterium, the presence of identical (and similar) transition frequencies (see tab. 2.1) may play an additional role in terms of internal cross-relaxation (see sec. 6.10.3).

Majorana calculated the transition probability for multiplets, respectively for particles with $I > \frac{1}{2}$ and obtained (see [Abr 61] and reference therein):

$$P_{m \leftrightarrow m'} = \cos \left(\frac{\alpha}{2} \right)^{4I} (I+m)!(I+m')!(I-m)!(I-m')! \times \left[\sum_{\lambda=0}^{2I} (-1)^\lambda \frac{\tan \left(\frac{\alpha}{2} \right)^{2\lambda-m+m'}}{\lambda!(\lambda-m+m')!(I+m-\lambda)!(I-m'-\lambda)!} \right]^2, \quad (\text{D.33})$$

where $\sin \left(\frac{\alpha}{2} \right)^2 = \frac{\Omega^2}{\Omega^2 + (\omega - \omega_0)^2} \sin \left(\frac{at}{2} \right)^2$ is the Rabi formula. For $I = \frac{1}{2}$, the results are identical with the Rabi formula, but for $I > \frac{1}{2}$ one obtains increased transition probabilities. The results are listed in tab. D.1. The multiplet structure of the hydrogen or deuterium hyperfine levels will of course only be significant, if the transition frequencies differ by less than the resonance width. In case of hydrogen, the multiplet structure should only matter in the low field limit $B \rightarrow 0$. The expected effect is a maximal increase of the transition probabilities for the 1 - 2 and 2 - 3 transition by a factor of 2. The low field limit of deuterium is a quadruplet and the expected maximal increase of the transition probabilities is a factor of 3 or 4 respectively, while the increase should in case of high field be maximal 2 due to the nuclear spin triplet of the deuteron.

In case of atoms with hyperfine structure, the strength of the distortion Ω^2 has to be replaced by the corresponding perturbations Ω_{ab}^2 as described in app. D.3. The transition probability W_{ab} is then given by:

$$W_{ab} = \frac{\Omega_{ab}^2 \tau_s}{2\sqrt{1 + \Omega_{ab}^2 \tau_s^2}} j_{ab}(\omega_{ab}). \quad (\text{D.34})$$

The function $j_{ab}(\omega)$ - which is not identical with the spectral density¹⁹¹ - is either (approximately) given by

$$j_{BPP}(\omega) = \tau_c \frac{b}{b^2 + \omega_0^2 \tau_c^2}, \quad (\text{D.35})$$

or by

$$j_{2D}(\omega) = \frac{\tau_c}{2} \ln \left(1 + \frac{\tau_s^2}{\tau_c^2} \frac{2b-1}{1 + (\Omega^2 + \omega_0^2) \tau_s^2} \right), \quad (\text{D.36})$$

depending on the properties of surface and diffusion.

One can define the spectrum J_{ab} of a transition $a \leftrightarrow b$ by

$$J_{ab} = \frac{W_{ab}}{\Omega_{ab}^2}. \quad (\text{D.37})$$

The spectrum will - in the simplest case of a "flat" spectral density¹⁹² $j(\omega) = \tau_c$ - be given by the saturation factor

$$J(\Omega_{ab}, \omega) = \frac{\tau_s \tau_c}{2 \sqrt{1 + \Omega_{ab}^2 \tau_s^2}}. \quad (\text{D.38})$$

D.3 The Matrix Elements of Wall Depolarization

The distortion Ω_{ab}^2 was defined by

$$\Omega_{ab}^2 = \frac{1}{\hbar^2} \frac{\omega_{HFS}^2}{B_C^2} \left\langle |\langle a | \vec{S} \vec{B}_{loc} | b \rangle|^2 \right\rangle. \quad (\text{D.39})$$

With $\vec{B}_{loc} = b_x \vec{e}_x + b_y \vec{e}_y + b_z \vec{e}_z$ one finds:

$$\vec{S} \vec{B}_{loc} = S_z b_z + \frac{1}{2} S_+ (b_x - i b_y) + \frac{1}{2} S_- (b_x + i b_y). \quad (\text{D.40})$$

It can easily be verified, that for the operators S_z , S_+ and S_- , represented by S_k , the following relation holds:

$$\langle a | S_j | b \rangle \langle b | S_k | a \rangle = |\langle a | S_j | b \rangle|^2 \delta_{jk}, \quad (\text{D.41})$$

so that

$$\left\langle |\langle a | \vec{S} \vec{B}_{loc} | b \rangle|^2 \right\rangle = \langle b_z^2 \rangle |\langle a | S_z | b \rangle|^2 + \langle b_x^2 + b_y^2 \rangle (|\langle a | S_+ | b \rangle|^2 + |\langle a | S_- | b \rangle|^2). \quad (\text{D.42})$$

The local fluctuating field can assumed to be isotropic ($\langle b_x^2 \rangle = \langle b_y^2 \rangle = \langle b_z^2 \rangle = \frac{1}{3} \langle \vec{B}_{loc}^2 \rangle$), so that

$$\left\langle |\langle a | \vec{S} \vec{B}_{loc} | b \rangle|^2 \right\rangle = \frac{2}{3} \langle \vec{B}_{loc}^2 \rangle |C_{ab}|^2. \quad (\text{D.43})$$

The matrix elements $|C_{ab}|^2$ are listed in tab. D.2. They include a factor $\frac{1}{2}$ for σ -transitions, which are caused by the parallel component b_z of the fluctuating field only. The distortion strength Ω_{ab}^2 is then given by:

$$\Omega_{ab}^2 = \frac{2}{3} \omega_{HFS}^2 \frac{\langle \vec{B}_{loc}^2 \rangle}{B_C^2} |C_{ab}|^2. \quad (\text{D.44})$$

¹⁹¹The spectral density $j(\omega)$ may - by its definition - not depend on the matrix element of a hyperfine transition, which is the case for j_{ab} . Nevertheless one finds, that $\lim_{\Omega^2 \rightarrow 0} j_{ab}(\omega) = j(\omega)$.

¹⁹²E.g. in the low frequency limit, where $\omega_{ab} \tau_c \ll 1$ holds.

D.4 Spin Exchange Collisions

Spin exchange collisions are caused by the difference of the molecular singlet V_s and triplet V_t interaction potentials¹⁹³. Two methods were used to calculate the cross section for spin exchange collisions σ_{se} . The first one, introduced by Purcell and Fields [Pur 56] is based on the calculation of the phase shift difference ϕ for both potentials, which can be written as:

$$\phi = \int \frac{V_t - V_s}{\hbar} dt. \quad (\text{D.45})$$

The spin exchange cross section is then

$$\sigma_{se} = \int \sin^2 \frac{\phi}{2} 2\pi r dr. \quad (\text{D.46})$$

The second method makes use of the partial wave analysis. It was introduced by Wittke and Dicke [Wit 56]:

$$\sigma_{se} = \frac{\pi}{k^2} \sum_{l=0}^{\infty} (2l+1) \sin^2 (\delta_l^s - \delta_l^t), \quad (\text{D.47})$$

where δ_l^s and δ_l^t are the phase shifts for the singlet and triplet potentials and k is the wave constant [Kni 88]. Fig. D.2 shows a graph of σ_{se} as calculated by Allison [All 72] and a fit with a polynomial of 5th degree in $\eta = T/100K$,

$$\sigma_{se} = p_0 + p_1 \eta + \dots + p_5 \eta^5. \quad (\text{D.48})$$

The coefficients of the polynomial are:

$$\begin{aligned} p_0 &= -6.14 \pm 0.6 & p_1 &= 89.9 \pm 1.15 \\ p_2 &= -105.9 \pm 0.69 & p_3 &= 60.8 \pm 0.28 \\ p_4 &= -16.85 \pm 0.1 & p_5 &= 1.7972 \pm 0.027. \end{aligned} \quad (\text{D.49})$$

As already mentioned in sec. 6, the number of spin exchange collisions per atom and unit time \dot{N}_{se} is in a gas with the particle density $\langle n \rangle$ given by:

$$\dot{N}_{se} = \langle n \rangle \sigma_{se} \langle v_r \rangle, \quad (\text{D.50})$$

¹⁹³”Singlet” or ”triplet” refers to the coupling of the *electron* spins of the atoms.

σ/π	Δm_F	ΔF	Δm_I	Δm_S	Hydrogen	Deuterium
σ	0	1	1	1	$2 \leftrightarrow 4 : \frac{\sin^2 2\theta}{2}$	$2 \leftrightarrow 6 : \frac{\sin^2 2\theta_+}{2}$
σ	0	1	1	1		$3 \leftrightarrow 5 : \frac{\sin^2 2\theta_-}{2}$
π	1	1	0	1	$1 \leftrightarrow 4 : \cos^2 \theta$	$1 \leftrightarrow 6 : \cos^2 \theta_+$
π	1	1	0	1		$2 \leftrightarrow 5 : \cos^2 \theta_+ \cos^2 \theta_-$
π	1	1	2	1		$3 \leftrightarrow 6 : \sin^2 \theta_+ \sin^2 \theta_-$
π	1	1	1	0	$3 \leftrightarrow 4 : \sin^2 \theta$	$4 \leftrightarrow 5 : \sin^2 \theta_-$
π	1	0	1	0	$1 \leftrightarrow 2 : \sin^2 \theta$	$1 \leftrightarrow 2 : \sin^2 \theta_+$
π	1	0	1	0		$2 \leftrightarrow 3 : \sin^2 \theta_- \cos^2 \theta_+$
π	1	0	1	0		$5 \leftrightarrow 6 : \sin^2 \theta_+ \cos^2 \theta_-$
π	1	0	0	1	$2 \leftrightarrow 3 : \cos^2 \theta$	$3 \leftrightarrow 4 : \cos^2 \theta_-$

Tab. D.2: Matrix elements of the hyperfine transitions of hydrogen and deuterium as functions of the mixing angles. The mixing angles are functions of the scaling variable $x = B/B_C^{H,D}$. They are listed in tab. B.1.

The transition coefficients for a transition $|ab\rangle \rightarrow |cd\rangle$ can be explicitly calculated. The total rate into state $|c\rangle$ is given by:

$$\dot{n}_c = \sigma_{se} \langle v_r \rangle \sum_{a,b} M_{ab}^c n_a n_b, \quad (\text{D.51})$$

with the number densities n_a for hyperfine state $|a\rangle$. The same equation can be written - using the hyperfine population numbers N_c - as:

$$\dot{N}_c = \langle n \rangle \sigma_{se} \langle v_r \rangle \sum_{a,b} M_{ab}^c N_a N_b. \quad (\text{D.52})$$

If $|a\rangle$ is given by

$$|a\rangle = a_\uparrow |\uparrow, m_a - 1/2\rangle + a_\downarrow |\downarrow, m_a + 1/2\rangle \quad (\text{D.53})$$

with $m_a = \langle a | F_z | a \rangle$, the tensor M_{ab}^c is given by [Wal 93]¹⁹⁴:

$$\begin{aligned} M_{ab}^c = & \sum_d -2 \langle c | a \rangle \langle d | b \rangle (a_\uparrow b_\downarrow c_\uparrow d_\downarrow + a_\downarrow b_\uparrow c_\downarrow d_\uparrow) \\ & + \langle m_c | m_a \rangle \langle m_d | m_b \rangle (a_\uparrow b_\downarrow c_\uparrow d_\downarrow + a_\downarrow b_\uparrow c_\downarrow d_\uparrow)^2 \\ & + \langle m_c | m_a - 1 \rangle \langle m_d | m_b + 1 \rangle (a_\uparrow b_\downarrow c_\uparrow d_\downarrow)^2 \\ & + \langle m_c | m_a + 1 \rangle \langle m_d | m_b - 1 \rangle (a_\downarrow b_\uparrow c_\downarrow d_\uparrow)^2. \end{aligned} \quad (\text{D.54})$$

The coefficients a_\uparrow, a_\downarrow are listed in tab. D.3 and tab. D.4 for hydrogen and deuterium respectively. The first two terms of M_{ab}^c are symmetric in the indices $a \leftrightarrow c$, the last two terms in $a \leftrightarrow b$.

As spin exchange collisions are atom-atom-collisions, the total angular momentum is conserved: $\Delta \sum_i m_F = 0$. This leads in case of hydrogen-hydrogen collisions to

$$\langle m_F \rangle = \frac{N_1 - N_3}{2} = \frac{P_e + P_z}{4} = \text{const} \quad (\text{D.55})$$

and in case of deuterium-deuterium collisions to

$$\langle m_F \rangle = \frac{P_e + 2P_z}{2} = \frac{3}{2} (N_1 - N_4) + \frac{N_2 - N_3 - N_5 + N_6}{2} = \text{const}. \quad (\text{D.56})$$

Another effect of the angular momentum conservation is, that pairs of hyperfine states form groups. This groups can not be left by means of spin exchange collisions: Any initial configuration

¹⁹⁴ M_{ab}^c is in the definition of Walker and Anderson only half of the value given in eq. D.54. This difference cancels out, as they define the number of spin exchange collisions to be $2n \sigma_{se} \langle v_r \rangle$.

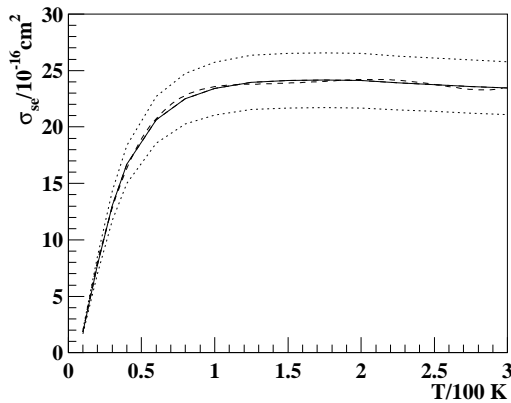


Fig. D.2: The solid line shows the cross section for spin exchange collisions $\sigma_{se} = \frac{\sigma_+ + \sigma_-}{2}$ vs. temperature as calculated by Allison in units of 10^{-16} cm^2 [All 72]. The claimed systematical error limits of $\pm 10\%$ are shown as dotted curves. The dashed line is a fit with a polynomial of 5th degree in $\eta = T/100K$.

a	m_a	a_{\uparrow}	a_{\downarrow}
1	+1	1	0
2	0	$\cos \theta$	$\sin \theta$
3	-1	0	1
4	0	$-\sin \theta$	$\cos \theta$

Tab. D.3: Coefficients $a_{\uparrow}, a_{\downarrow}$ of the hydrogen spin exchange tensor.

a	m_a	a_{\uparrow}	a_{\downarrow}
1	+3/2	1	0
2	+1/2	$\cos \theta_{+}$	$\sin \theta_{+}$
3	-1/2	$\cos \theta_{-}$	$\sin \theta_{-}$
4	-3/2	0	1
5	-1/2	$-\sin \theta_{-}$	$\cos \theta_{-}$
6	+1/2	$-\sin \theta_{+}$	$\cos \theta_{+}$

Tab. D.4: Coefficients $a_{\uparrow}, a_{\downarrow}$ for deuterium.

$|ab\rangle$ must result a final configuration $|cd\rangle$ of the same group. Tab. D.6 gives an overview over these groups for \vec{H} and \vec{D} . By looking at these groups, one can immediately see, that the collisions of atoms in the same *pure* states - $|1\rangle$ and $|3\rangle$ in case of \vec{H} and $|1\rangle$ and $|4\rangle$ in case of \vec{D} - cannot change the hyperfine population.

Pure spin exchange relaxation leads in the limiting case $t \rightarrow \infty$ to the so-called *spin temperature equilibrium* (STE). The population numbers fulfill in this case the following condition [Wal 93]:

$$N_a^{\text{ste}} = \frac{e^{\beta m_a}}{\sum_a e^{\beta m_a}}. \quad (\text{D.57})$$

If one defines $\eta = \tanh \frac{\beta}{2}$, the hyperfine population N_a^{ste} is given by the relations in tab. D.5. Fig. D.3 shows the population numbers for the STE state for hydrogen and deuterium as a function of η . The range for the spin temperature parameter β is given by $-\infty \leq \beta \leq +\infty$, while η ranges in $-1 \leq \eta \leq 1$, which is easier to handle. Even though the STE is not reached in case of the typical HERMES running conditions, one can use the STE values to understand the tendency of the spin exchange effect.

Value	Hydrogen	Deuterium
$\langle m_F \rangle$	η	$\eta \frac{11+\eta^2}{6+2\eta^2}$
β	$\ln \left(\frac{1+\eta}{1-\eta} \right)$	$\ln \left(\frac{1+\eta}{1-\eta} \right)$
$Z = \sum_a e^{m_a \beta}$	$\frac{4}{1-\eta^2}$	$\frac{6+2\eta^2}{(1-\eta^2)^{\frac{3}{2}}}$
N_a^{ste}	$N_1 = \frac{(1+\eta)^2}{4}$ $N_3 = \frac{(1-\eta)^2}{4}$ $N_2 = N_4 = \frac{1-\eta^2}{4}$	$N_1 = \frac{(1+\eta)^3}{6+2\eta^2}$ $N_2 = N_6 = \frac{(1+\eta)^2(1-\eta)}{6+2\eta^2}$ $N_4 = \frac{(1-\eta)^3}{6+2\eta^2}$ $N_3 = N_5 = \frac{(1-\eta)^2(1+\eta)}{6+2\eta^2}$
P_e	η	η
P_z	η	$\frac{4\eta}{3+\eta^2}$
P_{zz}		$\frac{4\eta^2}{3+\eta^2} = P_e P_z$

Tab. D.5: Characteristic properties of the spin temperature equilibrium for hydrogen and deuterium. The polarization values in STE are a function of $\langle m_F \rangle$, but independent of the magnetic holding field. The tensor polarization of deuterium is always positive.

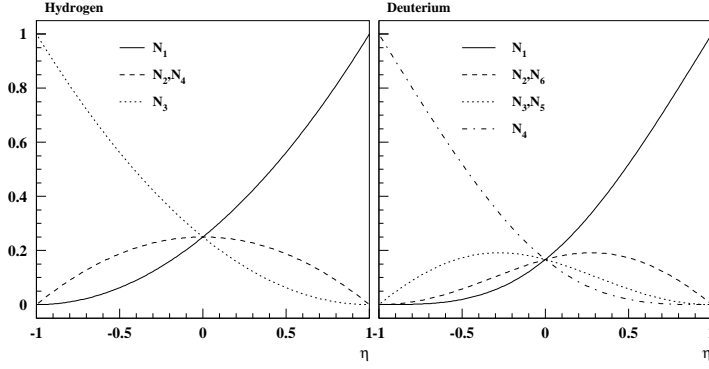


Fig. D.3: Hyperfine population numbers N_a^{ste} in spin temperature equilibrium for hydrogen (left figure) and deuterium (right figure).

The properties of M_{ab}^c are:

$$\begin{aligned}
 0 &= \sum_c M_{ab}^c \\
 0 &= \sum_c \langle c | m_F | c \rangle M_{ab}^c \\
 \sum_{ab} M_{ab}^c N_a N_b &= \frac{1}{2} \sum_{ab} (M_{ab}^c + M_{ba}^c) N_a N_b \\
 0 &= \sum_{a,b} M_{ab}^c N_a^{ste} N_b^{ste}.
 \end{aligned} \tag{D.58}$$

The first equation is clear: The sum over all hyperfine states does not change by spin exchange collisions. The second equation is an expression for the angular momentum conservation. The third one expresses the possibility to build a modified tensor, which is completely symmetric in the indices a and b without changing the calculation formula of the spin exchange rates. The last equation expresses the equilibrium condition for the spin temperature.

The modified matrices M^c for hydrogen are - using $S^2 = \sin^2 2\theta$ - explicitly given by:

$$\begin{aligned}
 M^1 = M^3 &= \frac{1}{4} \begin{pmatrix} 0 & 0 & -2 & 0 \\ 0 & S^2 & 0 & 2 - S^2 \\ -2 & 0 & 0 & 0 \\ 0 & 2 - S^2 & 0 & S^2 \end{pmatrix}, \\
 M^2 &= \frac{1}{4} \begin{pmatrix} 0 & -S^2 & 2 & S^2 \\ -S^2 & -3S^2 & -S^2 & -2 + S^2 \\ 2 & -S^2 & 0 & S^2 \\ S^2 & -2 + S^2 & S^2 & S^2 \end{pmatrix}, \\
 M^4 &= \frac{1}{4} \begin{pmatrix} 0 & S^2 & 2 & -S^2 \\ S^2 & S^2 & S^2 & -2 + S^2 \\ 2 & S^2 & 0 & -S^2 \\ -S^2 & -2 + S^2 & -S^2 & -3S^2 \end{pmatrix}.
 \end{aligned}$$

It is worth noting, that in the high field limit $x \rightarrow \infty$ and $S \rightarrow 0$, the following relations hold:

$$M^1 + M^2 = M^3 + M^4 = M^1 + M^4 = M^2 + M^3 = 0. \tag{D.59}$$

In other words: the polarization does not change. Only the collisions $|13\rangle \leftrightarrow |24\rangle$, which do not change the polarization, but the alignment of the spins $\langle \vec{I}\vec{S} \rangle$, are not suppressed by a high magnetic holding field.

Another interesting result of the angular momentum conservation in spin exchange collisions is the polarization transfer between nucleons and electrons. It can be used to polarize nucleons, which is a standard technique for instance in laser driven sources [St 95a].

$\sum_i m_F$	Hydrogen	Deuterium
3		$ 11\rangle$
2	$ 11\rangle$	$ 12\rangle 16\rangle$
1	$ 12\rangle 14\rangle$	$ 13\rangle 15\rangle 22\rangle 26\rangle 66\rangle$
0	$ 13\rangle 22\rangle 24\rangle 44\rangle$	$ 14\rangle 23\rangle 25\rangle 36\rangle 56\rangle$
-1	$ 23\rangle 34\rangle$	$ 24\rangle 33\rangle 35\rangle 46\rangle 55\rangle$
-2	$ 33\rangle$	$ 34\rangle 45\rangle$
-3		$ 44\rangle$

Tab. D.6: Pairs of hyperfine states of hydrogen and deuterium, for which spin exchange collisions are allowed by angular momentum conservation.

D.5 The Transformed Master Equation for Hydrogen

A fairly simple set of equations to describe relaxation of hydrogen can be obtained by a Hadamard transformation of the *master equation* eq. 6.1. The transformed variables are given by:

$$\begin{pmatrix} \mathcal{W}_0 \\ \mathcal{W}_e \\ \mathcal{W}_z \\ \mathcal{W}_p \end{pmatrix} = \frac{1}{2} \begin{pmatrix} 1 & 1 & 1 & 1 \\ 1 & 1 & -1 & -1 \\ 1 & -1 & -1 & 1 \\ 1 & -1 & 1 & -1 \end{pmatrix} \cdot \begin{pmatrix} N_1 \\ N_2 \\ N_3 \\ N_4 \end{pmatrix}, \quad (\text{D.60})$$

where the self-orthogonal transformation matrix is T_{ab} . The transformed master equation is then:

$$\begin{aligned} 0 &= \mathcal{W}_a^{inj} - \mathcal{W}_a + \langle b_{eff} \rangle \tilde{R}_{ab} \mathcal{W}_b + \langle b_{eff} \rangle \frac{\tau_f}{\tau_{se}} \tilde{M}_{bc}^a \mathcal{W}_b \mathcal{W}_c \\ \tilde{R}_{ab} &= T_{ac} R_{cd} T_{db} \\ \tilde{M}_{bc}^a &= T_{ad} M_{ef}^d T_{ec} T_{fb}. \end{aligned} \quad (\text{D.61})$$

Using the following shortcuts

$$\begin{aligned} a &= \langle W_{12} \rangle & b &= \langle W_{14} \rangle \\ c &= \langle W_{23} \rangle & d &= \langle W_{34} \rangle \\ e &= \langle W_{24} \rangle & f &= \frac{\sin^2 2\theta}{2}, \end{aligned} \quad (\text{D.62})$$

and the first order approximation for the wall relaxation term, the resulting transformed matrices \tilde{R}_{ab} and \tilde{M}_{bc}^a are:

$$\begin{aligned} \tilde{R}_{ab} &= \begin{pmatrix} 0 & 0 & 0 & 0 \\ 0 & -b-c-e & e & c-b \\ 0 & e & -a-d-e & d-a \\ 0 & c-b & d-a & -a-b-c-d \end{pmatrix} \\ \tilde{M}_{bc}^2 &= -M_{bc}^3 = \begin{pmatrix} 0 & -f & f & 0 \\ -f & 0 & 0 & 0 \\ f & 0 & 0 & 0 \\ 0 & 0 & 0 & 0 \end{pmatrix} & \tilde{M}_{bc}^4 &= \begin{pmatrix} 0 & 0 & 0 & -1 \\ 0 & f & 1-f & 0 \\ 0 & 1-f & f & 0 \\ -1 & 0 & 0 & 0 \end{pmatrix}. \end{aligned} \quad (\text{D.63})$$

In addition one has $\tilde{M}_{bc}^1 = 0$. The resulting transformed master equations are¹⁹⁵:

$$\begin{aligned}
0 &= \mathcal{W}_e^{inj} - \mathcal{W}_e + \langle b_{eff} \rangle \{ -(b+c+e)\mathcal{W}_e + e\mathcal{W}_z + (c-b)\mathcal{W}_p \} + \langle b_{eff} \rangle \frac{\tau_f}{\tau_{se}} f(\mathcal{W}_z - \mathcal{W}_e) \\
0 &= \mathcal{W}_z^{inj} - \mathcal{W}_z + \langle b_{eff} \rangle \{ -(a+d+e)\mathcal{W}_z + e\mathcal{W}_e + (d-a)\mathcal{W}_p \} + \langle b_{eff} \rangle \frac{\tau_f}{\tau_{se}} f(\mathcal{W}_e - \mathcal{W}_z) \\
0 &= \mathcal{W}_p^{inj} - \mathcal{W}_p + \langle b_{eff} \rangle \{ (c-b)\mathcal{W}_e + (d-a)\mathcal{W}_z - (a+b+c+d)\mathcal{W}_p \} \\
&\quad + \langle b_{eff} \rangle \frac{\tau_f}{\tau_{se}} \{ 2\mathcal{W}_e\mathcal{W}_z - \mathcal{W}_p + f(\mathcal{W}_e - \mathcal{W}_z)^2 \}.
\end{aligned} \tag{D.64}$$

The first and the second equation are linear in \mathcal{W}_e , \mathcal{W}_z and \mathcal{W}_p .

D.5.1 Hydrogen Spin Exchange Relaxation

If wall depolarization is neglected ($a = b = c = d = e = 0$), eq. D.64 yields:

$$\begin{aligned}
0 &= \mathcal{W}_e^{inj} - \mathcal{W}_e + \langle b_{eff} \rangle \frac{\tau_f}{\tau_{se}} f(\mathcal{W}_z - \mathcal{W}_e) \\
0 &= \mathcal{W}_z^{inj} - \mathcal{W}_z + \langle b_{eff} \rangle \frac{\tau_f}{\tau_{se}} f(\mathcal{W}_e - \mathcal{W}_z) \\
0 &= \mathcal{W}_p^{inj} - \mathcal{W}_p + \langle b_{eff} \rangle \frac{\tau_f}{\tau_{se}} \{ 2\mathcal{W}_e\mathcal{W}_z - \mathcal{W}_p + f(\mathcal{W}_e - \mathcal{W}_z)^2 \}.
\end{aligned} \tag{D.65}$$

These equations can be solved directly ($\gamma_{se} = 2 \frac{\tau_f}{\tau_{se}} f$):

$$\mathcal{W}_e = \mathcal{W}_e^{inj} - \frac{1}{2} \frac{\langle b_{eff} \rangle \gamma_{se}}{1 + \langle b_{eff} \rangle \gamma_{se}} (\mathcal{W}_e^{inj} - \mathcal{W}_z^{inj}) \tag{D.66}$$

$$\mathcal{W}_z = \mathcal{W}_z^{inj} - \frac{1}{2} \frac{\langle b_{eff} \rangle \gamma_{se}}{1 + \langle b_{eff} \rangle \gamma_{se}} (\mathcal{W}_z^{inj} - \mathcal{W}_e^{inj}). \tag{D.67}$$

It follows, that $\mathcal{W}_e + \mathcal{W}_z = N_1 + N_3 = const$ and:

$$\mathcal{W}_e - \mathcal{W}_z = N_2 - N_4 = \frac{\mathcal{W}_e^{inj} - \mathcal{W}_z^{inj}}{1 + \langle b_{eff} \rangle \gamma_{se}}. \tag{D.68}$$

Due to the linearity and symmetry of eq. D.67, they are also valid for P_e and P_z correspondingly. In case of the upper 3 hydrogen injection modes from tab. 3.1, either $(P_e)_0$ or $(P_z)_0$ are close to zero, so that the relative polarization loss¹⁹⁶ ΔP_{se} by spin exchange collisions is:

$$\Delta P_{se} \simeq \frac{P^{inj} - P}{P^{inj}} = \frac{1}{2} \frac{\langle b_{eff} \rangle \gamma_{se}}{1 + \langle b_{eff} \rangle \gamma_{se}}. \tag{D.69}$$

Fig. D.4 shows the effect of spin exchange relaxation for the HERMES storage cell vs. the magnetic holding field for the first injection modes of tab. 3.1. Concerning spin exchange collisions, the relaxation of electron spin and proton spin is *symmetric*¹⁹⁷. The relaxation is in addition independent on the sign of the injected polarization.

¹⁹⁵By the normalization of the hyperfine population ($\sum N_a = 1$) one has $\mathcal{W}_0 = \frac{1}{2}$. The corresponding master equation is trivial: $\mathcal{W}_0 = \mathcal{W}_0^{inj} = \frac{1}{2}$.

¹⁹⁶In fact, the polarization is not really "lost", but transferred from nucleus to electron or vice versa.

¹⁹⁷The situation is different for wall depolarization, where the electrons depolarize nearly independent of the holding field, while the nuclear depolarization can be suppressed by decoupling the nucleon from the electron in a high holding field.

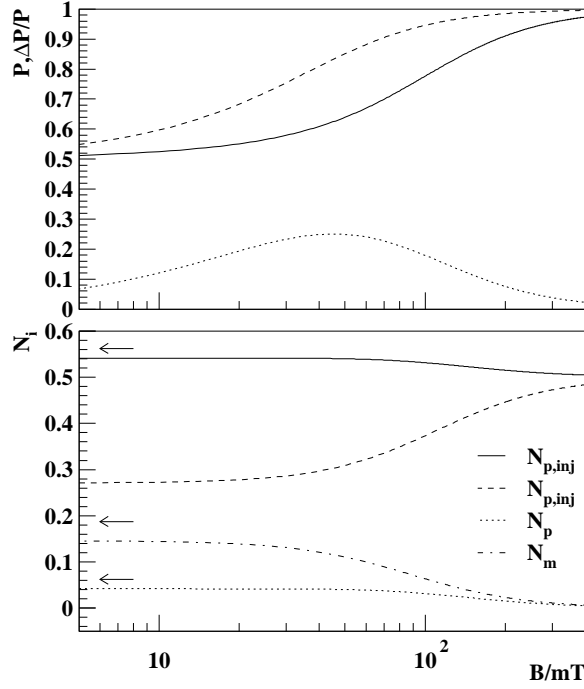


Fig. D.4: Top: Effect of spin exchange collisions on the polarization of \vec{H} atoms versus the magnetic holding field for the injection modes with two hyperfine states and a typical ratio $\tau_d/\tau_{se} = 3.0$ (see tab. 6.1). The dashed curve represents the injected and the solid curve the expected measured polarization of the BRP. The dotted line is the relative loss of polarization caused by spin exchange collisions. Bottom: Hyperfine population vs. magnetic holding field for the same conditions. The solid line represents the injected pure state $|1\rangle$ or $|3\rangle$, the dashed line the mixed state. The dotted line is the pure state, which is not injected and the dash-dotted curve the other mixed state. The spin temperature equilibrium values are indicated by arrows. Because both mixed states have the same hyperfine population in equilibrium, only 3 arrows are drawn.

D.5.2 Approximate Solution of the Master Equation for Hydrogen

If the spectral density $j(\omega)$ is approximately constant or if - in case of a high holding field - the frequencies for the two electron transitions respectively the two proton transitions are close to each other ($\omega_{23} \simeq \omega_{14}$ and $\omega_{23} \simeq \omega_{14}$), eq. D.64 simplify even more, as in this case $c \simeq b$ and $d \simeq a$:

$$\begin{aligned}
 0 &= \mathcal{W}_e^{inj} - \mathcal{W}_e + \langle b_{eff} \rangle \{ -(2b + e)\mathcal{W}_e + e\mathcal{W}_z \} + \langle b_{eff} \rangle \frac{\tau_f}{\tau_{se}} f(\mathcal{W}_z - \mathcal{W}_e) \\
 0 &= \mathcal{W}_z^{inj} - \mathcal{W}_z + \langle b_{eff} \rangle \{ -(2a + e)\mathcal{W}_z + e\mathcal{W}_e \} + \langle b_{eff} \rangle \frac{\tau_f}{\tau_{se}} f(\mathcal{W}_e - \mathcal{W}_z) \\
 0 &= \mathcal{W}_p^{inj} - \mathcal{W}_p + \langle b_{eff} \rangle \{ -2(a + b)\mathcal{W}_p \} \\
 &\quad + \langle b_{eff} \rangle \frac{\tau_f}{\tau_{se}} \{ 2\mathcal{W}_e\mathcal{W}_z - \mathcal{W}_p + f(\mathcal{W}_e - \mathcal{W}_z)^2 \}
 \end{aligned} \tag{D.70}$$

The first two equations are linear and decoupled from the third and can therefore be solved directly. With the spin relaxation constants γ_e , γ_z , γ_{se} and γ_{tr} defined by

$$\begin{aligned}
 \gamma_e &= 2b + e \\
 \gamma_z &= 2a + e \\
 \gamma_{se} &= \frac{\tau_f}{\tau_{se}} f = \frac{\tau_f \sin^2 2\theta}{2} \\
 \gamma_{tr} &= e + \gamma_{se},
 \end{aligned} \tag{D.71}$$

one finds:

$$\mathcal{W}_e = \frac{\mathcal{W}_e^{inj}}{1 + \langle b_{eff} \rangle (\gamma_e + \gamma_{se} - \eta_e)} + \Delta \mathcal{W}_z^{inj} \tag{D.72}$$

$$\mathcal{W}_z = \frac{\mathcal{W}_z^{inj}}{1 + \langle b_{eff} \rangle (\gamma_z + \gamma_{se} - \eta_z)} + \Delta \mathcal{W}_e^{inj}, \tag{D.73}$$

where

$$\eta_e = \frac{\langle b_{eff} \rangle \gamma_{tr}^2}{1 + \langle b_{eff} \rangle (\gamma_z + \gamma_{se})} \quad (D.74)$$

$$\eta_z = \frac{\langle b_{eff} \rangle \gamma_{tr}^2}{1 + \langle b_{eff} \rangle (\gamma_e + \gamma_{se})} \quad (D.75)$$

$$\Delta = \frac{\langle b_{eff} \rangle \gamma_{tr}}{1 + \langle b_{eff} \rangle (\gamma_e + \gamma_z + 2\gamma_{se}) + \langle b_{eff} \rangle^2 (\gamma_e \gamma_z + \gamma_{se}(\gamma_e + \gamma_z) - \gamma_{tr}^2)}. \quad (D.76)$$

In high holding field, one has $\mathcal{W}_e \simeq P_e$ and $\mathcal{W}_z \simeq P_z$ and the contributions of $\eta_{e,z}$ in the denominator of eq. D.72 and eq. D.73 can be neglected compared to γ_e , γ_z and γ_{se} , so that one obtains:

$$P_{e,z} \simeq \frac{P_{e,z}^{inj}}{1 + \langle b_{eff} \rangle (\gamma_{e,z} + \gamma_{se})} + \Delta P_{z,e}^{inj}. \quad (D.77)$$

Also in the denominator of Δ the bilinear terms are typically smaller than the linear terms, so that one obtains in the high field limit, where $e \simeq 2a$:

$$\Delta \simeq \frac{\langle b_{eff} \rangle (\frac{1}{2}\gamma_z + \gamma_{se})}{1 + \langle b_{eff} \rangle (\gamma_e + \gamma_z + \gamma_{se})}. \quad (D.78)$$

In the standard injection modes of the ABS, either $P_e^{inj} \simeq 0$ or $P_z^{inj} \simeq 0$ and one obtains in this case eq. 6.11.

D.5.3 Exact Solution of the Master Equation for Hydrogen

This section describes the solution of the eq.6.1 for the steady state conditons $\dot{N}_a = 0$. If one uses the following variable transformation

$$x = N_1 - N_3 \quad y = N_2 - N_4 \quad z = N_2 + N_4, \quad (D.79)$$

and the following shortcuts

$$\begin{aligned} \Pi_e &= \langle b_{eff} \rangle (W_{14} + W_{23}) & \Pi_z &= \langle b_{eff} \rangle (W_{12} + W_{34}) \\ \Pi &= \Pi_e + \Pi_z & A_0 &= x^{inj} - \frac{A_z}{2} \\ A_x &= -\frac{\Pi}{2} - 1 & A_y &= \frac{\Pi_z - \Pi_e}{2} \\ A_z &= \langle b_{eff} \rangle (W_{12} + W_{14} - W_{23} - W_{34}) & B_0 &= y^{inj} - \frac{B_z}{2} \\ B_x &= A_y & B_y &= A_x - \frac{\tau_d}{\tau_{se}} \sin^2 2\theta - 2 \langle b_{eff} \rangle W_{24} \\ B_z &= \langle b_{eff} \rangle (-W_{12} + W_{14} - W_{23} + W_{34}) & C_0 &= z^{inj} + \frac{\tau_d}{2\tau_{se}} + \frac{\Pi}{2} \\ C_x &= \frac{A_z}{2} & C_y &= \frac{B_z}{2} \\ C_z &= -\frac{\tau_d}{\tau_{se}} - 1 - \Pi, \end{aligned} \quad (D.80)$$

and resorts the equations, one obtains:

$$\begin{aligned} 0 &= A_0 + A_x x + A_y y + A_z z \\ 0 &= B_0 + B_x x + B_y y + B_z z \\ 0 &= C_0 + C_x x + C_y y + C_z z - \frac{\tau_d}{2\tau_{se}} (x^2 - \cos^2 2\theta y^2). \end{aligned} \quad (D.81)$$

In case of the validity of $W_{12} = W_{34}$ and $W_{14} = W_{14}$ - for example in case of a flat spectral density - the solution is:

$$\begin{aligned} x &= (A_y y^{inj} - B_y x^{inj}) / D \\ y &= (A_y x^{inj} - A_x y^{inj}) / D \\ z &= \left(\frac{1}{2} \frac{\tau_d}{\tau_{se}} (x^2 - \cos^2 2\theta y^2) - C_0 \right) / C_z, \end{aligned} \quad (D.82)$$

with $D = A_x B_y - A_y^2$. In order to calculate the general solution, the following shortcuts are used:

$$\begin{aligned} a_0 &= A_0 - \frac{A_z C_0}{C_z} & b_0 &= B_0 - \frac{B_z C_0}{C_z} \\ a_x &= A_x - \frac{A_z C_x}{C_z} & b_x &= B_x - \frac{B_z C_x}{C_z} \\ a_y &= A_y - \frac{A_z C_y}{C_z} & b_y &= B_y - \frac{B_z C_y}{C_z} \\ k &= \frac{\tau_d}{2C_z \tau_{se}}, \end{aligned} \quad (D.83)$$

so that:

$$\begin{aligned} 0 &= a_0 + a_x x + a_y y + A_z k (x^2 - \cos^2 2\theta y^2) = 0 \\ 0 &= b_0 + b_x x + b_y y + B_z k (x^2 - \cos^2 2\theta y^2) = 0. \end{aligned} \quad (D.84)$$

With U, V, P, Q, S, T defined by

$$\begin{aligned} U &= A_z b_0 - a_0 B_z & V &= A_z b_0 + a_0 B_z \\ Q &= A_z b_x - a_x B_z & P &= A_z b_y - a_y B_z \\ S &= A_z b_y + a_y B_z & T &= A_z b_x + a_x B_z, \end{aligned} \quad (D.85)$$

one obtains the solution:

$$K_1 = QS - PT \quad (D.86)$$

$$K_2 = P^2 - \cos^2 2\theta Q^2 \quad (D.87)$$

$$\begin{aligned} R &= \sqrt{K_1^2 + 8A_z B_z k (PSU + U \cos^2 2\theta (2A_z B_z k U - QT) - V K_2)} \\ x &= \frac{P(K_1 + R)}{4A_z B_z k K_2} + \frac{UQ \cos^2 2\theta}{K_2} \\ y &= -\frac{Q(K_1 + R)}{4A_z B_z k K_2} - \frac{UP}{K_2} \\ z &= -\frac{C_0 + C_x x + C_y y}{C_z} + k (x^2 - \cos^2 2\theta y^2). \end{aligned} \quad (D.88)$$

The population numbers $N_1 \dots N_4$ and polarization values can be calculated using:

$$\begin{aligned} N_1 &= \frac{1}{2}(1 - z + x) & N_2 &= \frac{1}{2}(z + y) \\ N_3 &= \frac{1}{2}(1 - z - x) & N_4 &= \frac{1}{2}(z - y) \\ P_e &= x + \cos 2\theta y & P_z &= x - \cos 2\theta y. \end{aligned} \quad (D.89)$$

D.6 Deuterium Spin Exchange Collisions

The calculation of the modified tensor M_{ab}^c results for \vec{D} :

$$\begin{aligned}
M^1 &= \frac{1}{2} \begin{pmatrix} 0 & 0 & -s & -1 & -c & 0 \\ 0 & 2SC & Sc & 0 & Ss & 1-2SC \\ -s & Sc & 0 & 0 & 0 & Cc \\ -1 & 0 & 0 & 0 & 0 & 0 \\ -c & Ss & 0 & 0 & 0 & Cs \\ 0 & 1-2SC & Cc & 0 & Cs & 2SC \end{pmatrix} \\
M^2 &= \frac{1}{2} \begin{pmatrix} 0 & -2SC & s & S & c & 2SC \\ -2SC & -6SC & -Sc-SC(1+s) & -C(1+S) & -Ss-SC(1+c) & -1+2SC \\ s & -Sc-SC(1+s) & 2Csc & 0 & C(1-2sc) & SC(1+s) \\ S & -C(1+S) & 0 & 0 & 0 & SC \\ c & -Ss-SC(1+c) & C(1-2sc) & 0 & 2Csc & SC(1+c) \\ 2SC & -1+2SC & SC(1+s) & SC & SC(1+c) & 2SC \end{pmatrix} \\
M^3 &= \frac{1}{2} \begin{pmatrix} 0 & 0 & -s-sc & c & sc & 0 \\ 0 & 2SCs & -Sc-sc(1+C) & C & sc(1+C) & s(1-2SC) \\ -s-sc & -Sc-sc(1+C) & -6sc & -2sc & -1+2sc & -Cc-sc(1+S) \\ c & C & -2sc & 0 & 2sc & S \\ sc & sc(1+C) & -1+2sc & 2sc & 2sc & sc(1+S) \\ 0 & s(1-2SC) & -Cc-sc(1+S) & S & sc(1+S) & 2SCs \end{pmatrix} \\
M^4 &= \frac{1}{2} \begin{pmatrix} 0 & 0 & 0 & -1 & 0 & 0 \\ 0 & 0 & Sc & -C & Ss & 0 \\ 0 & Sc & 2sc & 0 & 1-2sc & Cc \\ -1 & -C & 0 & 0 & 0 & -S \\ 0 & Ss & 1-2sc & 0 & 2sc & Cs \\ 0 & 0 & Cc & -S & Cs & 0 \end{pmatrix} \\
M^5 &= \frac{1}{2} \begin{pmatrix} 0 & 0 & sc & s & -c-sc & 0 \\ 0 & 2SCc & sc(1+C) & C & -Ss-sc(1+C) & c(1-2SC) \\ sc & sc(1+C) & 2sc & 2sc & -1+2sc & sc(1+S) \\ s & C & 2sc & 0 & -2sc & S \\ -c-sc & -Ss-sc(1+C) & -1+2sc & -2sc & -6sc & -Cs-sc(1+S) \\ 0 & c(1-2SC) & sc(1+S) & S & -Cs-sc(1+S) & 2SCc \end{pmatrix} \\
M^6 &= \frac{1}{2} \begin{pmatrix} 0 & 2SC & s & C & c & -2SC \\ 2SC & 2SC & SC(1+s) & SC & SC(1+c) & -1+2SC \\ s & SC(1+s) & 2Ssc & 0 & S(1-2sc) & -Cc-SC(1+s) \\ C & SC & 0 & 0 & 0 & -S-SC \\ c & SC(1+c) & S(1-2sc) & 0 & 2Ssc & -Cs-SC(1+c) \\ -2SC & -1+2SC & -Cc-SC(1+s) & -S-SC & -Cs-SC(1+c) & -6SC \end{pmatrix},
\end{aligned}$$

with the following shortcuts:

$$\begin{aligned} c &= \cos^2 \theta_- & s &= \sin^2 \theta_- \\ C &= \cos^2 \theta_+ & S &= \sin^2 \theta_+ . \end{aligned} \quad (\text{D.90})$$

D.6.1 The High Field Limit of Deuterium Spin Relaxation

In the limit of high magnetic holding field ($x \rightarrow \infty$), one finds

$$\begin{aligned} \lim_{x \rightarrow \infty} c &= 1 & \lim_{x \rightarrow \infty} s &= 0 \\ \lim_{x \rightarrow \infty} C &= 1 & \lim_{x \rightarrow \infty} S &= 0 , \end{aligned} \quad (\text{D.91})$$

and therefore:

$$\begin{aligned} \sum_{a,b} M_{a,b}^1 N_a N_b &= -N_1(N_4 + N_5) + (N_2 + N_3)N_6 \\ \sum_{a,b} M_{a,b}^2 N_a N_b &= -N_2(N_4 + N_6) + (N_1 + N_3)N_5 \\ \sum_{a,b} M_{a,b}^3 N_a N_b &= -N_3(N_5 + N_6) + (N_1 + N_2)N_4 \\ \sum_{a,b} M_{a,b}^4 N_a N_b &= -N_4(N_1 + N_2) + (N_5 + N_6)N_3 \\ \sum_{a,b} M_{a,b}^5 N_a N_b &= -N_5(N_1 + N_3) + (N_4 + N_6)N_2 \\ \sum_{a,b} M_{a,b}^6 N_a N_b &= -N_6(N_2 + N_3) + (N_4 + N_5)N_1 . \end{aligned} \quad (\text{D.92})$$

One can verify easily by the symmetry of these equations, that P_e , P_z and P_{zz} are unchanged by spin exchange collisions in high holding field. Nevertheless the hyperfine population is changed. The expectation value of A_{IS} is in the high field limit given by

$$A_{IS} = N_1 + N_4 - N_3 - N_6 . \quad (\text{D.93})$$

The master equation yields in this case:

$$0 = A_{IS}^{inj} - A_{IS} - \langle b \rangle 2 \langle W_e \rangle A_{IS} - \frac{\tau_d}{\tau_{se}} (A_{IS} - P_e P_z) . \quad (\text{D.94})$$

The transition probabilities of the electron transitions are - in the high field limit - approximately the same:

$$W_{16} \simeq W_{25} \simeq W_{34} = W_e , \quad (\text{D.95})$$

while the 2-6, 3-5 and 3-6 transitions are suppressed by the small matrix elements. If the term $P_e P_z$ is small - for example in injection mode P_{zz+} - one obtains:

$$A_{IS} = \frac{A_{IS}^{inj}}{1 + \langle b \rangle \gamma_e + \frac{\tau_d}{\tau_{se}}} , \quad (\text{D.96})$$

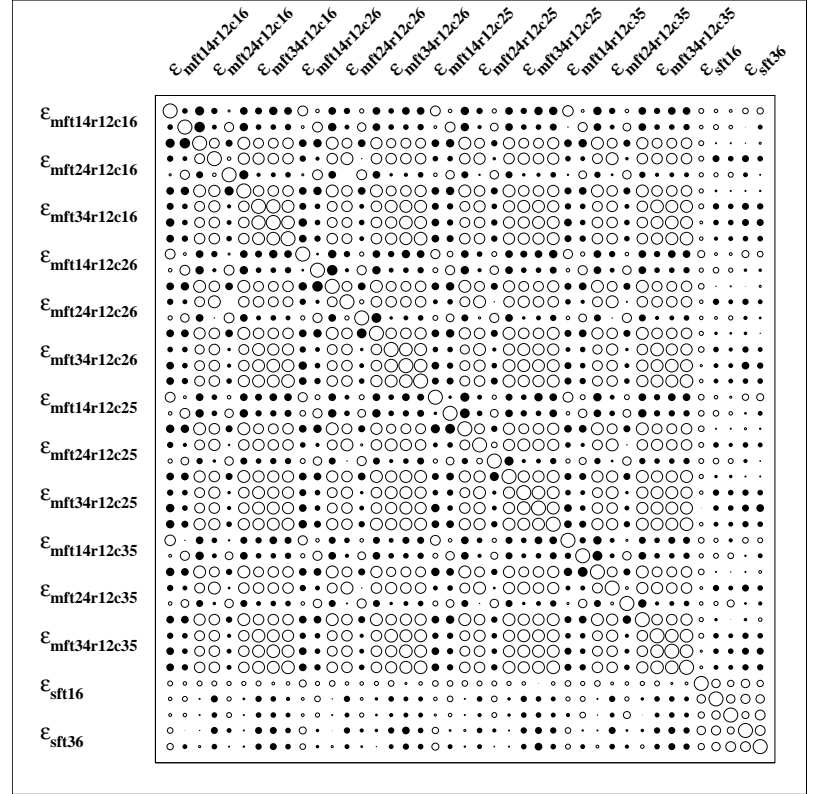
where γ_e is - similar to hydrogen - approximately given by $\gamma_e = 2 W_e$.

E Target Setup For Deuterium Running

BRP-Signal	Name	MFT-RF	MFT-B	SFT-RF	SFT-B
Beam Shutter Closed	bsc	OFF	OFF	OFF	OFF
OFF	off	OFF	OFF	OFF	OFF
SFT 1-6	s16	OFF	OFF	ON	1-6
SFT 2-6	s26	OFF	OFF	ON	2-6
SFT 2-5/3-6	s25	OFF	OFF	ON	2-5
SFT 3-5	s35	OFF	OFF	ON	3-5
MFT 1-4	m14c16	ON	1-4	OFF	1-6
MFT 1-4	m14c26	ON	1-4	OFF	2-6
MFT 1-4	m14c25	ON	1-4	OFF	2-5
MFT 1-4	m14c35	ON	1-4	OFF	3-5
MFT 2-4	m24c16	ON	2-4	OFF	1-6
MFT 2-4	m24c26	ON	2-4	OFF	2-6
MFT 2-4	m24c25	ON	2-4	OFF	2-5
MFT 2-4	m24c35	ON	2-4	OFF	3-5
MFT 3-4	m34c16	ON	3-4	OFF	1-6
MFT 3-4	m34c26	ON	3-4	OFF	2-6
MFT 3-4	m34c25	ON	3-4	OFF	2-5
MFT 3-4	m34c35	ON	3-4	OFF	3-5
MFT 1-4 + SFT 1-6	m14s16	ON	1-4	ON	1-6
MFT 1-4 + SFT 2-6	m14s26	ON	1-4	ON	2-6
MFT 1-4 + SFT 2-5/3-6	m14s25	ON	1-4	ON	2-5
MFT 1-4 + SFT 3-5	m14s35	ON	1-4	ON	3-5
MFT 2-4 + SFT 1-6	m24s16	ON	2-4	ON	1-6
MFT 2-4 + SFT 2-6	m24s26	ON	2-4	ON	2-6
MFT 2-4 + SFT 2-5/3-6	m24s25	ON	2-4	ON	2-5
MFT 2-4 + SFT 3-5	m24s35	ON	2-4	ON	3-5
MFT 3-4 + SFT 1-6	m34s16	ON	3-4	ON	1-6
MFT 3-4 + SFT 2-6	m34s26	ON	3-4	ON	2-6
MFT 3-4 + SFT 2-5/3-6	m34s25	ON	3-4	ON	2-5
MFT 3-4 + SFT 3-5	m34s35	ON	3-4	ON	3-5

Tab. E.1: Switching modes of the BRP and corresponding signals in case of deuterium. During a calibration measurement, all listed signals are measured, while a polarization measurement is performed with a subset of at least 6 signals plus the BSC-signal.

Efficiency	Value	Error
$\varepsilon_{m14r12c16}$	0.927	± 0.011
$\varepsilon_{m14r23c16}$	0.979	± 0.012
$\varepsilon_{m14r34c16}$	0.932	± 0.016
$\varepsilon_{m24r12c16}$	0.007	± 0.013
$\varepsilon_{m24r23c16}$	0.922	± 0.010
$\varepsilon_{m24r34c16}$	0.986	± 0.016
$\varepsilon_{m34r12c16}$	-0.538	± 0.884
$\varepsilon_{m34r23c16}$	0.025	± 0.017
$\varepsilon_{m34r34c16}$	0.965	± 0.017
$\varepsilon_{m14r12c26}$	0.932	± 0.011
$\varepsilon_{m14r23c26}$	0.985	± 0.012
$\varepsilon_{m14r34c26}$	0.908	± 0.015
$\varepsilon_{m24r12c26}$	0.014	± 0.014
$\varepsilon_{m24r23c26}$	0.935	± 0.011
$\varepsilon_{m24r34c26}$	0.987	± 0.016
$\varepsilon_{m34r12c26}$	-0.162	± 0.218
$\varepsilon_{m34r23c26}$	0.074	± 0.016
$\varepsilon_{m34r34c26}$	0.968	± 0.017
$\varepsilon_{m14r12c25}$	0.931	± 0.010
$\varepsilon_{m14r23c25}$	0.998	± 0.012
$\varepsilon_{m14r34c25}$	0.917	± 0.015
$\varepsilon_{m24r12c25}$	0.001	± 0.014
$\varepsilon_{m24r23c25}$	0.917	± 0.010
$\varepsilon_{m24r34c25}$	0.986	± 0.016
$\varepsilon_{m34r12c25}$	-0.194	± 0.166
$\varepsilon_{m34r23c25}$	0.095	± 0.015
$\varepsilon_{m34r34c25}$	0.993	± 0.016
$\varepsilon_{m14r12c35}$	0.926	± 0.011
$\varepsilon_{m14r23c35}$	0.988	± 0.012
$\varepsilon_{m14r34c35}$	0.926	± 0.015
$\varepsilon_{m24r12c35}$	-0.002	± 0.013
$\varepsilon_{m24r23c35}$	0.942	± 0.010
$\varepsilon_{m24r34c35}$	0.972	± 0.015
$\varepsilon_{m34r12c35}$	-0.412	± 0.594
$\varepsilon_{m34r23c35}$	0.033	± 0.017
$\varepsilon_{m34r34c35}$	0.962	± 0.017
ε_{s16}	0.986	± 0.012
ε_{s26}	0.957	± 0.009
ε_{s25}	0.982	± 0.013
ε_{s36}	0.804	± 0.009
ε_{s35}	0.923	± 0.010



Tab. E.2: The table contains the list of transition efficiencies, which are needed to describe the BRP signals in case of deuterium running and the corresponding results of a calibration measurement. The errors are of statistical nature and therefore Gaussian. The high errors of the $\varepsilon_{m34r12cxx}$ -efficiencies confirm, that the measured signals are not sensitive to these values. They could also be neglected completely. The figure visualizes the correlation matrix; see the explanation for tab. 3.6. It shows, that the correlation between SFT and MFT efficiencies is lower than within the MFT-block and within the SFT-block.

Mode	N_1	N_2	N_3	N_4	N_5	N_6
P_e	33.3 ± 0.0	33.3 ± 0.0	33.3 ± 0.0	0.0 ± 0.0	0.0 ± 0.0	0.0 ± 0.0
P_{z+}	46.4 ± 0.0	1.3 ± 0.0	3.8 ± 0.1	0.0 ± 0.0	3.4 ± 0.0	45.2 ± 0.1
P_{z-}	0.0 ± 0.0	3.8 ± 0.1	46.4 ± 0.0	46.4 ± 0.0	0.1 ± 0.1	3.3 ± 0.1
P_{zz+}	2.7 ± 0.2	1.3 ± 0.1	47.0 ± 0.2	3.6 ± 0.1	0.0 ± 0.1	45.5 ± 0.2
P_{zz-}	2.7 ± 0.2	46.7 ± 0.2	1.3 ± 0.1	3.6 ± 0.1	45.7 ± 0.2	0.0 ± 0.1
$ 1\rangle$	76.4 ± 0.0	8.0 ± 0.1	4.4 ± 0.1	5.7 ± 0.0	0.0 ± 0.0	5.4 ± 0.0
$ 2\rangle$	8.2 ± 1.1	70.5 ± 2.9	9.6 ± 0.7	6.1 ± 1.1	5.6 ± 1.1	0.0 ± 1.1
$ 3\rangle$	2.2 ± 1.5	7.4 ± 0.6	78.4 ± 3.5	6.2 ± 1.5	0.0 ± 1.5	5.8 ± 1.5
$ 4\rangle$	5.7 ± 0.0	4.4 ± 0.1	8.0 ± 0.1	76.4 ± 0.0	5.3 ± 0.1	0.1 ± 0.1
$ 5\rangle$	2.2 ± 1.4	7.4 ± 0.7	2.1 ± 1.4	6.2 ± 1.4	76.3 ± 3.4	5.8 ± 1.4
$ 6\rangle$	8.2 ± 1.0	1.9 ± 1.1	9.6 ± 0.8	6.1 ± 1.0	5.6 ± 1.0	68.6 ± 2.7

Tab. E.3: Injected hyperfine population of the atomic beam injected by the ABS for deuterium running in 1998. The values are calculated with the ABS efficiencies of the tab. 6.4. All values are given in percent. The quoted errors take only the uncertainty of the ABS efficiencies into account.

Mode	P_e	P_z	P_{zz}	A_{IS}	Rel. Int.
P_e	100.00 ± 0.00	0.00 ± 0.00	0.00 ± 0.00	0.00 ± 0.00	100.00 ± 0.00
P_{z+}	2.92 ± 0.15	87.78 ± 0.07	86.09 ± 0.23	-2.54 ± 0.03	71.82 ± 0.04
P_{z-}	0.41 ± 0.07	-89.50 ± 0.10	88.44 ± 0.27	-3.32 ± 0.03	71.82 ± 0.04
P_{zz+}	1.87 ± 0.34	-2.46 ± 0.32	96.22 ± 0.38	-86.14 ± 0.12	70.47 ± 0.12
P_{zz-}	1.34 ± 0.36	-2.19 ± 0.28	-177.30 ± 0.61	5.03 ± 0.08	70.47 ± 0.12
$ 1\rangle$	77.71 ± 0.26	71.70 ± 0.06	76.09 ± 0.22	72.26 ± 0.02	43.61 ± 0.06
$ 2\rangle$	76.61 ± 0.16	-7.49 ± 1.78	-128.22 ± 5.32	4.73 ± 0.34	42.44 ± 0.04
$ 3\rangle$	75.94 ± 0.19	-76.61 ± 2.06	77.71 ± 6.18	-75.83 ± 0.39	41.75 ± 0.04
$ 4\rangle$	-63.73 ± 0.06	-78.59 ± 0.23	70.64 ± 0.48	74.08 ± 0.03	43.61 ± 0.06
$ 5\rangle$	-76.59 ± 4.02	-0.35 ± 0.22	-151.08 ± 0.61	0.43 ± 0.03	41.75 ± 0.04
$ 6\rangle$	-60.56 ± 3.46	61.10 ± 3.49	77.54 ± 0.37	-63.85 ± 0.05	42.44 ± 0.04

Tab. E.4: Initial polarization values in the high field limit and relative intensity for deuterium running. The values are calculated with the ABS efficiencies of the tab. 6.4. All values are given in percent. The quoted errors take only the uncertainty of the ABS efficiencies into account.

F Geometry of Target Hardware

The cross section S of an elliptical shaped tube of radius $a \times b$ is given by:

$$S = \pi a b,$$

and its circumference U approximately by [Bro 79]:

$$U \simeq \pi [1.5 (a + b) - \sqrt{ab}].$$

The conductance is given by eq. C.25:

$$C = \frac{16}{3\sqrt{2\pi}} \frac{S^2}{UL + \frac{16}{3}S} \sqrt{\frac{kT}{m}}. \quad (\text{F.1})$$

	beam tube		sample tube		inj. tube	ext. tube
	large cell	small cell	large cell	small cell		
radius R/mm	14.9×4.9	9.9×4.5	2.5	3.0	5.0	5.0
length L/mm	200		100		100	120
cross section S/mm^2	223.2	119.38	19.63	28.27	78.54	78.54
circumference U/mm	64.94	44.25	15.7	18.85	31.4	31.4
conductance C	0.682	0.291	0.0446	0.076	0.336	0.286
$\delta l = 4 \frac{S}{U}/mm$	13.75	10.8	5	6	10	10
$\varepsilon = \frac{\sqrt{3}}{4} \frac{UL}{S}$	25.2	32.1	34.6	28.9	17.3	20.8
$\langle b \rangle (0)$	195	256	195	256	-	-
$\overline{\langle b \rangle}$	248	342	295	326	-	-
$\langle b \rangle (L)$	301	428	395	395	-	-

Tab. F.1: Geometry of the HERMES storage cell. The conductances have to be multiplied by a factor $\sqrt{\frac{T_{[K]}}{m_{[amu]}}}$ to obtain meaningful values; the unit is l/s . The average collision ages of the storage cells are calculated with eq. C.65, where the extension tube was neglected.

	Large cell	Small cell
Flow out off injection tube	19.35 %	34.34%
Flow out off sample tube	2.2 %	6.14 %
Flow out off beam tube	78.4 %	59.5 %
Conductance C^{TGA}	0.0386	0.06
Conductance $C^{IT} + C^{TGA}$	0.37488	0.3964
Ratio $\varepsilon = \frac{C^{IT} + C^{TGA}}{C^{BT}}$	0.55	1.36
Total conductance C_{tot}	1.738	0.979

Tab. F.2: Comparison between the geometry of the large and small storage cell. The conductances have to be treated in the same way as in tab. F.1. The numbers for the relative flux are calculated under the assumption, that all tubes have the same temperature.

	z-pos	length	radius	B_{pt}
Sample tube	0	100	2.5	
Ext. tube	100	120	5.0	
Beam blocker	850	1	4.5	
1. Magnet	851	70	12.5	1.45 T
2. Magnet	1056	110	12.5	1.45 T
Detector	1455	-	4×8	

Tab. F.3: Geometry of the Breit-Rabi type polarimeter. All dimensions are given in [mm].

	z-pos	length	outer radius	inner radius	segments
Nozzle	-1208			1	
Collimator	-1163			3.7	
1. Magnet	-1150	30	30	4.3...5.2	12
2. Magnet	-1100	55	40	6.0...8.0	12
3. Magnet	-1025	75	40	8.35...12.5	12
4. Magnet	-600	75	-	13.3	24
5. Magnet	-485	85	40	13.3...11.0	24
Inj. tube	-100	100.		5.0	

Tab. F.4: Geometry of the Atomic Beam Source. All dimensions are given in [mm]. All magnets have a fill factor f of $f = 0.98$ and a magnetization of 1.132 T.

$\langle b \rangle$ in...	total	BT	IT	ST	ET	IP
BRP	405 ± 19	165 ± 2	18.65 ± 1.25	124 ± 4.8	44 ± 2.5	54.5 ± 3.2
TGA	635 ± 12.6	154.4 ± 1.25	17 ± 0.7	211 ± 2.7	112 ± 1.9	140 ± 2.4
TC	306.544(2)	265.98 ± 0.03	29.84 ± 0.02	10.71 ± 0.02	0	0
TGA ch.	641.6 ± 0.2	154.7 ± 0.16	16.84 ± 0.09	209.75 ± 0.34	115.4 ± 0.24	144.8 ± 0.3

Tab. F.5: Average wall collision ages obtained by a molecular flow Monte Carlo simulation for the large storage cell. The average collision age of atoms entering BRP and TGA are distinguished in the right columns with respect to the surface, where the wall collisions appeared: Beam tube (BT), injection tube (IT), sample tube (ST), extension tube (ET) and intermediate plane (IP). The left column refers to the atomic sample: Atoms entering BRP or TGA acceptance, atoms entering the target chamber (TC) or the TGA vacuum chamber (TGA Ch.).

	Beam Tube	BRP	TGA	Target-Ch.	TGA-Ch.
$\langle b \rangle$	265.688(2)	399.6 ± 3.85	636.4 ± 2.4	306.574(36)	641.5 ± 0.3
$\langle b^2 \rangle$	136944	280923	532308	161095	539498
$\langle l \rangle$ [mm]	358.3340(28)	420.8 ± 4	594.6 ± 2.6	414.7 ± 0.05	598.2 ± 0.31
$\langle l_\rho \rangle$ [mm]	489.4220(38)	459.8 ± 4.8	517 ± 3	528.9 ± 0.06	512.6 ± 0.36
ρ_c	1.365820(15)	1.093 ± 0.015	0.87 ± 0.0063	1.2754(2)	0.85696(75)

Tab. F.6: Numerical results of the molecular flow simulation. $\langle b \rangle$ is the average wall collision age, $\langle l \rangle$ the average trajectory length of the diffusing atoms or molecules. For the definition of $\langle l_\rho \rangle$ and ρ_c refer to sec. C.6.2. The column of the target chamber contains results from all atoms, that reached either the end of the beam tube or of the injection tube. The results were calculated for the large storage cell.

G Slow Control, Data Acquisition and Online Monitoring

The target data acquisition (DAQ) is an integrated part of the HERMES DAQ system. The slow control (SC) software of the HERMES target can be subdivided into two parts - real "slow" control programs, that are reading ADC modules via CAMAC interface in time intervals of typically several seconds up to a minute and the *brpclient* program, that has control over the hyperfine transitions states of ABS and BRP and therefore defines the target operation and polarization status. For performance reasons, the *brpclient* communicates with a digital signal processor (DSP), that is connected via a Fastbus and can control the measurement process with minimal delay. This is possible with a so-called "front end list" (FEL), which is a batch like collection of commands, that can be executed by the DAQ electronics. In its default operation mode, the *brpclient* fills the FEL, sends it to the DAQ and is idle until a polarization measurement is finished, so that the "slow" bottle neck between the online computers and the DAQ system has to be passed only twice. The measurement itself and optional the evaluation of the spectra¹⁹⁸ of the time resolving counter (TRC) is done by the multi scaler input (MSI) of the DSP board. When the *brpclient* receives the results in form of a list of BRP and TGA count rates for the chopper open and chopper closed position of each measured beam signal, it evaluates the beam signal by background subtracting and calculates the hyperfine population and atomic fraction respectively. Raw data and results are filled in ADAMO tables and send to the DAD server¹⁹⁹. Additionally, so-called "user events" are created by the *brpclient*, send to the HERMES DAQ and taped as EPIO records. Beneath these connections, the *brpclient* can be used interactively as a menu controlled terminal program. This is typically only the case, when special target studies have to be performed. In this mode, the results are optionally also written directly to files.

¹⁹⁸See fig. 3.8.

¹⁹⁹DAD (=Distributed ADAMO Database) is a client-server extension of ADAMO [Wan 95].

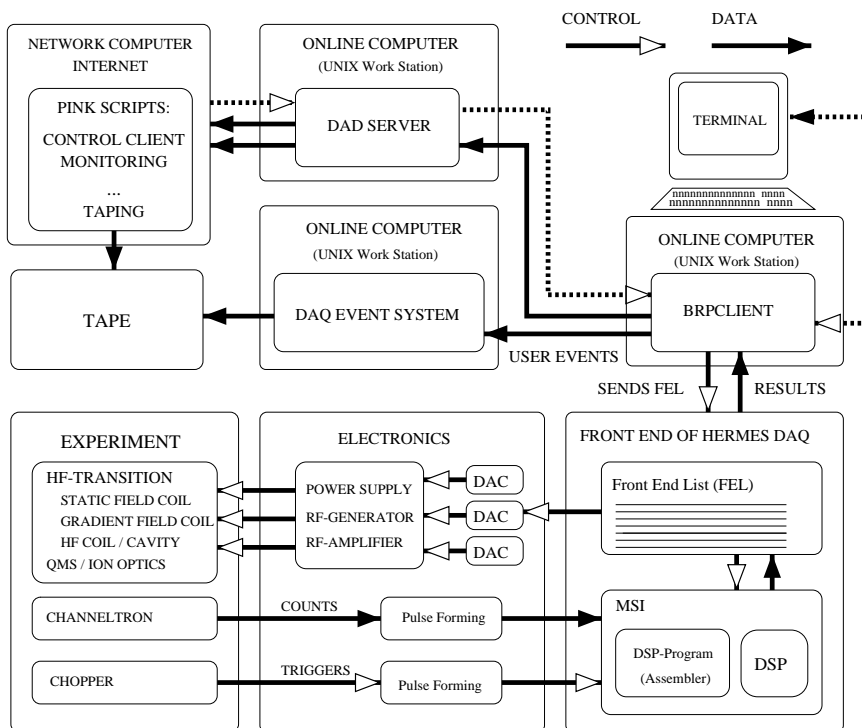


Fig. G.1: Schematic of the HERMES target data acquisition (DAQ). Dotted arrows correspond to optional connections.

mode	identifier	controlled	measurement
beam	bm_	-	TRC spectrum
corrected beam	hcb	QMS	$3 \times \mathbf{bm}_-$
polarization	hpx	QMS+BRP HFTs	$5 \times \mathbf{hcb}$ (BRP)
atomic fract.	hmf	QMS of TGA	av. of $5 \times \mathbf{hmf}$ (TGA)
$2 \times$ pol.	rhx	QMS+BRP HFTs+ABS HFTs	$2 \times \mathbf{hpx}$ for $P_{z\pm}^{inj}$
$3 \times$ pol.	ahx	QMS+BRP HFTs+ABS HFTs	$3 \times \mathbf{hpx}$ for P_e^{inj} and $P_{z\pm}^{inj}$

Tab. G.1: Measurement modes of the *brpclient* for polarized hydrogen operation.

During HERMES data taking, the *brpclient* runs as a UNIX job control task and is automatically restarted in case of failure. All commands are transferred to the program with a PinK-script, the *brpclient control panel* via the DAD-server connection²⁰⁰. Fig. G.1 shows the main relevant parts of the HERMES target controlling/monitoring system.

The *brpclient* disposes of an internal list of *devices*, each consisting of a list of *parameters*, that are representing the setup and status of all hardware components, that are relevant for the setup of the ABS injection modes and the measurement of the polarization and atomic fraction. The program can be operated in different measurement modes, which are organized in a hierarchy. The simplest mode in the *beam* measurement (**bm_**). In this mode, time spectra of both - TGA and BRP - as shown in fig. 3.8 are taken and the beam signal is calculated as the difference between the countrates of the intervals for chopper open and closed. This measurement mode does not require the change of any parameter. The next level are the *corrected beam measurements* (**hcb**), that consists (in case of hydrogen) of 3 beam measurements and allows the calculation of the corrected beam with eq. 3.37. During a **hcb** measurement, the mass set point of the quadrupole mass spectrometers of TGA and BRP are controlled by the measurement mode. The third level is the *polarization* measurement, consisting of several **hcb** measurements. This mode requires control of all parameters of the BRP transitions. The highest level is build by the measurement modes, that are measuring the polarization for a collection of ABS injection modes. A list of the operation modes for hydrogen/deuterium is given in tab. G.1 and tab. G.2 respectively.

A hydrogen polarization measurement (**hpx**) consists of 5 **hcb** measurements²⁰¹, so that the measured atomic fraction is the average of five single measurements. The level of the **hcb** measurements between a beam and a polarization measurement was - by the usage of the beam shutter - superfluous, so that the TGA and BRP modes are asynchronously overlapping.

The *time order* of the **bm_** measurements within a **hcb** measurement and of the **hcb** measurement within a **hpx** measurement etcpp. is chosen randomly. The purpose of the randomization is the avoidance of eventual effects of ordering and synchronicity of measurements. A beam measurement consists of the sum of a certain number of TRC spectra - each representing two complete chopper turns, which is called the number of *single cycles*. During 1996 and the first half of 1997, the number of single cycles was the same for each beam measurement within a **hcb** measurement. This was changed in the middle of 1997 in order to improve the statistical

²⁰⁰PinK is a DAD-extension of Tcl/Tk, which allows to write small - optional interactive - monitoring and controlling tasks, that are able to send and receive data and commands via a DAD-server connection [Ack 95]. Major parts of the HERMES online monitoring system are written in PinK, which was developed - as DAD - by the HERMES software group.

²⁰¹In principle, only 4 measurements would be required. The fifth corrected beam signal is redundant and allows to quality check by the calculation of a χ^2 -value. Alternatively it can be used to fit the internal BRP parameter of the transmission ratio $\frac{\sigma_2}{\sigma_1}$.

mode	identifier	controlled	measurement
beam	bm_	-	TRC spectrum
corrected beam	dcb	QMS of BRP	$6 \times \mathbf{bm}_-$ (BRP)
atomic fract.	dmf	QMS of TGA	$6 \times \mathbf{bm}_-$ (TGA)
polarization	dps	QMS+BRP HFTs+beam shutter	$10 \times \mathbf{bm}_-$ (BRP)
atomic fract.	dmf	QMS of TGA	$6 \times \mathbf{bm}_-$ (TGA)
$2 \times \text{pol.}$	vdps	QMS+BRP HFTs+ABS HFTs	$2 \times \mathbf{dps}$ for $P_{z\pm}^{inj}$
$5 \times \text{pol.}$	adps	QMS+BRP HFTs+ABS HFTs	$5 \times \mathbf{dps}$ for P_e^{inj} , $P_{z\pm}^{inj}$ and $P_{zz\pm}^{inj}$
$6 \times \text{pol.}$	sdps	QMS+BRP HFTs+ABS HFTs	$6 \times \mathbf{dps}$ for $ 1\rangle^{inj} \dots 6\rangle^{inj}$
pol./calibration	dpc	QMS+BRP HFTs+beam shutter	$30 \times \mathbf{bm}_-$ (BRP)
calibration	dcl	QMS+BRP HFTs+ABS HFTs	$5 \times \mathbf{dpc}$ for P_e^{inj} , $P_{z\pm}^{inj}$ and $P_{zz\pm}^{inj}$
calibration	sdcl	QMS+BRP HFTs+ABS HFTs	$6 \times \mathbf{dpc}$ for $ 1\rangle^{inj} \dots 6\rangle^{inj}$

Tab. G.2: Measurement modes of the *brpclient* for the operation with polarized deuterium. The measurement of the atomic fraction consists of beam measurements for the masses 2,3,4,18,19 and 20 *amu*.

precision especially of the α^{TGA} -measurement as shown by fig. G.2. The fraction of single cycles, that are used for the measurement of the beam signal of a certain mass, is no more fixed. It can be optimized with respect to the statistical uncertainty.

The deuterium software has a different hierarchy and synchronization scheme as shown in the lower part of fig. G.2. The QMS of the BRP measures continuously on mass 2 *amu* and is asynchrone with the TGA switching scheme.

All measurement modes can be run periodically. Optionally, it is possible to change a parameter of the hardware setup in regular intervals between the measurements so that the result is obtained in dependence of this parameter.

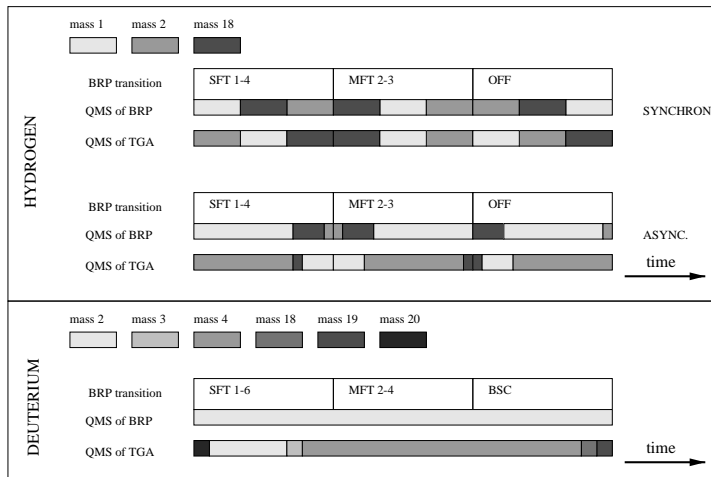


Fig. G.2: Scheme of the synchronization of the measurements of BRP and TGA. The first version of the *brpclient*, which was running 1996 and during the first half of 1997, was switching the mass setting of BRP and TGA synchron and with a fixed number of single cycles for each mass. From mid 1997 on, the scheme was changed to an asynchronous mode. The deuterium software does not foresee a mass switching of the BRP QMS during a pol. meas.. Instead it takes a BSC (*beam shutter closed*) signal.

H Data Analysis

The expectation or mean value $\langle x \rangle$ of the measured values x_k , $k = 1 \dots N$ is defined by:

$$\langle x \rangle = \frac{1}{N} \sum_{k=1}^N x_k. \quad (\text{H.1})$$

The unbiased estimation of the variance σ^2 of the single measurement is given by:

$$\sigma^2(x_k) = \langle (x - \langle x \rangle)^2 \rangle = \langle x^2 \rangle - \langle x \rangle^2. \quad (\text{H.2})$$

The unbiased estimator of the variance σ_x^2 of $\langle x \rangle$ is given by:

$$\sigma^2(\langle x \rangle) = \frac{1}{N-1} (\langle x^2 \rangle - \langle x \rangle^2). \quad (\text{H.3})$$

The covariance c_{jk} of two measured values x_j and x_k is defined by:

$$c_{jk} = \langle (x_j - \langle x_j \rangle)(x_k - \langle x_k \rangle) \rangle. \quad (\text{H.4})$$

The diagonal elements c_{kk} of the square and symmetric covariance matrix $\mathbf{C} = c_{jk}$ are identical to the variance of x_k .

The correlation matrix $Corr(\mathbf{x})_{jk}$ of the vector \mathbf{x} is given by:

$$Corr_{jk} = \frac{\{C_x\}_{jk}}{\sigma(x_j)\sigma(x_k)}, \quad (\text{H.5})$$

where C_x is the covariance matrix.

The general least square fit algorithm, which was used for the evaluation of the BRP calibration measurements and other fits, is based on the book of S. Brandt [Bra 92].

Given the vector of n measured values \mathbf{y} , which differ from the *true* values η by the statistical error ε :

$$\eta = \mathbf{y} + \varepsilon. \quad (\text{H.6})$$

C_y is the covariance matrix of \mathbf{y} and $G_y = C_y^{-1}$ the matrix of the statistical weights.

\mathbf{x} is the vector of r unknown parameters, which are to be determined by the measurement and a set of functions $\mathbf{f}(\mathbf{x}, \eta)$ builds the theoretical relation between the measurements by the m equations

$$f_k(\mathbf{x}, \eta) = 0 \quad k = 1 \dots m. \quad (\text{H.7})$$

The initial estimation of the parameter vector is \mathbf{x}_0 , the estimation of η is $\eta_0 = \mathbf{y}$. The matrices \mathbf{A} and \mathbf{B} and the vector \mathbf{c} are then defined by:

$$a_{kl} = \left(\frac{\partial f_k}{\partial x_l} \right)_{\mathbf{x}_0, \eta_0}, \quad \mathbf{A} = \begin{pmatrix} a_{11} & a_{12} & \dots & a_{1r} \\ a_{21} & a_{22} & \dots & a_{2r} \\ \vdots & & & \\ a_{m1} & a_{m2} & \dots & a_{mr} \end{pmatrix}$$

$$b_{kl} = \left(\frac{\partial f_k}{\partial \eta_l} \right)_{\mathbf{x}_0, \eta_0}, \quad \mathbf{B} = \begin{pmatrix} b_{11} & b_{12} & \dots & b_{1n} \\ b_{21} & b_{22} & \dots & b_{2n} \\ \vdots & & & \\ b_{m1} & b_{m2} & \dots & b_{mn} \end{pmatrix} \quad (\text{H.8})$$

$$c_k = f_k(\mathbf{x}_0, \eta_0), \quad \mathbf{c} = \begin{pmatrix} c_1 \\ c_2 \\ \vdots \\ c_m \end{pmatrix}$$

The iteration to improve the estimators \mathbf{x}_0 and η_0 is then given by:

$$G_B = (BC_y B^T)^{-1} \quad (\text{H.9})$$

$$\mathbf{x}_1 = \mathbf{x}_0 + \tilde{\zeta} \quad (\text{H.10})$$

$$\tilde{\zeta} = -(A^T G_B A)^{-1} A^T G_B \mathbf{c} \quad (\text{H.11})$$

$$\eta_1 = \eta_0 + \tilde{\delta} \quad (\text{H.12})$$

$$\tilde{\delta} = -C_y B^T G_B (\mathbf{c} + A \tilde{\zeta}) \quad (\text{H.13})$$

$$C_{x_1} = (A^T G_B A)^{-1} \quad (\text{H.14})$$

$$C_{\eta_1} = C_y - C_y B^T G_B B C_y + C_y B^T G_B A C_{x_1} A^T G_B B C_y \quad (\text{H.15})$$

The χ^2 -value for $m - r$ degrees of freedom is given by:

$$\chi^2 = (\mathbf{B}(\mathbf{y} - \eta))^T G_B (\mathbf{B}(\mathbf{y} - \eta)). \quad (\text{H.16})$$

There is no guaranty, that the algorithm is convergent in all cases. In fact, it was convergent in case of the BRP calibration within 4 – 5 iterations, if the transmissions of the BRP were kept fixed. The attempt to fit both - efficiencies and transmissions - within the same iterational procedure, failed.

If the functions \mathbf{f}_k are linear in \mathbf{x} and \mathbf{y} , only one iteration step is required. The initial estimator \mathbf{x}_0 can be set to zero in this case and the final estimator \mathbf{x}_f is directly given by $\mathbf{x}_f = \tilde{\zeta}$.

If the matrix \mathbf{B} is in addition a unit matrix - which is the case for the calculation of the polarization from the measured BRP signals, the algorithm simplifies significantly:

$$C_x = (A^T G_y A)^{-1} \quad (\text{H.17})$$

$$\mathbf{x} = C_x A^T G_y \mathbf{y} \quad (\text{H.18})$$

I Physical Constants

Quantity	Symbol, equation	Value
speed of light in vacuum	c	$299\,792\,458\,m\,s^{-1}$
plank constant	h	$6.626\,075\,5(40) \times 10^{-34}\,J\,s$
plank constant, reduced	\hbar	$1.054\,572\,66(63) \times 10^{-34}\,J\,s$
electron charge magnitude	e	$1.602\,177\,33(49) \times 10^{-19}\,C$
electron mass	m_e	$9.109\,389\,7(54) \times 10^{-31}\,Kg$ $= 0.510\,999\,06(15)\,MeV/c^2$
proton mass	m_p	$1.672\,623\,1(10) \times 10^{-27}\,Kg$ $= 938.272\,31(28)\,MeV/c^2$ $= 1.007\,276\,470(12)\,u$ $= 1836.152\,701(37)\,m_e$
deuteron mass	m_d	$1875.613\,39(57)\,MeV/c^2$
atomic mass unit	u	$1.660\,540\,2(10) \times 10^{-27}\,Kg$ $= 931.494\,32(28)\,MeV/c^2$
permittivity of free space	ϵ_0	$8.854\,187\,817 \dots \times 10^{-12}\,F\,m^{-1}$
permeability of free space	μ_0	$4\pi \times 10^{-7}\,N\,A^{-2}$ $= 12.566\,370\,614 \dots \times 10^{-7}\,N\,A^{-2}$
fine-structure constant	$\alpha = e^2/4\pi\epsilon_0\hbar c$	$1/137.035\,989\,5(61)$
Bohr magneton	$\mu_B = e\hbar/2m_e$	$5.788\,382\,63(52) \times 10^{-5}\,eV\,T^{-1}$
nuclear magneton	$\mu_N = e\hbar/2m_p$	$3.152\,451\,66(28) \times 10^{-8}\,eV\,T^{-1}$
Boltzmann constant	k	$1.380\,658(12) \times 10^{-23}\,J\,K^{-1}$ $= 8.617\,385(73) \times 10^{-5}\,eV\,K^{-1}$
Avogadro constant	N_A	$6.022\,136\,7(36) \times 10^{23}\,mol^{-1}$
magnetic moment of electron	$\frac{1}{2}g_S\mu_B$	$1.001\,159\,652\,193(10)\,\mu_B$
magnetic moment of proton	$\frac{1}{2}g_P\mu_N$	$2.792\,847\,39(6)\,\mu_N$

Tab. I.1: List of physical constants used in this work (taken from [PPB 98]).

The magnetic moment of the deuteron μ_d is $\mu_d = 0.857\,438\,230(24)\,\mu_N$ [Fir 96].

Value	Hydrogen	Deuterium
ν_{HFS}/MHz	1420.405 751 768	327.384 352 51
E_{HFS}/eV	$5.874\,328\,324 \times 10^{-6}$	$1.353\,953\,384 \times 10^{-6}$
B_C/mT	50.683 622 91	11.681 890 93
ϵ	$1.519\,270\,379 \times 10^{-3}$	$2.332\,033\,388 \times 10^{-4}$

Tab. I.2: List of physical constants related to the hyperfine structure of hydrogen and deuterium atoms. The frequencies ν_{HFS}^H and ν_{HFS}^D were very precisely measured with masers (see references in [Br 95] resp. [Aud 71]).

Figures

1.1	The HERMES Experiment	1
1.2	The Setup of the Polarized Hydrogen/Deuterium Target.	2
2.1	Breit-Rabi-Diagrams of Hydrogen and Deuterium	6
2.2	Hydrogen Mixing Coefficients and Polarization	7
2.3	Deuterium Mixing Coefficients and Polarization of Hyperfine States	7
2.4	Schematic Diagram of the Adiabatic Passage	10
2.5	Trajectories of Atoms in ABS	11
2.6	Density Profile in HERMES Storage Cell	13
2.7	Atomic Density Versus Atomic Fraction	15
3.1	The Target Chamber	17
3.2	Field Map of the Longitudinal Target Magnet	18
3.3	Chemical Structure of Drifilm Coating	18
3.4	The Storage Cell	19
3.5	Thermal Expansion of the Storage Cell	19
3.6	The Setup of the Atomic Beam Source	20
3.7	The Setup of the Target Gas Analyzer (TGA)	24
3.8	Time Spectrum of Countrates in BRP and TGA	25
3.9	Beam Signal in TGA as Function of Emission Current	26
3.10	Calibration of the TGA by Variation of Cell Temperature	28
3.11	Behavior of TGA Rates After a HERA Beam Loss	29
3.12	Rest Gas Correction of the Molecular Beam into TGA	30
3.13	Measurement of Ballistically Injected Molecular Beam	31
3.14	The Vacuum System of the Breit-Rabi Polarimeter (BRP)	34
3.15	The Setup of the Breit-Rabi Type Polarimeter (BRP)	34
3.16	Transmission Ratio of the BRP for Hydrogen	40
3.17	Sextupole Transmission of the BRP	42
3.18	Time of Flight Measurement of Atoms in the BRP	44
3.19	Total Intensity of the BRP Signal	45
3.20	Target Density Measured by the Luminosity Monitor vs. TGA Flux	46
4.1	Geometrical Acceptance of BRP and TGA	48
4.2	Acceptance of BRP and TGA obtained by MC Simulation	49
4.3	Atomic Beam Signal in BRP and TGA after HERA Beam Loss	50
4.4	Atomic Beam Signal in BRP and TGA by Temperature Variation	51
4.5	Measurement of Diffusion Length Distribution	51
4.6	Measurement of Diffusion Time in the Presence of Recombination	53
5.1	Illustration of the Potential Energy Curve in Physisorption	56
5.2	Measured Temperature Dependence of the Atomic Fraction	58
5.3	Scheme of Surface Potentials of Recombination	60
5.4	Temperature Dependence of Recombination for Deuterium	60
5.5	Measured Beam Rates at First Exposure of a New Storage Cell	61
5.6	Measurement of the Density Dependence of Surface Recombination	62
5.7	Measurement of The Diffusion Time at Low Cell Temperature.	63
5.8	Measurement of Low Temperature Recombination without Density Dependence	64
5.9	Temperature Dependence of Different Recombination Processes	65
5.10	Change of Recombination Behavior with Target Operation Time	67
5.11	Temperature Dependence of Different Recombination Processes	67

6.1	The Density Dependence of Spin Exchange Effect	74
6.2	Influence of Recombination on Electron Polarization	75
6.3	Influence of Recombination on Nuclear Polarization	76
6.4	Measured Polarization and ABS Efficiencies of Hydrogen	77
6.5	Temperature Dependence of Wall Depolarization for Hydrogen	83
6.6	Temperature Dependence of Residual Polarizations	85
6.7	Equilibrium Electron Polarization vs. Temperature	86
6.8	Measured Electronic Asymmetry vs. Target Holding Field	87
6.9	Overview of Temperature Scans in 1997	89
6.10	Measured Hyperfine Population vs. Magnetic Field for Hydrogen	89
6.11	Measured Polarization vs. Magnetic Field for Hydrogen	90
6.12	Hyperfine Population vs. Magnetic Field for Hydrogen at High Temperature	91
6.13	Hyperfine Population vs. Magnetic Field for Hydrogen at 75 K	91
6.14	Hyperfine Population vs. Magnetic Field for Hydrogen at 48 K	92
6.15	Atomic Density Determined by Spin Exchange Compared to Measured Atomic Fraction	94
6.16	Frequency Range of the Hydrogen Transitions	95
6.17	Measured Hydrogen Spectra at a Storage Cell Temperature of 100 K	96
6.18	Spectra of Hydrogen Relaxation at Low Storage Cell Temperatures	97
6.19	Measurement of the Deuterium Spin Relaxation vs. Temperature	99
6.20	Measurement of the Deuterium Spin Relaxation vs. Temperature	100
6.21	Scope of the Transition Frequencies of Deuterium	102
6.22	Measured Spectrum of the Deuterium 3-4 Transition	103
6.23	Frequencies and Frequency Differences of Deuterium Transitions	104
6.24	Measured Spectrum of the Deuterium 3-4 Transition	105
6.25	Measured Spectrum of the Deuterium 3-4 Transition	105
6.26	Measured Spectrum of the Deuterium 5-6 Transition	106
6.27	Parameters of the Modified Spectral Density of Deuterium	107
6.28	Deuterium $\langle \vec{I}\vec{S} \rangle$ -Relaxation	108
6.29	Bunch Field Resonances of Deuterium	109
6.30	Measured Bunch Field Induced Resonances of Deuterium	110
6.31	Measured Bunch Field Induced Depolarization of Deuterium	110
6.32	Bunch Field Resonant Strength vs. Beam Current	111
7.1	The Sampling Corrections c_α and c_P	115
7.2	Measured Polarization of Deuterium vs. Storage Cell Temperature	118
A.1	Measured Hyperfine Population of Deuterium vs. Magnetic Holding Field	123
A.2	Measured Hyperfine Population of Deuterium vs. Magnetic Holding Field	124
A.3	Polarization of Deuterium vs. Magnetic Holding Field	125
A.4	Measured Polarization of Deuterium vs. Temperature	126
A.5	Measured Polarization of Deuterium vs. Temperature	127
B.1	Hydrogen Transition Frequencies	133
B.2	Adiabatic Eigenstates of a Hydrogen SFT 2-4.	134
B.3	Adiabatic Eigenstates of a Deuterium WFT	136
B.4	Measured Amplitude Dependence of Deuterium WFT Operation	137
C.1	Molecular Diffusion in Storage Cell	143
C.2	Collision Age Distributions in the Storage Cell	145
C.3	Average Collision Age of Atoms in the HERMES Storage Cell	149
C.4	Collision Age Distributions of Atoms Entering BRP and TGA	150

C.5	Expected TGA Measurement for Density Dependent Recombination	151
C.6	Differential Collision Age of TGA/BRP Sample Beam	153
C.7	Sampling Correction C_α in the Model of Distributed Sources	158
C.8	Minimal Atomic Density in Case of Recombination	159
C.9	Atomic Density in the Model of Localized Sources	160
C.10	Sampling Corrections by the Model of Localized Sources	162
D.1	Transition Amplitude Weight Function	165
D.2	Cross Section for Spin Exchange Collisions vs. Temperature	172
D.3	Hyperfine Population in Spin Temperature Equilibrium (STE).	174
D.4	Effect of Spin Exchange Collisions on Hydrogen	177
G.1	The Data Acquisition System of the HERMES Target	187
G.2	Synchronization Scheme of TGA and BRP Measurements	189

Tables

2.1	Hyperfine Transitions of Hydrogen and Deuterium.	9
2.2	Relations Between Atomic Fraction and Normalized Density	15
3.1	Injection Modes of the ABS for Polarized Hydrogen Running.	22
3.2	Injection Modes of the ABS for Deuterium Running.	22
3.3	Transmission Probabilities of the ABS Sextupole System	23
3.4	Example for the Analysis of the Atomic Fraction	32
3.5	Signals of the BRP for Hydrogen Running	38
3.6	Transition Efficiencies of the BRP for Hydrogen	39
6.1	Fit Results of Measured Magnetic Field Dependence of Hydrogen	90
6.2	Fit Results for ABS Transition Efficiencies (Hydrogen)	93
6.3	Results of Spin Relaxation Measurements with Deuterium vs. Temperature	99
6.4	ABS Transition Efficiencies of Deuterium	101
6.5	Bunch Field Induced Resonant Dep. vs. HERA Beam Current	111
7.1	Linear Approximations of Sampling Corrections	116
7.2	Example for the Calculation of the Atomic Fraction and its Uncertainty	120
B.1	Mixing Angles and Eigenenergies of the Hyperfine States.	129
B.2	Magnetic Field Values of Hyperfine Transitions of Hydrogen and Deuterium	130
B.3	Frequency Shifts for the Calculation of Adiabatic Eigenstates	134
B.4	Magnetic Moments of Hydrogen/Deuterium Hyperfine States	138
C.1	List of Relations of Diffusive Molecular Flow in Tubes	142
D.1	Transitions Probabilities in Multiplets	169
D.2	Matrix Elements of Hyperfine Transitions	171
D.3	Coefficients of the Hydrogen Spin Exchange Tensor.	173
D.4	Coefficients of the Deuterium Spin Exchange Tensor.	173
D.5	Characteristic Properties of Spin Temperature Equilibrium.	173
D.6	Possible Pairs of Hyperfine States for Spin Exchange Collisions	175
E.1	Signals of the BRP for Deuterium Running	182
E.2	Transition Efficiencies of the BRP for Deuterium	183
E.3	Injected Hyperfine Population for Deuterium Running	184
E.4	Initial Polarization and Intensity for Deuterium	184
F.1	Geometry of the HERMES Storage Cell	185
F.2	Geometry of the HERMES Storage Cell	185
F.3	Geometry of the Breit Rabi Polarimeter	186

F.4	Geometry of the Atomic Beam Source	186
F.5	Average Wall Collision Ages Calculated by Monte Carlo	186
F.6	Numerical Results of the Molecular Flow Monte Carlo Simulation	186
G.1	Measurement Modes of Hydrogen	188
G.2	Measurement Modes of Deuterium	189
I.1	List of Used Physical Constants	192
I.2	List of Hyperfine Structure Constants	192

References

- [Ack 95] K. Ackerstaff *et al.*; HERMES interner Report 41, 1995.
- [Ab 84] M. Abramowitz, I.A. Stegun; Pocketbook of Math. Func. Thun, 1984.
- [Abe 95] E 143: K. Abe *et al.*; Phys. Rev. Lett. 74 (1995), 346-350.
- [Abe 97] E 154: K. Abe *et al.*; Phys. Rev. Lett. 79 (1997), 26-30.
- [Abr 58] A. Abragam, J.M. Winter; Phys. Rev. Lett. Vol. 1, No. 10 (1958), 374-375.
- [Abr 61] A. Abragam: The Principles Of Nuclear Magnetism; Oxford At The Clarendon Press 1961.
- [Ade 93] B. Adeva *et al.*; Phys. Lett. B 302 (1993), 533-539.
- [Ada 94] D. Adams *et al.*; Phys. Lett. B 329 (1994), 399-406.
- [Ada 97a] D. Adams *et al.*; Phys. Lett. B 396 (1997), 338-348.
- [Ada 97b] D. Adams *et al.*; Phys. Rev. D 56 (1997), 5330-5358.
- [Alb 97] D. Albers *et al.*; Phys. Lett. 78 (1997), 1652-1655.
- [All 72] A.C. Allison; Phys. Rev. A Vol. 5, No. 6 (1972), 2695-2696.
- [Ant 93] E 142: P.L. Anthony *et al.*; Phys. Rev. Lett. 71 (1993), 959-962.
- [Ard 73] M.v. Ardenne, Tab. z. ang. Physik III, Berlin 1973.
- [Aud 71] C. Audoin *et al.*; Adv. in At. and Mol. Phys. Vol. 7; Academic Press N.Y. 1971.
- [Avo 76] A. Avogadro and M.Villa; J. Chem. Phys. 66, No. 6 (1977), 2359-2367.
- [Bar 93] D.P. Barber *et al.*; Nucl.Instr.Meth. A 329 (1993), 79-111.
- [Bar 94] D.P. Barber *et al.*; Nucl.Instr.Meth. A 338 (1994), 166-184.
- [Bau 96] C. Baumgarten; Diplomarbeit, Hamburg 1996.
- [Be 94] T. Benisch; Diploma Thesis, Univ. Erlangen-Nürnberg 1994.
- [Be 98] T. Benisch; Ph.D. Thesis, Universität Erlangen 1998.
- [Bec 85] R. Becker; Theorie der Wärme, Springer 1985.
- [Ben 83] J. Benard; Adsorption on Metal Surfaces; Elsevier, Amsterdam 1983.

- [Ber 73] S.L. Bernasek *et al.*; Phys. Rev. Lett. 30 (1979), 1202-1204.
- [Bli 98] R. Blinc *et al.*; J. Phys.: Cond. Matter 10 (1998), 6813-6824.
- [Blo 48] N. Bloembergen, E.M. Purcell and R.V. Pound; Phys. Rev. 73 (1948), 679-712.
- [Blo 59] N. Bloembergen, S. Shapiro, P.S. Pershan and O. Artman; Phys. Rev. 114 (1959), 445-479. Reprint in: J. Weber (Edt.); Masers, Gordon and Breach (1967), 454-468.
- [Boh 98] J. Boh, G. Eilmsteiner, K.D. Rendulic, A. Winkler; Surf. Sci. 395 (1998), 98-110.
- [Bor 98] H. Borel for the E155 coll.; Proc. Int. Worksh. on DIS and QCD, DIS 98; World Scientific (1998), 607.
- [Bou 63] M.-A. Bouchiat; Le Journal de Physique 24 (1963), 379-390 u. 611-621.
- [Bou 65] M.-A. Bouchiat and J. Brossel; Phys. Rev. 147, No. 1 (1966), 41-54.
- [Br 91] B. Braun, Diplomarbeit, MPI Heidelberg, 1991.
- [Br 95] B. Braun, Dissertation, LMU München, 1995.
- [Bra 92] S. Brandt; Datenanalyse, BI-Wissenschaftsverlag 1992.
- [Brg 65] H.C. Berg; Phys. Rev. A 137 (1965), 1621-1634.
- [Bro 79] I.N. Bronstein, K.A. Semendjajew; Moscow 1979.
- [Ca 87a] J.C. Camparo, J. Chem. Phys. 86, Vol. 3 (1987), 1533-1539.
- [Ca 87b] J.C. Camparo, R.P. Frueholz and B. Jadászliwer; J. Appl. Ph. 62 (1987), 676-681.
- [Cam 99] L.M. Cameron and C.A. Sholl; J. Phys.: Cond. Matter 11 (1999), 4491-4497.
- [Chu 90] M.-R. Chudoba, U. Memmert and D. Fick; Surf. Sci. 245 (1991), 180-190.
- [Coh 77] C. Cohen-Tannoudji, B. Diu, F. Laloë; Quantum Mechanics Vol. II (1977).
- [Con 78] H. Conrad, G. Ertl and J. Küppers; Surf. Sci. 76 (1978), 323-342.
- [Cha 67] E. Chanoch Beder; Adv. in At. and Mol. Phys. Vol. 2; Academic Press N.Y. 1967.
- [Chr 76] K. Christmann and G. Ertl; Surface Science 60 (1976), 365-384.
- [Dal 67] A. Dalgarno and W.D. Davison; Adv. in At. and Mol. Phys. Vol. 3; Academic Press N.Y. 1967.
- [Des 76] M. Desaintfusicion, C. Audoin; Phys. Rev. A 13 (1976), 2070-2073.
- [Dre 83] W. Drewes, H. Jänsch, E. Koch and D. Fick; Phys. Rev. Lett. 50 (1983), 1759-1762.
- [Due 90] M. Düren, A Luminosity Monitor for the HERMES Exp., DESY-HERMES 5/90.
- [Ebi 98] H.D. Ebinger *et al.*; Surf. Sci. 412/413 (1998), 586-615.
- [Ehr 94] Gert Ehrlich; Surf. Sci. 299/300 (1994), 628-642.
- [Eil 96] G. Eilmsteiner, W. Walkner, A. Winkler; Surf. Sci. 352-354 (1996), 263-267.

- [Eng 78] T. Engel and G. Ertl; *J. Chem. Phys.* 69 (1978), 1267-1281.
- [Fed 97] J.A. Fedchak *et al.*; *Nucl. Instr. Meth. A* 391 (1997), 405-416.
- [Fic 71] D. Fick, *Einführung in die Physik mit polarisierten Teilchen*; BI Mannheim 1971.
- [Fin 75] H.-U. Finzel *et al.*; *Surf. Sci.* 49 (1975), 577-605.
- [Fir 96] R.B. Firestone and V.S. Shirley (Edts.); *Table of Isotopes*, 8th Edt., Vol. 1; Wiley-Interscience, N.Y. 1996.
- [Flo 67] E.A. Flood (Edt.); *The Solid-Gas Interface*, Vol. 1; Marcel Dekker, N.Y. 1967.
- [Fre 57] J.L. Frenkel; *Statistische Physik*, Akademie Verlag, Berlin 1957.
- [Fra 77] H. Frank, H. Hoinkes and H. Wilsch; *Surf. Sci.* 63 (1977), 121-142.
- [Fun 95] U. Funk; *Diplomarbeit*, Univ. Heidelberg 1995.
- [Gau 92] H.-G. Gaul and E. Steffens; *Nucl. Instr. Meth. A* 316 (1992), 297-305.
- [Gel 71] A. Gelb and Shoon K. Kim, *J. of Chem. Ph.* 55 (1971), 4935-4939.
- [Ghi 80] E. Ghio, L. Mattera, C. Salvo, F. Tommasini and U. Valbusa; *J. Chem. Phys.* 73 (1980), 556-561.
- [Gil 93] R. Gilman *et al.*; *Nucl. Instr. Meth. A* 327 (1993), 277-286.
- [Gol 61] H.M. Goldenberg, D. Kleppner and N.F. Ramsey; *Phys. Rev.* 123 (1961), 530-537.
- [Gom 90] Robert Gomer; *Rep. Prog. Phys.* 53 (1990), 917-1002.
- [Got 66] Kurt Gottfried; *Quantum Mechanics Vol. I*; Benjamin N.Y. 1966, 427-433.
- [HER 90] HERMES-Proposal, HERMES Collaboration 1990.
- [HER 93] HERMES Technical Design Report, HERMES Coll. 1993.
- [HER 97] HERMES Coll.; *Phys. Lett. B* 404 (1997), 383-389.
- [HER 98a] HERMES Coll.; *Phys. Lett. B* 442 (1998), 484-492.
- [HER 98b] HERMES Coll.; *Phys. Rev. Lett.* 6, vol.82 (1999), 1164.
- [HER 98c] HERMES Coll.; *Nucl. Instr. Meth. A* 417 (1998), 230-265.
- [HER 98d] HERMES Coll.; *Phys. Rev. Lett.* 81, No. 25 (1998), 5519-5523.
- [HER 98e] HERMES Coll.; *Phys. Lett. B* 444 (1998), 531-538.
- [HER 99a] HERMES Coll.; *Phys. Rev. Lett.* 82, No. 15 (1999), 3025-3029.
- [HER 99b] HERMES Coll.; *Phys. Lett. B* 464 (1999), 123-134.
- [Hae 67] W. Haeberli, *Ann. Rev. Nucl. Sci.* 17 (1967), 373.
- [Hag 86] R.F. Haglund, D. Fick, B. Horn and E. Koch; *Hyperfine Interactions* 30 (1986), 73-108.

- [Hal 80] K. Halbach; Nucl. Instr. Meth. 169 (1980), 1-10.
- [Har 81a] J. Harris and B. Kasemo; Surf. Sci. (Lett.) 105 (1981), L281-L287.
- [Har 81b] J. Harris, B. Kasemo and E. Törnquist; Surf. Sci. (Lett.) 105 (1981), L288-L296.
- [HTB 90] P. Hänggi, P. Talkner and M. Borkovec; Rev. Mod. Phys. 62 (1990), 251-341.
- [Hen 98] M. Henoeh; Diploma thesis, Universität Münster 1998.
- [Her 61] R. Herman and H. Margenau; Phys. Rev. 122 (1961), 1204-1206.
- [Hoi 80] H. Hoinkes; Rev. Mod. Phys. 52 (1980), 933-970.
- [Hol 94] Stephen Holloway; Surf. Sci. 299/300 (1994), 656-666.
- [Hlm 71] U. Holm and H. Ebinghaus; NIM 95 (1971),39-44.
- [Hor 82] B. Horn, W. Drewes and D. Fick; Z. Phys. B 48 (1982), 335-345.
- [Jac 94] T.A. Jachimowski and W.H. Weinberg; J. Chem. Phys. 101 (1994), 10997-11003.
- [Jac 63] I.S. Jacobs and C.P. Bean in: Magnetism Vol. 3 (Edts. G.T. Rado and H. Suhl), Academic Press 1963.
- [Kam 95] Th. Kammler, S. Wehner and J. Küppers; Surf. Sci. 339 (1995), 125-134.
- [Kit 69] C. Kittel: *Thermal Physics*; John Wiley & Sons, Inc.; N.Y. 1969.
- [Kit 86] C. Kittel: *Introduction to Solid State Physics, 6th Edition*; John Wiley & Sons, Inc.; N.Y. 1986.
- [Kle 80] R.L. Kleinberg and B.G. Silbernagel; Solid State Comm. Vol. 33 (1980), 867-871.
- [Kle 98] Hubertus Kleine; PhD-Thesis, Verlag Görlich und Weiershäuser, Marburg 1998.
- [Klp 62] D. Kleppner, H.M. Goldenberg and N.F. Ramsey; Phys. Rev. 126 (1962), 603-615.
- [Kni 88] R.J. Knize, Z. Wu, W. Happer; Adv. in At. and Mol. Phys. Vol. 24; Academic Press N.Y. 1988.
- [Ko 98] H. Kolster, Dissertation LMU München 1998.
- [Koc 99] N. Koch; Ph.D. thesis, Univ. Erlangen 1999.
- [Koe 88] J.M.V.A. Koelman *et al.*; Phys. Rev. A, Vol. 38, No. 7 (1998), 3535-3547.
- [Kol 94] D.D. Koleske and S.M. Gates; J. Chem. Phys. 101 (1994), 3301-3309.
- [Kor 83] J.P. Korb, D.C. Torney and H.M. McConnell; J. Chem. Phys. 78 (1983), 5782-5789.
- [Kor 84] J.P. Korb, M. Winterhalter and H.M. McConnell; J. Chem. Phys. 80 (1984), 1059-1068.
- [Kor 83] J.P. Korb *et al.*; J. Chem. Phys. 86 (1987), 1125-1130.
- [Kor 83] J.P. Korb *et al.*; J. Chem. Phys. 93 (1990), 1965-1972.
- [Kra 96] P. Kratzer and W. Brenig; Z. Phys. B 99 (1996), 571-576.

- [Kui 91] E.W. Kuipers, A. Vardi, A. Danon, A. Amirav; Phys. Rev. Lett. 66 (1991), 116-119.
- [Len 99] Paolo Lenisa; *private communication*. See also:
http://hermes.fe.infn.it/SemReport/sem_report.htm to be published as HERMES internal report.
- [Lev 88] C.D.P. Levy and P.W. Schmor; J. Appl. Phys. 63, No. 10 (1988), 4819-4822.
- [Lid 98] David R. Lide; Handbook of Chemistry and Physics, CRC Press, 79th Ed. 1998-1999.
- [Lor 93] Bernd Lorentz, Diploma thesis, Heidelberg 1993.
- [Loz 97] W. Lorenzon; 7th Int. Workshop on Pol. Gas Targets and Pol. Beams; AIP Conf. Proc. 421, Urbana-Champaign 1997.
- [Mar 59] H. Margenau, P. Fontana and L. Klein; Phys. Rev. 115 (1959), 87-92.
- [Mem 88] U. Memmert *et al.*; Hyperfine Interactions 39 (1988), 295-302.
- [Mes 90] A. Messiah, Quantenmechanik II, Berlin 1990.
- [Mey 98] H.O. Meyer *et al.*; Phys. Rev. Lett. 81 (1998), 3096.
- [Mil 97] R.G. Milner; Nucl. Phys. A 622 (1997), 16c-30c.
- [Oh 70] Saewoong Oh; Nucl. Instr. Meth. 82 (1970), 189-197.
- [PPB 98] Particle Physics Booklet, July 1998, Springer, <http://pdg.lbl.gov/>.
- [Phi 87] R.J. Philpott; Nucl. Instr. Meth. A259 (1987), 317-323.
- [Pri 93] J.S. Price and W. Haeberli; Nucl. Instr. Meth. A 326 (1993), 416-423.
- [Pri 94] J.S. Price and W. Haeberli; Nucl. Instr. Meth. A 349 (1994), 321-333.
- [Prz 98] B. v. Przewoski *et al.*; Phys. Rev. C 58 (1998), 1897-1912.
- [Pur 56] E.M. Purcell and G.B. Fields; Astrophys. J. 124(1956), 542-549.
- [Rab 37] I.I. Rabi; Phys. Rev. 51 (1937), 652-654.
- [Rad 63] G.T. Rado and H. Suhl (Edts.); Magnetism Vol. I, Academic Press, N.Y. 1963.
- [Rap 65] D. Rapp and P.E. Golden, J. Chem. Ph. 43 (1965), 1464-1479.
- [Rat 98] F. Rathmann *et al.*; Phys. Rev. C 58 (1998), 658-673.
- [Ree 80] David A. Reed and Gert Ehrlich; Surf. Sci. 102 (1981), 588-609.
- [Ret 92] C.T. Rettner; Phys. Rev. Lett. 69 (1992), 383-386.
- [Ret 94] C.T. Rettner; J. Chem. Phys. 101 (1994), 1529-1546.
- [Ric 73] P.M. Richards and M.B. Salamon, Phys. Rev. B, Vol 9, Number 1 (1974), 32-45.
- [Ric 78] P.M. Richards, Solid State Comm. 25 (1978), 1019-1021.
- [Rie 79] C. Riekel *et al.*; J. Chem. Phys. 71 (1979), 530-537.

- [Ro 92] A.D. Roberts *et al.*; Nucl. Instr. Meth. A 322 (1992), 6-12.
- [Rob 93] M.W. Roberts; Surf. Sci. 299/300 (1994), 769-784.
- [Rol 64] S. Ross and J.P. Olivier; On Physical Adsorption, Interscience, N.Y. 1964.
- [Rot 90] A. Roth; Vacuum Technology, 3rd Ed., Elsevier, Amsterdam 1990.
- [San 87] D.P. Sanderson, S.P. Van Verst, G.A. Hall, B.G. Schmidt, D.E. Trcka, K.R. Chapman, K.W. Kemper and R.J. Philpott; Nucl. Instr. Meth. A 259 (1987), 324-328.
- [Sch 91] P. Schiemenz, A. Ross and G. Graw; Nucl. Instr. Meth. A 305 (1991), 15-18.
- [Sha 87] M.B. Shah, D.S. Elliott and H.B. Gilbody, J. Phys. B 20 (1987), 3501.
- [She 98] D. De Shepper *et al.*; Nucl. Instr. Meth. A 419 (1998), 16-44.
- [Sho 81] C.A. Sholl; J. Phys. C, 14 (1981), 447-464.
- [Sho 92] P.C.L Stephenson and C.A. Sholl; J.Phys.: Condens. Matter 5 (1993), 2809-2824.
- [Sil 74] B.G. Silbernagel and F.R. Gamble; Phys. Rev. Lett. 32 (1974), 1437.
- [Sli 64] C.P. Slichter: Principles of Magnetic Resonance; Harper & Row, N.Y. 1963.
- [Sol 64] A.A. Solokov und I.M. Ternov, Sov. Phys. Dokl. 8 (1964), 1203-1205.
- [Som 47] A. Sommerfeld; Partielle Differentialgleichungen der Physik, Leipzig 1947; Nachdruck von Harri Deutsch, Thun 1978.
- [Som 93] G.A. Somorjai; Surf. Sci. 299/300 (1994), 848-866.
- [St 95a] J. Stenger; Dissertation, Universität Erlangen Nürnberg 1995.
- [St 95b] J. Stenger and K. Rith; Nucl. Instr. Meth. A 361 (1995), 60-71.
- [Ste 94] M. Stephens, R. Rhodes and C. Wieman; J. Appl. Phys. 76, Vol. 6 (1994), 3479-3488.
- [Sti 67] R.E. Stickney; Atomic and Molecular Scattering From Solid Surfaces, in: Advances in Atomic and Molecular Physics Vol. 3; Academic Press N.Y. 1967.
- [Stn 21] W. Gerlach und O. Stern: Z. Physik 8 (1921), 110.
- [Sto 94a] F. Stock, Dissertation, MPI Heidelberg 1994.
- [Sto 94b] F. Stock *et al.*; Nucl. Instr. Meth. A 343 (1994), 334-342.
- [Sto 94c] F. Stock *et al.*; Contr. to SPIN 94, Bloomington (1994).
- [Sto 2000] Uta Stoesslein; *private communication*.
- [Sth 92] R. Storch, H. Stolz and H.W. Wassmuth; Ann. Physik 1 (1992), 315-320.
- [Str 63] R.L. Stratonovich; Topics in the Theory of Random Noise; Gordon and Breach, London 1961, 1967, 1981.
- [Stw 95] J. Stewart *et al* in: 6th Int. Workshop on Pol. Beams and Pol. Gas Targets, Cologne 1995; World Scientific 1996.

- [Stw 97] J. Stewart; 7th Int. Workshop on Pol. Gas Targets and Pol. Beams; AIP Conf. Proc. 421, Urbana-Champaign 1997.
- [Stw 98] J. Stewart, P. Lenisa; *private communication*.
- [Swe 88] D.R. Swenson und L.W. Anderson, Nucl. Instr. Meth. B 29 (1988), 627-642.
- [Ter 99] A. Terkulov, R. Potashov; *private communication*, 1999.
- [Tho 87] G.E. Thomas *et al.*; Nucl. Instr. Meth. A 257 (1987), 32-34.
- [Tom 78] F.C. Tompkins; Chemisorption of Gases on Metals; Academic Press, London 1978.
- [Tor 53] H.C. Torrey; Phys. Rev. 92 (1953), 962-969.
- [Tow 92] J.S. Townsend; Quantum Mechanics, McGraw-Hill 1992.
- [Wac 76] I.E. Wachs and R.J. Madix; Surface Science 58 (1976), 590-596.
- [Wag 79] H. Wagner in: Sol. Surf. Phys. (Springer Tracts on Modern Physics Vol. 85); Springer 1979.
- [Wal 93] T. Walker and L.W. Anderson; Nucl. Instr. Meth. A 334 (1993); pp. 313.
- [Wan 95] W. Wander *et al.*; HERMES interner Report 40, 1995.
- [Wea 78] H.T. Weaver, J.E. Schirber and B.G. Silbernagel; Sol. State Comm. 28 (1978), 21-25.
- [Wei 98] C. Weiskopf; Diploma Thesis, Universität Erlangen 1998.
- [Wise 99] Tom Wise; *private communication* 1999.
- [Wit 56] J.P. Wittke and R.H. Dicke; Phys. Rev. 103 (1956), 620-631.

Lebenslauf

Name	Christian Baumgarten
geboren	am 21.06.1965 in Hannover
Staatsangehörigkeit	deutsch
Familienstand	ledig
Schulbildung	1971-1976 Grundschule in Pattensen bei Hannover 1976-1981 Gymnasium in Hannover, Abschluß mittlere Reife 1981-1982 Lehre als Betriebsschlosser in Hannover 1983-1985 Gymnasium in Hamburg, Abschluß Abitur in den Hauptfächern Physik und Kunst
Zivildienst	1986-1987 zuerst in der Altenpflege, später individuelle Schwerbehindertenbetreuung
Studium	1988-1996 Studium Physik mit Nebenfach Philosophie an der Universität Hamburg, Abschluß Diplom
Diplomarbeit	<i>Aufbau und Kalibration eines Gasanalysators für das HERMES-Wasserstofftarget</i>
Lehrtätigkeiten	Betreuung von Übungsgruppen zur Vorlesung <i>Mathematik für Physiker</i> , Betreuung eines Praktikums zur Meßdatenerfassung mit dem PC
Nebentätigkeiten	Entwicklung einer Software zur Datenaufnahme und Experimentsteuerung im FB Physik der Uni Hamburg, Tätigkeit als freier Software Entwickler bei HAB Software Hamburg, Veröffentlichung eines IT-Fachbuches mit dem Titel <i>Systemnahe Programmierung mit Borland-Pascal</i>
Wissenschaftliche Tätigkeit	Seit 1997 als wissenschaftlicher Mitarbeiter an der Ludwigs-Maximilians-Universität München
Aufgaben im Rahmen des HERMES Experiments	Einstellung und Kalibration des Target Polarimeters, Vorbereitung und Durchführung der Umstellung von Wasserstoff auf Deuterium, Modifikation und Pflege der Software zur Steuerung des Targets, Durchführung und Analyse von Targetstudien und die Errechnung der systematischen Ungenauigkeit der Targetpolarisation